FORCED EMISSIONS OF NONLINEAR WATER WAVES IN CHANNELS OF ARBITRARY SHAPE

Thesis by

Michelle Hsiao Tsing Teng

In Partial Fulfillment of the Requirements

for the Degree of

Doctor of Philosophy

California Institute of Technology

Pasadena, California

1990

(Submitted May 7, 1990)

Dedicated to

the High School attached to Qinghua University, Beijing, China

ACKNOWLEDGMENTS

My sincere thanks and respects go to my thesis advisor, Professor Theodore Yao-Tsu Wu, who suggested the topic and offered the most valuable guidance throughout my graduate study.

Special thanks are due Dr. George T. Yates for his kindness, patience and valuable help and advice. I appreciate greatly the assistance from Mr. Raymond Mak in carrying out the experiments. I am also indebted to Dr. Keh-Han Wang, who was always ready to help and discuss the problems with me.

I am very grateful to Professors Norman H. Brooks, Anthony Leonard, Daniel I. Meiron and Fredric Raichlen, who served on my committee, and my thanks go to all professors who have ever taught me in Caltech.

Friends from the graduate dormitory Keck House have made Caltech a warm place to stay.

My deepest appreciation goes to my parents, Aimin Shi and Zichao Deng, who have provided me with constant love and support. Mom and Dad always dreamed of their only child becoming a Ph.D., and Dad, who studied and taught fluid mechanics in China, is the person who led me into this wonderful field.

I gratefully acknowledge financial support from the National Science Foundation, the Office of Naval Research, the Powell Foundation Graduate Fellowship and the California Institute of Technology.

ABSTRACT

This thesis is a joint theoretical, numerical and experimental study concentrated on investigating the phenomenon of weakly nonlinear, weakly dispersive long water waves being generated and propagating in a channel of arbitrary cross section. The water depth and channel width are assumed comparable in size and they may vary both in time and space. Two types of theoretical models, i.e., the generalized channel Boussinesq (gcB) two-equation model and the forced channel Korteweg-de Vries (cKdV) model, are derived by using perturbation expansions for quasi-one-dimensional long waves in shallow water. In the special case for channels of variable shape and dimension but fixed in time, the motion of free traveling solitons may be calculated by our models to predict their propagation with modulated amplitude, velocity and phase. In the precence of external forcings, such as a surface pressure distribution or a submerged obstacle moving with a near critical speed, solitary waves can be produced periodically to advance upstream. Analytical solutions for three specific cross-sectional shapes, namely, the rectangular, triangular and semi-circular sections, are obtained in closed form and with the main features of the solutions examined. The specific geometry of the cross section is found to affect only the magnitude of the dispersive terms in the equations. For a submerged moving object taken as an external forcing, its effective strength of forcing is directly related to the blockage-ratio of the cross-sectional area. Our long-wave models have their useful applications to the areas of river dynamics, near-coastal engineering, and other related fields.

TABLE OF CONTENTS

I. INTRODUCTION

In recent years, theory of nonlinear water waves has been a very active field and the subject of long waves in nonuniform medium, which is of particular interest here, has also received considerable attention. Peregrine[21] studied waves climbing up a sloping beach; Peters[23] and Peregrine[22] investigated waves traveling in a straight uniform channel with arbitrary cross section. David, Levi and Winternitz[4] studied the propagation of large solitary waves in a wide marine strait whose width is much larger than its depth. The propagation of long waves in a rectangular channel with spatially varying depth and width was investigated by Shuto[26] who obtained a KdV-type equation with variable coefficients for wave motions in the channel. Chang et al.[2] carried out numerical and experimental studies on the evolution of a solitary wave traveling in a rectangular channel with a linearly varying width but a uniform depth, and with their numerical computations based on Shuto's equation. Similarly, a variable coefficient K-P (Kadomtsev-Petviashvili) equation for the weakly three-dimensional case has been derived by David, Levi and Winternitz[4]. A set of long wave equations in the Lagrangian description was obtained by Zelt[31] to study the long wave response of bays and harbors. An analytical harbor response model, capable of treating narrow rectangular harbors with variable bathymetry and sidewall geometry, was developed and applied to several simple geometries. He also applied a three-dimensional finite element model to investigate the runup of solitary waves on a coastline with variable bottom topography and a curved shoreline. Zelt's models included the study of the viscous dissipation in long wave propagations. In these studies, channel width and depth are permitted to vary only in space but not with time. In addition, no external forcings have been considered.

Several studies have been directed to investigate the phenomenon of long wave generations. Solitary waves can be generated in many ways. They can be generated by evolution from an initial hump of water (Hammack and Segur[9]), by boundary forcing at one end of a semi-infinite physical domain (Chu et al.[3]; Camassa and Wu[1]), or by a moving disturbance with a near-critical speed. In the last case, a moving disturbance can be a pressure distribution moving on the free surface (Wu and Wu[28]; Ertekin[6]; Ertekin et al.[7]; Katsis and Akylas[11]), a topography moving along the bottom of a channel (Lee[14]; Lee, Yates and Wu[15]) or submerged moving slender bodies, like a ship, in a water channel (Mei[17]). The salient features of soliton generation by steadily moving disturbances are that a series of solitons are generated periodically in a vicinity of the disturbance, to advance, in succession, upstream of the disturbance with a greater speed, while a train of weakly nonlinear and weakly dispersive waves develop downstream of a region of depressed water surface immediately trailing behind the disturbance.

To describe the phenomena of forced generation of nonlinear water waves, many different models have been developed and applied. Wu and Wu[28] carried out numerical computations based on the generalized Boussinesq equations which allow multi-directional motions and give detailed three-dimensional features of the wave field. The simplest model is perhaps the forced KdV equation which can be applied, as in Lee's case, to the two-dimensional, unidirectional traveling and near-resonant forced waves. Another model, called the forced Kadomtsev-Petviashvili (fKP) equation, was studied by Katsis and Akylas[11]. The forced KP equation is valid for quasi-two-dimensional case and allows weak variations in the transverse direction of the channel. Lepelletier[16] carried out both theoretical and experimental studies to investigate the process of excitation of harbors and bays by transient nonlinear long waves. In addition, nonlinear shallow water waves

generated in a closed rectangular basin by the motion of the basin and the effects of viscous dissipation in a harbor with simple geometry were also examined. However, in these studies of forced waves, most of the papers are confined to investigations of generation of waves in a straight uniform rectangular channel, rather than on the effects of varying depth and width or of different geometries of the channel cross section.

The main objective of the present study is to investigate the more general case of generation and propagation of nonlinear long waves in a water channel with arbitrary cross section and with moving disturbances as external forcings. The width and the depth of the channel are assumed to be of the same order in magnitude and can vary both in space and time. As is proper for a long wave model, the characteristic lengths of the cross section are supposed to be much smaller than a typical wavelength, we may assume that the detailed wave features in the cross-flow plane are less important than those in the longitudinal direction, so that it is meaningful to integrate all quantities over the cross section of the channel to obtain the section-mean equations. For the general case of varying width and depth, we develop the two-equation model which we call the "generalized channel Boussinesq model". This two-equation model can be further reduced to a one-equation model, or the forced channel KdV equation (with variable coefficients) for the unidirectional motion near resonance. In Chapter II, the detailed derivations of our two theoretical models by using perturbation expansions are presented. Several topics associated with these models, e.g., the validity criteria, the conservation of mass and energy, and the existence of steady solutions of waves of permanent form for both models, are analysed and discussed. We study the effects of various cross-sectional geometrical shapes by examining three specific configurations, i.e., rectangular, triangular and semi-circular cross sections. The theoretical results

show that the difference in shape of the cross section only affects the coefficients of the dispersive terms in the gcB model and in the cKdV equation, with no effects on the other terms in the equation, provided the mean hydraulic depth remains the same. Based on our models, we also find that the effective strength of a three-dimensional external forcing is directly related to the area blockage ratio of the moving disturbance to the cross-sectional area.

Our two theoretical models are applied to study the evolution of a free solitary wave propagating in a channel of variable section. This problem of evolution of free solitary waves is interesting and important to study, not only for its significance in the physical contexts, but also for its providing a fundamental case to investigate the general validity of the cKdV equation. Since the cKdV equation is derived only for unidirectional wave motion, it should not be able to account for the reflected wave traveling in the opposite direction that must arise as the main wave is continually transmitted while traveling forward in a gradually variable channel. A natural consequence to this is that the cKdV does not conserve mass. In our studies, we carried out numerical computations based on both the gcB and the cKdV models. Since gcB model permits multi-directional motions and conserves mass exactly, by comparing the results between the two models, we are able to examine the conservation properties and the validity criteria of the cKdV model. Our numerical results show that even the cKdV equation does not conserve mass by a large margin on account of the reflected wave that actually transports some mass away or into the main transmitted wave, it still provides quite a good prediction for the magnitude and the phase velocity of the main transmitted wave. The detailed analysis and numerical results can be found in Chapter IV.

We performed laboratory measurements to investigate the long wave generation by three-dimensional submerged moving objects in a rectangular shallow

water tank. The experimental results are seen to confirm the theoretical conclusion drawn from the wave models that the effective strength of a moving disturbance is directly related to the blockage ratio of the cross-sectional area. Various numerical calculations were also carried out based on both models for the forced cases to examine the effect of the speed, the longitudinal length and the geometric shape of the external forcings. The discussions and results regarding the forced generation of nonlinear long waves are presented in Chapter V.

II. THEORY OF GENERATION AND PROPAGATION OF NONLINEAR WATER WAVES

In this chapter, certain theoretical models of the generation and propagation of weakly nonlinear, weakly dispersive and weakly forced waves in shallow water will be presented. The study is concentrated on modeling long waves being generated and propagating in a channel with variable cross sections. Two types of theoretical models — the generalized channel Boussinesq two-equation model (gcB) and the forced channel Korteweg-de Vries (cKdV) one-equation model — are derived by using perturbation expansions. The models can be applied to channels of arbitrary shape, which may vary gradually in space and time. Such applications are illustrated for three specific cross-sectional shapes, namely, rectangular, triangular and semi-circular cross sections. The effective strength of a submerged disturbance as an external forcing function and the effect of a specific geometry of the cross section are examined. Discussions on the general properties of the two models, including results regarding their validity criteria, the conservation laws and the existence of permanent wave form solutions, will also be presented.

2.1 The Physical Background and the Basic Assumptions

A sketch of the water channel is shown in Figure 2.1. The fluid in the channel will be assumed inviscid and incompressible, with constant density ρ, and the flow, irrotational. The effects of surface tension are neglected. The width and depth of the channel are taken to be of the same order, and for simplicity, to be symmetric about the mid-channel $x - z$ plane. The long wave assumption implies that a typical wavelength of the surface wave $\zeta(x, y, t)$ is much greater than the characteristic lengths in the cross-flow plane.

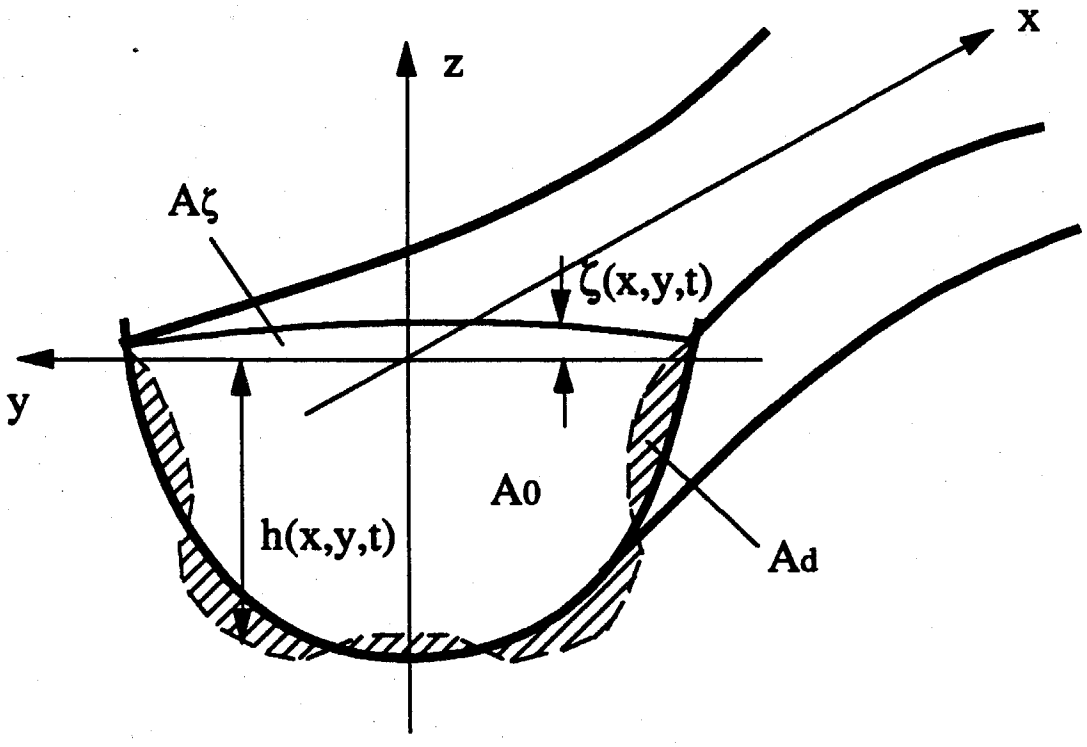

Figure 2.1 A channel with variable cross sections

Thus we consider the motion of three-dimensional water waves of rather arbitrary amplitude and wave number (in two horizontal dimensions x, y), propagating in a channel with variable cross section of arbitrary shape, provided it is not too wide compared to its depth and there are no excessively sloped banks. Also the centerplane of the channel is assumed to be straight. The water in the channel is supported by the bottom $z = -h(x, y, t)$ from underneath, has its free surface displaced at time t to $z = \zeta(x, y, t)$, and has this surface extended across the channel to the waterline at $y = \pm b(x, y)$, at which the bank may be vertical or inclined with a slope.

2.2 The Basic Equations

The motion of the water, with velocity $\mathbf{U} = (u, v, w)$ and the pressure $p(x, y, z, t)$, satisfies the Euler equations

$$\nabla \cdot \mathbf{U} = 0, \tag{2.1}$$

$$\frac{d\mathbf{U}}{dt} \equiv \mathbf{U}_t + \mathbf{U} \cdot \nabla \mathbf{U} = -\frac{1}{\rho} \nabla p_e, \qquad (p_e = p + \rho g z) \tag{2.2}$$

and the boudary conditions

$$w = \frac{d\zeta}{dt} = \zeta_t + u\zeta_x + v\zeta_y, \qquad z = \zeta(x, y, t), \ |y| < b(x, t), \tag{2.3}$$

$$p = p_a(x, y, t), \qquad z = \zeta(x, y, t), \ |y| < b(x, t), \tag{2.4}$$

$$w = -\frac{dh}{dt} = -(h_t + uh_x + vh_y), \qquad z = -h(x, y, t), \tag{2.5}$$

$$v = \pm(b_t + ub_x), \qquad y = \pm b(x, t), \tag{2.6}$$

where $\nabla = (\partial_x, \partial_y, \partial_z)$ denotes a vector differential operator, p_e is the excess pressure, p_a the specified ambient surface pressure, and g the constant acceleration

due to gravity. The flow is assumed irrotational, so that the velocity potential $\phi(x, y, z, t)$, where $\mathbf{U} = \nabla\phi$, satisfies the Laplace equation,

$$\nabla^2\phi = 0, \tag{2.7}$$

and we also have the Bernoulli equation

$$\frac{\partial\phi}{\partial t} + \frac{1}{2}\mathbf{U}^2 + \frac{p}{\rho} + gz = \frac{p_\infty}{\rho}, \tag{2.8}$$

where p_∞ is a constant reference pressure.

Equations (2.1)-(2.8) present a complicated three-dimensional nonlinear system whose direct solutions are in general difficult to determine, whether by analytical or numerical methods. The goal of the present study is to derive from this set of basic equations appropriate theoretical models for specific wave problems of interest. The theoretical models we obtain will be convenient for numerical computations and can give insights into certain physical features like the conservation properties and energy exchange between the waves generated and the external forcing.

2.3 The Section-Mean Approach

The basic long-wave-model assumption implies that the main wave features manifest primarily in the longitudinal direction whereas the detailed three-dimensional wave motions in the cross-flow direction are less important. Thus we can integrate (2.1) and (2.2) over the wetted cross-sectional area to obtain a set of one-dimensional section-mean equations which describe the dominant wave motions in the x-direction. It will be seen that the detailed three-dimensional wave features can nevertheless be recovered after the section-mean flow is determined.

We define a section-mean quantity as

$$\bar{f}(x,t) = \frac{1}{A}\int\int_A f(x,y,z,t)dydz, \tag{2.9}$$

where A is the wetted cross-sectional area, which is yet unknown. By applying Reynolds' transport theorem on a material volume $V(t)$ which at time t coincides with a vertical column of water lying between two sections at two different locations, we can show, using the kinematic conditions (2.3), (2.5) and (2.6), that,

$$\langle \frac{df}{dt} \rangle = \frac{\partial}{\partial t}\langle f \rangle + \frac{\partial}{\partial x}\langle uf \rangle, \tag{2.10}$$

or

$$A\overline{\frac{df}{dt}} = \frac{\partial}{\partial t}(A\bar{f}) + \frac{\partial}{\partial x}(A\overline{uf}), \tag{2.11}$$

where $\langle f \rangle$ is defined as $\langle f \rangle = A\bar{f} = \int\int_A f(x,y,z,t)dydz$. (A detailed proof of the section-mean transport theorem (2.10) and (2.11) is presented in Appendix I.)

A set of the section-averaged continuity, momentum and energy equations can be obtained by applying (2.11) to equations (2.1), (2.2) and (2.8). The quantities of particular interest are $f = 1, u, v, w$ and

$$f = H \equiv \frac{1}{2}\rho(u^2 + v^2 + w^2) + \rho gz = (p_\infty - p) - \rho\phi_t. \tag{2.12}$$

For H, we have

$$\langle H \rangle = \int_{-b}^{b} dy \int_{-h}^{\zeta} \frac{1}{2}\rho U^2 dz + \int_{-b}^{b} \frac{1}{2}\rho g(\zeta^2 - h^2)dy = E_k + E_p, \tag{2.13}$$

so $\langle H \rangle$ is the sum of the kinetic and potential energy density of a water slab of unit thickness in x. By taking these quantities in turn for f in (2.11), we obtain the following section-mean equations

$$A_t + (A\bar{u})_x = 0, \tag{2.14}$$

$$(A\bar{u})_t + (A\overline{uu})_x = -\frac{A}{\rho}\overline{p_x}, \tag{2.15}$$

$$(A\bar{v})_t + (A\overline{uv})_x = -\frac{A}{\rho}\overline{p_{ey}}, \tag{2.16}$$

$$(A\bar{w})_t + (A\overline{uw})_x = -\frac{A}{\rho}\overline{p_{ez}}, \tag{2.17}$$

$$(A\overline{H})_t + [A(\overline{H} + \frac{\bar{p}}{\rho})\bar{u}]_x = \frac{A}{\rho}\overline{p_t} - \frac{1}{\rho}\frac{\partial}{\partial t}(A\bar{p}). \tag{2.18}$$

These five equations give the section-mean conservation laws for mass, horizontal and vertical momenta and also energy. They are exact, aside from excluding dissipation. However, if we now consider the averaged quantities as our new unknowns, this set of equations is not closed, for there are more number of unknowns than number of equations.

For long wave models, the first two equations (2.14) and (2.15) are of our main interest, since they are directly associated with the dominant wave features in the longitudinal direction of the channel.

The total cross-sectional area can be written into three parts:

$$A(x,t) = A_0(x) - A_d(x,t) + A_\zeta(x,t), \tag{2.19}$$

where A_0 is the unperturbed wetted area, A_d the variation in area due to a moving boundary of the channel or a moving submerged body as forcing function, and A_ζ the area variation due to wave motions at the free surface.

Writing $A_0(x) - A_d(x,t) \equiv A_h(x,t)$ and $A_\zeta = 2b\tilde{\zeta}$, where

$$\tilde{(.)}(x,t) = \frac{1}{2b}\int_{-b}^{b}(.)(x,y,t)dy \tag{2.20}$$

is the sectional free-surface mean of (.), we can rewrite (2.14) and list it with (2.15) together as:

$$(2b\tilde{\zeta})_t + [(A_h + 2b\tilde{\zeta})\bar{u}]_x = -(A_h)_t, \tag{2.21}$$

$$(A\bar{u})_t + (A\overline{uu})_x = -\frac{A}{\rho}\overline{p_x}, \tag{2.15}$$

where the unknowns of interest are $\tilde{\zeta}$ and $\bar{u}$, while b and A_h are prescribed functions of x and t. Again this set of equations (2.21) and (2.15) is not sufficient to describe

the mean wave motions represented by $\tilde{\zeta}$ and $\bar{u}$, because there are four unknowns $\tilde{\zeta}$, $\bar{u}$, $\overline{uu}$ and $\overline{p_x}$ but only two equations. Our goal is to relate the two unknown variables $\overline{uu}$ and $\overline{p_x}$ to the two unknowns $\tilde{\zeta}$ and $\bar{u}$ in order to make the system closed. This can be accomplished, to a second-order approximation, by using the perturbation expansions and applying the Laplace equation (2.7) and the Bernoulli equation (2.8).

From the section-mean equations, a set of integral conservation laws for the excess mass, the total energy and other physical quantities can also be derived. These properties along with different invariants associated with our wave models will be discussed in a separate section later in this chapter.

2.4 Nondimensionalization

For the long wave models in question, we introduce the following dimensionless variables (with *)

$$x^* = x/\lambda,\ (y^*, z^*, \zeta^*, h^*, b^*) = (y, z, \zeta, h, b)/h_c,\ A^* = A/A_c,\ t^* = c_0 t/\lambda,$$

$$(u^*, v^*, w^*) = (u, v, w)/c_0,\ \phi^* = \phi/c_0\lambda,\ (p^*, p_a^*) = (p - p_\infty, p_a - p_\infty)/\rho g h_c, \quad (2.22)$$

where h_c is the typical constant mean water depth, λ a typical wavelength, A_c the unperturbed mean wetted cross-sectional area, and $c_0 = \sqrt{gh_c}$ is the linear critical wave speed.

Two important parameters, α and ϵ, arise from the nondimensionalization, namely,

$$\alpha = a/h_c, \qquad \epsilon = h_c/\lambda, \quad (2.23)$$

where a is a typical wave amplitude. In particular, we are interested in the Boussinesq class of wave motion characterized by $\alpha = O(\epsilon^2)$, which signifies that the nonlinear effects (scaled by α) and the dispersive effects (scaled by ϵ^2) are well

balanced with each other and are of equal importance in comparison with the net inertial effects.

Omitting *, we write the section-mean equations of motion and the Laplace equation and the Bernoulli equation in the nondimensional form as:

$$(2b\tilde{\zeta})_t + [(A_h + 2b\tilde{\zeta})\bar{u}]_x = -(A_h)_t, \tag{2.24}$$

$$(A\bar{u})_t + (A\overline{uu})_x = -A\overline{p_x}, \tag{2.25}$$

$$\phi_{xx} + \frac{1}{\epsilon^2}\phi_{yy} + \frac{1}{\epsilon^2}\phi_{zz} = 0, \tag{2.26}$$

$$p + \phi_t + \frac{1}{2}(\phi_x^2 + \frac{1}{\epsilon^2}\phi_y^2 + \frac{1}{\epsilon^2}\phi_z^2) + z = 0, \tag{2.27}$$

along with the boundary conditions at the free surface and on the channel walls:

$$\left.\frac{\partial\phi}{\partial n}\right|_{z=\zeta} = \epsilon^2(\zeta_t + u\zeta_x)/\sqrt{1+\zeta_y^2}, \tag{2.28}$$

$$p|_{z=\zeta} = p_a, \tag{2.29}$$

$$\left.\frac{\partial\phi}{\partial n}\right|_{z=-h} = \epsilon^2(h_t + uh_x)/\sqrt{1+h_y^2}, \tag{2.30}$$

$$\left.\frac{\partial\phi}{\partial y}\right|_{y=\pm b} = \pm\epsilon^2(b_t + ub_x), \tag{2.31}$$

where $\vec{n}$ is the unit outward normal to the boundary curve in the cross-flow plane of the channel.

In our case $A_0(x) = O(1)$ and $A_d(x,t)$, $A_\zeta(x,t) = O(\alpha)$ by assumption. It is clear that $\bar{u} = O(\alpha)$ by (2.24), while v and w are of $O(\alpha\epsilon)$ by (2.28)-(2.31) if $h_t, b_t = O(\alpha)$, $h_x, b_x = O(1)$, which we assume to hold. However, h_y, the section slope of the channel boundary, need not be limited to certain bounds, such as for vertical walls.

Our next step is to seek expressions for $\overline{uu}$ and $\overline{p_x}$ in terms of $\tilde{\zeta}$ and $\bar{u}$ so as to make the system (2.24)-(2.25) closed. This can be done by using perturbation

expansions based on the long wave assumptions and by applying the Bernoulli equation.

2.5 Perturbation Expansions

The above set of basic equations and boundary conditions and the relations between the velocity and its potential imply the following expansions for ϕ, u, v, w, and ζ:

$$\phi = \alpha[\phi_1(x,t) + \epsilon^2\phi_2(x,y,z,t) + O(\epsilon^4)], \tag{2.32}$$

$$\zeta = \alpha[\zeta_1(x,t) + \epsilon^2\zeta_2(x,y,t) + O(\epsilon^4)], \tag{2.33}$$

$$u = \phi_x = \alpha[u_1(x,t) + \epsilon^2 u_2(x,y,z,t) + O(\epsilon^4)], \tag{2.34}$$

$$v = \frac{1}{\epsilon}\phi_y = \alpha\epsilon[v_2(x,y,z,t) + O(\epsilon^2)], \tag{2.35}$$

$$w = \frac{1}{\epsilon}\phi_z = \alpha\epsilon[w_2(x,y,z,t) + O(\epsilon^2)], \tag{2.36}$$

where the first order terms in expansions (2.32), (2.33) and (2.34), which are independent of y and z on account of v and w being of $O(\alpha\epsilon)$, represent the dominant section-mean wave motion. Thus we see that $u - \bar{u} = O(\alpha\epsilon^2)$, $v - \bar{v} = O(\alpha\epsilon)$, $w - \bar{w} = O(\alpha\epsilon)$, and by (2.34) and (2.27),

$$\overline{uu} - \bar{u}\bar{u} = O(\alpha^2\epsilon^4), \tag{2.37}$$

$$p_e - \bar{p}_e = O(\alpha\epsilon^2, \alpha^2). \tag{2.38}$$

The last relation, where $p_e = p + z$, holds true throughout the depth and gives a measure of $|\frac{\partial p_e}{\partial z}| = O(\alpha\epsilon^2)$ for the assumption of the pressure being hydrostatic as generally adopted in classical long wave theory. In particular, at the free surface, (2.38) becomes $|(p_a + \zeta) - (\tilde{p}_a + \tilde{\zeta})| = O(\alpha\epsilon^2)$; hence if $|p_a - \tilde{p}_a| \leq O(\alpha\epsilon^2)$, then $|\zeta - \tilde{\zeta}| = O(\alpha\epsilon^2)$, indicating that the transverse variations of ζ from its transverse surface mean is always of higher order than $|\zeta|$, which is of $O(\alpha)$.

With $\overline{uu}$ approximated in (2.37), we now seek an expression for $\overline{p_x}$ in terms of $\bar{u}$ and $\tilde{\zeta}$. We apply the Bernoulli equation at the free surface and at an arbitrary elevation z as follows:

$$p_a + \phi_t|_{z=0} + \frac{1}{2}\phi_x^2|_{z=0} + \zeta = 0, \tag{2.39}$$

$$p + \phi_t + \frac{1}{2}\phi_x^2 + z = 0, \tag{2.40}$$

where the higher order terms (of $O(\alpha^2\epsilon)$) have been neglected. Differentiating the two equations (2.39) and (2.40) with respect to x, we have:

$$p_{ax} + \phi_{xt}|_{z=0} + \phi_x\phi_{xx}|_{z=0} + \zeta_x = 0, \tag{2.41}$$

$$p_x + \phi_{xt} + \phi_x\phi_{xx} = 0. \tag{2.42}$$

Now we substitute the expansion (2.32) in (2.41) and (2.42), find the sectional free-surface-mean of (2.41) and the section-mean of (2.42) and take their difference so that all the depth-independent terms cancel. This gives, to the $O(\alpha^2)$,

$$\overline{p_x} = \widetilde{p_{ax}} + \tilde{\zeta}_x - \epsilon^2 f_x(x,t) + O(\alpha\epsilon^3), \tag{2.43}$$

where

$$f(x,t) = \alpha(\overline{\phi_{2t}} - \widetilde{\phi_{2t}}|_{z=0}). \tag{2.44}$$

Relation (2.43) provides an expression for $\overline{p_x}$ in terms of $\tilde{\zeta}$ and f_x. The term $f_x(x,t)$ depends on the solution of $\phi_2(x,y,z,t)$ which is the second order term in the expansion (2.32) for ϕ and which can be solved explicitly once the specific geometry of the cross section is given. It will be seen that the term f_x contains the highest order derivatives of $\bar{u}$ or $\tilde{\zeta}$ and it represents the dispersive effects: namely, the longer the waves, the greater the phase velocity.

Before we investigate any specific geometry of the channel cross section, we will employ expression (2.43) with the understanding that the term f_x can be determined, for a given channel sectional geometry, in terms of $\bar{u}$, as will be shown below.

2.6 The Boussinesq Two-Equation Model

Substituting the results (2.37) and (2.43) back into (2.24)-(2.25) yields:

$$(2b\tilde{\zeta})_t + [(A_h + 2b\tilde{\zeta})\bar{u}]_x = -(A_h)_t, \tag{2.45}$$

$$\bar{u}_t + \bar{u}\bar{u}_x + \tilde{\zeta}_x = -\tilde{p}_{ax} + \epsilon^2 f_x(x,t). \tag{2.46}$$

Equation (2.45) is exact and equation (2.46) has an error of $O(\alpha\epsilon)$ relative to the leading terms $\bar{u}_t$ and $\tilde{\zeta}_x$. The set of equations (2.45) and (2.46) is our Boussinesq class two-equation model in the general form, with $f(x,t)$ to be determined from the solution of ϕ_2.

Thus our remaining task is to solve the 'cross-flow' boundary-value problem for ϕ_2. Substituting expansion (2.32) into the Laplace equation (2.26) along with boundary conditions (2.28), (2.30), (2.31) and matching at different orders of $\alpha\epsilon^n$, we see that the boundary-value problem for ϕ_2 can be prescribed as follows:

$$\phi_{2yy} + \phi_{2zz} = -u_{1x}, \qquad (y,z \in S_l(x,t)), \tag{2.47}$$

$$\frac{\partial \phi_2}{\partial z} = \zeta_{1t}, \qquad (z=0), \tag{2.48}$$

$$\frac{\partial \phi_2}{\partial n} = (\frac{1}{\alpha}h_t + u_1 h_x)/\sqrt{1+h_y^2}, \qquad (z=-h(x,y,t)), \tag{2.49}$$

$$\frac{\partial \phi_2}{\partial y} = \pm(\frac{1}{\alpha}b_t + u_1 b_x), \qquad (y=\pm b(x,t)), \tag{2.50}$$

where S_l denotes the cross-sectional flow region. This Neumann problem for the leading order cross-flow velocity potential ϕ_2 has a unique solution since the boundary conditions are easily seen to satisfy the solvability condition

$$\oint_l \frac{\partial \phi_2}{\partial n} ds = -A(x,t) u_{1x} \tag{2.51}$$

which results from application of Green's integral formula to (2.47), l being the bounding curve of $S_l(x,t)$. The solution ϕ_2 will depend on $\alpha u_1 \simeq \bar{u}(x,t)$ (as a parameter) in addition to the geometric configuration of the boundary. With ϕ_2 so resolved, (2.45) and (2.46) are two equations of the Boussinesq class, applicable to weakly nonlinear, weakly dispersive and weakly forced long waves propagating, possibly in both directions, in a channel of arbitrary, non-uniform and varying cross section. The forcing functions can be a submerged topography or a free-surface pressure distribution oscillating and moving along the channel.

2.7 The Korteweg-de Vries One-Equation Model

With additional assumptions that the main waves move in one direction and the external forcing is near resonance, the Boussinesq two-equation model (2.45)-(2.46) can be further reduced to a one-equation model which we will call the channel Korteweg-de Vries (cKdV) equation.

First we decompose the channel width and the mean water depth as follows:

$$b(x,t) = b_0(x) - b_d(x,t), \qquad \tilde{h}(x,t) = \tilde{h}_0(x) - \tilde{h}_d(x,t), \tag{2.52}$$

where $b_0(x)$ and $\tilde{h}_0(x)$ represent the fixed components to which the small time-dependent perturbations $b_d(x,t)$ and $\tilde{h}_d(x,t)$ are superposed as forcing functions (taken positive if they reduce the flow cross-section area and negative otherwise).

To model the KdV class of channel wave motions, we may adopt the following

stretched coordinates (see Johnson[10])

$$\xi = \int^x \frac{dx}{c(x)} - t, \tag{2.53}$$

$$X = \epsilon^2 x, \tag{2.54}$$

where the ξ-coordinate is fixed with the wave frame which moves in the positive x-direction with a local linearized wave speed $c(x)$, and X-coordinate signifies the slow variations of long waves in space as viewed in the wave frame. In this coordinate system, $c(x)$, $\tilde{h}_0(x)$ and $b_0(x)$ become functions of X only.

We further assume for $\psi = u, \zeta, p_a, b_d, h_d, A_d$ and f the expansion

$$\psi(x,t;\epsilon) = \epsilon^2\psi_1(\xi, X) + \epsilon^4\psi_2(\xi, X) + O(\epsilon^6), \tag{2.55}$$

where for brevity the bar for $\bar{u}$ and the tilde for $\tilde{\zeta}$, $\tilde{p}_a$, $\tilde{h}_d$ are omitted.

We first transform (2.45)-(2.46) into the stretched coordinates and then substitute the expansion (2.55) into the two equations and match the terms at different orders of ϵ^2. For the first order terms we obtain the equations

$$\partial_\xi(2b_0\zeta_1 - \frac{2b_0h_0}{c}u_1 + A_{d1}) = 0, \tag{2.56}$$

$$\partial_\xi(\zeta_1 - cu_1 + p_{a1}) = 0. \tag{2.57}$$

Upon integration of (2.56) and (2.57) from the rest state at infinity, we obtain

$$\zeta_1 = \frac{h_0}{c}u_1 = cu_1, \tag{2.58}$$

$$A_{d1} = p_{a1} = 0, \tag{2.59}$$

and from (2.58), the well known result

$$c^2 = h_0(x), \qquad \text{or} \qquad c = \pm\sqrt{h_0(x)}, \tag{2.60}$$

where the sign +(-) is for right(left)-going waves. The two equations (2.58)-(2.59) must hold if the surface pressure and the moving boundary topography are to be arbitrary disturbances. This result thus shows that any forcing imposed on the system at the critical state must be weaker than those of $O(\epsilon^2)$.

Equations (2.58)-(2.60) are compatibility conditions which are necessary for the solvability of ζ_1 and u_1 if b_d, h_d and p_a are all arbitrary as assumed. The second order terms in (2.45)-(2.46) then give, with making use of (2.58)-(2.60),

$$\partial_X(b_0h_0u_1)+\partial_\xi(-b_0\zeta_2+\frac{b_0h_0}{c}u_2+\frac{b_0}{c}\zeta_1u_1+\frac{1}{2}A_{d2})=0, \tag{2.61}$$

$$\partial_X\zeta_1+\partial_\xi(-u_2+\frac{1}{2c}u_1^2+\frac{1}{c}\zeta_2+\frac{1}{c}p_{a2}-\frac{1}{c}f_1)=0. \tag{2.62}$$

Multiplying (2.61) by $1/c$ and (2.62) by b_0, then adding the two resulting equations, we have, upon using (2.58), the result for right-going waves

$$h_0^{1/2}\zeta_{1X}+\frac{3}{2}\frac{1}{h_0}\zeta_1\zeta_{1\xi}-\frac{1}{2}f_{1\xi}+\frac{1}{4}\frac{h_{0X}}{h_0^{1/2}}\zeta_1+\frac{1}{2}\frac{h_0^{1/2}b_{0X}}{b_0}\zeta_1=-\frac{1}{2}(\frac{1}{2b_0}A_{d2}+p_{a2})_\xi. \tag{2.63}$$

Subtracting (2.61) from (2.62), we obtain, upon integration with respect to ξ,

$$h_0^{1/2}u_2=\zeta_2-\frac{1}{4}\frac{1}{h_0}\zeta_1^2-\frac{1}{4}\frac{1}{b_0}A_{d2}+\frac{1}{2}p_{a2}-\frac{1}{2}f_1-\frac{1}{2}\frac{(b_0h_0^{1/2})_X}{b_0}\int_\xi\zeta_1d\xi. \tag{2.64}$$

Equation (2.63) is a generalized variable coefficient KdV equation written in the stretched coordinates. It can be converted back to the original physical (x,t) plane by using the inverse transformation of (2.53)-(2.54) and restoring the order of different quantities from the expansions. We then have, in the (x,t) plane,

$$h_0^{1/2}\zeta_x+\zeta_t-\frac{3}{2}\frac{1}{h_0}\zeta\zeta_t+\frac{1}{2}\epsilon^2f_t+\frac{1}{4}\frac{h_{0x}}{h_0^{1/2}}\zeta+\frac{1}{2}\frac{h_0^{1/2}b_{0x}}{b_0}\zeta=\frac{1}{2}(\frac{1}{2b_0}A_d+p_a)_t, \tag{2.65}$$

and by the first order linear approximation $\partial/\partial t\simeq-c\partial/\partial x$, (2.65) can be written in another form as follows:

$$\frac{1}{h_0^{1/2}}\zeta_t+\zeta_x+\frac{3}{2}\frac{1}{h_0}\zeta\zeta_x-\frac{1}{2}\epsilon^2f_x+\frac{1}{4}\frac{h_{0x}}{h_0}\zeta+\frac{1}{2}\frac{b_{0x}}{b_0}\zeta=-\frac{1}{2}(\frac{1}{2b_0}A_d+p_a)_x, \tag{2.66}$$

and (2.64) combines with (2.58) to give

$$h_0^{1/2}u = \zeta - \frac{1}{4}\frac{1}{h_0}\zeta^2 - \frac{1}{2}\epsilon^2 f - \frac{1}{4}\frac{1}{b_0}A_d + \frac{1}{2}p_a - \frac{1}{2}\frac{(b_0 h_0^{1/2})_x}{b_0 h_0^{1/2}}\int^x \zeta dx. \qquad (2.67)$$

The above results are obtained for right-going waves. In general, (2.66) can be written as

$$\pm\frac{1}{h_0^{1/2}}\zeta_t + \zeta_x + \frac{3}{2}\frac{1}{h_0}\zeta\zeta_x - \frac{1}{2}\epsilon^2 f_x + \frac{1}{4}\frac{h_{0x}}{h_0}\zeta + \frac{1}{2}\frac{b_{0x}}{b_0}\zeta = -\frac{1}{2}(\frac{1}{2b_0}A_d + p_a)_x, \quad (2.68)$$

where the + sign is taken for main waves going to the right and - sign for the left-going waves.

Equation (2.68) is our KdV type one-equation model in the general form. The term f_x can be explicitly solved in terms of u and ζ once the geometric configuration of the cross section is given. In the following section we will study three specific cases where closed form solutions to the Poisson equation (2.47) can be easily found.

2.8 Three Specific Channel Configurations

As we have seen in the previous section, for a given channel configuration we have only to determine the solution ϕ_2 of the Neumann problem with the Poisson equation (2.47)-(2.50). This problem has solutions in closed form when the geometry is of some simple shape. We present here a few typical examples before we consider the general case.

I. Variable Rectangular Channel

The channel has its vertical walls at $y = \pm b(x,t) = \pm[b_0(x) - b_d(x,t)]$ and its bottom at $z = -h(x,t) = -[h_0(x) - h_d(x,t)]$ (see Figure 2.2(a)). For simplicity, we let depth h and width b be functions of x and t only. This assumption does not lose generality of specifying the disturbances (here represented by b_d and h_d), if the

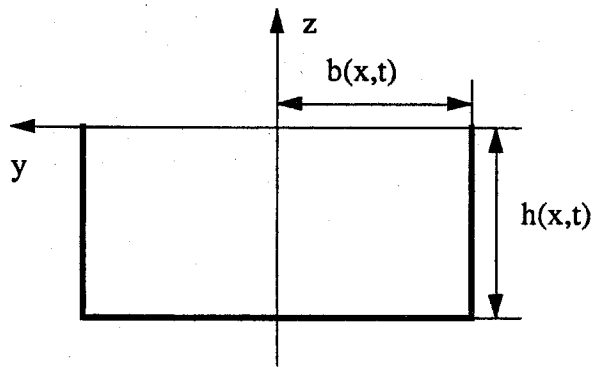

Figure 2.2(a) A rectangular cross section

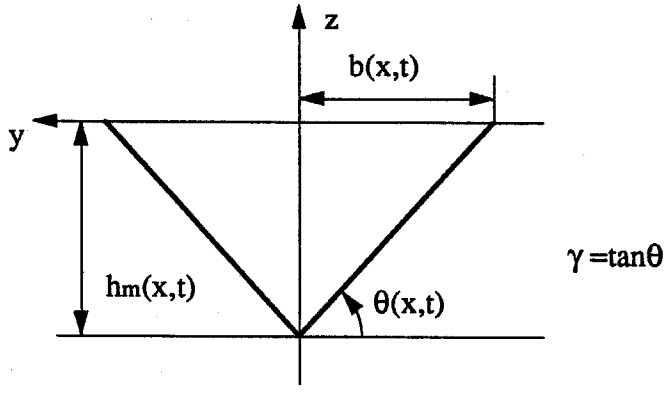

Figure 2.2(b) A triangular cross section

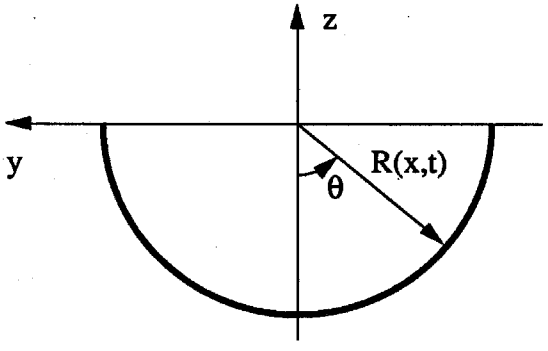

Figure 2.2(c) A semi-circular cross section

disturbances take the form of a moving topography of arbitrary shape superposed to the basic rectangular frame, but with the actual $b_d(x,z,t)$ only slightly varying in z and $h_d(x,y,t)$ only gradually changing in y, because all perturbation quantities are assumed to be of $O(\epsilon^2)$ or weaker and in our modeling each variable is averaged over the cross section, so detailed variations in perturbation of h in y or of b in z will be of the same order as the error term of the equation. As we have seen in (2.68), the effect of a moving disturbance as an external forcing appears as a blockage ratio of the cross-sectional area, while its detailed shape or position in the (y,z) plane can have only slight effect on the resultant flow field by our model. In later chapters, the experimental results will be seen to confirm the validity of our section-mean appoach and the blockage-ratio concept in the region where long waves (run-away solitons) are generated and propagate forward of the disturbance. However, in the trailing wave region, the detailed geometry of the disturbance does show significant three-dimensional effects.

Thus, we have for ϕ_2,

$$\phi_{2yy} + \phi_{2zz} = -u_{1x}(x,t) \qquad (-h(x,t) < z < 0,\ |y| < b(x,t)), \tag{2.69}$$

$$\frac{\partial \phi_2}{\partial z} = D\zeta \qquad (z = 0,\ |y| < b(x,t)), \tag{2.70}$$

$$\frac{\partial \phi_2}{\partial z} = -Dh \qquad (z = -h(x,t)), \tag{2.71}$$

$$\frac{\partial \phi_2}{\partial y} = \pm Db \qquad (y = \pm b(x,t)), \tag{2.72}$$

where $D \equiv \frac{1}{\alpha}\partial_t + u_1 \partial_x$.

By inspection, we assume the solution to be of the following form:

$$\phi_2(x,y,z,t) = F(x,t) + zG(x,t) + K(x,t)(y^2 - z^2) - \frac{1}{2}z^2 u_{1x}, \tag{2.73}$$

which is easily seen to satisfy equation (2.69).

Substituting (2.73) into the boundary conditions (2.71) and (2.72), we have

$$G(x,t) = -Dh - 2Kh - hu_{1x}, \tag{2.74}$$

$$K(x,t) = \frac{1}{2b}Db. \tag{2.75}$$

The solvability condition (2.51) for the present case

$$2bD\zeta + 2bDh + 4bhK = -2bhu_{1x}$$

gives

$$D\zeta = -Dh - 2Kh - hu_{1x},$$

which is identical to boundary condition (2.70).

In solution (2.73) for ϕ_2, $F(x,t)$ is a constant of integration for the cross-flow problem and can be incorporated into the first-order term $\phi_1(x,t)$ in the expansion (2.32).

Thus solution (2.73)-(2.75) gives

$$\phi_{2xt} = zG_{xt} + y^2K_{xt} - \frac{1}{2}z^2u_{1xxt} - z^2K_{xt} \tag{2.76}$$

and

$$\begin{aligned}\overline{\phi_{2xt}} &= \frac{1}{A}\int\int \phi_{2xt}dydz \\ &= \frac{1}{2bh}\int_{-h}^{0}\int_{-b}^{b}[zG_{xt} + y^2K_{xt} - \frac{1}{2}z^2u_{1xxt} - z^2K_{xt}]dydz + \text{h.o.t.} \\ &= -\frac{h}{2}G_{xt} + \frac{1}{3}b^2K_{xt} - \frac{h^2}{6}u_{1xxt} - \frac{h^2}{3}K_{xt} + \text{h.o.t.},\end{aligned} \tag{2.77}$$

$$\begin{aligned}\widetilde{\phi_{2xt}}|_{z=0} &= \frac{1}{2b}\int_{-b}^{b}\phi_{2xt}|_{z=0}dy \\ &= \frac{1}{2b}\int_{-b}^{b}y^2K_{xt}dy \\ &= \frac{1}{3}b^2K_{xt}.\end{aligned} \tag{2.78}$$

From these results, we readily deduce that

$$\begin{aligned} f_x(x,t) &= \alpha(\overline{\phi_{2xt}} - \widetilde{\phi_{2xt}}) \\ &= \alpha[-\frac{h}{2}G_{xt} - \frac{h^2}{6}u_{1xxt} - \frac{h^2}{3}K_{xt}] \\ &= \frac{h}{2}[h_t + (uh)_x]_{xt} - \frac{h^2}{6}u_{xxt} + \frac{h^2}{3}Q_{xt} + \frac{h}{2}h_tQ_x + \frac{h}{2}h_{xt}Q + \frac{h}{2}h_xQ_t, \end{aligned} \tag{2.79}$$

where $Q = \alpha\frac{Db}{b}$.

Use of this f_x in (2.45)-(2.46) completes the gcB model for the rectangular channel

$$(2b\zeta)_t + [(A_h + 2b\zeta)u]_x = -(A_h)_t, \tag{2.80}$$

$$\begin{aligned} u_t + uu_x + \zeta_x = -p_{ax} + \epsilon^2[&\frac{h}{2}(h_t + (uh)_x)_{xt} - \frac{h^2}{6}u_{xxt} \\ &+ \frac{h^2}{3}Q_{xt} + \frac{h}{2}h_tQ_x + \frac{h}{2}h_{xt}Q + \frac{h}{2}h_xQ_t]. \end{aligned} \tag{2.81}$$

It also gives the corresponding cKdV equation as

$$\pm\frac{1}{h_0^{1/2}}\zeta_t + \zeta_x + \frac{3}{2}\frac{1}{h_0}\zeta\zeta_x + \frac{\epsilon^2}{6}h_0^2\zeta_{xxx} + \frac{1}{4}\frac{h_{0x}}{h_0}\zeta + \frac{1}{2}\frac{b_{0x}}{b_0}\zeta = -\frac{1}{2}(\frac{1}{2b_0}A_d + p_a)_x. \tag{2.82}$$

II. Variable Triangular Channel

The triangular channel is bounded by two inclined plane walls subtending an angle $\pm\gamma$ with the horizontal, i.e., by

$$z + (h_m - \gamma|y|) = 0 \qquad (|y| \le h_m/\gamma = b), \tag{2.83}$$

where h_m and γ may vary with x and t (see Figure 2.2(b)). The cross-flow potential ϕ_2 must satisfy the Poisson equation (2.47) and the following boundary conditions,

$$\frac{\partial\phi_2}{\partial z} = D\zeta \qquad (z = 0,\ |y| \le b(x,t)), \tag{2.84}$$

$$\gamma\frac{\partial\phi_2}{\partial y}\mathrm{sgn}y - \frac{\partial\phi_2}{\partial z} = Dh_m - |y|D\gamma \qquad (z = -h_m + \gamma|y|,\ |y| < b(x,t)). \tag{2.85}$$

We assume the same form of solution as in (2.73) and for the present case, we have,

$$G(x,t) = -2D\tilde{h} - \tilde{h}u_{1x} + \tilde{h}\frac{D\gamma}{\gamma}, \tag{2.86}$$

$$K(x,t) = -\frac{1}{4}u_{1x} - \frac{1}{4}\frac{D\gamma}{\gamma}, \tag{2.87}$$

and from these we deduce,

$$f_x(x,t) = (\frac{b^2}{24} - \frac{\tilde{h}^2}{6})u_{xxt} + \frac{4\tilde{h}}{3}[\tilde{h}_t + (u\tilde{h})_x - \frac{\tilde{h}}{2}u_x]_{xt} + \frac{1}{4}(\frac{b^2}{6} + \frac{2\tilde{h}^2}{3})q_{xt} - \frac{2\tilde{h}}{3}(\tilde{h}q)_{xt}, \tag{2.88}$$

where $q = \alpha\frac{D\gamma}{\gamma}$ and we have converted the maximum depth h_m into the mean depth $\tilde{h}$ for this wedge shaped channel by

$$\tilde{h} = \frac{A}{2b} = \frac{1}{2}h_m. \tag{2.89}$$

The $f_x(x,t)$ given by (2.88) completes the gcB model; and the dispersive term in the cKdV model for this case appears as

$$\frac{\epsilon^2}{4}(h_0^2 - \frac{b^2}{12})\zeta_{xxx}. \tag{2.90}$$

III. Variable Semi-Circular Channel

For a channel with semi-circular cross section of variable radius $R(x,t)$ (see Figure 2.2(c)), it is convenient to employ the cylindrical coordinate system (x,r,θ,t), with $z = -r\cos\theta$, $y = r\sin\theta$ so that the boundary-value problem for ϕ_2 can be prescribed as

$$(\frac{\partial^2}{\partial r^2} + \frac{1}{r}\frac{\partial}{\partial r} + \frac{1}{r^2}\frac{\partial^2}{\partial\theta^2})\phi_2 = -u_{1x} \qquad (0 \le r \le R,\ |\theta| < \frac{\pi}{2}), \tag{2.91}$$

$$\frac{1}{r}\frac{\partial\phi_2}{\partial\theta} = \pm D\zeta \qquad (\theta = \pm\frac{\pi}{2},\ 0 \le r \le R), \tag{2.92}$$

$$\frac{\partial\phi_2}{\partial r} = DR \qquad (r = R(x,t),\ |\theta| < \frac{\pi}{2}), \tag{2.93}$$

and with the solvability condition (2.51) given by

$$\oint_l \frac{\partial \phi_2}{\partial n} ds = \pi R D R + 2RD\zeta = -\frac{\pi}{2} R^2 u_{1x}. \tag{2.94}$$

In the present case, a solution of the simple form as was given in (2.73) cannot satisfy the Poisson equation (2.91) and all the boundary conditions (2.92)-(2.93) at the same time. Thus we will reach a slightly more complicated form of solution which appears as

$$\phi_2 = \phi_p + \phi_c, \tag{2.95}$$

where

$$\phi_p = F(x,t) - rG(x,t)\cos\theta - K(x,t)r^2\cos 2\theta - \frac{1}{4}r^2 u_{1x} - \frac{1}{4}u_{1x}r^2\cos 2\theta, \tag{2.96}$$

$$\phi_c = \sum_{n=1}^{\infty} C_{2n} r^{2n} \cos 2n\theta. \tag{2.97}$$

Here the particular solution ϕ_p satisfies the Poisson equation (2.91); the complementary solution ϕ_c satisfies the Laplace equation in (r,θ) and has the symmetry $\phi_c(r,-\theta) = \phi_c(r,\theta)$ as assumed for the flow. Further, $\phi_2 = \phi_p + \phi_c$ satisfies the free surface condition (2.92). The solvability condition (2.94) gives

$$G(x,t) = -2D\tilde{h} - \tilde{h}u_{1x}, \tag{2.98}$$

$$K(x,t) = \frac{1}{3\tilde{h}} D\tilde{h} - \frac{1}{12}u_{1x}, \tag{2.99}$$

and invoking the channel boundary condition (2.93), we obtain, for $|\theta| \le \pi/2$,

$$G\cos\theta = \sum_{n=1}^{\infty} C_{2n} 2nR^{2n-1}\cos 2n\theta - DR - 2KR\cos 2\theta - \frac{1}{2}Ru_{1x} - \frac{1}{2}Ru_{1x}\cos 2\theta. \tag{2.100}$$

The integral of (2.100) with respect to θ produces an equation which verifies the solvability condition (2.94). By using

$$\int_{-\frac{\pi}{2}}^{\frac{\pi}{2}} \cos\theta\cos 2n\theta d\theta = \frac{2(-1)^{n+1}}{4n^2-1} \qquad (n = 1, 2, ...), \tag{2.101}$$

the coefficients C_{2n} are determined as c_2=0 and for n=2,3,...

$$C_{2n} = -\frac{2}{\pi}\frac{(-1)^n}{n(4n^2-1)}[(\frac{4}{\pi}\tilde{h})^{-2n+1}]G, \tag{2.102}$$

where the radius R has been converted into the mean water depth $\tilde{h}$ by

$$\tilde{h} = \frac{\pi}{4}R. \tag{2.103}$$

These results give the function $f_x(x,t)$ as

$$\begin{aligned} f_x(x,t) = {} & \frac{32\tilde{h}}{3\pi^2}(D\tilde{h}+\frac{\tilde{h}}{2}u_x)_{xt} - \frac{16\tilde{h}^2}{9\pi^2}(\frac{1}{\tilde{h}}D\tilde{h}+\frac{7}{8}u_x)_{xt} \\ & - \frac{16\tilde{h}}{\pi^2}(D\tilde{h}+\frac{\tilde{h}}{2}u_x)_{xt}\sum_{n=2}^{\infty}\frac{1}{n(2n+1)(4n^2-1)}, \end{aligned} \tag{2.104}$$

in which the higher order terms are neglected.

For a semi-circular channel, the dispersive term in the final cKdV equation will be

$$\epsilon^2\frac{h_0^2}{\pi^2}[\frac{17}{9} - 4\sum_{n=2}^{\infty}\frac{1}{n(2n+1)(4n^2-1)}]\zeta_{xxx}. \tag{2.105}$$

In the general case where the channel has an arbitrarily shaped cross section, for which the solution ϕ_2 cannot be obtained straightforwardly, we may always apply conformal mapping technique to transform the cross section into one of the three specific shapes discussed above, and use the results we have obtained for these specific cases to derive the gcB and cKdV models for the new geometric configuration.

2.9 General Discussions on the gcB and the cKdV Models

Up to now, we have derived two types of theoretical models – the generalized channel Boussinesq model (gcB) and the channel KdV model (cKdV) – to describe the generation and propagation of nonlinear long waves in a channel of variable

cross section. Before we seek any quantatitive data from numerical computations and experimental measurements, we may already see several characteristic aspects of significance from our theoretical models, which we will present and discuss in this section. More detailed discussions on some particular topics can be found in later chapters with the numerical and experimental results.

2.9.1 Validity of the Two Models

Based on their underlying assumptions, the gcB model has a broader region of general validity than the cKdV model. The magnitude of the perturbed quantities is of $O(\alpha)$ for the gcB model while for the cKdV model, it requires that the magnitude of the external forcing functions be of the next higher order, i.e., of $O(\alpha^2)$ due to the limitation by resonance. Further, the gcB model allows multi-directional motions and is valid for a considerably larger range of Froude number. The cKdV model is best suitable for studying unidirectional wave motions with near resonant external forcing as originally meant. In that premise, the cKdV model has its own advantage over the gcB model in being much simpler to obtain solutions and more direct to see some theoretical points such as the net effect of external forcing functions or the mass and energy conservation laws.

2.9.2 Effects of a Specific Geometry of the Cross Section

The formulations presented in sections (2.5), (2.6) and (2.7) show that the specific cross-sectional configuration only affects the dispersive terms in the two models. In this case, the cKdV model gives a clearer picture on this particular effect. It is easy to see that for the final cKdV equation, a different geometry of the cross section only changes the coefficient in front of the dispersive term ζ_{xxx} while the other terms are indifferent. Quantatitively, we may list the dispersive terms in the cKdV equations for uniform channels with rectangular, semi-circular

and triangular cross sections as

Geometry of the Cross Section	Dispersive Term
Rectangular	$0.167\epsilon^2\zeta_{xxx}$
Semi-Circular	$0.189\epsilon^2\zeta_{xxx}$
Triangular	$0.255\epsilon^2\zeta_{xxx}$

From these results we can see that the slope of the channel side walls play an explicit role in producing the dispersive effects: the smaller the slope of the channel walls versus the horizontal, the greater the dispersive effect.

2.9.3 The Effective Strength of a Submerged Moving Disturbance

Solitary waves can be generated by an external near-resonant forcing, and the cKdV model shows that a moving pressure distribution at the free surface and a floating or submerged moving object, like a ship, play an equivalent role as forcing functions. This is true provided the magnitude of the external forcing is small, being of $O(\alpha^2)$. When external forcings become stronger, the validity of the cKdV model becomes questionable, but the gcB model is seen capable of distinguishing between a free-surface pressure distribution and a submerged moving object as external forcing functions. For a semi-submerged moving object, the cKdV equation (2.68) shows that the effective strength of the forcing is directly related to the blockage-ratio of the disturbance projectional area to the cross-sectional area, while the specific shape and the position in the (y, z) plane of the disturbance have little effects on altering long wave generation so resulted, other qualifying conditions being equal. This important blockage-ratio concept will be further discussed in Chapter V along with numerical and experimental results.

2.9.4 Recovering the Three – Dimensional Wave Features

As presented in the formulation sections, both the gcB and the cKdV models

are written in terms of section-mean quantities. Since a typical wave length is much greater than the characteristic length in the cross-flow plane, these section-mean equations provide a good representation of the dominant features of the wave field. In addition, the detailed three-dimensional wave features in the cross-flow plane can always be recovered at certain order once we have solved the gcB or the cKdV equations with some given initial and boundary conditions. This can be accomplished by substituting the section-mean solutions $\tilde{\zeta}$ and $\bar{u}$ back into the truncated perturbation expansions (2.32) to get

$$\phi(x,y,z,t) = \alpha\phi_1(x,t) + \alpha\epsilon^2\phi_2(x,y,z,t), \tag{2.106}$$

and then applying the Bernoulli equation to give the free surface elevation $\zeta(x,y,t)$ by

$$\zeta(x,y,t) = -p_a - \left.\frac{\partial\phi}{\partial t}\right|_\zeta - \frac{1}{2}\left.(\frac{\partial\phi}{\partial x})^2\right|_\zeta. \tag{2.107}$$

2.9.5 Rescaling of the Nonlinear Wave Models

In deriving the gcB and the cKdV models, we normalized the cross-flow quantities with the unperturbed mean water depth h_c, and the longitudinal spatial coordinate x, velocity potential ϕ and time t with a typical wavelength λ, based on the physical background of the problem. The parameter ϵ that appears accordingly in the equations is

$$\epsilon = \frac{h_c}{\lambda},$$

which is small according to the long-wave assumption.

However, since a typical wavelength λ is an unknown itself (except that we know it is much greater than h_c), it will be more convenient to renormalize all quantities based on one single scale, namely, the unperturbed mean water depth h_c.

Introducing

$$x' = \frac{1}{\epsilon}x, \tag{2.108}$$

$$t' = \frac{1}{\epsilon}t, \tag{2.109}$$

we may rewrite the gcB model (2.80)-(2.81) for the rectangular channel case as

$$(b\zeta)_{t'} + [b(h+\zeta)u]_{x'} = -(bh)_{t'}, \tag{2.110}$$

$$\begin{aligned} u_{t'} + uu_{x'} + \zeta_{x'} = -p_{ax'} + \frac{h}{2}[h_{t'} + (uh)_{x'}]_{x't'} - \frac{h^2}{6}u_{x'x't'} \\ + \frac{h^2}{3}Q^*_{x't'} + \frac{h}{2}h_{t'}Q^*_{x'} + \frac{h}{2}h_{x'}Q^*_{t'}, \end{aligned} \tag{2.111}$$

and the corresponding cKdV equation (2.82) as

$$\begin{aligned} &\pm \frac{1}{h_0^{1/2}}\zeta_{t'} + \zeta_{x'} + \frac{3}{2}\frac{1}{h_0}\zeta\zeta_{x'} + \frac{1}{6}h_0^2\zeta_{x'x'x'} + \frac{1}{4}\frac{h_{0x'}}{h_0}\zeta + \frac{1}{2}\frac{b_{0x'}}{b_0}\zeta \\ &= -\frac{1}{2}(\frac{1}{2b_0}A_d + p_a)_{x'}, \end{aligned} \tag{2.112}$$

where $Q^* = (\frac{\partial b}{\partial t'} + u\frac{\partial b}{\partial x'})/b$.

We notice that with the new scaling, the small parameter ϵ no longer appears in the equations. Thus from here on it will be understood that all the quantities in our equations are normalized with one scale h_c and for brevity the notation $'$ will be ommitted.

Two other important topics on the steady solutions and the conservation laws based on the gcB and the cKdV models will be discussed in the following two separate sections.

2.10 Steady Solutions of Permanent Wave Form

For waves traveling in a straight uniform channel without forcing, the gcB and the cKdV equations can be much simplified. Since in this case, the effect of a specific cross-sectional geometry affects only the constant coefficient in front of the

dispersive term(i.e., u_{xxt} in the Boussinesq model and ζ_{xxx} in the KdV model, as illustrated in section 2.8.2), we will study the case for a rectangular channel only. Results for other kinds of cross-sectional shapes can be readily obtained once the rectangular case is solved.

Taking $b(x,t)$=constant and $h(x,t)$=constant in the gcB equations (2.110)-(2.111) and the cKdV equation (2.112), we have

$$\zeta_t + [(1+\zeta)u]_x = 0, \tag{2.113}$$

$$u_t + uu_x + \zeta_x = \frac{1}{3}u_{xxt}, \tag{2.114}$$

and

$$\zeta_t + \zeta_x + \frac{3}{2}\zeta\zeta_x + \frac{1}{6}\zeta_{xxx} = 0, \tag{2.115}$$

where (2.115) is written for right-going waves.

An alternative form of the KdV equation can be obtained by applying the linear approximation $\partial/\partial t \equiv -\partial/\partial x$ to the highest order term in (2.115). It gives

$$\zeta_t + \zeta_x + \frac{3}{2}\zeta\zeta_x - \frac{1}{6}\zeta_{xxt} = 0, \tag{2.116}$$

which is equivalent to (2.115) to the order of ϵ^4 and is usually refered to as the regularized KdV equation. This regularized KdV equation was first introduced for consideration of numerical instabilities (Whitham[24]). (Comparison between the KdV equation and the regularized KdV equation for the forced case will be presented in Chapter V.)

It has long been known that there exist closed form steady solutions to the KdV equations (2.115) and (2.116). The steady solution takes the form

$$\zeta(x,t) = a_0 \mathrm{sech}^2(k_0(x-ct)), \tag{2.117}$$

$$k_0 = \sqrt{\frac{3a_0}{4}}, \tag{2.118}$$

$$c = 1 + \frac{a_0}{2}, \tag{2.119}$$

for equation (2.115), and

$$\zeta(x,t) = a_0 \mathrm{sech}^2(k_0(x - ct)),$$

$$k_0 = \sqrt{\frac{3a_0}{2(2+a_0)}}, \tag{2.120}$$

$$c = 1 + \frac{a_0}{2},$$

for equation (2.116).

These solutions indicate that a single-humped positive wave of the form given by (2.117) will travel in a straight uniform channel without changing its shape or speed. This wave has been called the solitary wave. The phenomenon of the solitary wave in reality was first observed by John Scott Russell (1834) in a canal, when a solitary wave was generated by a moving boat and propagated upstream with a "permanent" wave form. Figure 2.3 shows the pictures of the solitary wave solutions to the KdV equations (2.115) and (2.116).

The steady solitary wave solution to the Boussinesq equations (2.113)-(2.114) has been studied by many authors with different approximating methods. However, closed form solutions have not been reported. In this section, we will present our analytical method to solve the Boussinesq equations for the steady solutions. It will be seen that the Boussinesq model also possesses a permanent solitary wave form solution, but the solution will be different from that of the KdV equations.

Seeking the steady solution to (2.113)-(2.114) in the wave frame $s = x - ct$ that moves with constant velocity c, we let

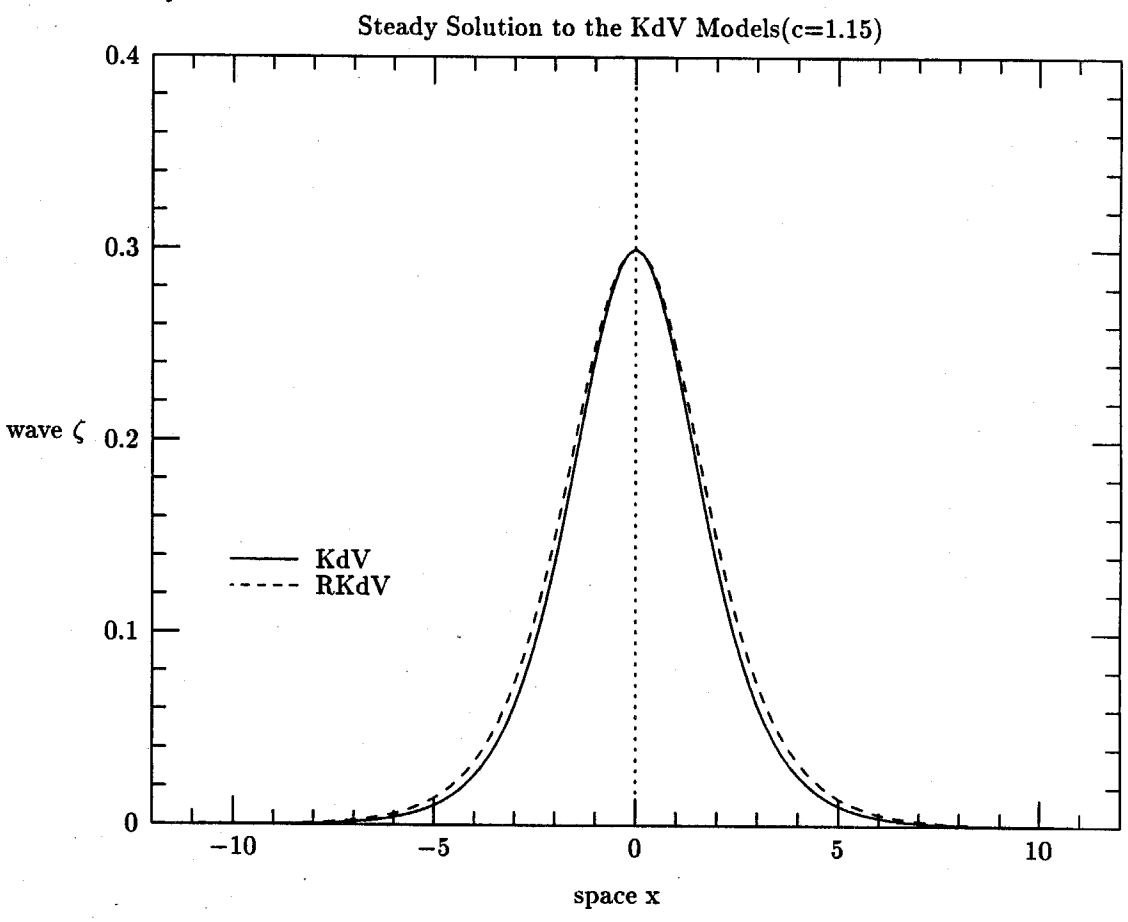

Figure 2.3 Comparison of steady solutions between KdV and RKdV

$$\zeta = \zeta(s) = \zeta(x - ct),$$

$$u = u(s) = u(x - ct),$$

thus

$$\frac{\partial}{\partial t} = -c\frac{d}{ds}, \tag{2.121}$$

$$\frac{\partial}{\partial x} = \frac{d}{ds}. \tag{2.122}$$

Substituting (2.121)-(2.122) into equations (2.113)-(2.114), we have

$$-c\zeta' + [(1+\zeta)u]' = 0, \tag{2.123}$$

$$-cu' + uu' + \zeta' = -\frac{1}{3}cu''', \tag{2.124}$$

where $'$ denotes the derivative with respect to s.

Equations (2.123)-(2.124) can be integrated once to give

$$-c\zeta + (1+\zeta)u = 0, \tag{2.125}$$

$$-cu + \frac{u^2}{2} + \zeta = -\frac{1}{3}cu''. \tag{2.126}$$

From (2.125) we obtain a relation between the wave amplitude ζ and the wave speed u as follows

$$\zeta = \frac{u}{c-u}, \tag{2.127}$$

or

$$u = \frac{c\zeta}{1+\zeta}. \tag{2.128}$$

These relations show that if ζ has the form of a single positive hump, so will u.

Eliminating ζ from (2.125)-(2.126), we get

$$(1-c^2)u + \frac{3}{2}cu^2 - \frac{1}{2}u^3 + \frac{1}{3}c^2u'' - \frac{1}{3}cuu'' = 0, \tag{2.129}$$

which is a nonlinear ordinary differential equation with one free parameter, namely c, and may possess more than one solutions. In the present case, we are particularly interested in a solution of the solitary wave form which is similar to the waves shown in Figure 2.3, and which may exist for an "eigenvalue " of c. This implies the following boundary conditions

$$u = 0, \qquad \text{at } s = \pm\infty. \tag{2.130}$$

Since equation (2.129) is invariant to transformation $s^* = -s$, it permits the existence of symmetric solutions which have the property

$$\frac{du}{ds} = 0, \qquad \text{at } s = 0. \tag{2.131}$$

Furthermore, for solutions of regular smooth functions,

$$\frac{du}{ds} = 0, \qquad \text{at } s = \pm\infty. \tag{2.132}$$

Now we let

$$P = \frac{du}{ds}, \tag{2.133}$$

thus

$$\frac{d^2u}{ds^2} = \frac{dP}{ds} = P\frac{dP}{du}. \tag{2.134}$$

Substituting (2.134) into (2.129), we obtain

$$(1-c^2)u + \frac{3}{2}cu^2 - \frac{1}{2}u^3 + \frac{1}{3}c^2P\frac{dP}{du} - \frac{1}{3}cuP\frac{dP}{du} = 0, \tag{2.135}$$

where the new unknown variable P is considered as a function of the independent variable u and the parameter c.

From (2.135), we have

$$\begin{aligned} \frac{dP^2}{du} &= \beta\frac{(1-c^2)u + \frac{3}{2}cu^2 - \frac{1}{2}u^3}{u-c} \\ &= \beta[1 + \frac{1}{2}c^2 - \frac{c}{c-u} - \frac{1}{2}(c-u)^2], \end{aligned} \tag{2.136}$$

where $\beta = 6/c$.

Integrating (2.136) from 0 to u and applying boundary condition (2.130), we reach

$$P^2(u;c) = \beta g(u;c), \tag{2.137}$$

where

$$g(u;c) \equiv \beta[(1+\frac{1}{2}c^2)u + c\ln(c-u) + \frac{1}{6}(c-u)^3 - c\ln c - \frac{c^3}{6}]. \tag{2.138}$$

Equation (2.137) further gives

$$\frac{du}{\sqrt{g(u;c)}} = ds, \tag{2.139}$$

where we need only to study the positive branch, because of the symmetry of the solution.

The existence of real solutions to (2.137) requires that $g(u;c) \geq 0$ for certain domain of u. A plot of the function $g(u;c)$ for various values of c is shown in Figure 2.4. It is easily seen that the two zero crossing points of $g(u;c)$ correspond to $\frac{du}{ds} = 0$ where the first point $u = 0$ corresponds to $u \to 0$ as $s \to \infty$ while the second point $u = u_c$ represents the maximum amplitude of u at $s = 0$. Thus the procedure to solve for the steady solution is that we first find the second zero crossing point u_c of $g(u;c)$ corresponding to a specific value of c and then integrate (2.139) from u_c to u to have

$$s = \int_{u_c}^{u} \frac{dv}{\sqrt{g(v;c)}}. \tag{2.140}$$

These last two steps can be easily accomplished with certain numerical schemes:

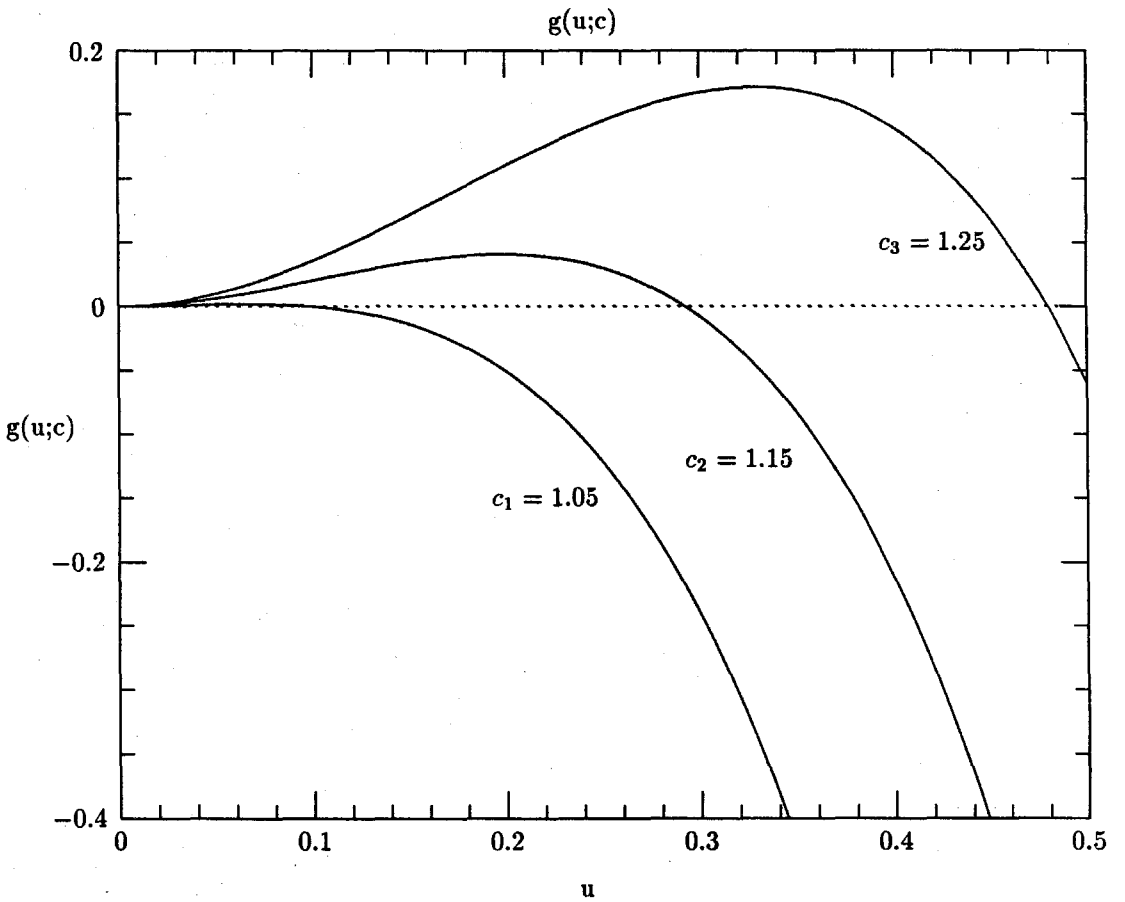

Figure 2.4 A plot of function $g(u; c)$ for different c's

the zero crossing point can be found by applying Newton's iteration method and the integration (2.140) can be done with a second order trapezoidal scheme. The next step is to map the results symmetrically to the other half domain, i.e., $s < 0$ domain and then by using (2.127) to get the steady solitary wave solution for ζ, which travels with constant speed c of a permanent wave form.

A comparison of the solitary wave solutions between the Boussinesq model and the KdV model is shown in Figure 2.5. The results show that the shapes of the solitary waves for both models are very similar. However, quantitively they are noticeably different. The conclusion is that for waves traveling at the same speed, the Boussinesq model requires a higher maximum wave amplitude. Russell (1845) studied the relationship between the maximum wave amplitude a_0 and the wave speed c experimentally and he suggested the following empirical formula

$$c = \sqrt{1 + a_0} \qquad \text{or} \qquad a_0 = c^2 - 1. \tag{2.141}$$

Results obtained from the three models, i.e., the KdV model, the Boussinesq model and the Russell formula are given in Table 2.1 and shown in Figure 2.6.

Table 2.1 The Relationship between the Amplitude and the Speed of a Solitary Wave

c	a_0 (KdV)	a_0 (gB)	a_0 (Russell)
1.050	0.10	0.1043	0.1025
1.075	0.15	0.1598	0.1556
1.100	0.20	0.2177	0.2100
1.125	0.25	0.2782	0.2656
1.150	0.30	0.3413	0.3225
1.175	0.35	0.4070	0.3806
1.200	0.40	0.4757	0.4400
1.225	0.45	0.5475	0.5006
1.250	0.50	0.6223	0.5625

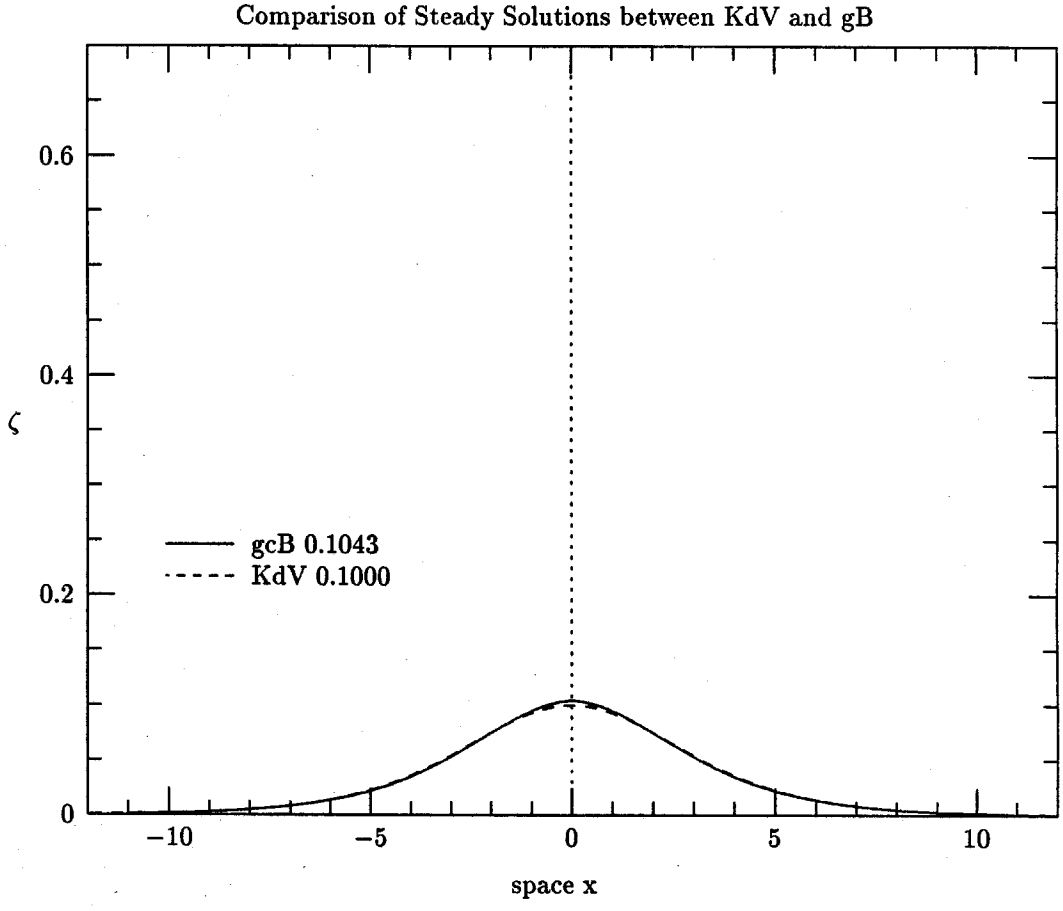
Comparison of Steady Solutions between KdV and gB
0.6
0.4
ζ
0.2
0
gcB 0.1043
KdV 0.1000
−10
−5
0
5
10
space x

Figure 2.5(a)

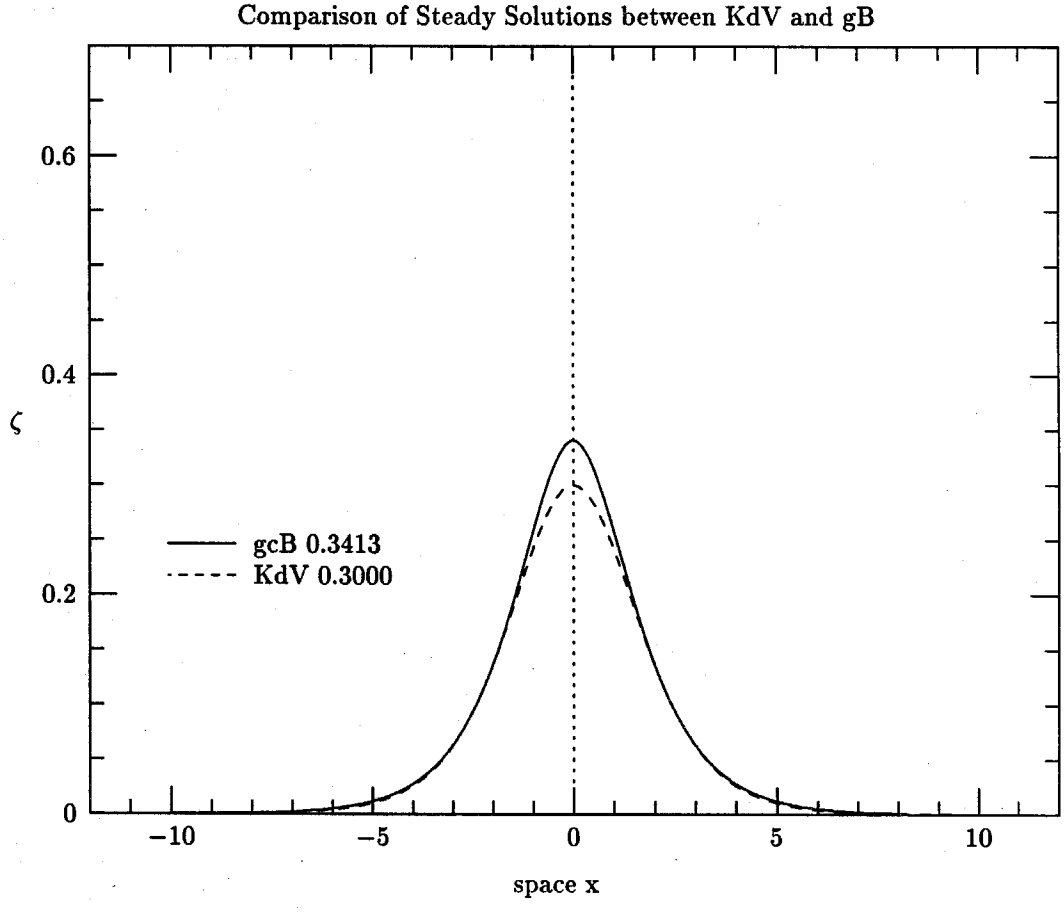
Comparison of Steady Solutions between KdV and gB
0.6
0.4
ζ
0.2
0
gcB 0.3413
KdV 0.3000
−10
−5
0
5
10
space x

Figure 2.5(b)

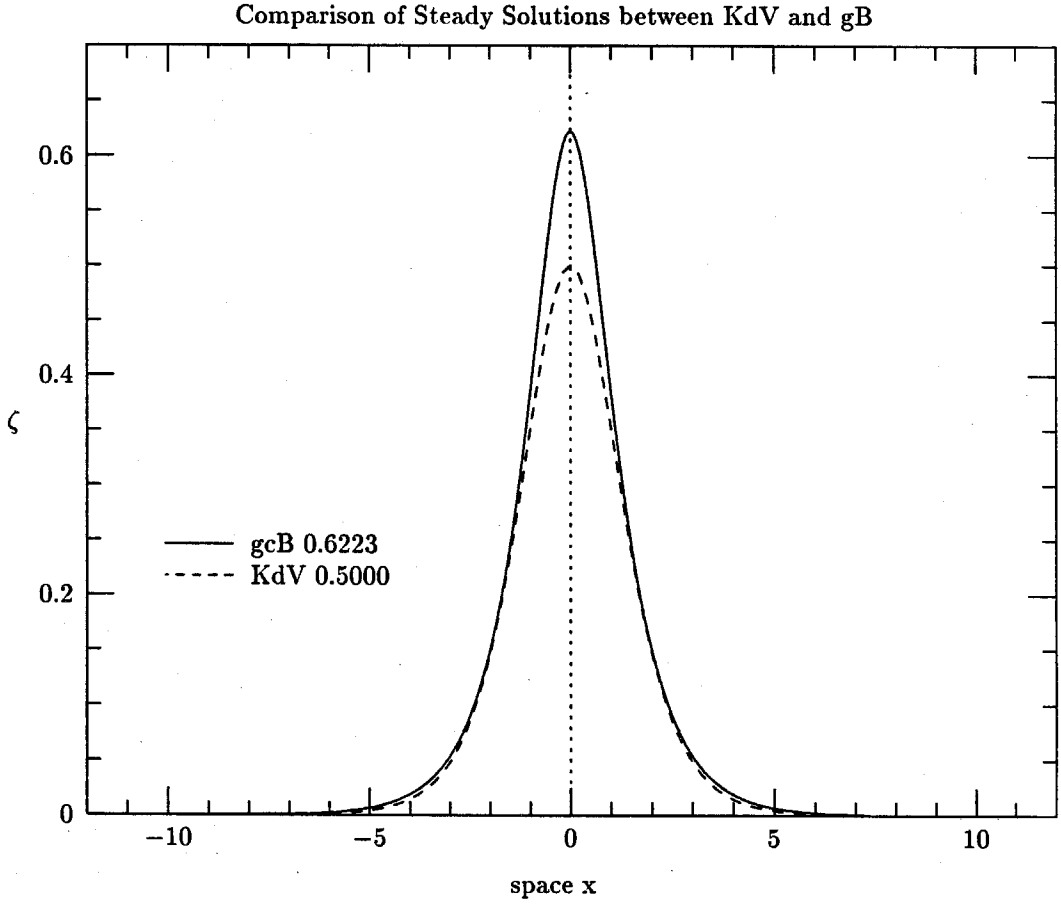
Comparison of Steady Solutions between KdV and gB
0.6
0.4
ζ
0.2
0
gcB 0.6223
KdV 0.5000
−10
−5
0
5
10
space x

Figure 2.5(c)

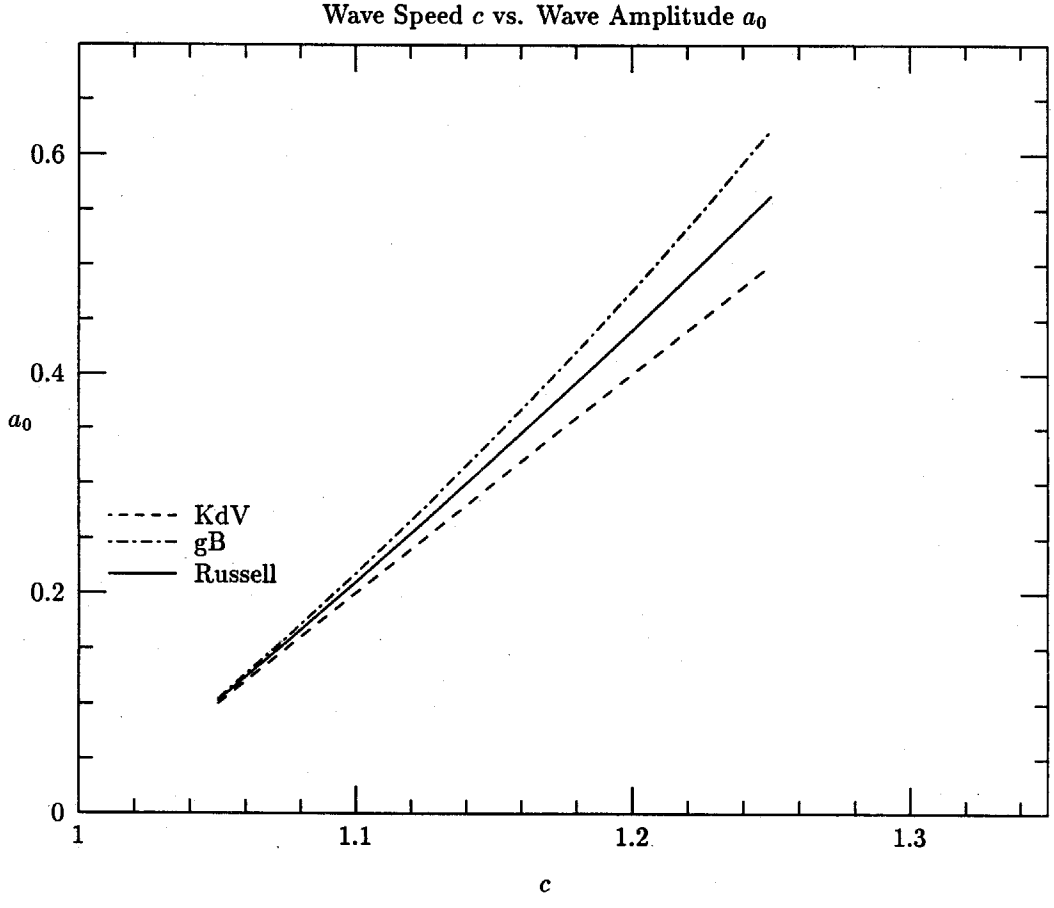

Figure 2.6 Comparison among the three models

2.11 Conservation Laws and the Related Invariants by the gcB and the cKdV Models

As we know, for fluid mechanics, or for any other subjects in the field of classical mathematical physics, the basic mass, momentum and energy conservation laws form the fundations of all our theories. Thus upon deriving new theoretical models, it is essential for us to study and analyze the conservation principles and the related invariants based on these models.

In this section, we will present the analysis of conservation laws on the gcB and cKdV models for variable rectangular channels. The physical domain is from $x = -\infty$ to $x = +\infty$ and we assume that the flow field at the two ends, i.e., at $x = \pm\infty$, remains at rest for all times. The submerged moving objects as external forcing functions are assumed to move along the bottom or along the sidewalls of the channel. All external forcing functions are assumed to be of higher order, i.e., of $O(\epsilon^4)$. For channels of other geometric shapes, or for cases with semi-infinite or finite domains, the analysis can be carried out following similar procedures as will be presented in the sequel.

To study a wave field, we have at least two quantities which are of particular interest. One is the total excess mass of fluid, M_e, which is equal to the mass above the undisturbed water surface, and is defined as

$$M_e = \int_{-\infty}^{+\infty} \int_{-b}^{b} \zeta dy dx = \int_{-\infty}^{+\infty} 2b\tilde{\zeta} dx, \tag{2.142}$$

where the integral is assumed to exist.

This excess mass M_e is related to the total mass M of the fluid by the following relation

$$M = \int_{-\infty}^{+\infty} A(x,t)dx = M_e + \int_{-\infty}^{+\infty} A_h(x,t)dx. \tag{2.143}$$

The other quantity of interest is the total energy of the wave field

$$\begin{aligned} E = & \ E_k + E_p \\ = & \int_{-\infty}^{+\infty} \int_{-b}^{b} \int_{-h}^{\zeta} [\frac{1}{2}(u^2 + v^2 + w^2) + z] dz dy dx \qquad (2.144) \\ = & \int_{-\infty}^{+\infty} (b\tilde{h}\bar{u}^2 + b\tilde{\zeta}^2) dx - \int_{-\infty}^{+\infty} b\tilde{h}^2 dx. \qquad (2.145) \end{aligned}$$

For brevity we now omit the bars and the tildes for the mean quantities and expand

$$h(x,t) = h_0(x) - d(x,t), \qquad (2.146)$$

$$b(x,t) = b_0(x) - B(x,t), \qquad (2.147)$$

where $d(x,t)$ and $B(x,t)$ represent the external forcing functions which are higher order perturbations to the wave system.

Substituting (2.146) and (2.147) into (2.145), we have

$$E(t) = \int_{-\infty}^{+\infty} (b_0 h_0 u^2 + b_0 \zeta^2) dx - \int_{-\infty}^{+\infty} b_0 h_0^2 dx + \int_{-\infty}^{+\infty} h_0 (h_0 B + 2 b_0 d) dx + \text{h.o.t.} \qquad (2.148)$$

We may also define

$$\begin{aligned} E_2(t) = & E(t) + \int_{-\infty}^{+\infty} b h^2 dx \\ = & \int_{-\infty}^{+\infty} (b_0 h_0 u^2 + b_0 \zeta^2) dx + \text{h.o.t.}, \end{aligned} \qquad (2.149)$$

such that

$$\frac{dE}{dt} = \frac{dE_2}{dt} + \int_{-\infty}^{+\infty} h_0 (h_0 B_t + 2 b_0 d_t) dx + \text{h.o.t.}$$

The total mass M by (2.143) and the total energy E of the wave field by (2.144) are defined in the physical sense, thus they by nature obey the basic mass and energy conservation laws.

According to the mass conservation law, the total mass M shoud always be conserved if there are no mass sources in the system. This gives

$$\frac{dM}{dt} = 0,$$

or

$$\frac{dM_e}{dt} = -\frac{d}{dt}\int_{-\infty}^{+\infty} A_h(x,t)dx = \frac{d}{dt}\int_{-\infty}^{+\infty} A_d(x,t)dx. \tag{2.150}$$

If the submerged three-dimensional moving disturbance A_d is a rigid object without expanding or decreasing its wetted volume, which is the true for the present study, then

$$\frac{dM_e}{dt} = 0,$$

i.e., the total excess mass M_e=constant is always conserved.

The rate of change of the total energy E is governed by the energy-work relation for an incompressible and inviscid fluid

$$\begin{aligned}\frac{dE}{dt} &= -\int\int\int_V \mathbf{u}\cdot\nabla p dV \\ &= -\int\int\int_V \nabla\cdot(\mathbf{u}p)dV \\ &= -\int_{-\infty}^{+\infty}\int_{-b}^{b}\int_{-h}^{\zeta}[(pu)_x + (pv)_y + (pw)_z]dzdydx,\end{aligned}$$

where

$$-\int_{-\infty}^{+\infty}\int_{-b}^{b}\int_{-h}^{\zeta}(pu)_x dzdydx =$$
$$\int_{-\infty}^{+\infty}[2\int_{-h}^{\zeta} p_b b_x u|_b dz + \int_{-b}^{b} p_a\zeta_x u|_\zeta dy + \int_{-b}^{b} p_d h_x u|_{-h} dy]dx,$$
$$-\int_{-\infty}^{+\infty}\int_{-b}^{b}\int_{-h}^{\zeta}(pv)_y dzdydx = -\int_{-\infty}^{+\infty}\int_{-h}^{\zeta} 2p_b v|_b dzdx,$$
$$-\int_{-\infty}^{+\infty}\int_{-b}^{b}\int_{-h}^{\zeta}(pw)_z dzdydx = -\int_{-\infty}^{+\infty}\int_{-b}^{b}[p_a w|_\zeta - p_d w|_{-h}]dydx.$$

In these expressions, p_b, p_d and p_a are the pressures at the surfaces of B, d and at the free surface, respectively.

By applying the kinematic boundary conditions

$$w|_\zeta = \zeta_t + u\zeta_x,$$

$$w|_{-h} = -h_t - uh_x,$$

$$v|_b = b_t + ub_x,$$

we get

$$\frac{dE}{dt} = -2\int_{-\infty}^{+\infty}(b_0 p_a \zeta_t - h_0 p_b B_t - b_0 p_d d_t)dx, \tag{2.151}$$

or

$$\frac{dE_2}{dt} = -2\int_{-\infty}^{+\infty}[b_0 p_a \zeta_t - h_0(p_b - \frac{1}{2}h_0)B_t - b_0(p_d - h_0)d_t]dx, \tag{2.152}$$

where p_b and p_d can be obtained by applying the Bernoulli equation on the surfaces of the moving disturbances.

Assuming the moving disturbance $d(x,t)$ is a bottom topography and applying the Bernoulli equation on the surface of d at $z = -h_0(x) + d$, we have

$$p_d = h_0 - d - \phi_t + O(\epsilon^4). \tag{2.153}$$

Application of the Bernoulli equation at the free surface gives

$$\phi_t = -\zeta - p_a + \text{h.o.t.} \tag{2.154}$$

Noting that to the leading order ϕ_t is independent of z, we substitute (2.154) into (2.153) and neglect the higher order forcing terms to get

$$p_d = \zeta + h_0 + O(\epsilon^4). \tag{2.155}$$

Similarly for a sidewall topography $B(x,t)$, we apply the Bernoulli equation at $y = b$ to get

$$p_b = \zeta + \frac{1}{2}h_0 + O(\epsilon^4). \tag{2.156}$$

By using the results (2.155) and (2.156), equation (2.152) can be evaluated to yield

$$\frac{dE_2}{dt} = -2\int_{-\infty}^{+\infty}(b_0 p_a \zeta_t - h_0 B_t \zeta - b_0 d_t \zeta)dx. \tag{2.157}$$

For cases where no external forcing functions are present, the total energy

$$E = \int_{-\infty}^{+\infty}(b_0 h_0 u^2 + b_0 \zeta)dx - \int_{-\infty}^{+\infty} b_0 h_0^2 dx$$

and also

$$E_2 = \int_{-\infty}^{+\infty}(b_0 h_0 u^2 + b_0 \zeta^2)dx$$

are conserved, i.e.,

$$\frac{dE}{dt} = \frac{dE_2}{dt} = 0$$

for all times.

The above analyses are based on the general conservation laws in the physical sense. Now we will proceed to examine the conservation properties and the related invariants possessed by the gcB and cKdV models. These analyses will help to gain a better understanding on the validity criteria of the wave models we have derived.

2.11.1 The Generalized Channel Boussinesq Model

For long waves generated and propagating in a rectangular channel, the wave field can in general be described by the gcB model

$$(b\zeta)_t + [(bh + b\zeta)u]_x = -(bh)_t, \tag{2.158}$$

$$u_t + uu_x + \zeta_x = -p_{ax} + \frac{h}{2}[h_t + (uh)_x]_{xt} - \frac{h^2}{6}u_{xxt} + \frac{h^2}{3}Q_{xt} + \frac{h}{2}h_x Q_t, \tag{2.159}$$

where $Q = (b_t + ub_x)/b$. In equation (2.159) the higher order terms hh_tQ_x and $hh_{xt}Q$ have been neglected.

The first equation (2.158) in the gcB model is actually the mass conservation law in the exact form. Thus as we already discussed, if the submerged moving disturbance is a rigid body, then the total excess mass is conserved, or M_e=constant, and M_e is an invariant of the gcB model.

Integrating the second equation (2.159) in the gcB model and upon using the undisturbed boundary conditions at $x = \pm\infty$, we have

$$\frac{d}{dt}\int_{-\infty}^{+\infty} udx = \int_{-\infty}^{+\infty} [\frac{h}{2}(h_t + (uh)_x)_{xt} - \frac{h^2}{6}u_{xxt} + \frac{h^2}{3}Q_{xt} + \frac{h}{2}h_x Q_t]dx. \tag{2.160}$$

We first study the case without external forcings. In this case $h = h_0(x), b = b_0(x)$ and equation (2.160) is reduced to

$$\frac{d}{dt}\int_{-\infty}^{+\infty} udx = \int_{-\infty}^{+\infty} [\frac{h_0}{2}(uh_0)_{xxt} - \frac{h_0^2}{6}u_{xxt} + \frac{h_0^2}{3}Q_{xt} + \frac{h_0}{2}h_{0x}Q_t]dx. \tag{2.161}$$

Integrating by parts gives

$$\frac{d}{dt}\int_{-\infty}^{+\infty} [1 + \frac{1}{6}(2h_{0x}^2 - h_0 h_{0xx} + h_0 h_{0x}\frac{b_{0x}}{b_0})]udx = 0. \tag{2.162}$$

Define

$$c_1(x) = \frac{1}{6}(2h_{0x}^2 - h_0 h_{0xx} + h_0 h_{0x}\frac{b_{0x}}{b_0}), \tag{2.163}$$

$$M_{b2} = \int_{-\infty}^{+\infty} [1 + c_1(x)]udx, \tag{2.164}$$

we can write

$$\frac{dM_{b2}}{dt} = 0,$$

i.e., M_{b2} is a constant of motion to the gcB model provided there are no external forcing functions present.

For a channel of variable width but constant depth, c_1 vanishes, and

$$M_{b2} = M_{b2}^* = \int_{-\infty}^{+\infty} u dx$$

is conserved.

In the cases where external forcings are involved, we may write

$$h(x,t) = h_0(x) - d(x,t),$$

$$b(x,t) = b_0(x) - B(x,t),$$

and follow the same procedure as in the previous case to get

$$\frac{dM_{b2}}{dt} = -\int_{-\infty}^{+\infty} (\frac{h_0}{2} d_{xtt} + \frac{h_0^2}{3b_0} B_{xtt} + \frac{h_0}{2} h_{0x} B_{tt}) dx. \tag{2.165}$$

To consider the property of conserving energy for the gcB model, we multiply the continuity equation (2.158) by ζ and integrate the product over x to have for the case of time-independent variable channels,

$$\frac{d}{dt}\int_{-\infty}^{+\infty} \frac{1}{2} b_0 \zeta^2 dx = \int_{-\infty}^{+\infty} b_0 h_0 u \zeta_x dx + \int_{-\infty}^{+\infty} (b_0 d_t + h_0 B_t)\zeta dx, \tag{2.166}$$

where the higher order terms (of $O(\epsilon^6)$ like $u\zeta\zeta_x$) are neglected.

The momentum equation (2.159) in the gcB model gives, upon multiplication with $b_0 h_0 u$ and integration over x,

$$\begin{aligned}
&\frac{d}{dt}\int_{-\infty}^{+\infty} \frac{1}{2} b_0 h_0 u^2 dx + \int_{-\infty}^{+\infty} b_0 h_0 u \zeta_x dx \\
&= -\int_{-\infty}^{+\infty} b_0 h_0 p_{ax} u dx + \frac{1}{2}\int_{-\infty}^{+\infty} b_0 h_0^2 (u h_0)_{xxt} u dx - \frac{1}{6}\int_{-\infty}^{+\infty} b_0 h_0^3 u u_{xxt} dx \\
&+ \frac{1}{3}\int_{-\infty}^{+\infty} b_0 h_0^3 (\frac{b_{0x}}{b_0} u)_{xt} u dx + \frac{1}{2}\int_{-\infty}^{+\infty} h_0^2 h_{0x} b_{0x} u u_t dx + \text{h.o.t.}
\end{aligned} \tag{2.167}$$

Upon integration by parts, (2.167) can be rewritten as

$$\begin{aligned}\frac{d}{dt}\int_{-\infty}^{+\infty}\frac{1}{2}b_0h_0u^2dx+\int_{-\infty}^{+\infty}b_0h_0u\zeta_xdx\\ =-\int_{-\infty}^{+\infty}b_0h_0p_{ax}udx-\frac{d}{dt}\int_{-\infty}^{+\infty}c_2(x,t;u^2,u_x^2)dx,\end{aligned}\tag{2.168}$$

where

$$c_2(x,t;u^2,u_x^2)=\frac{1}{6}b_0h_0^3u_x^2-[\frac{1}{4}b_0h_{0xx}+\frac{1}{6}b_0h_0(\frac{b_{0x}}{b_0})_x+\frac{1}{4}h_{0x}b_{0x}]h_0^2u^2.\tag{2.169}$$

Since c_2 involves only the x-derivatives of various functions, it is actually a small quantity of higher order, based on our assumption that the spatial variations of all variables are small.

Adding (2.168) to (2.166) and multiplying the resulting equation by two, we have

$$\frac{dE_{b1}}{dt}=-2\int_{-\infty}^{+\infty}(b_0h_0p_{ax}u-b_0d_t\zeta-h_0B_t\zeta)dx,\tag{2.170}$$

where

$$\begin{aligned}E_{b1}&=\int_{-\infty}^{+\infty}(b_0h_0u^2+b_0\zeta^2)dx+2\int_{-\infty}^{+\infty}c_2(x,t;u^2,u_x^2)dx\\ &=E_2+2\int_{-\infty}^{+\infty}c_2(x,t;u^2,u_x^2)dx.\end{aligned}\tag{2.171}$$

By applying the continuity equation to the leading order, i.e.,

$$(b_0h_0u)_x=-b_0\zeta_t,$$

we see that

$$\int_{-\infty}^{+\infty}b_0h_0p_{ax}udx=-\int_{-\infty}^{+\infty}p_a(b_0h_0u)_xdx=\int_{-\infty}^{+\infty}p_ab_0\zeta_tdx.\tag{2.172}$$

Substituting (2.172) in (2.170), we rewrite (2.170) as

$$\frac{dE_{b1}}{dt}=-2\int_{-\infty}^{+\infty}(b_0p_a\zeta_t-b_0d_t\zeta-h_0B_t\zeta)dx.\tag{2.173}$$

Thus we observe that the gcB model conserves mass exactly, and by comparing (2.173) with (2.157), we see that the gcB model also preserves the energy-work relation, to the order of ϵ^4.

2.11.2 The Channel Korteweg – de Vries Model

For waves generated by moving disturbances near resonance and propagating in unidirection, the wave field can be described by the cKdV model:

$$\frac{1}{c}\zeta_t+\zeta_x+\frac{3}{2}\frac{1}{h_0}\zeta\zeta_x+\frac{1}{6}h_0^2\zeta_{xxx}+\frac{1}{4}\frac{h_{0x}}{h_0}\zeta+\frac{1}{2}\frac{b_{0x}}{b_0}\zeta=-\frac{1}{2}(d+\frac{h_0}{b_0}B+p_a)_x. \quad (2.174)$$

where $c=\sqrt{h_0(x)}$.

To study the conservation properties of the cKdV model, we first examine the case for a uniform channel where b_0=1 and h_0=1. In this case, (2.174) is reduced to

$$\zeta_t+\zeta_x+\frac{3}{2}\zeta\zeta_x+\frac{1}{6}\zeta_{xxx}=-\frac{1}{2}(d+B+p_a)_x. \quad (2.175)$$

It is easily seen that, upon integration of (2.175) over x and applying the undisturbed boundary conditions at $x=\pm\infty$, (2.175) conserves excess mass, since

$$\frac{d}{dt}\int_{-\infty}^{+\infty}\zeta dx=0.$$

For energy-work relation, (2.175) gives

$$\frac{d}{dt}\int_{-\infty}^{+\infty}\frac{1}{2}\zeta^2dx=-\frac{1}{2}\int_{-\infty}^{+\infty}\zeta(d+B+p_a)_xdx. \quad (2.176)$$

Multiplying (2.176) with four and by using the linear approximation $\partial/\partial t\simeq -\partial/\partial x$ which is applicable to the cases with near-critical forcing disturbances, we get

$$\frac{dE_{k0}^*}{dt}=-2\int_{-\infty}^{+\infty}(p_a\zeta_t-\zeta B_t-\zeta d_t)dx, \quad (2.177)$$

where

$$E_{k0}^{*} = \int_{-\infty}^{+\infty} 2\zeta^2 dx. \tag{2.178}$$

To understand the meaning of E_{k0}^{*}, we apply the leading order approximation from (2.67) that

$$h_0^{1/2} u = \zeta \tag{2.179}$$

on equation (2.149) to have

$$\begin{aligned} E_2 &= \int_{-\infty}^{+\infty} (b_0 h_0 u^2 + b_0 \zeta^2) dx \\ &= \int_{-\infty}^{+\infty} 2 b_0 \zeta^2 dx + O(\epsilon^6); \end{aligned} \tag{2.180}$$

thus if we define

$$E_{k0} = \int_{-\infty}^{+\infty} 2 b_0 \zeta^2 dx, \tag{2.181}$$

then

$$E_2 = E_{k0} + O(\epsilon^6),$$

and in the case for a uniform channel,

$$E_{k0} = E_{k0}^{*}.$$

Comparing (2.177) with (2.157), we see that the KdV equation (2.175) preserves the physical energy-work relation up to the order of ϵ^4.

It has been known that for the unforced constant coefficient KdV equation, there exist an infinite number of constants of motion (see Miura et al.[20]).

However, in the general case of waves being generated and propagating in a variable channel, the cKdV model (2.174) is much more complicated than the classical KdV equation (2.175) by having variable coefficients and more terms.

Multiplying (2.174) with cb_0 and integrating over x, we have

$$\frac{d}{dt}\int_{-\infty}^{+\infty} b_0\zeta dx + \int_{-\infty}^{+\infty} h_0^{1/2} b_0\zeta_x dx + \frac{3}{2}\int_{-\infty}^{+\infty} \frac{b_0}{h_0^{1/2}}\zeta\zeta_x dx$$
$$+ \frac{1}{6}\int_{-\infty}^{+\infty} h_0^{5/2} b_0\zeta_{xxx} dx + \frac{1}{4}\int_{-\infty}^{+\infty} \frac{h_{0x}}{h_0^{1/2}} b_0\zeta dx + \frac{1}{2}\int_{-\infty}^{+\infty} h_0^{1/2} b_{0x}\zeta dx \qquad (2.182)$$
$$= -\frac{1}{2}\int_{-\infty}^{+\infty} h_0^{1/2} b_0 (d + \frac{h_0}{b_0}B + p_a)_x dx.$$

Integration by parts gives

$$\frac{d}{dt}\int_{-\infty}^{+\infty} b_0\zeta dx = \int_{-\infty}^{+\infty} [c_3(x)\zeta^2 + c_4(x)\zeta] dx - \frac{1}{2}\int_{-\infty}^{+\infty} h_0^{1/2} b_0 (d + \frac{h_0}{b_0}B + p_a)_x dx, \qquad (2.183)$$

where

$$c_3(x) = \frac{3}{4}(\frac{b_0}{h_0^{1/2}})_x, \qquad (2.184)$$

$$c_4(x) = \frac{1}{6}(h_0^{5/2} b_0)_{xxx} + \frac{1}{4}\frac{h_{0x}}{h_0^{1/2}} b_0 + \frac{1}{2} h_0^{1/2} b_{0x} - (h_0^{1/2} b_0)_x. \qquad (2.185)$$

Since in general the integrals on the right-hand-side of (2.183) do not vanish, the cKdV equation (2.174) is seen not conserving mass for the cases with variable channels.

Similarly, if we multiply equation (2.174) with $cb_0\zeta$ and integrate over x, we can show that (2.174) does not preserve the correct energy-work relation (such as (2.177)) between E_{k0} and the external forcing functions.

The reason for (2.174) to fail preserving the original physical conservation laws, we believe, lies in the violation, in reality, of the basic assumption of unidirectional motion for the cKdV model. As waves travel in a variable channel, there are waves being reflected and since the cKdV model is derived for unidirectional wave motions, it cannot include the reflected waves traveling in the opposite direction that must carry with them certain mass of the fluid, and thus the mass and energy are not conserved due to the loss to the reflected waves.

The fact that the cKdV equation does not conserve either mass or energy raises an immediate question on the validity of the cKdV model. It is thus necessary for us to analyze and determine in what cases and in which way can this model be applied and how good a prediction it can give for a real wave field.

To answer these questions, we carried out further theoretical and numerical studies on waves traveling in a divergent and, separately, a convergent channel. Both models – the cKdV model and the gcB model – are used to study the changes in wave amplitude and in wave speed when waves are traveling in a variable channel. The results from the cKdV model are compared with that from the gcB model, the latter of which possesses quite good conservation properties, as the above analysis has indicated. The detailed analysis and results on this problem are presented in Chapter IV.

III. NUMERICAL SCHEMES FOR SOLVING THE BOUSSINESQ AND THE KDV EQUATIONS

In our studies we have adopted and applied several different numerical schemes to compute the Boussinesq two-equation model and the cKdV one-equation model for various wave phenomena. These schemes are mainly based on the finite difference approach. The structures of these schemes, along with their properties of accuracy, instability and efficiency, are presented and discussed in this chapter.

3.1 Finite Difference Schemes for the KdV-Type Equations

The KdV-type equations (2.66) or (2.82) can be written in a general form as

$$a_1\zeta_t + \zeta_x + a_2\zeta\zeta_x + a_3\zeta_{xxx} + a_4\zeta = a_5, \tag{3.1}$$

or be regularized to

$$a_1\zeta_t + \zeta_x + a_2\zeta\zeta_x - a_3\zeta_{xxt} + a_4\zeta = a_5, \tag{3.2}$$

where the a_i's are known functions of (x,t) through $h_0(x,t)$ and $b_0(x,t)$.

Zabusky and Kruskal[27] constructed an energy-conserved finite difference scheme to carry out numerical experiments on homogeneous KdV equation of constant coefficients in 1965. In our studies on the forced cKdV equation with variable coefficients, we basically adopted their method to compute equation (3.1) and equation (3.2) for the problems of the forced generation of run-away solitons and free-traveling solitary waves propagating into a divergent or convergent channel.

For each term in both (3.1) and (3.2), we use the same differencing – Leapfrog in time and central difference in space:

$$\frac{\partial\zeta}{\partial t} = \frac{\zeta_i^{j+1} - \zeta_i^{j-1}}{2\Delta t} + O((\Delta t)^2), \tag{3.3}$$

$$\zeta\frac{\partial\zeta}{\partial x} = \frac{1}{3}(\zeta_{i+1}^j + \zeta_i^j + \zeta_{i-1}^j)\frac{\zeta_{i+1}^j - \zeta_{i-1}^j}{2\Delta x} + O((\Delta x)^2), \tag{3.4}$$

$$\frac{\partial^3\zeta}{\partial x^3} = \frac{\zeta_{i+2}^j - 2\zeta_{i+1}^j + 2\zeta_{i-1}^j - \zeta_{i-2}^j}{2(\Delta x)^3} + O((\Delta x)^2), \tag{3.5}$$

$$\frac{\partial^3\zeta}{\partial x^2\partial t} = \frac{\zeta_{i+1}^{j+1} - 2\zeta_i^{j+1} + \zeta_{i-1}^{j+1} - \zeta_{i+1}^{j-1} + 2\zeta_i^{j-1} - \zeta_{i-1}^{j-1}}{2(\Delta t)(\Delta x)^2} + O((\Delta t)^2, (\Delta x)^2). \tag{3.6}$$

Substituting these finite difference approximations back into the original partial differential equations, for equation (3.1), we reach an explicit scheme as follows

$$\begin{aligned}\zeta_i^{j+1} = \zeta_i^{j-1} &- (\frac{1}{a_1})_i^j\frac{\Delta t}{\Delta x}[1 + (\frac{a_3}{3})_i^j(\zeta_{i+1}^j + \zeta_i^j + \zeta_{i-1}^j)](\zeta_{i+1}^j - \zeta_{i-1}^j) \\ &- (\frac{a_3}{a_1})_i^j\frac{\Delta t}{(\Delta x)^3}(\zeta_{i+2}^j - 2\zeta_{i+1}^j + 2\zeta_{i-1}^j - \zeta_{i-2}^j) + 2\Delta t(\frac{a_4}{a_1})_i^j\zeta_i^j + 2\Delta t(\frac{a_5}{a_1})_i^j,\end{aligned} \tag{3.7}$$

and for equation (3.2), an implicit scheme of tridiagonal system:

$$\begin{aligned}(\frac{a_3}{(\Delta x)^2})_i^j\zeta_{i-1}^{j+1} + (a_1 - \frac{2a_3}{(\Delta x)^2})_i^j\zeta_i^{j+1} + (\frac{a_3}{(\Delta x)^2})_i^j\zeta_{i+1}^{j+1} \\ = (a_1)_i^j\zeta_i^j + (\frac{a_3}{(\Delta x)^2})_i^j(\zeta_{i+1}^{j-1} - 2\zeta_i^{j-1} + \zeta_{i-1}^{j-1}) \\ - \frac{\Delta t}{\Delta x}[1 + (\frac{a_3}{3})_i^j(\zeta_{i+1}^j + \zeta_i^j + \zeta_{i-1}^j)](\zeta_{i+1}^j - \zeta_{i-1}^j) \\ - 2\Delta t(a_4)_i^j\zeta_i^j + 2\Delta t(a_5)_i^j.\end{aligned} \tag{3.8}$$

Both of the schemes (3.7) and (3.8) are second order accurate in time and space and are conditionally stable. For the simple case of waves traveling in a rectangular uniform channel where $a_1 = 1$, $a_2 = 3/2$, $a_3 = 1/6$, $a_4 = 0$ and $a_5 = 0$, by the von Neumann method of stability analysis, we can obtain the stability criteria for scheme (3.7) and (3.8) as

$$\frac{\Delta t}{\Delta x}[1 + \frac{3}{2}|\zeta_0|] + \frac{2}{3}\frac{\Delta t}{(\Delta x)^3} \leq 1 \tag{3.9}$$

and

$$\Delta t \leq \sqrt{\frac{1}{3}}(1 + \frac{3}{2}|\zeta_0|) \tag{3.10}$$

respectively. Here ζ_0 is a typical wave amplitude.

From our experience in practical computations, we found condition (3.9) too strict. Thus instead of (3.9), we may suggest the following criterion for scheme (3.7):

$$\frac{1}{6}\frac{\Delta t}{(\Delta x)^3} \leq 0.39. \tag{3.11}$$

The first step in the iterations is done by similar schemes but with Euler forward in time. For scheme (3.7), the typical Δt and Δx being used in our computations are Δt =0.002 and Δx =0.1. For scheme (3.8), we mostly used $\Delta t = \Delta x = 0.1$. Computations based on these two schemes may cost from 15 seconds to less than 5 minutes of CPU time on a Cray supercomputer depending on different cases.

Since there exist steady solutions of permenant wave forms to the constant coefficient KdV equations (2.115) and (2.116), we can always test our numerical schemes on these solutions and compare the numerical results with the analytical solutions given by (2.117)-(2.120) to examine the accuracy and the convergence of our schemes. Figure 3.1 shows the comparison between the numerical result and the analytical solution based on the KdV equation (2.115) with scheme (3.7), after a left-going solitary wave ($a_0 = 0.3$) having traveled 92 water depth. Figure 3.2 shows similar results based on the regularized KdV equation (2.116) with scheme (3.8). In these figures the solid lines represent the numerical result and the dashed lines the analytical solutions. In these two test cases, the results show that the relative errors in maximum wave amplitude for both cases are about 0.3%.

Schemes (3.7) and (3.8) are applied in our computations to study the forced generation of run-away solitons, free-traveling waves propagating in a divergent or convergent channel and the comparison made between the forced KdV equation

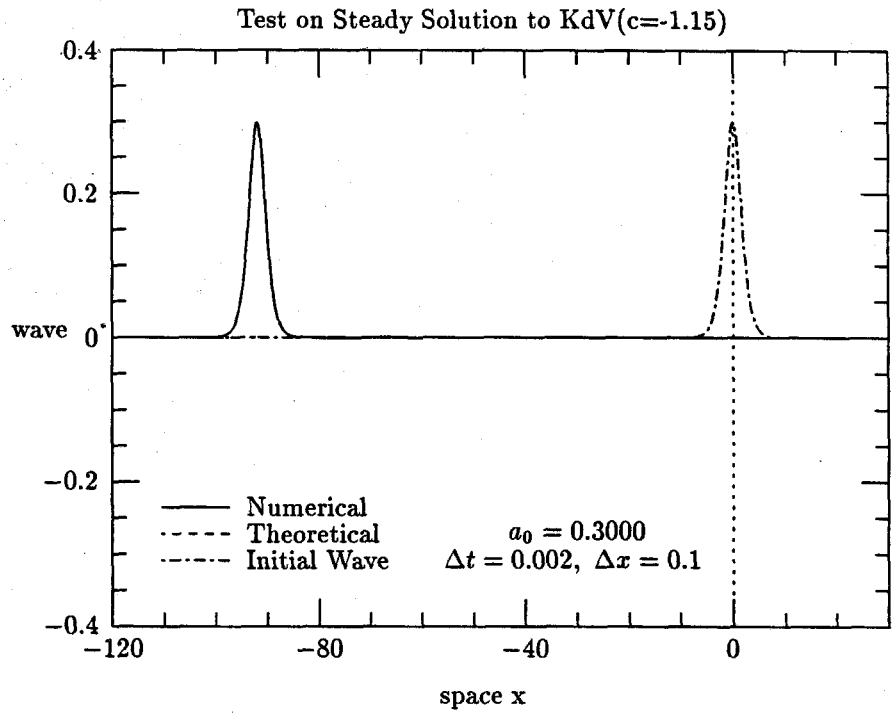

Figure 3.1(a)

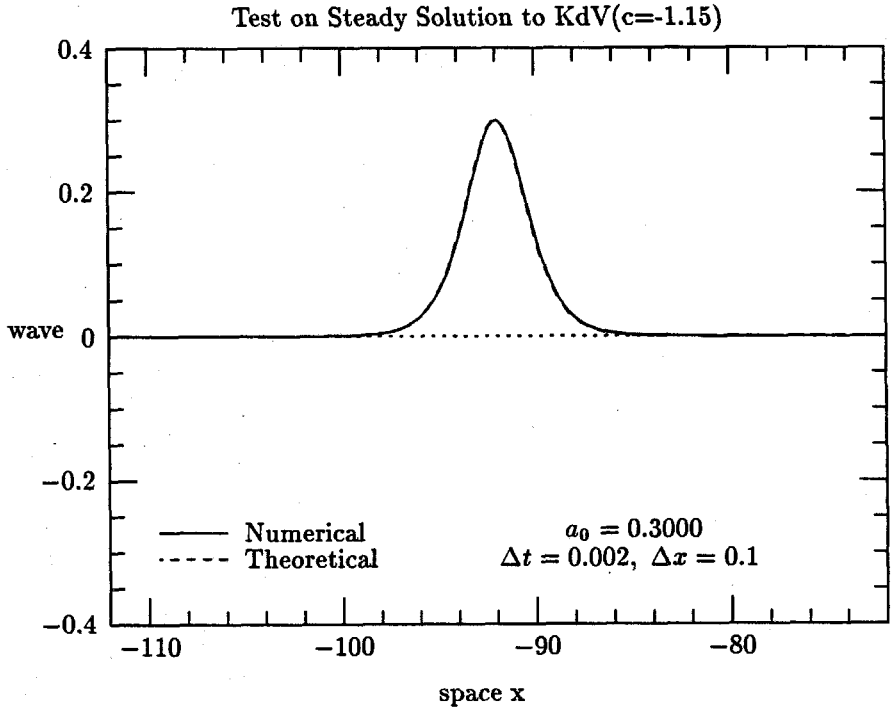

Figure 3.1(b)

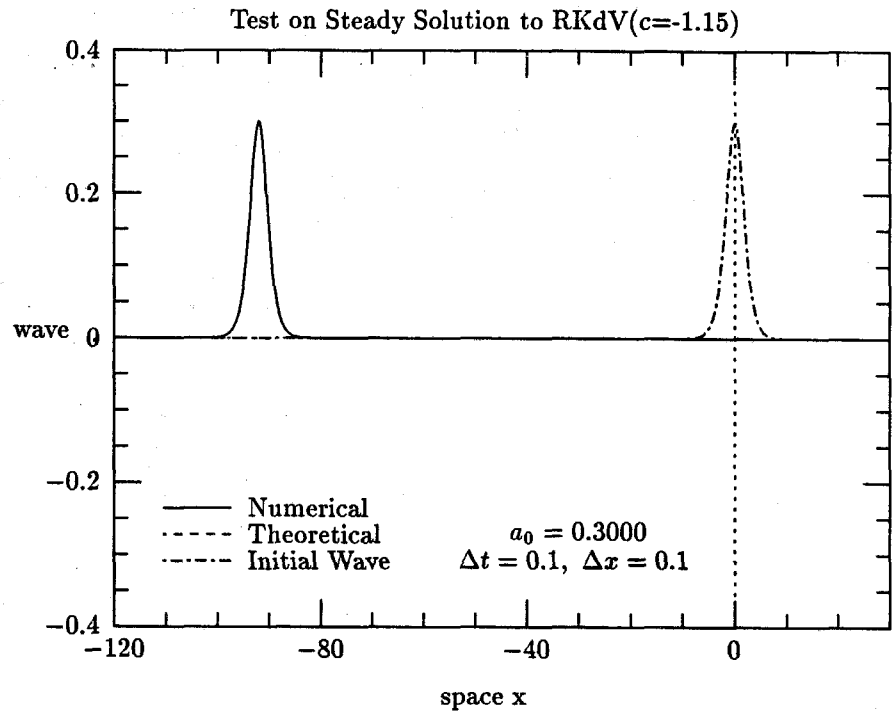

Figure 3.2(a)

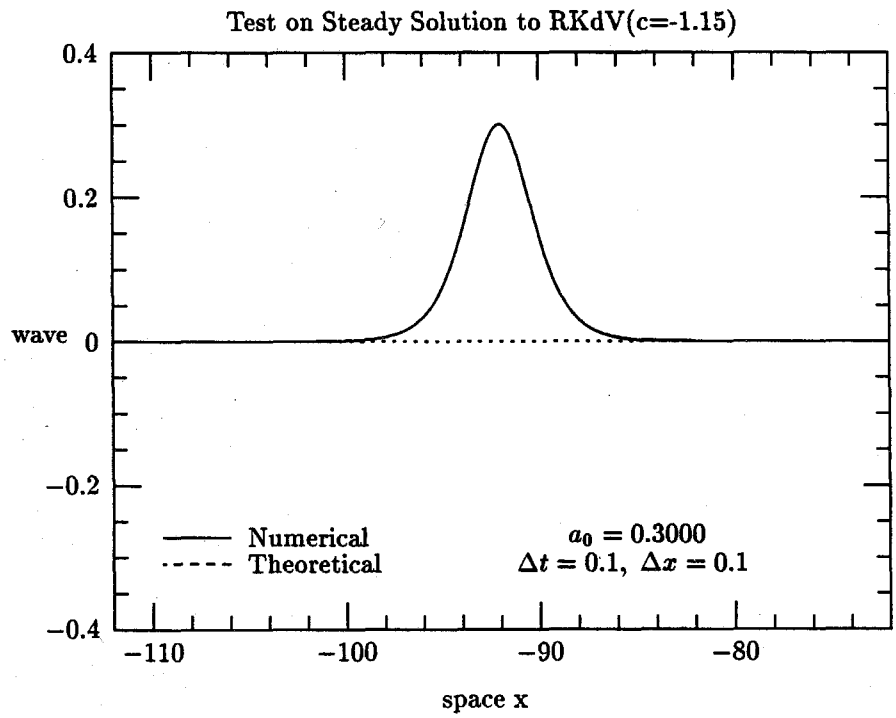

Figure 3.2(b)

and the regularized KdV equation.

A simple algorithm to solve a tridiagonal matrix like (3.8) is presented in Appendix II and the detailed von Neumann instabilty analysis of different numerical schemes can be found in Appendix III.

3.2 Predictor-Corrector Finite Difference Schemes for the gcB Model

In this section we present the numerical schemes to compute the gcB model (2.110)-(2.111) for a rectangular channel of variable width but constant depth. We are interested in two cases. In the first case, waves are traveling into a divergent or convergent channel without external moving disturbances, and the half-width $b = b(x)$ is a function of x only. In the second case, waves are generated by a disturbance of finite longitudinal length moving along the two side-walls of a uniform rectangular channel. So the half-width in this case is $b(x,t) = 1 - B(x,t)$ where $B(x,t)$ represents the disturbance.

Case I b=b(x)

For this case, the gcB model (2.110)-(2.111) can be written as

$$b\zeta_t + [b(1+\zeta)u]_x = 0, \tag{3.12}$$

$$u_t + uu_x + \zeta_x = \frac{1}{3}[u_{xxt} + \frac{b_x}{b}u_{xt} + (\frac{b_x}{b})_x u_t]. \tag{3.13}$$

Applying Euler forward in time and central difference in space, we obtain the following finite difference scheme for equations (3.12)-(3.13)

$$\zeta_i^{j+1} = \zeta_i^j - \frac{\Delta t}{2\Delta x}\frac{b_{i+1}}{b_i}(1+\zeta_{i+1}^j)u_{i+1}^j + \frac{\Delta t}{2\Delta x}\frac{b_{i-1}}{b_i}(1+\zeta_{i-1}^j)u_{i-1}^j, \tag{3.14}$$

$$[-\frac{1}{3(\Delta x)^2}+\frac{1}{6\Delta x}(\frac{b_x}{b})_i]u_{i-1}^{j+1}+[1+\frac{2}{3(\Delta x)^2}-\frac{1}{3}((\frac{b_x}{b})_x)_i]u_i^{j+1}$$
$$+[-\frac{1}{3(\Delta x)^2}-\frac{1}{6\Delta x}(\frac{b_x}{b})_i]u_{i+1}^{j+1}=u_i^j-\frac{\Delta t}{6\Delta x}(u_{i+1}^j+u_i^j+u_{i-1}^j)(u_{i+1}^j-u_{i-1}^j)$$
$$-\frac{\Delta t}{2\Delta x}(\zeta_{i+1}^j-\zeta_{i-1}^j)-\frac{1}{3(\Delta x)^2}(u_{i+1}^j-2u_i^j+u_{i-1}^j)$$
$$-\frac{1}{6\Delta x}(\frac{b_x}{b})_i(u_{i+1}^j-u_{i-1}^j)-\frac{1}{3}((\frac{b_x}{b})_x)_iu_i^j. \tag{3.15}$$

The first difference equation (3.14) is explicit while (3.15) is an implicit tridiagonal system. Together, scheme (3.14)-(3.15) is a straight forward one-step finite difference scheme. It is first-order accurate in time and second-order accurate in space. The scheme is conditionally stable. In our computations, the typical Δt and Δx we used are $\Delta t = 0.0005$ and Δx=0.1. The choice of the very small Δt is to ensure the high accuracy of the scheme that is required by the particular physical problem that we are studying in this case. To test the accuracy and the convergence of the scheme, we first run a case for a right-going solitary wave (based on the gcB model) propagating in a uniform channel and then compare the result with the theoretical solution given by (2.140). The results are shown in Figure 3.3. The relative change in the maximum wave amplitude of the 'permanent' solitary wave is about 0.5% after the wave has traveled 92 water depth by scheme (3.14)-(3.15). For a real case of waves traveling into a variable channel, the computation with 4000 grid pionts may cost about 20 minutes of CPU time on a Cray supercomputer for waves traveling out 300 water depth. A more efficient two-step predictor-corrector scheme can be constructed based on a one-step scheme, which we will show for Case II.

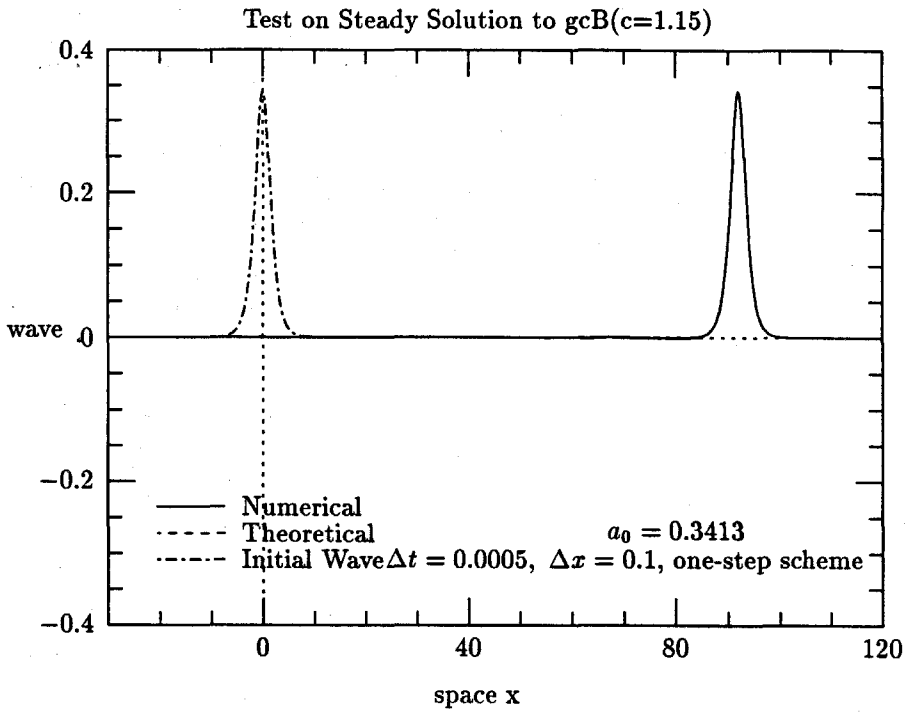

Figure 3.3(a)

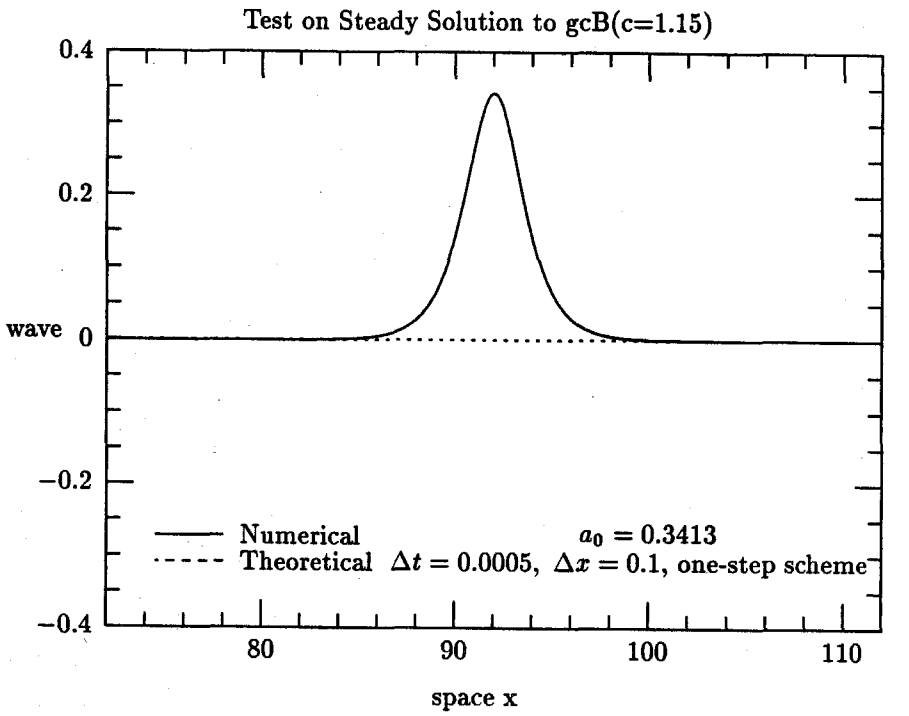

Figure 3.3(b)

Case II b(x,t)=1-B(x,t)

Since we assume that the external forcing function $B(x,t)$ is a small perturbation to the wave field, the gcB model (2.110)-(2.111) can be simplified by neglecting the higher order terms

$$(b\zeta)_t + [b(1+\zeta)u]_x = B_t, \tag{3.16}$$

$$u_t + uu_x + \zeta_x = -p_{ax} + \frac{1}{3}u_{xxt} - \frac{1}{3}B_{xtt}. \tag{3.17}$$

To solve equations (3.16)-(3.17) numerically, we construct a scheme that involves two steps to forward in time. The first step is called the predictor-step where we apply central difference in space and Euler forward in time. This step gives a 'predicted value' of the unknowns at the new time level. Denoting this predicted value with *, we have the scheme for the predictor-step as

$$b_i^{j+1}\zeta^* = (b\zeta)_i^j + \Delta t f_1(b,\zeta,u,B_t)_i^j, \tag{3.18}$$

$$-\sigma u_{i-1}^* + (1+2\sigma)u_i^* - \sigma u_{i+1}^* = u_i^j - \sigma(u_{i+1}^j - 2u_i^j + u_{i-1}^j) + \Delta t f_2(\zeta,u,B_{xtt})_i^j, \tag{3.19}$$

where

$$(f_1)_i^j = -\frac{1}{2\Delta x}[(b(1+\zeta)u)_{i+1}^j - (b(1+\zeta)u)_{i-1}^j] + (B_t)_i^j, \tag{3.20}$$

$$(f_2)_i^j = -\frac{1}{6\Delta x}(u_{i+1}^j + u_i^j + u_{i-1}^j)(u_{i+1}^j - u_{i-1}^j) - \frac{1}{2\Delta x}(\zeta_{i+1}^j - \zeta_{i-1}^j) - \frac{1}{3}(B_{xtt})_i^j, \tag{3.21}$$

$$\sigma = \frac{1}{3(\Delta x)^2}. \tag{3.22}$$

Scheme (3.18) is explicit, while (3.19) is an implicit scheme of tridiagonal system. The second step is called the corrector-step whose basic structures are the same as in the first step, except that for the second step we will make use of the results we just obtained from the predictor-step to reach a better or 'corrected ' finite difference approximation of the unknown values at the new time step. This

is done by taking the average of the values of the previous time level and the predictor-step for functions f_1 and f_2 in the corrector-step

$$b_i^{j+1}\zeta_i^{j+1} = (b\zeta)_i^j + \frac{1}{2}\Delta t[f_1(b,\zeta,u,B_t)_i^j + f_1(b_i^{j+1},\zeta_i^*,u_i^*,(B_t)_i^{j+1})], \tag{3.23}$$

$$-\sigma u_{i-1}^{j+1} + (1+2\sigma)u_i^{j+1} - \sigma u_{i+1}^{j+1} = u_i^j - \sigma(u_{i+1}^j - 2u_i^j + u_{i+1}^j)$$
$$\frac{1}{2}\Delta t[f_2(\zeta,u,B_{xtt})_i^j + f_2(\zeta_i^*,u_i^*,(B_{xtt})_i^{j+1})]. \tag{3.24}$$

This predictor-corrector two-step scheme (3.18)-(3.24) is second-order accurate both in time and in space. It is more stable than scheme (3.14)-(3.15) and thus permits the use of larger Δt's. The typical Δt and Δx we used are Δt=0.01 and Δx=0.1. The result of the test on solitary wave propagating in a uniform channel is shown in Figure 3.4. After the wave has traveled 92 water depth, the relative change in the maximum wave amplitude is about 0.3%. In a typical run for waves traveling out 200 water depths, the computation with 6000 grid points costs about 2 minutes of CPU time on Cray.

3.3 Discretization of the Computational Domain and the Boundary Conditions

In most of the cases in our studies, the physical domain of the problem is from $-\infty$ to $+\infty$ except in the case of waves being generated by boundary forcing where the domain is $[0,+\infty)$. In our numerical computations, we choose the computational domain to be of finite length as $[-s/2,s/2]$ or $[0,s/2]$. In order to make the numerical simulations consistent with the original physical problem, we choose s big enough such that the flow field at $x = \pm s/2$ is virtually unperturbed and thus remains at rest for all times.

The computational domain is always discretized into evenly spaced N grids and the iterations of the schemes are proceeded on the grid points. For scheme

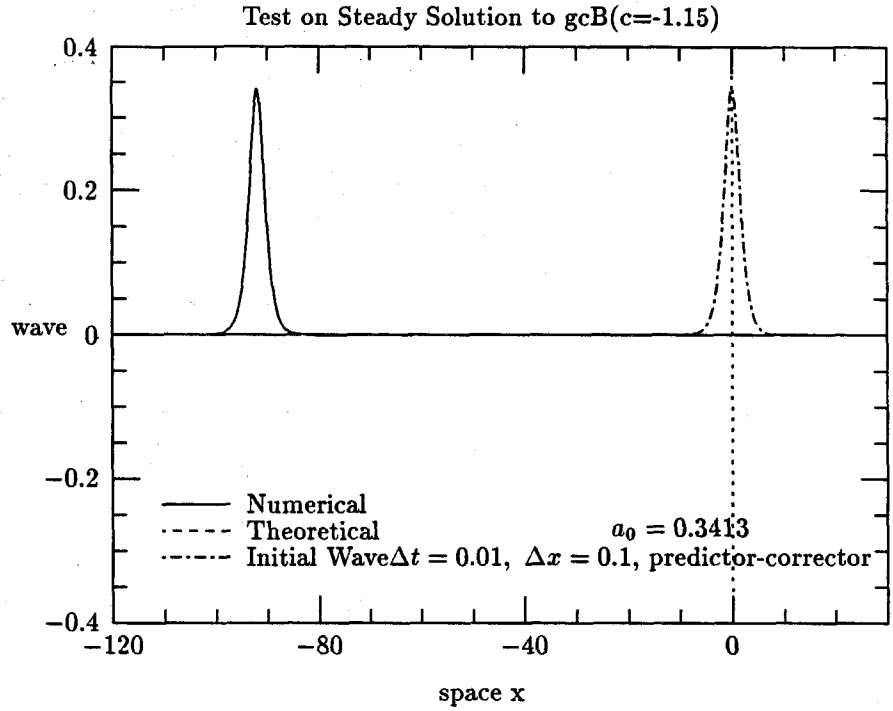

Figure 3.4(a)

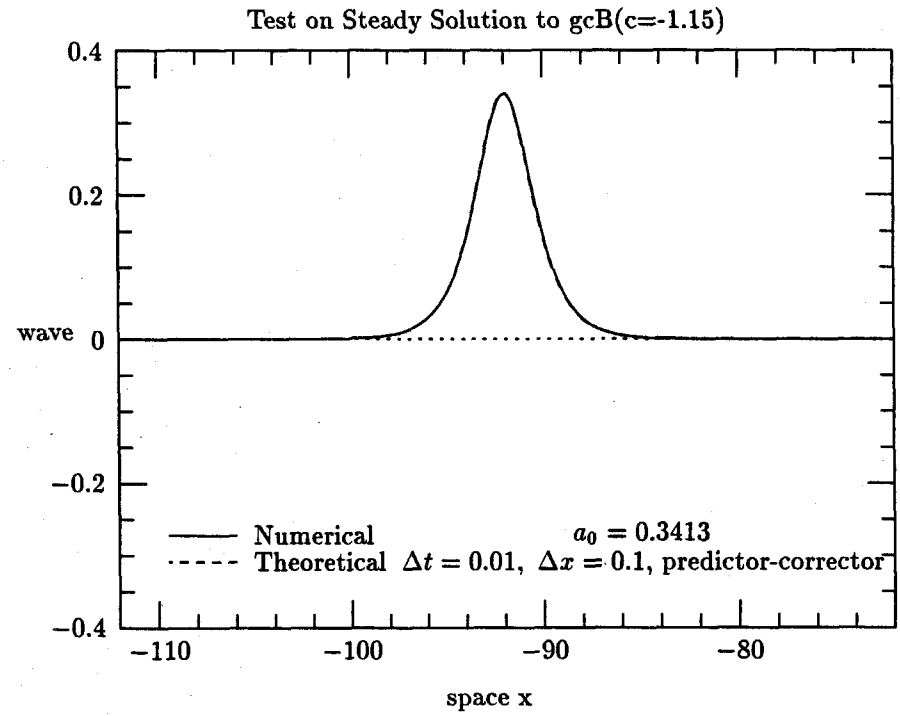

Figure 3.4(b)

(3.7), since a third derivative term is involved, we need to provide conditions for two end points at each boundary. This is easy to accomplish if the problem we are studying is for an infinite domain and for which we assume the unperturbed boundary conditions. In these cases, the numerical boundary conditions for scheme (3.7) will be

$$\zeta_1^j = \zeta_2^j = \zeta_N^j = \zeta_{N+1}^j = 0. \tag{3.25}$$

If the problem is for $[0, s/2]$, scheme (3.7) requires special treatment at the boundary $x = 0$. All other finite difference schemes require conditions for only one end point at each boundary.

IV. EVOLUTION OF A SOLITARY WAVE TRAVELING IN A DIVERGENT OR CONVERGENT CHANNEL

When a solitary wave travels in a channel of variable cross-sectional shape, its amplitude and speed will vary due to the change in channel width and depth. It is of significance to study quantitatively how the wave amplitude and wave speed will be modulated for a wave traveling into a variable channel. The results of the study, when further combined with the analysis of wave dissipation due to viscosity and the roughness of the channel bed in reality, can have useful applications to flood control problems in rivers or to near-coastal engineering. In recent years, several studies have been carried out on the evolution of a solitary wave traveling into a variable channel. Shuto[26] (1974) derived a KdV-type equation to describe the propagation of nonlinear long waves in a rectangular channel of variable section. Starting from the Euler equation and by using perturbation expansions, he reached a variable coefficient KdV equation written in the moving frame. Shuto's model is similar to the cKdV model we derived in the present study, except that in his case, the channel has rectangular sections and the external forcing functions were not considered. Miles[19] (1979) further studied on Shuto's KdV equation for a gradually varying channel. He examined the conservation properties of Shuto's model and pointed out that the variable coefficient KdV equation does not conserve mass due to the neglect of the reflected waves. The problem of the reflected waves was analyzed based on linear theory and an approximated correction to the KdV equation was given. Chang et al.[2] (1979) performed experimental measurements on solitary waves propagating in a linearly diverging or linearly converging channel of rectangular sections. The experimental data were compared with the numerical results based on Shuto's model. Their results for a linearly diverging channel

showed good agreement with the prediction that $a \propto W^{-2/3}$, where a is the amplitude of the solitary wave and W the channel width. For linearly converging channel the wave growth was approximated by $a \propto W^{-1/2}$. The analyses of all the above studies were performed in the moving wave-frame coordinate.

Our present study on the evolution of a solitary wave traveling into a variable channel is emphasized not only on the physical aspects, but further on a more careful examination of the conservation laws and the validity of the channel KdV model. Since we not only obtained a cKdV equation, but also derived a generalized channel Boussinesq model which conserves mass exactly and permits the traveling of waves in both directions, we are able to study the problem based on a more accurate model (i.e., the gcB model) than the cKdV model, and by comparing the results between the two models, we will be able to see quantitatively the loss of mass and energy due to the reflected waves, and further examine the effects of neglecting the reflected waves on the validity of the cKdV model.

Numerical computations were carried out to study the propagation of a solitary wave in a rectangular channel of linearly varying width but of constant depth. The computations are based on both the gcB and the cKdV models, and the equations are written in the fixed laboratory coordinates rather than the transformed wave coordinate system. The changes in wave amplitude and speed were examined. We also computed the total excess mass, the total energy and other related invariants. The results were compared between the two models. Our results show that even though the cKdV model can dictate solitary waves to lose or gain mass to more than 50% due to the reflected wave, it still provides quite correct predictions for the wave amplitude and the wave speed of the main transmitted waves.

4.1 Governing Equations

The motion of free waves traveling in a channel of variable width but constant depth is described by the generalized channel Boussinesq equations

$$b\zeta_t + [b(1+\zeta)u]_x = 0, \tag{4.1}$$

$$u_t + uu_x + \zeta_x = \frac{1}{3}u_{xxt} + \frac{1}{3}\frac{b_x}{b}u_{xt} + \frac{1}{3}(\frac{b_x}{b})_x u_t, \tag{4.2}$$

which are deduced from equations (2.109) and (2.110). This theoretical model will be employed to make comparisons with the results obtained from the channel KdV model,

$$\zeta_t + \zeta_x + \frac{3}{2}\zeta\zeta_x + \frac{1}{6}\zeta_{xxx} + \frac{1}{2}\frac{b_x}{b}\zeta = 0. \tag{4.3}$$

In the present case, the channel width $b = b(x)$ is linearly varying in space as follows:

$$b(x) = \begin{cases} b_0, & -s_1 \le x \le 0; \\ b_0 + \alpha x, & 0 < x \le s_2; \\ b_1, & s_2 < x \le s_2 + s_3; \end{cases}$$

where the expansion angle α is a small constant. This is the same configuration considered by Chang et al.[2] in their experimental and numerical studies.

Based on the results from section 2.11, the gcB model (4.1)-(4.2) gives the following conservation laws for the present case:

$$\frac{dM_e}{dt} = \frac{d}{dt}\int_{-\infty}^{+\infty} 2b\zeta dx = 0, \tag{4.4}$$

$$\frac{dM_{b2}^*}{dt} = \frac{d}{dt}\int_{-\infty}^{+\infty} u dx = 0, \tag{4.5}$$

$$\frac{dE_b}{dt} = \frac{d}{dt}\int_{-\infty}^{+\infty} b(u^2 + \zeta^2)dx + \text{h.o.t.} = 0, \tag{4.6}$$

while the channel KdV model (4.3) gives

$$\frac{dM_e}{dt} = \int_{-\infty}^{+\infty} (b_x\zeta + \frac{3}{2}b_x\zeta^2 + \frac{1}{3}b_x\zeta_{xx})dx, \tag{4.7}$$

and

$$\frac{dE_{k0}}{dt} = \frac{d}{dt}\int_{-\infty}^{+\infty} 2b\zeta^2 dx$$
$$= \int_{-\infty}^{+\infty} (2b_x\zeta^3 + \frac{2}{3}b_x\zeta\zeta_{xx} - \frac{1}{3}b_x\zeta_x^2)dx. \tag{4.8}$$

These results show that the gcB model conserves both the excess mass and the total energy while the cKdV model does not conserve either mass or energy, even though the rate of change in total energy may be slow, since the terms on the right hand side of (4.8) are small, being of $O(|\zeta|^2)$ versus the $O(|\zeta|)$ for the estimates of dM_e/dt.

4.2 Numerical Results

A sketch of the divergent and convergent channel is shown in Figure 4.1. The initial solitary wave is at $x = -s_0$. After it travels to the right in a uniform channel for a length of s_0, it enters a variable section, which is of length s_2, and propagates with modulated amplitude and speed. Finally it enters another uniform section which is of length s_3.

The essential parameters in our studies are c_0, the speed of the initial solitary wave, α, the expansion angle of the variable section of the channel, and also in the general case other than linearly varying channels, the curvature of the variable section.

The numerical computations are based on both the gcB and the cKdV models. The gcB model (4.1)-(4.2) is computed by applying scheme (3.14)-(3.15) presented in Chapter III. For the cKdV model (4.3), we use the explicit scheme given by (3.7). The results of test runs on accuracy showed that after a solitary wave (c_0=1.15, a_0=0.3 by KdV and a_0=0.3413 by gcB) has traveled 92 water depths in a uniform channel, the relative change in wave amplitude is less than 0.5% by both schemes.

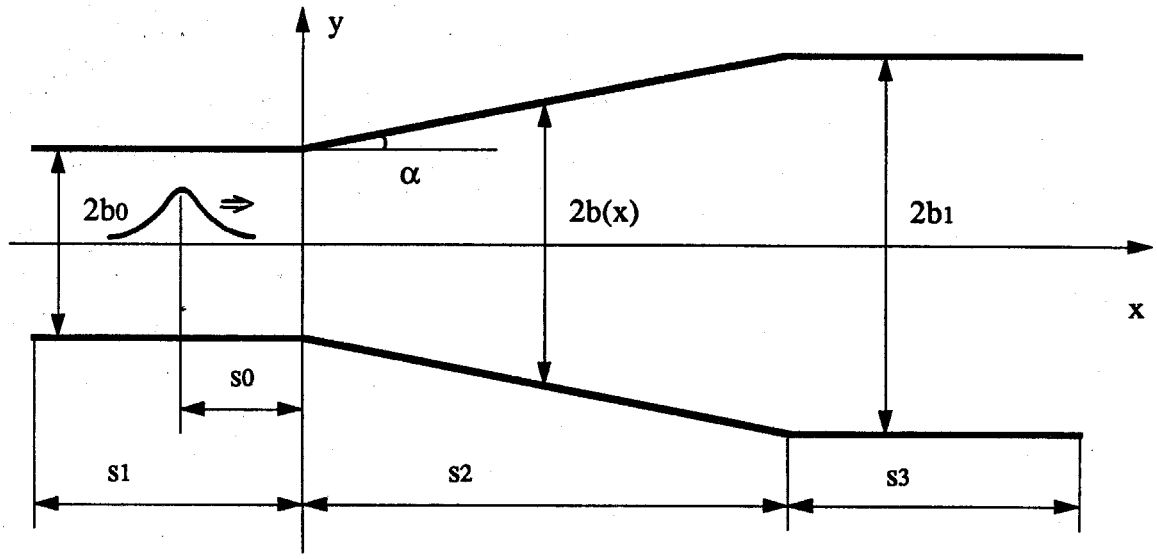

Figure 4.1(a) Divergent channel

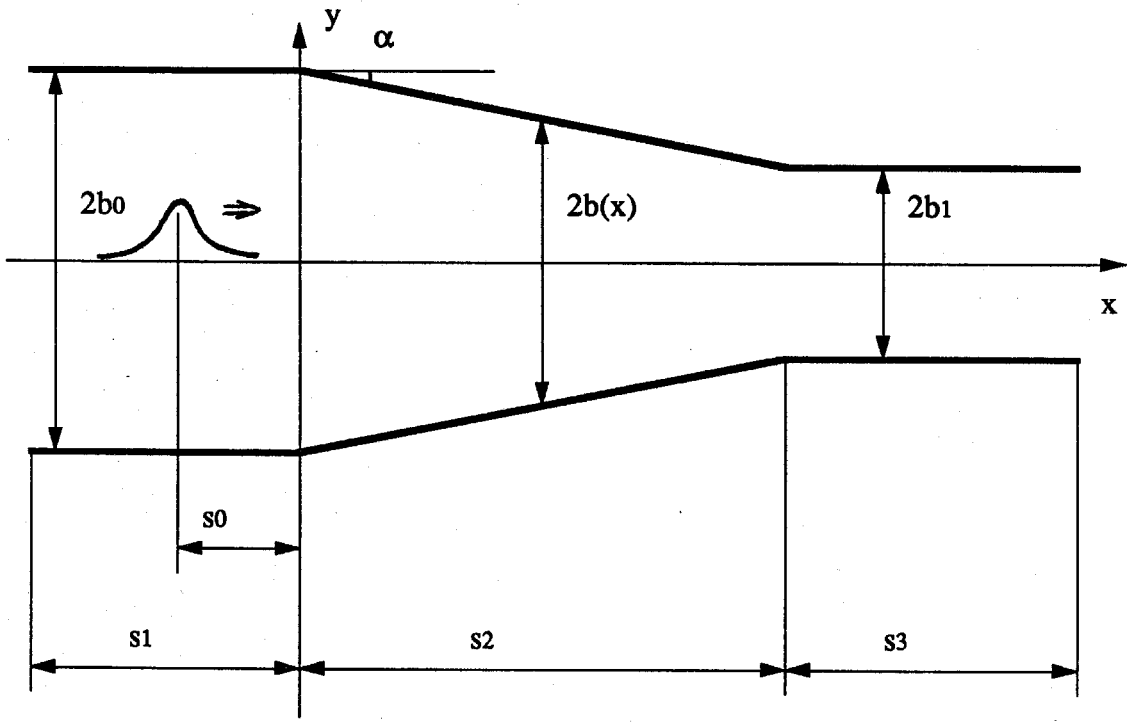

Figure 4.1(b) Convergent channel

The quantities and wave features that we are particularly interested in studying are the change of wave amplitude and wave speed in the variable section, the total excess mass and the total energy, the loss of mass and energy due to the reflected waves, and the change in the wave profile. Four cases with different sets of values of parameters are investigated and the results are compared between the two different models.

In our studies, the convergent channel may be regarded as the same channel as the divergent channel, only with a change of propagation in the opposite direction. We study the evolution of a solitary wave traveling in a divergent channel and in a convergent channel as a pair in each case. The speed of the initial solitary wave for the convergent channel is chosen to be the same as that of the terminal wave traveling out of the divergent channel. The parameter c_0 in the title of each of the following cases represents the speed of the initial solitary wave for the divergent channel. From the results presented in section 9.2, we observe that the steady solitary wave solutions for the gcB and the cKdV models are noticeablly different: for the same wave speed, the gcB model requires a higher wave amplitude. In each of the following cases, both the gcB and the cKdV models will be computed and the comparison between the two models will be based on the wave speed instead of the wave amplitude.

The total length of the channel is six hundred (water depths) with s_1= 300.0, s_2=100.0 and s_3=200.0. This is true for most of the cases. The detailed values of different parameters in all cases are summed in Table 4.1.

Table 4.1 Values of Different Parameters

	$2b_0$	α	$2b_1$	s_0	s_1	s_2	s_3	c_0	a_0
Case I (div.)	2.0	0.019	5.8	30.0	300.0	100.0	200.0	1.050	0.100
Case I (con.)	5.8	-0.019	2.0	30.0	300.0	100.0	200.0	1.027	0.054
Case II (div.)	2.0	0.038	9.6	30.0	300.0	100.0	200.0	1.050	0.100
Case II (con.)	9.6	-0.038	2.0	30.0	300.0	100.0	200.0	1.020	0.040
Case III (div.)	0.5	0.019	4.3	10.0	300.0	100.0	200.0	1.093	0.185
Case IV (con.)	3.0	-0.019	0.34	10.0	300.0	70.0	230.0	1.087	0.174

where c_0 is the speed of the initial solitary wave and a_0 is the initial amplitude based on the KdV model.

4.2.1 Case I $c_0 = 1.05$, $|\alpha| = 0.019$, $b(x)$ linearly varying

A. Results based on the gcB model

(1) Divergent channel

The channel width of the entrance uniform section is $2b_0$=2.0. The initial wave takes the form of a gcB-solitary wave of amplitude a_0=0.1043 and speed c_0=1.05. It starts at x=-30.0 and travels to the right to enter a linearly diverging channel. Computations are run for time t from 0.0 to 150.0. The numerical results for the wave amplitude are shown in Figure 4.2(a). It is a plot of the wave elevation in a time series with the increment of Δt=20.0. These results show that as a solitary wave travels in a divergent channel, its amplitude decreases. Also, a negative wave train is clearly reflected downstream. The front of the reflected wave travels in the negative x direction with a near critical speed ($c_f \approx$-1.0). For the transmitted wave, its profile remains close to a solitary wave form, except that it becomes steeper and has evolved an undular wave tail of very small amplitude. The detailed comparison between the transmitted wave and a permanent solitary

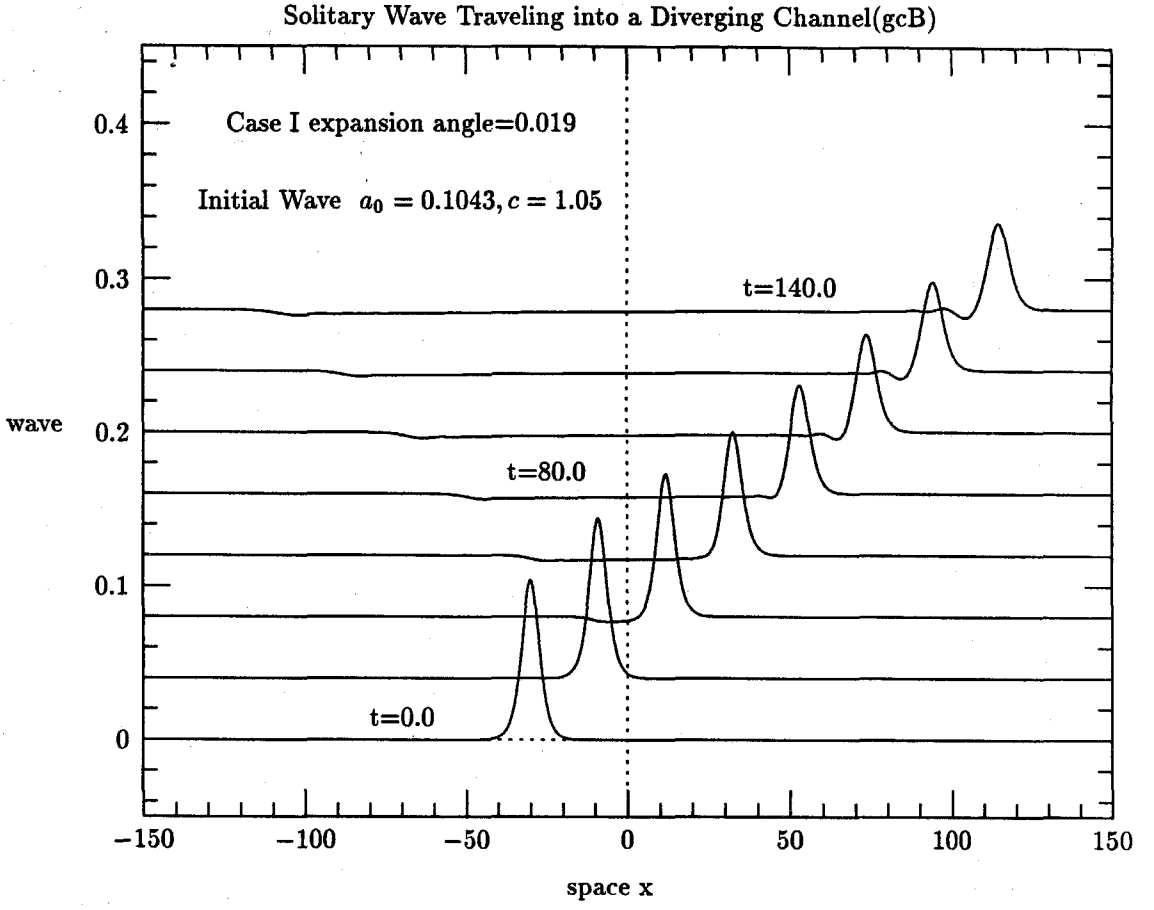
Solitary Wave Traveling into a Diverging Channel(gcB)
Case I expansion angle=0.019
Initial Wave $a_0 = 0.1043, c = 1.05$
t=140.0
t=80.0
t=0.0
wave
space x
0.4
0.3
0.2
0.1
0
−150
−100
−50
0
50
100
150

Figure 4.2(a)

wave is shown in Figure 4.2(b) and Figure 4.2(c) for the wave at x=53.1 and at x=124.6, respectively. When the wave enters and travels in the final uniform section, its wave amplitude continues to decrease, though at a lower rate. This continuous change in the wave amplitude is due to the negative wave tail in the trailing region. At the final time t=150.0, the wave travels to x=124.6 with the amplitude decreased to a=0.05548 (speed c=1.0271).

The total excess mass M_e is exactly conserved as shown by the solid line in Figure 4.2(d). The total energy E_b is also conserved, with an error of 2.1%. The result for E_b is shown in Figure 4.2(l) by the solid line. The dashed line in Figure 4.2(d) represents the gain of mass at the expense of the reflected waves. We can see that even though the wave amplitude of the reflected wave is small, the total mass it carries in is relatively large, because of the great length of the negative wave region. At the final time t=150.0, the local excess mass possessed by the reflected wave is about 75.7% of the original total excess mass. Since the total excess mass is always conserved, we expect that the local excess mass possessed by the transmitted solitary wave will increase by 75.7%. To compare with cKdV's results later, we also plot the time record for the approximate energy $\int_{-\infty}^{+\infty} 2b\zeta^2 dx$, which is shown in Figure 4.2(e) with a solid line. The dashed line in the same figure stands for the loss of energy due to the reflected waves, which we observe is very small. At the final time of t=150.0, the loss of energy due to the reflected waves is about 2.6% of the initial total energy.

(2) Convergent channel

The initial channel width for the convergent channel is taken to be the same as that of the exit channel width for the above divergent channel case, i.e., $2b_0$=5.8. The initial solitary wave has an amplitude a_0=0.05545 with speed c_0=1.0271. It also starts at x=-30.0 and travels to the right. A plot of the wave field in a time

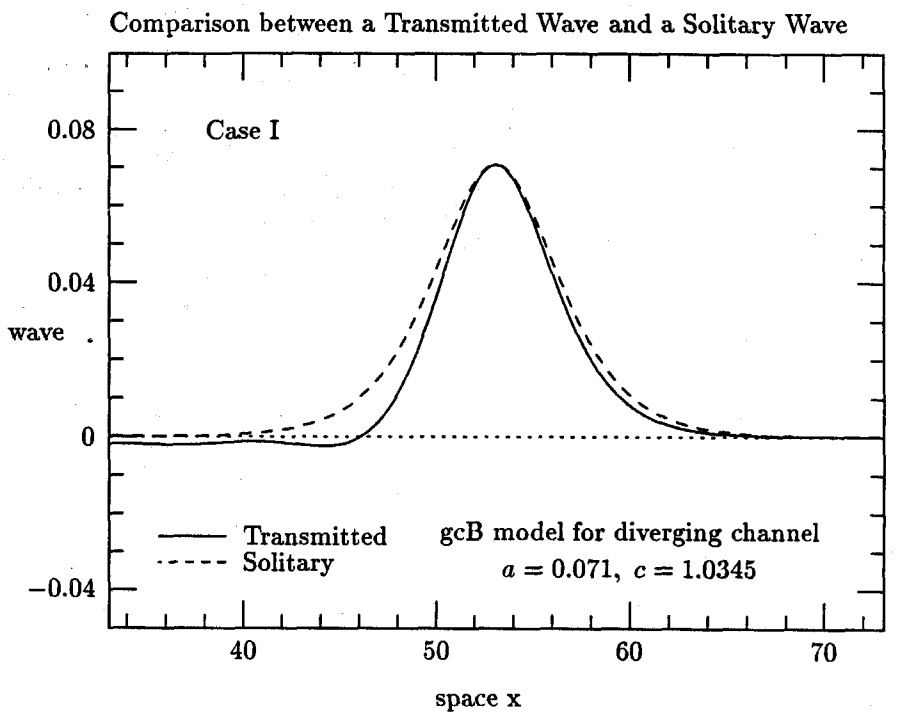

Figure 4.2(b)

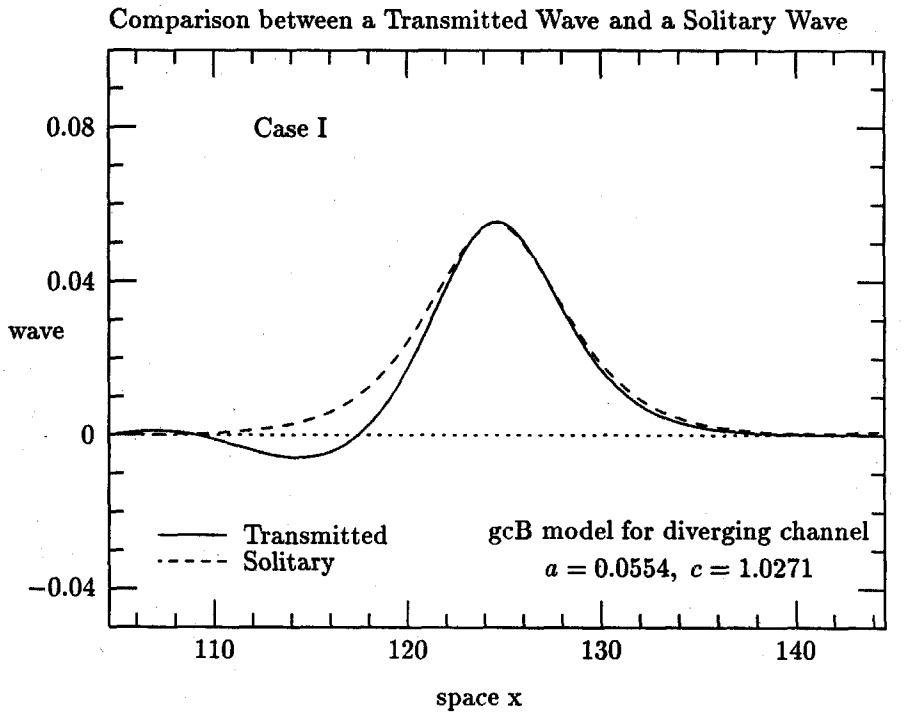

Figure 4.2(c)

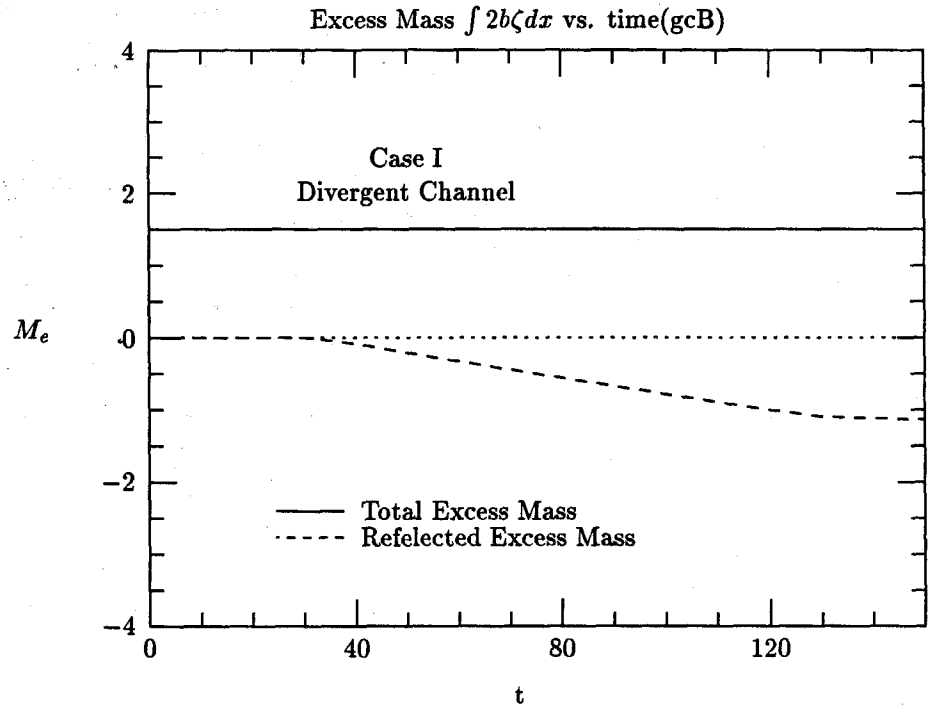

Figure 4.2(d)

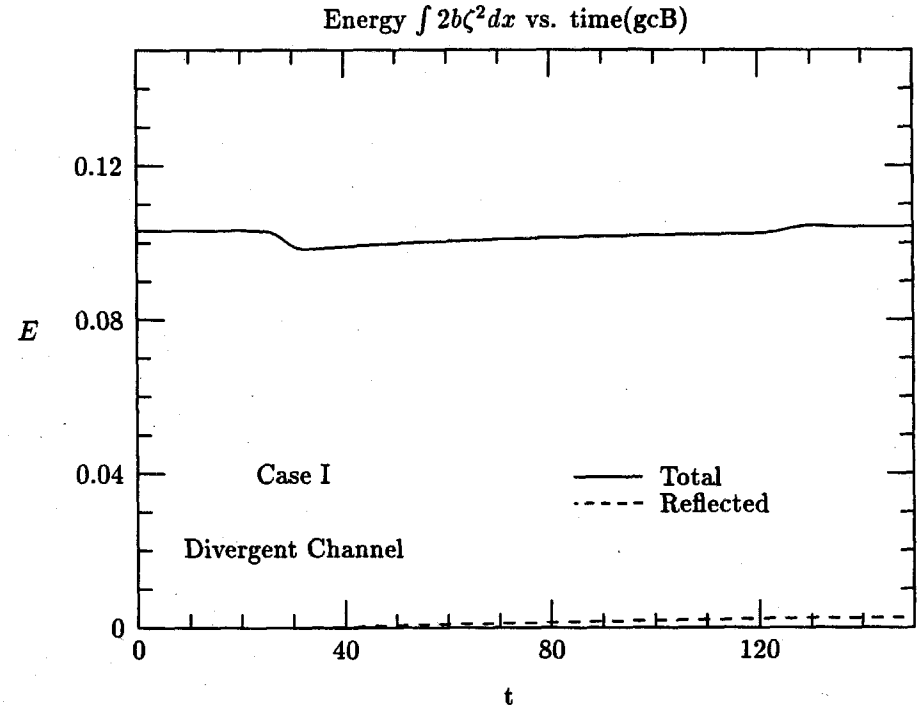

Figure 4.2(e)

series is shown in Figure 4.2(f). In this case the wave amplitude increases as the solitary wave travels in the convergent channel. Detailed comparisons between a solitary wave profile and a transmitted wave profile at two different locations are shown in Figures 4.2(g) and 4.2(h). We see that in this case the wave profiles become less steep than the corresponding free solitary waves of equal amplitude and they also travel with a reflected wave tail of very small positive amplitude. At the final time t=150.0, the wave travels to x=125.9 with the amplitude increased to a=0.0966 (speed c=1.0465).

The total excess mass M_e is exactly conserved. The relative change in the total energy E_b is about 1.1%. The time records for M_e and E_b are shown in Figure 4.2(i) and Figure 4.2(l), respectively.

For a solitary wave traveling in a convergent channel, a positive wave train is reflected in the downstream region. The front of the reflected wave travels with a near critical speed ($c_f \approx$-1.0) downstream. The final loss of mass of the transmitted wave due to the reflected wave (shown by the dashed line in Figure 4.2(i)) in this case is 42.4% of the initial total excess mass. The loss of the energy due to the reflected wave is about 1.8%. (See Figure 4.2(j).)

Figure 4.2(k) shows the change in the amplitude of the solitary wave when it travels in the variable sections. The solid line represents the results for the divergent channel case while the dashed line represents the results for the convergent channel. The results for the convergent channel are plotted in such a way that the wave is supposed to travel in the same divergent channel, but in the opposite direction, i.e., in the negative x direction. We see that at the final time for the convergent channel case, the wave amplitude does not come back exactly to the initial wave amplitude which is that before entering the divergent channel. The relative difference is about 7.2%. This can be attributed primarily to the fact that

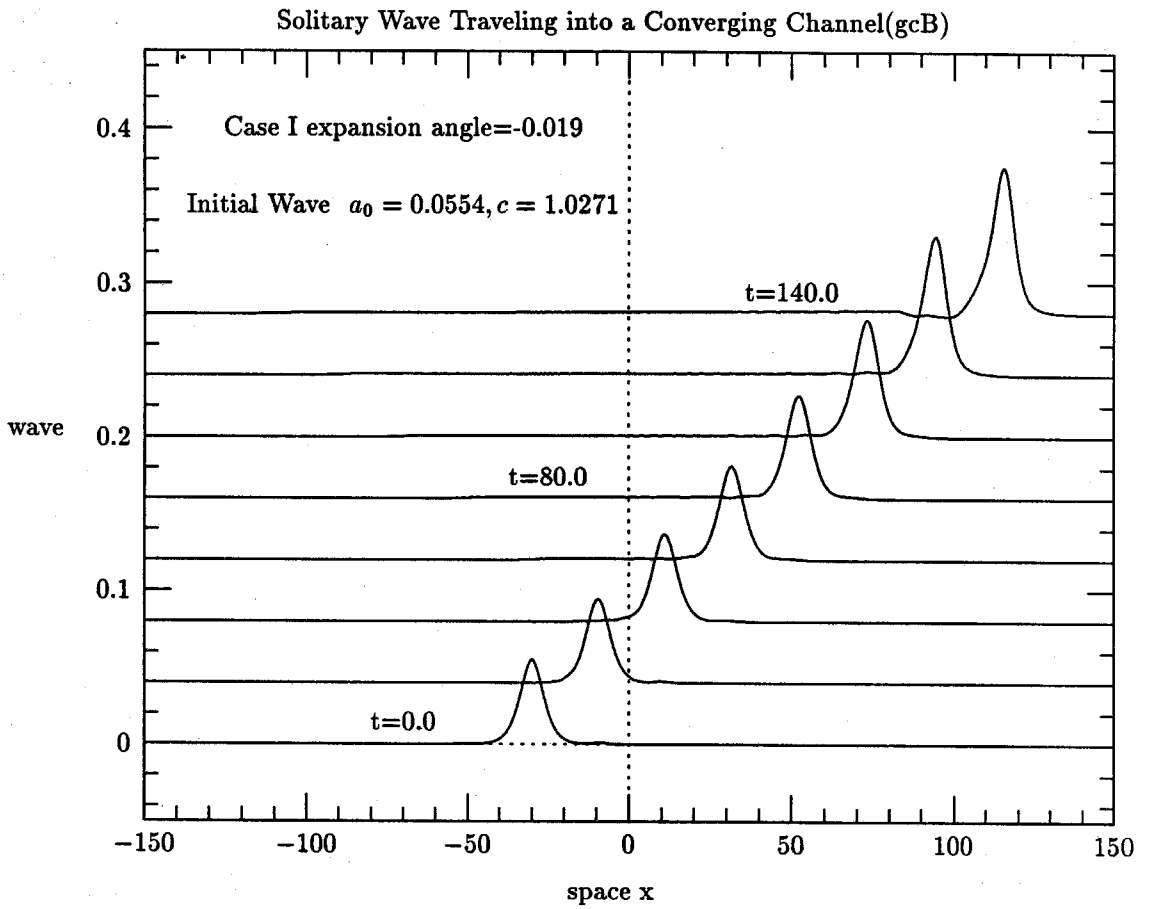
Solitary Wave Traveling into a Converging Channel(gcB)
Case I expansion angle=-0.019
Initial Wave $a_0 = 0.0554, c = 1.0271$
t=140.0
t=80.0
t=0.0
wave
0.4
0.3
0.2
0.1
0
−150
−100
−50
0
50
100
150
space x

Figure 4.2(f)

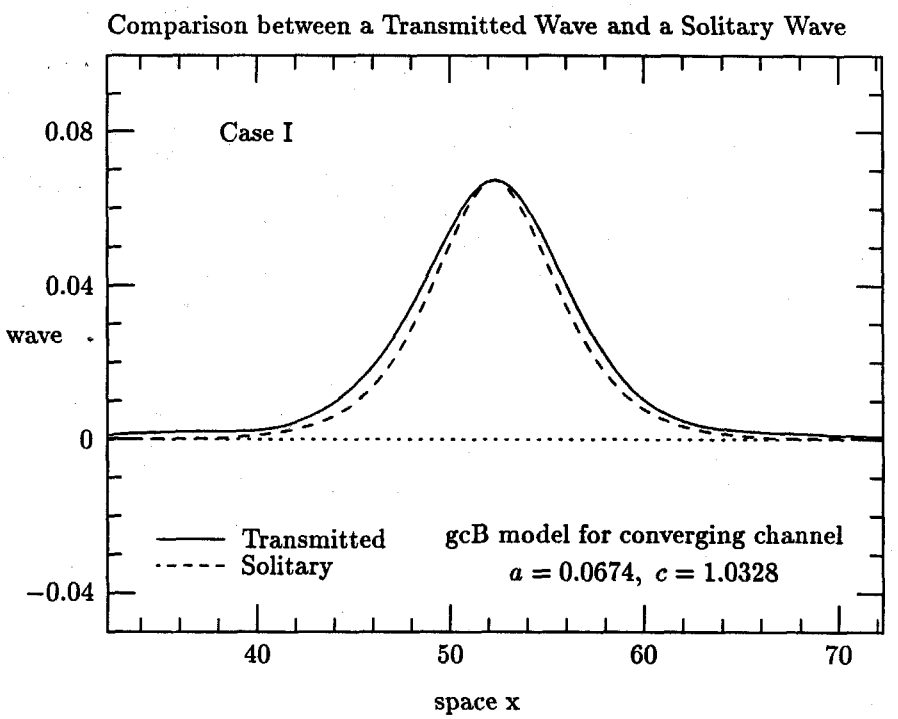

Figure 4.2(g)

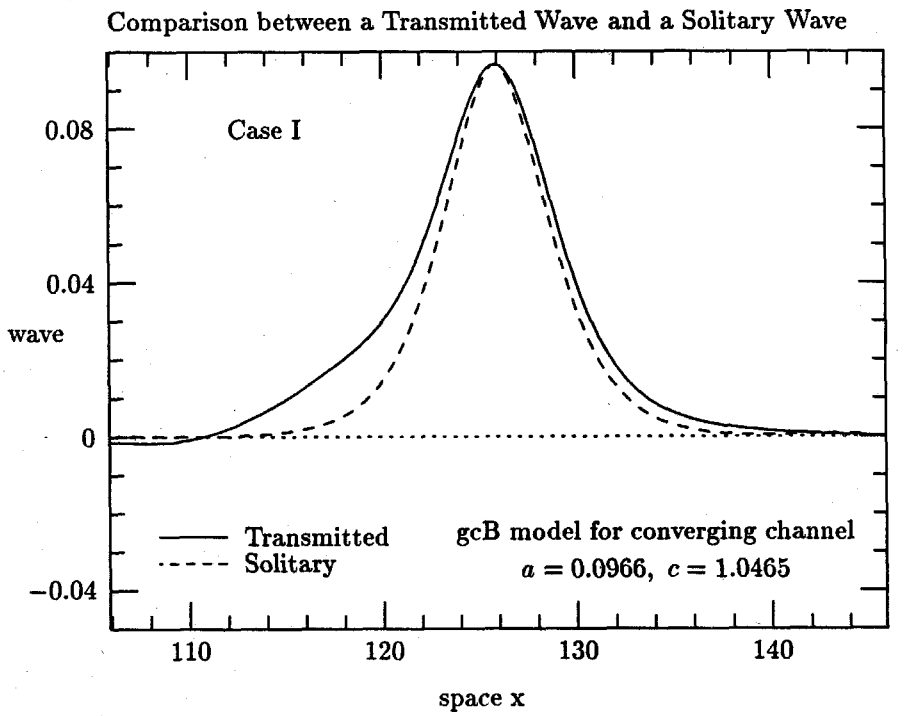

Figure 4.2(h)

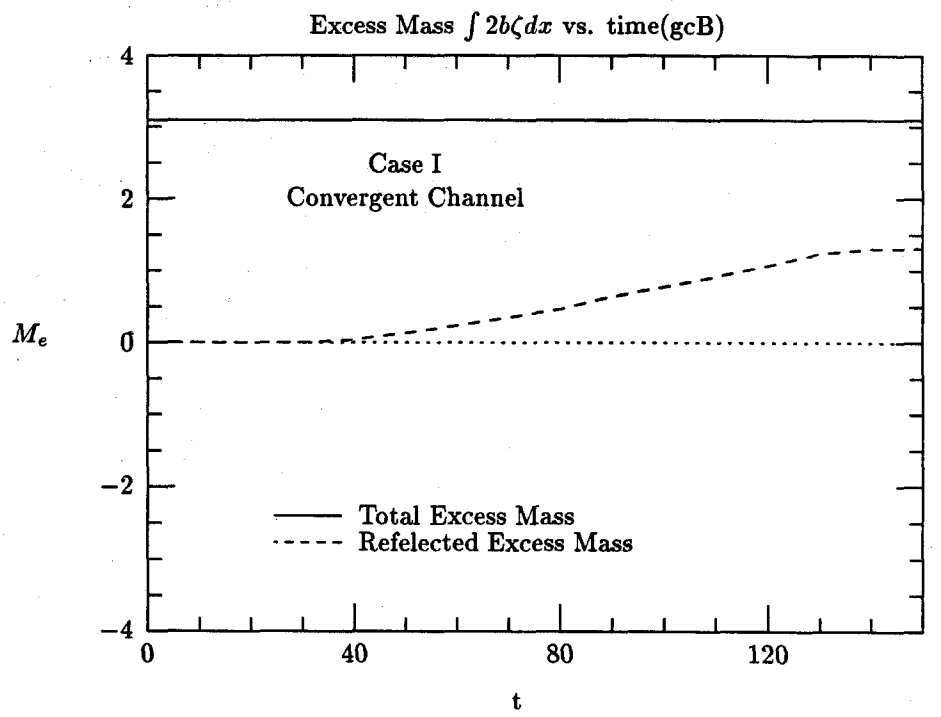

Figure 4.2(i)

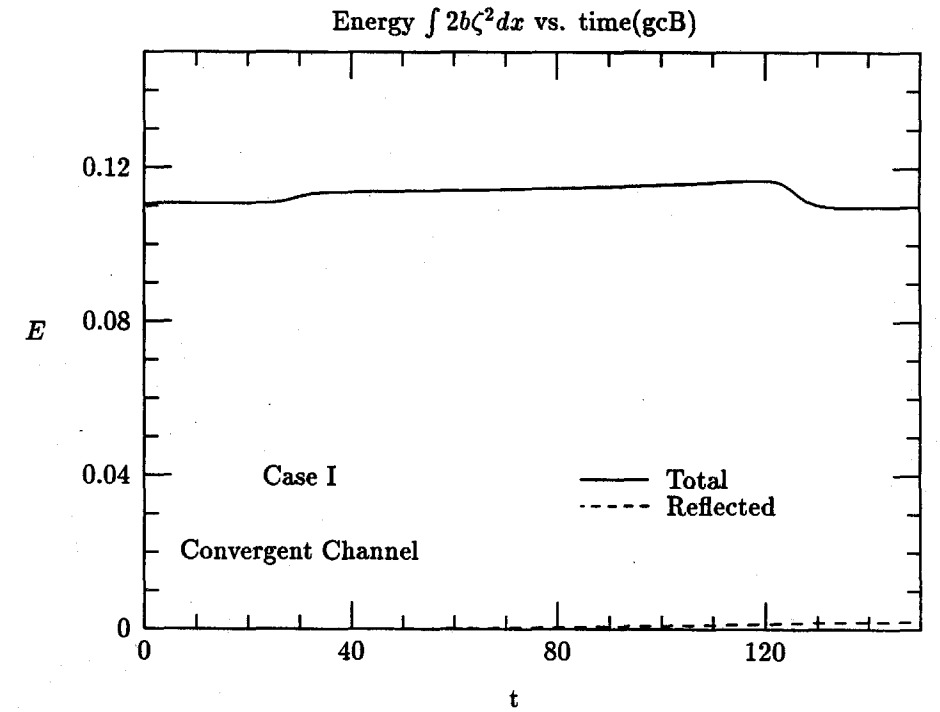

Figure 4.2(j)

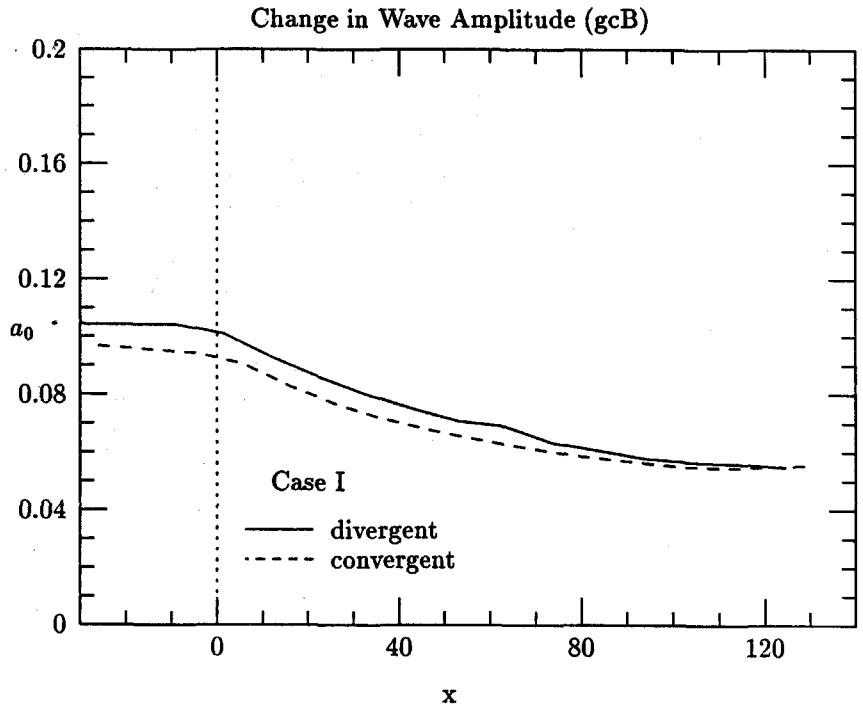

Figure 4.2(k)

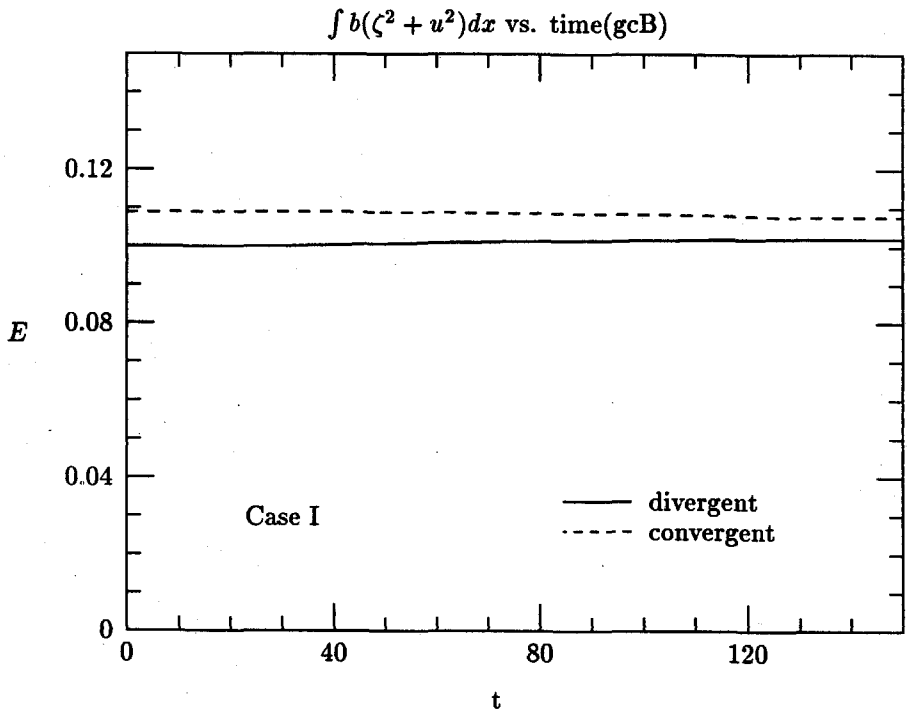

Figure 4.2(l)

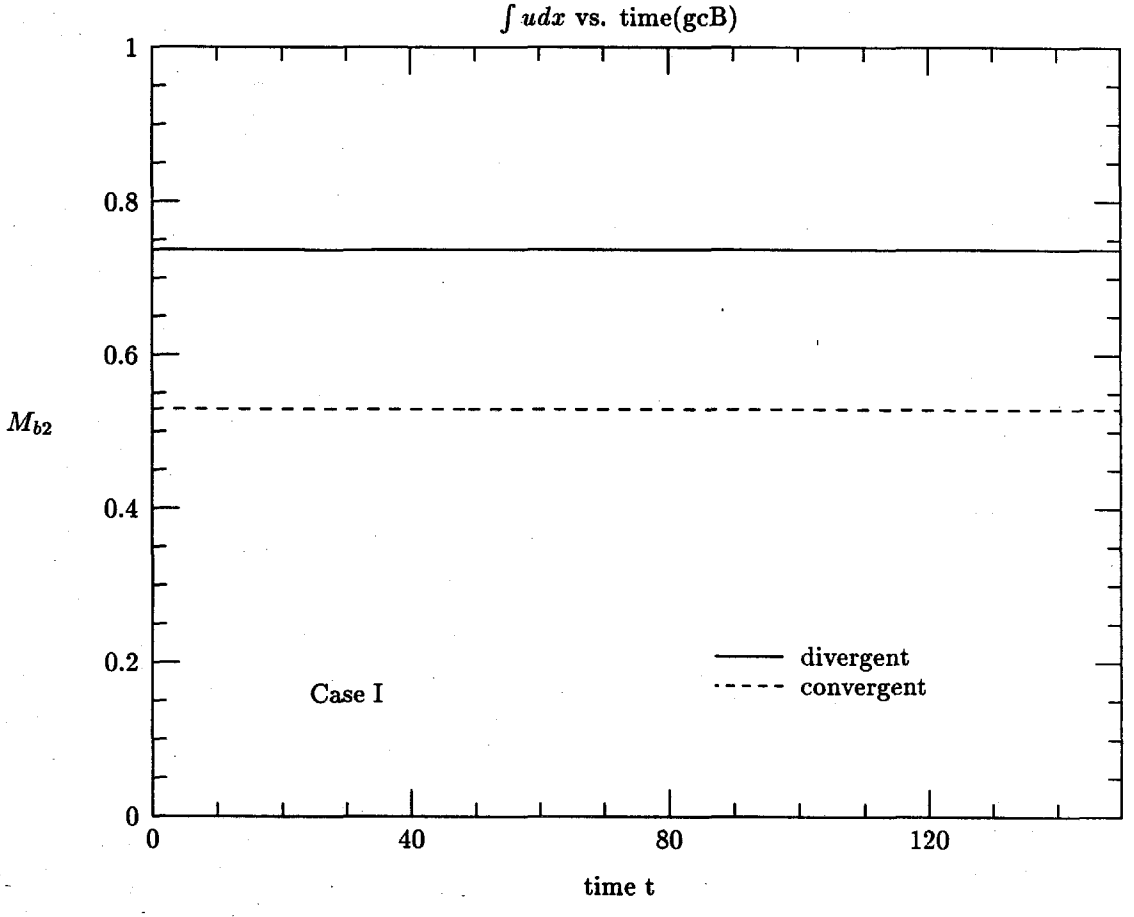
$\int udx$ vs. time(gcB)
1
0.8
0.6
M_{b2}
0.4
0.2
0
0
40
80
120
time t
Case I
divergent
convergent

the terminal wave out of a divergent channel is no longer an exact solitary wave due to the reflected wave tail. Thus even though we choose the amplitude of the initial solitary wave for the convergent channel to be of the same amplitude as that of the terminal wave out of the divergent channel, it is not an exact reversing case with respect to the divergent channel case. This also explains why in Figure 4.2 (l) there is a jump between the energy associated with the terminal wave exiting from the divergent channel and that of the initial solitary wave entering the convergent channel.

The power-laws ab^n=constant are also examined. The results are shown in Figures 4.2(m) and 4.2(n). For a solitary wave traveling in a divergent channel, we find that the change in wave amplitude is better approximated by the $\frac{3}{5}$-power law, rather than either $\frac{1}{2}$-power law or $\frac{2}{3}$-power law. For the convergent channel case, our numerical results agree with Chang's conclusion that the modulation of wave amplitude is predicted by the $\frac{1}{2}$-power law.

B. Results based on the cKdV model

(1) Divergent channel

The basic parameters are taken the same as that for the gcB model discussed above. An initial KdV-solitary wave of amplitude a_0=0.1 and speed 1.05 is placed at x=-30.0. It travels to the right to enter the diverging section of the channel. Figure 4.3(a) shows the numerical results for the wave elevation at different time levels. At the final time t=150.0, the wave arrives at x=124.7 with an amplitude of a=0.05433 and speed c=1.0272. The wave profiles at x=53.1 and x=124.7 are compared with the corresponding solitary wave profiles with equal amplitude. (See Figures 4.3(b) and 4.3(c).) These results show that for the main transmitted wave, the cKdV model predicts the waves to have very similar features as the gcB model does. Interestingly, they are found in quite good agreement, not withstanding that

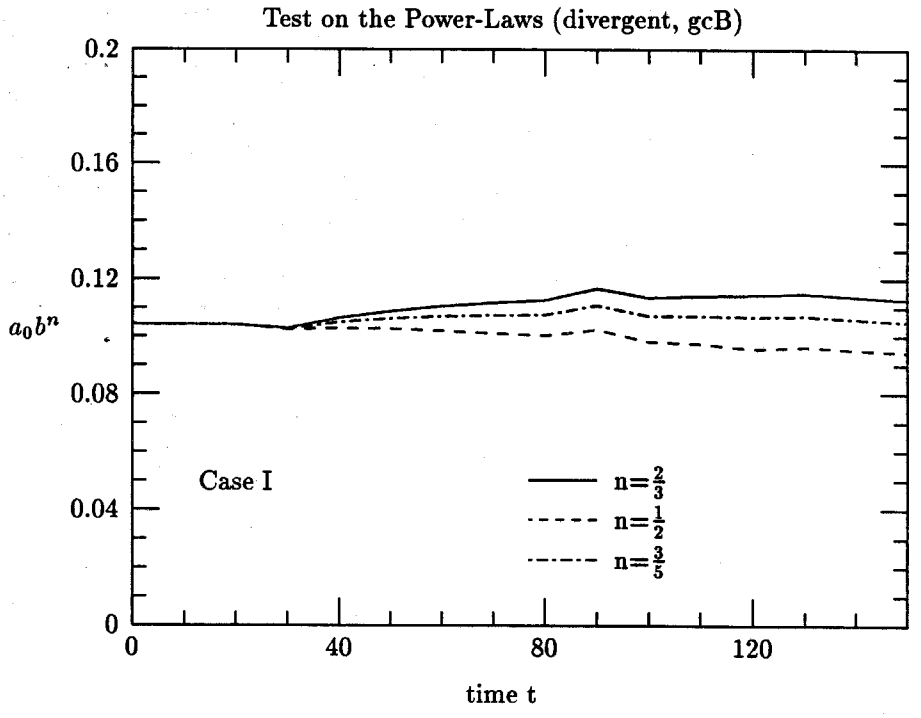

Figure 4.2(m)

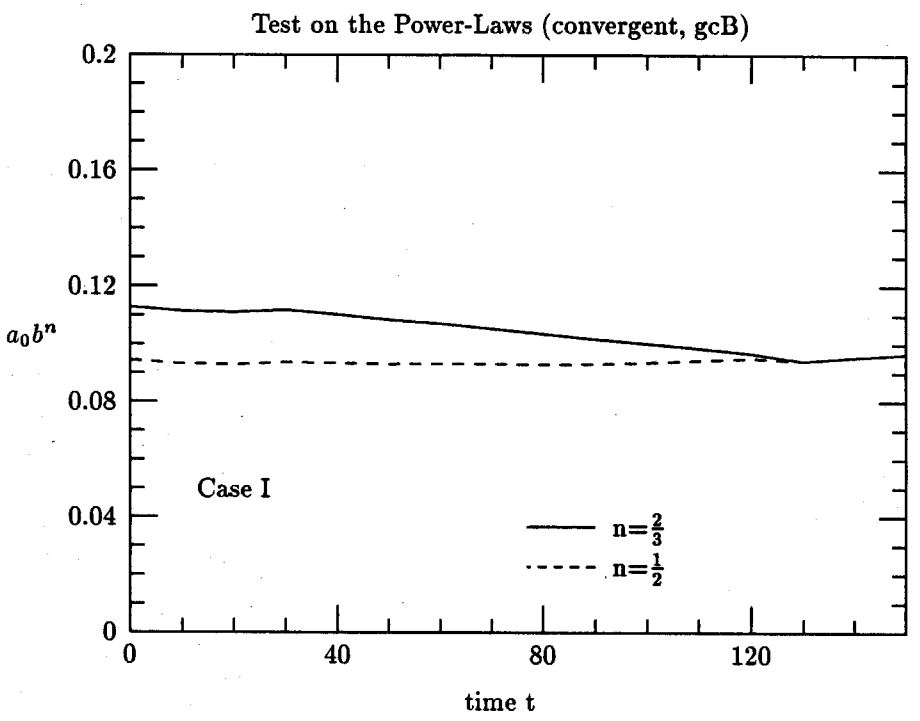

Figure 4.2(n)

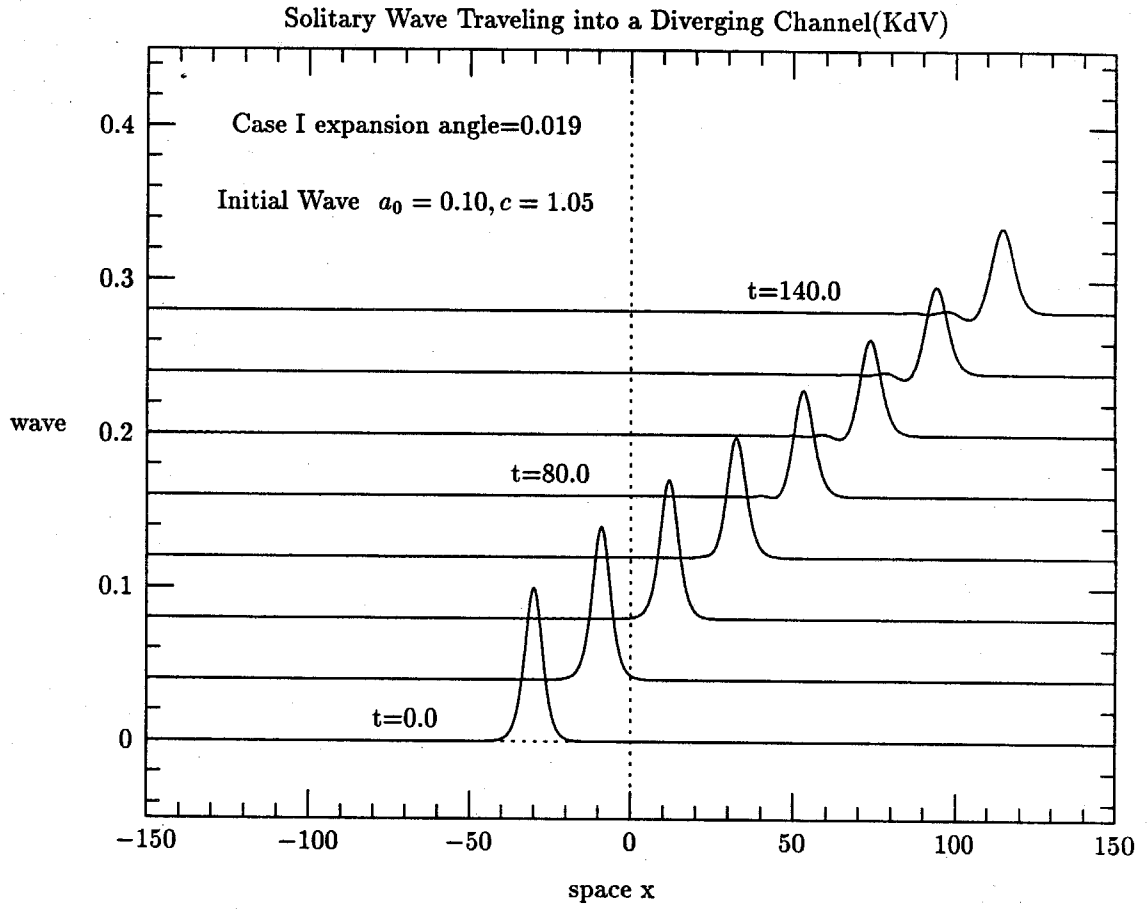
Solitary Wave Traveling into a Diverging Channel(KdV)
Case I expansion angle=0.019
Initial Wave $a_0 = 0.10, c = 1.05$
t=140.0
t=80.0
t=0.0
wave
space x
0.4
0.3
0.2
0.1
0
−150
−100
−50
0
50
100
150

Figure 4.3(a)

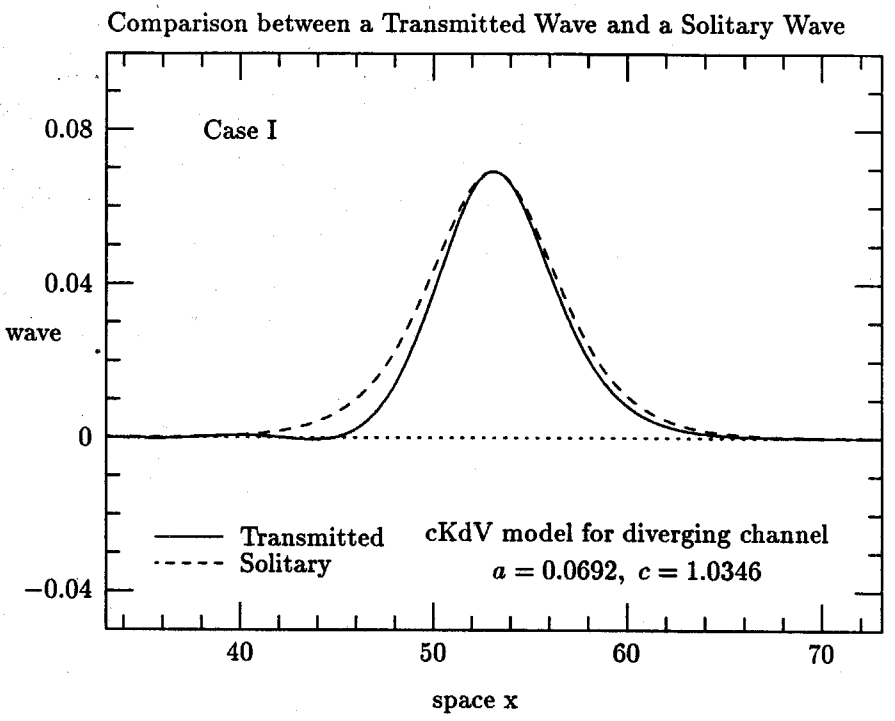

Figure 4.3(b)

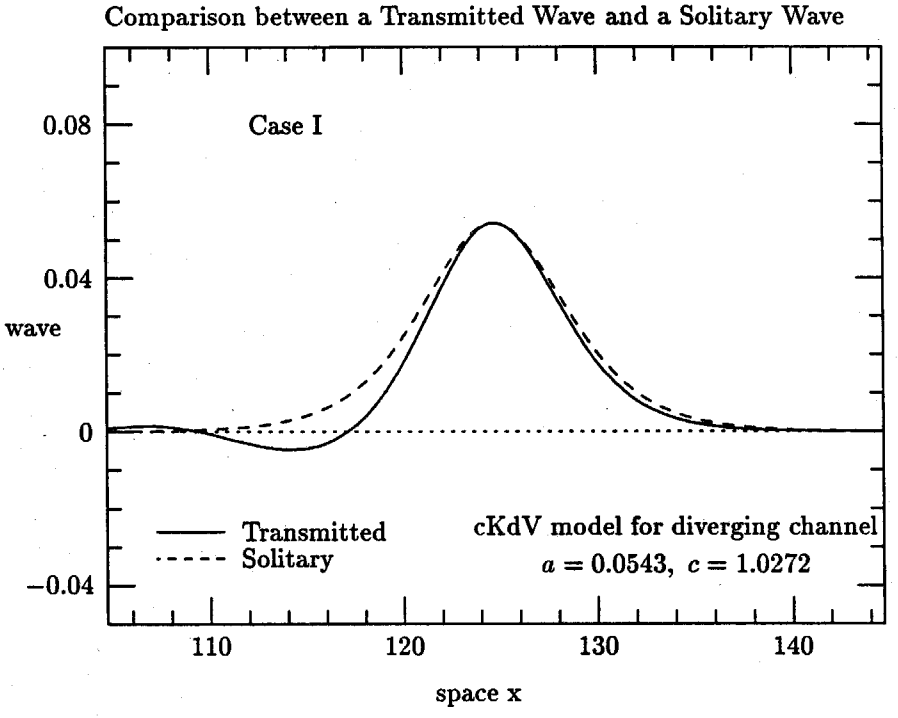

Figure 4.3(c)

the cKdV model fails in preserving the excess mass by a broad margin (see below). Table 4.2 gives a quantitative comparison between the two models for the wave speed at two different times.

Table 4.2 Comparison between the gcB Model and the cKdV Model for the Transmitted Wave Speed (divergent)

time	gcB	cKdV
80.0	1.3045	1.3046
150.0	1.0271	1.0272

The relative difference between the two models for the transmitted wave speed is within 0.01%.

The most significant differences between the two models are found in respect to the mass conservation properties and to the reflected waves in the downstream region. Figure 4.3(a) shows that the wave field in the downstream region is almost unperturbed according to the cKdV model, while in Figure 4.2(a) the gcB model predicts clearly a reflected wave that travels with near-critical speed in the negative x-direction, albeit very small amplitude. The time record of the total excess mass M_e based on the cKdV model is represented by the solid line in Figure 4.3(h). We see that according to the cKdV model, the total excess mass M_e is not conserved. At the final time t=150.0, the relative increase in the 'total' excess mass is about 73.5% with respect to the initial value for the divergent channel. Comparing this increase with the gain of mass by the transmitted wave due to the reflected waves which is 75.7% predicted by the gcB model, we can see that the 'total' excess mass given by the cKdV model is actually the local excess mass possessed by the transmitted wave. The final change in the total energy is about 3.5% by the cKdV model. (See Figure 4.3(i).) This also agrees with the prediction by the gcB model

that the loss of energy due to the reflected waves is small (2.1%).

As for the power-laws, the cKdV model gives similar results as the gcB model.

(2) Convergent channel

The numerical results are presented in Figures 4.3(d) to 4.3(k) and in Table 4.3.

Table 4.3 Comparison between the gcB Model and the cKdV Model for the Transmitted Wave Speed (convergent)

time	gcB	cKdV
80.0	1.0328	1.0335
150.0	1.0465	1.0482

The relative difference between the two models for the transmitted wave speed is within 0.2%.

The final decrease in the 'total' excess mass by the cKdV model is 42.2% compared to the loss of mass due to the reflected wave, 42.4%, by the gcB model. The change in energy is 4.0% at the final time, compared to 1.8% reflected according to the gcB model.

It is clear that the failure of the cKdV model in conserving the total mass and total energy is caused by the neglecting of the reflected wave. However, this neglect of the reflected wave does not affect the validity of the cKdV model in the transmitted wave region. Aside from the computational error, the cKdV model gives the same prediction for the main transmitted wave as the gcB model. The 'total' excess mass and energy given by the cKdV model are actually the excess mass and energy for the local transmitted wave.

4.2.2 Case II $c_0 = 1.05$, $|\alpha| = 0.038$, $b(x)$ linearly varying

In this case, the expansion angle is increased to $|\alpha|$=0.038, which is twice

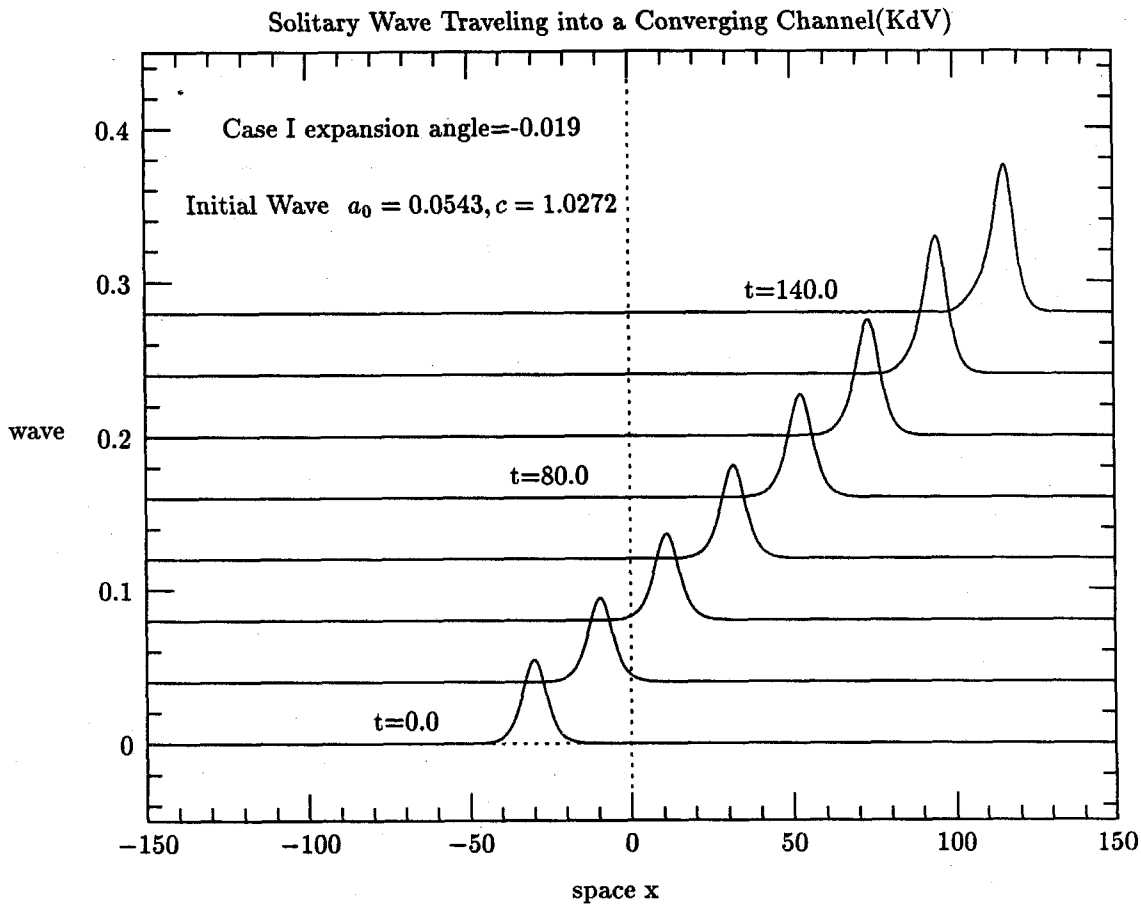
Solitary Wave Traveling into a Converging Channel(KdV)
Case I expansion angle=-0.019
Initial Wave $a_0 = 0.0543, c = 1.0272$
t=140.0
t=80.0
t=0.0
wave
0.4
0.3
0.2
0.1
0
−150
−100
−50
0
50
100
150
space x

Figure 4.3(d)

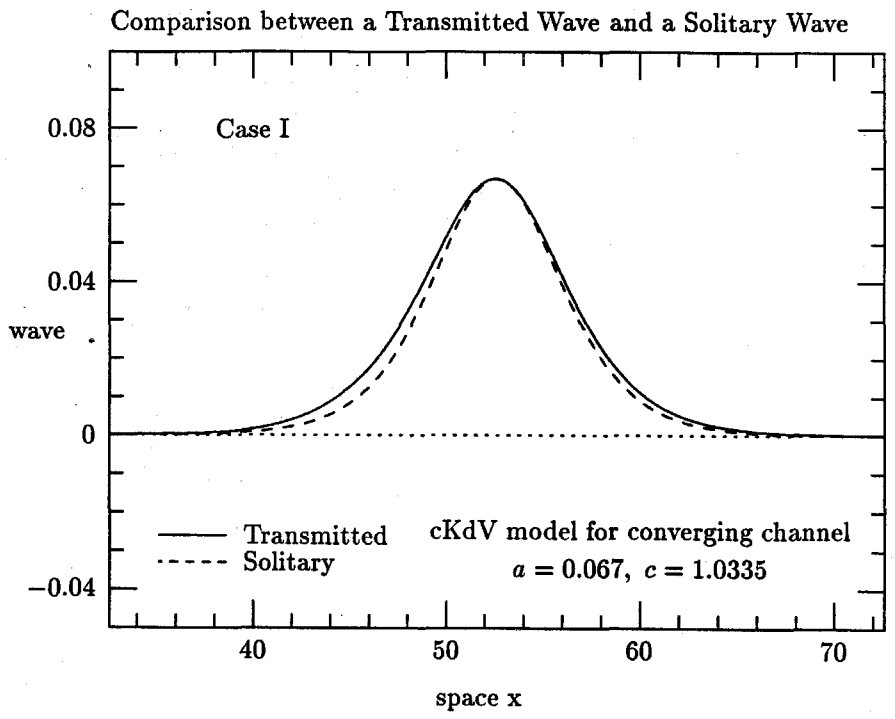

Figure 4.3(e)

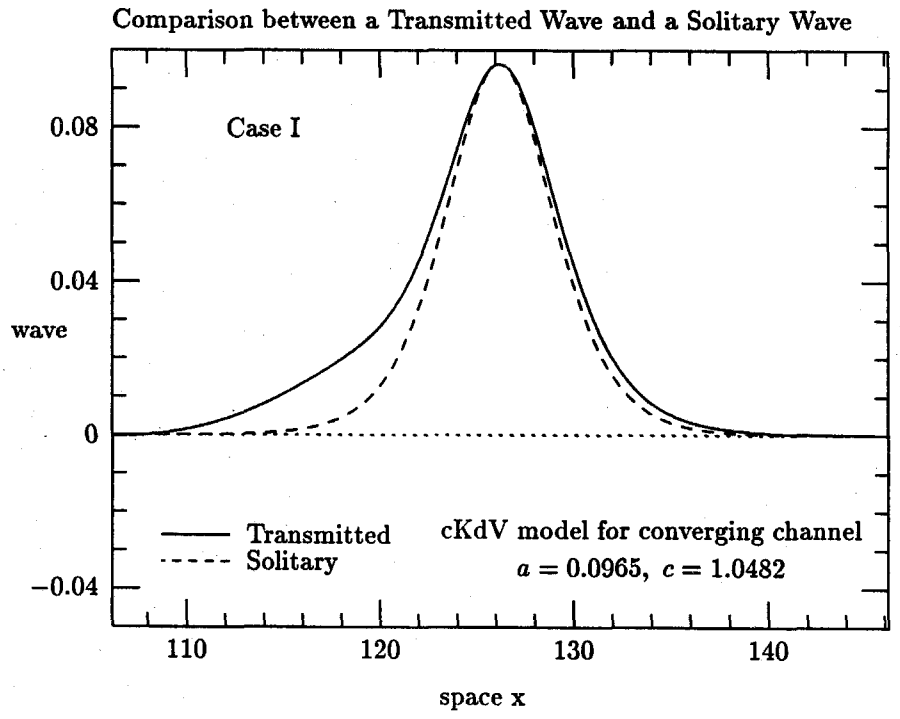

Figure 4.3(f)

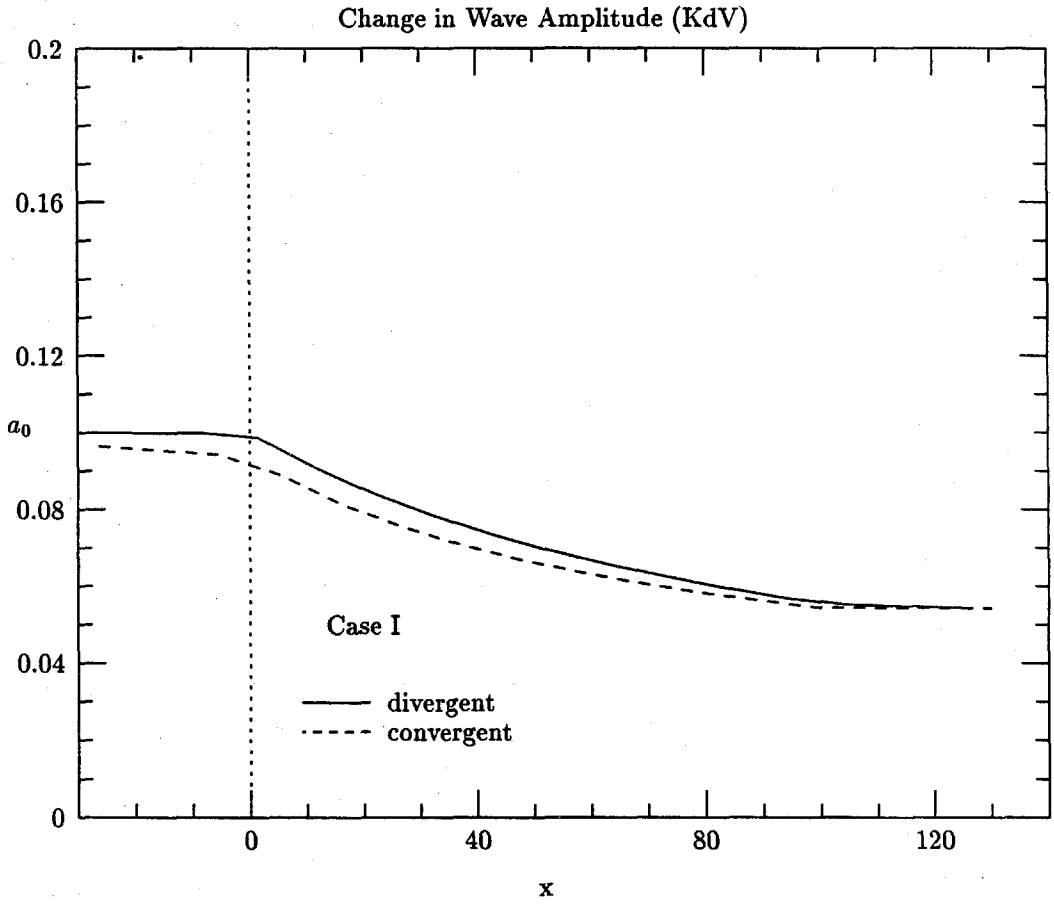
Change in Wave Amplitude (KdV)
0.2
0.16
0.12
a_0
0.08
0.04
0
0
40
80
120
x
Case I
divergent
convergent

Figure 4.3(g)

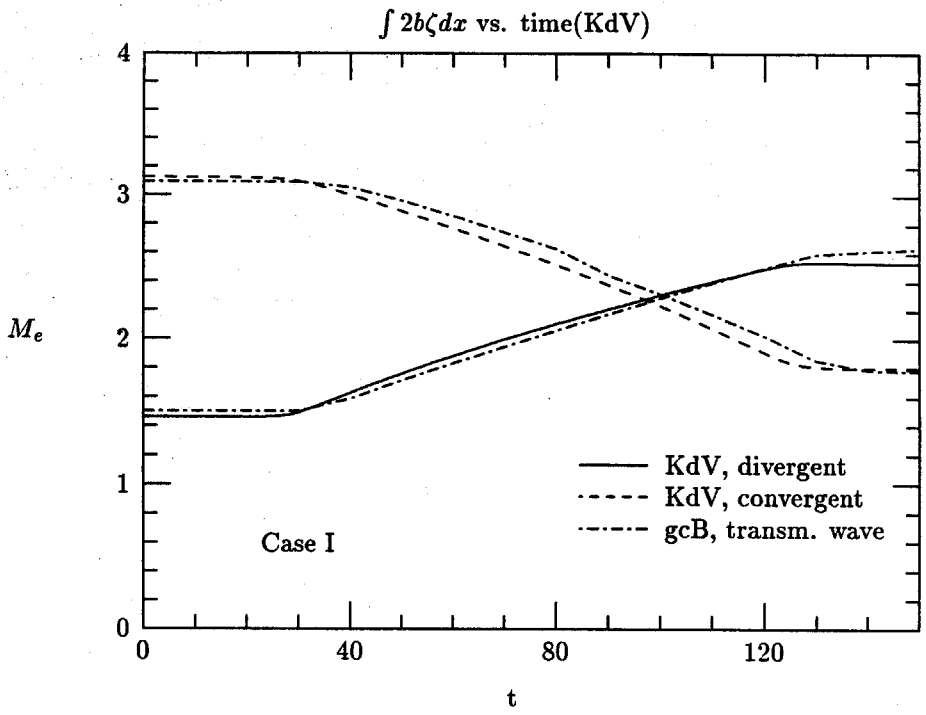

Figure 4.3(h)

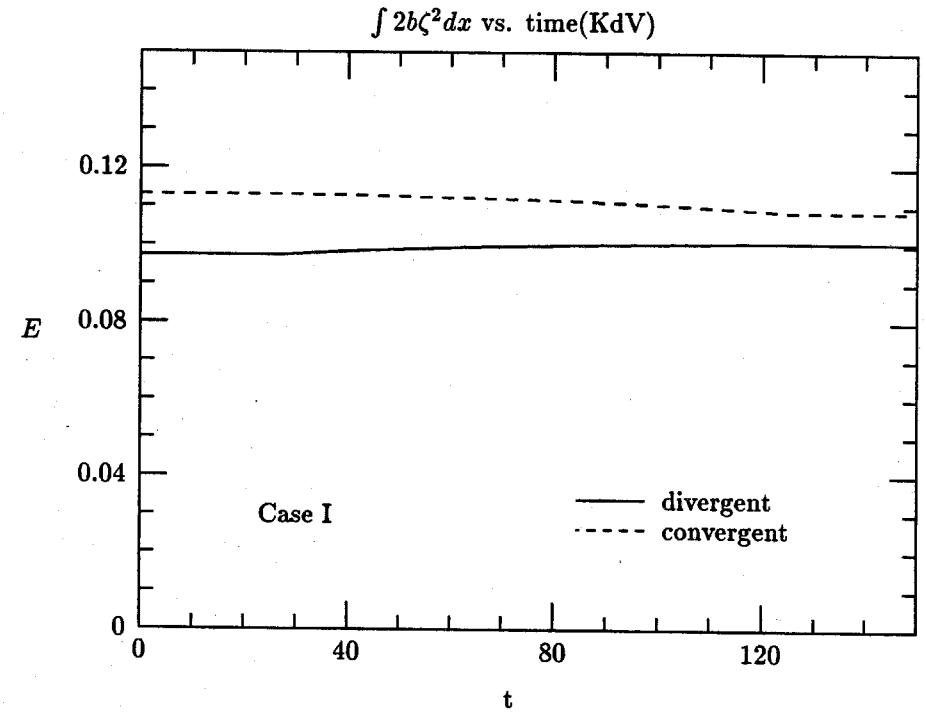

Figure 4.3(i)

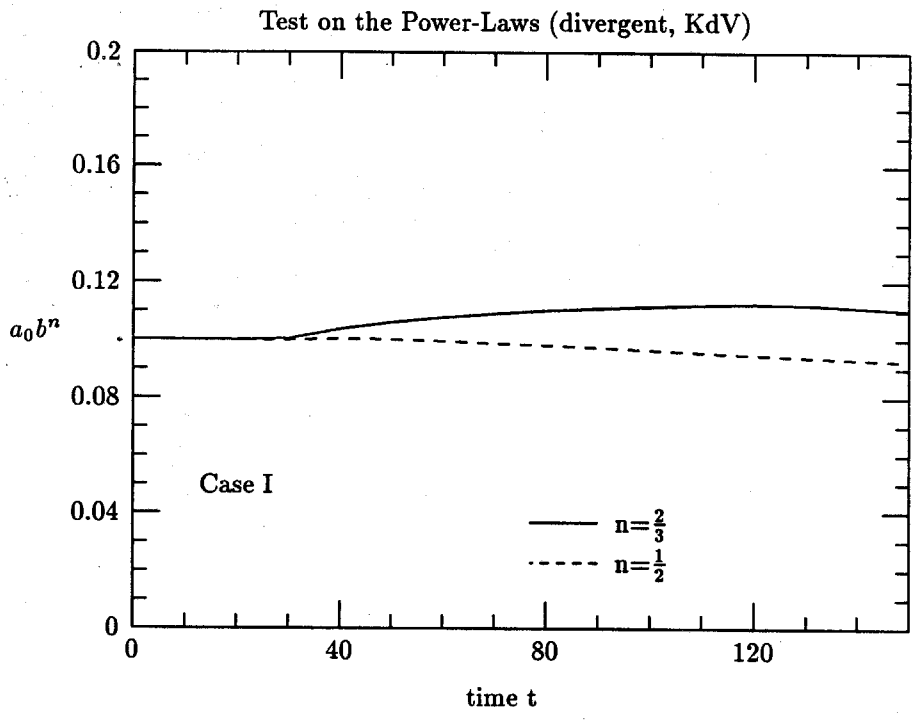

Figure 4.3(j)

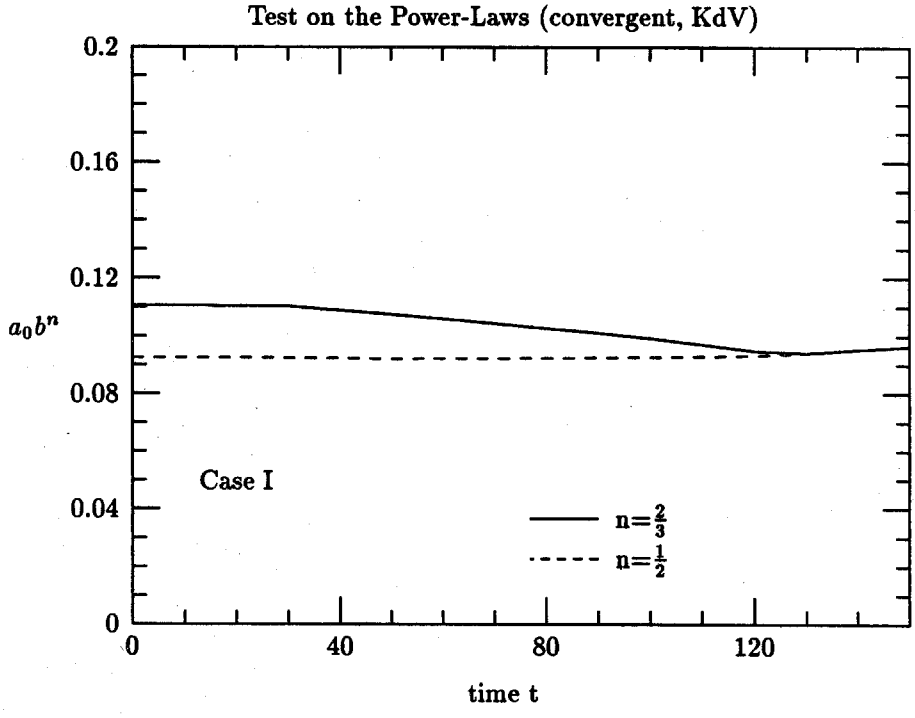

Figure 4.3(k)

as that in Case I. All other parameters remain the same as in the previous case, except that the final width ($2b_1$) in the terminal uniform section is increased to 9.6 in the present case. The numerical results for Case II are shown in Figures 4.4(a) to 4.5(g).

(1) Divergent channel

As we see from the numerical results, the general wave features in the present case are quite the same as that in Case I, except that when the expansion angle is increased, the reflection of waves becomes stronger. At the final time t=150.0, according to the gcB model, the reflected wave (with a negative amplitude) carries away a negative excess mass whose absolute value is 127.0% of the original total excess mass. The loss of energy due to the reflected wave is about 6.0%. Correspondingly, the cKdV model predicts an increase of 124.5% in the local excess mass possessed by the main transmitted wave. The final increase in energy based on the cKdV model is 4.3%.

Again, for the main transmitted wave, the two models give consistent predictions for the wave speed. At time t=150.0, the speed of the transmitted wave is c=1.0202 predicted by the gcB model while the cKdV model gives c=1.0205. The relative difference is about 0.03%.

(2) Convergent channel

The speed of the initial solitary wave is c_0=1.0202, which corresponds to a wave amplitude of a_0=0.0411 for the gcB model and a_0=0.0404 for the cKdV model. After the solitary wave with this initial speed travels for about 150 water depths from x=-30.0 to x=125.4 in a convergent channel, the loss of mass and energy due to the reflected wave based on the gcB model are 56.7% and 4.3%, respectively. The cKdV model predicts a decrease in both the excess mass and energy of the local transmitted wave. The quantitative numbers are 55.2% decrease

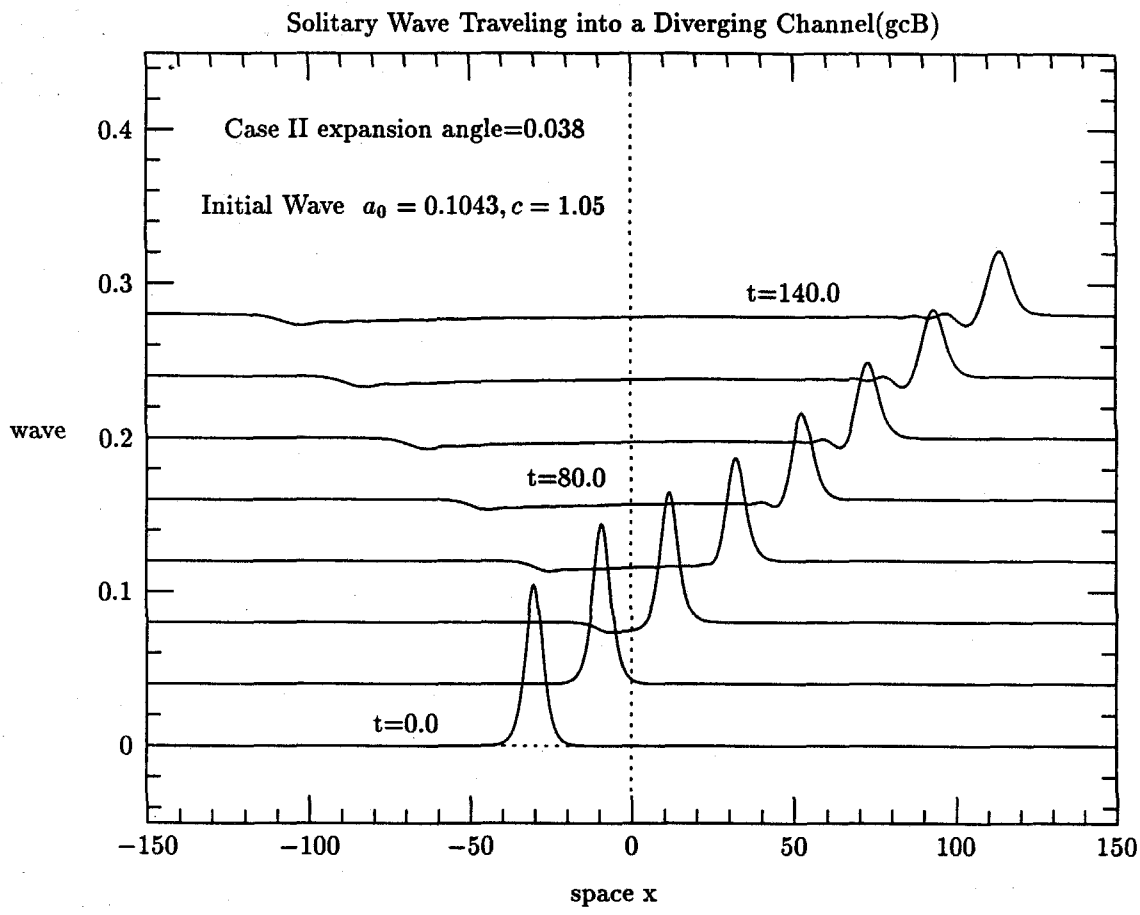
Solitary Wave Traveling into a Diverging Channel(gcB)
Case II expansion angle=0.038
Initial Wave $a_0 = 0.1043, c = 1.05$
t=140.0
t=80.0
t=0.0
wave
0.4
0.3
0.2
0.1
0
−150
−100
−50
0
50
100
150
space x

Figure 4.4(a)

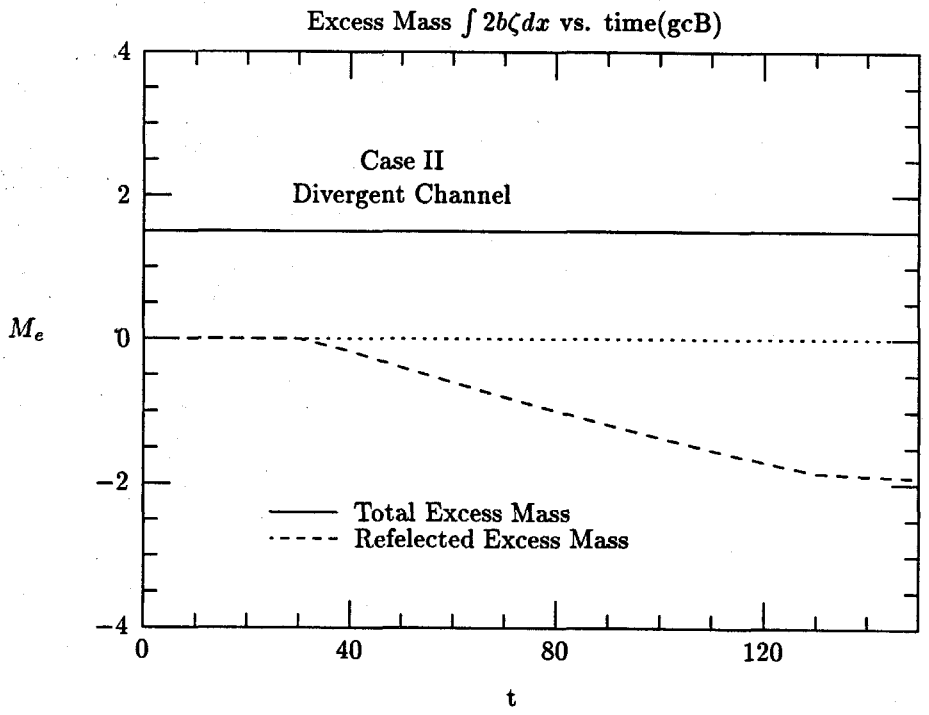

Figure 4.4(b)

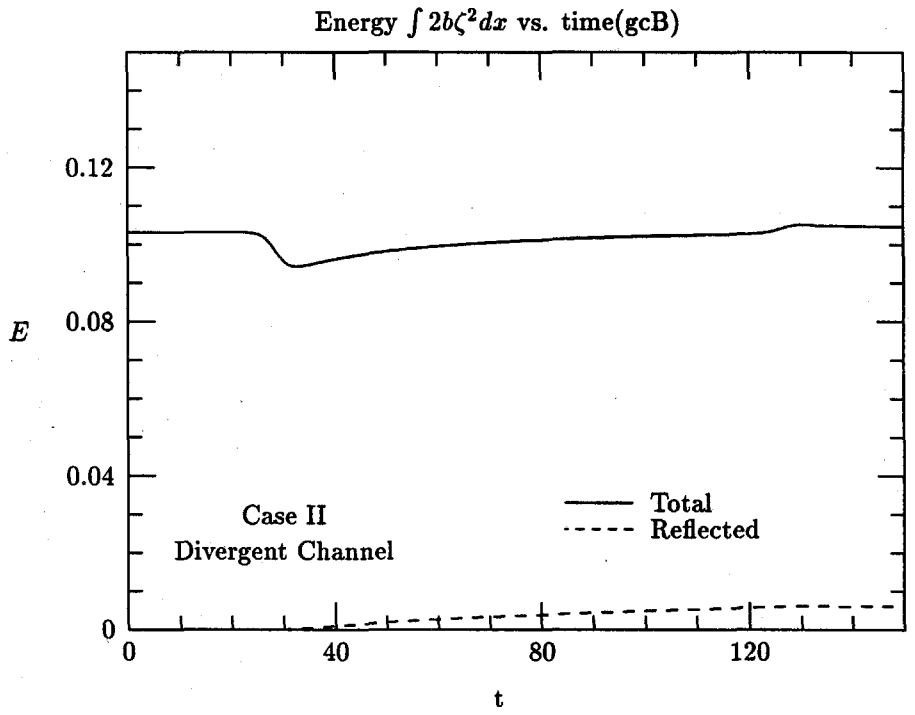

Figure 4.4(c)

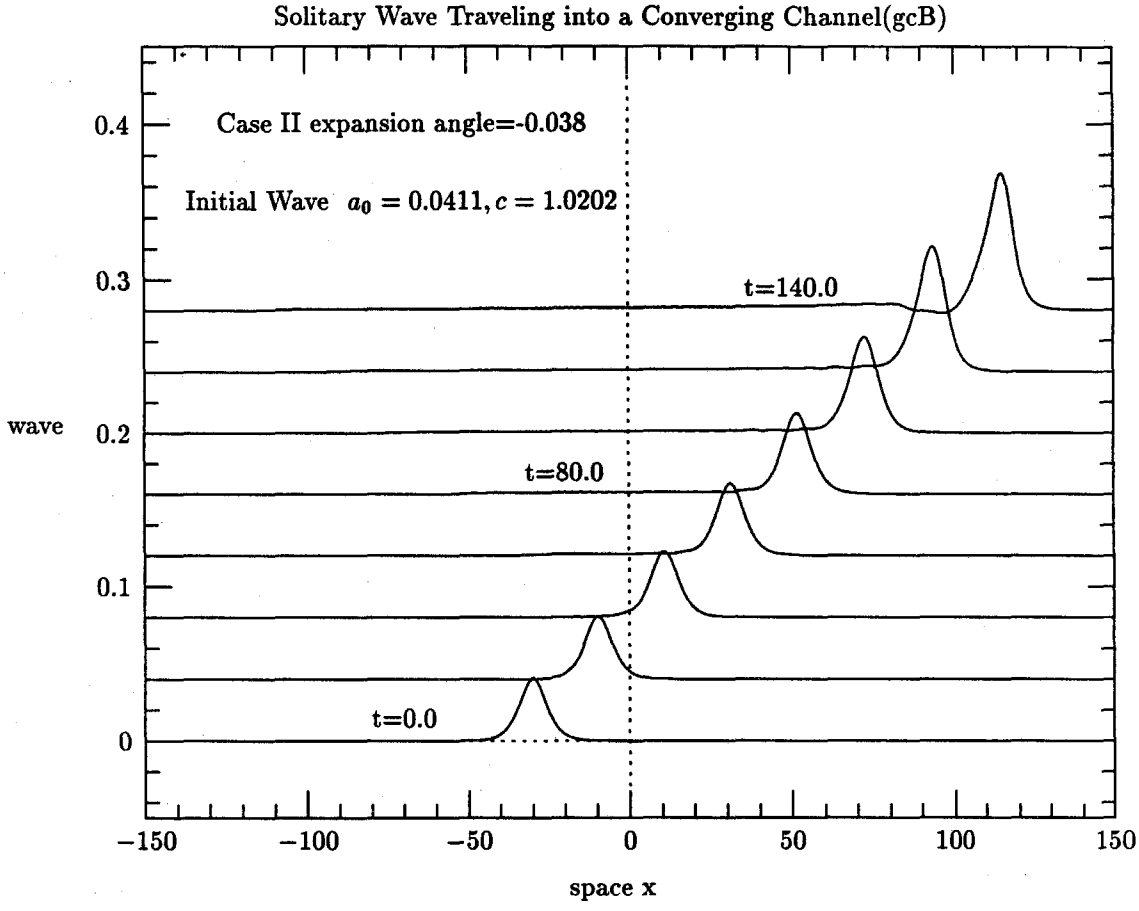
Solitary Wave Traveling into a Converging Channel(gcB)
Case II expansion angle=-0.038
Initial Wave $a_0 = 0.0411, c = 1.0202$
t=140.0
t=80.0
t=0.0
wave
0.4
0.3
0.2
0.1
0
−150
−100
−50
0
50
100
150
space x

Figure 4.4(d)

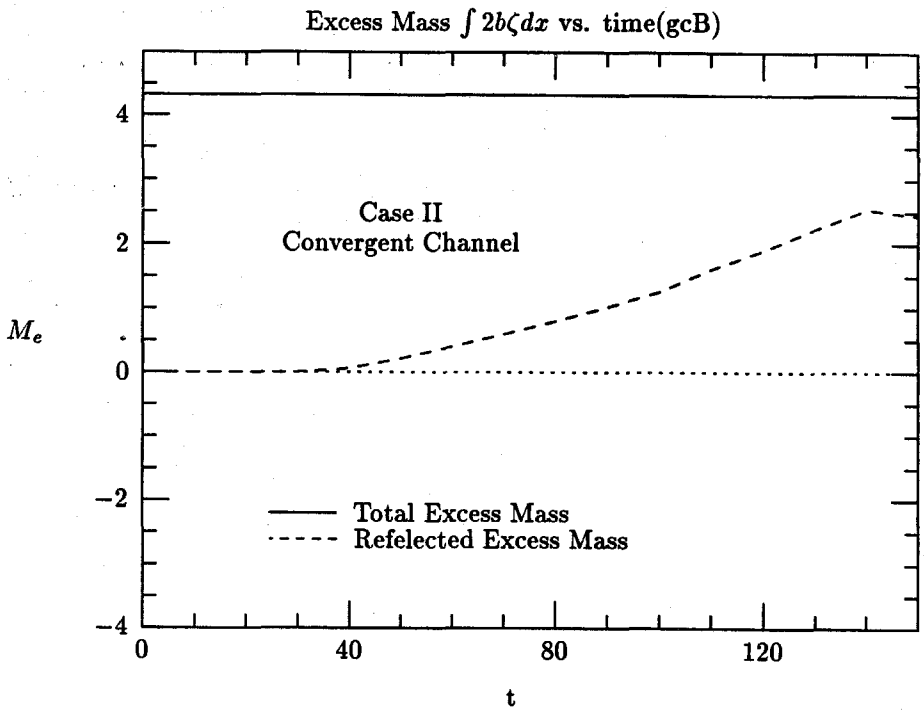

Figure 4.4(e)

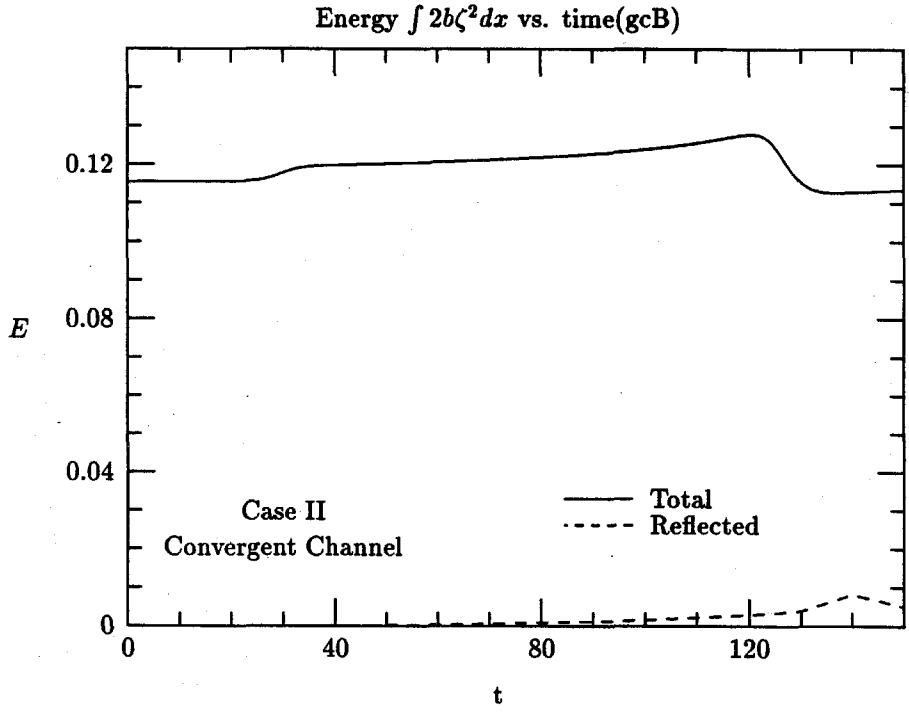

Figure 4.4(f)

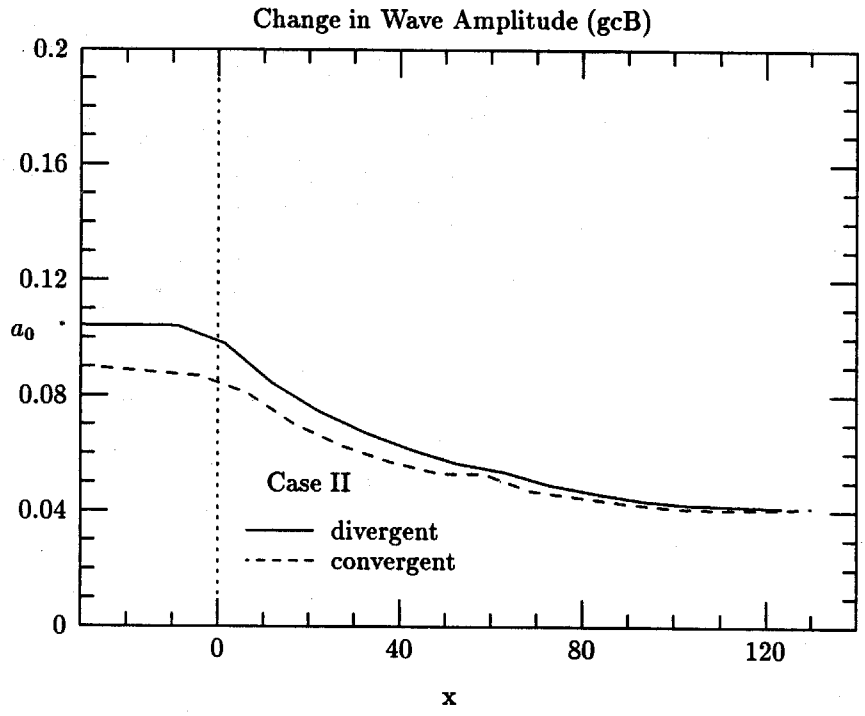

Figure 4.4(g)

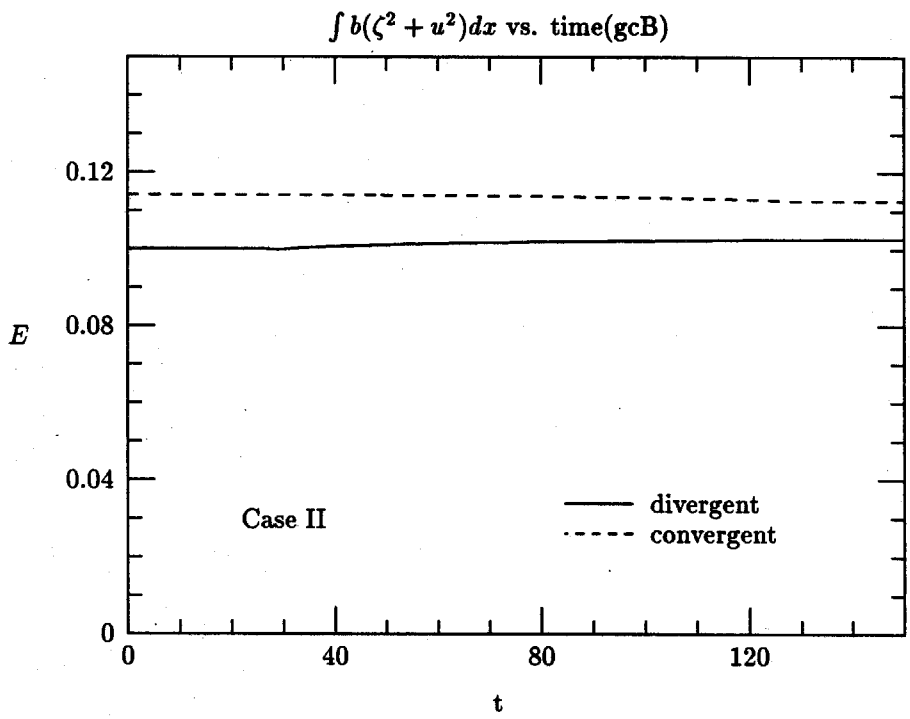

Figure 4.4(h)

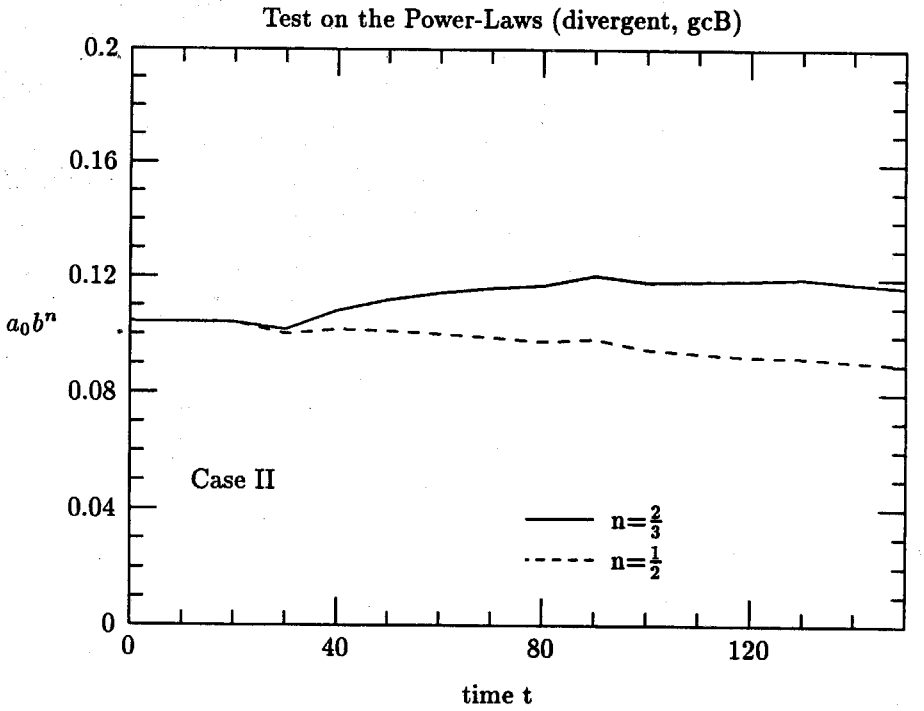

Figure 4.4(i)

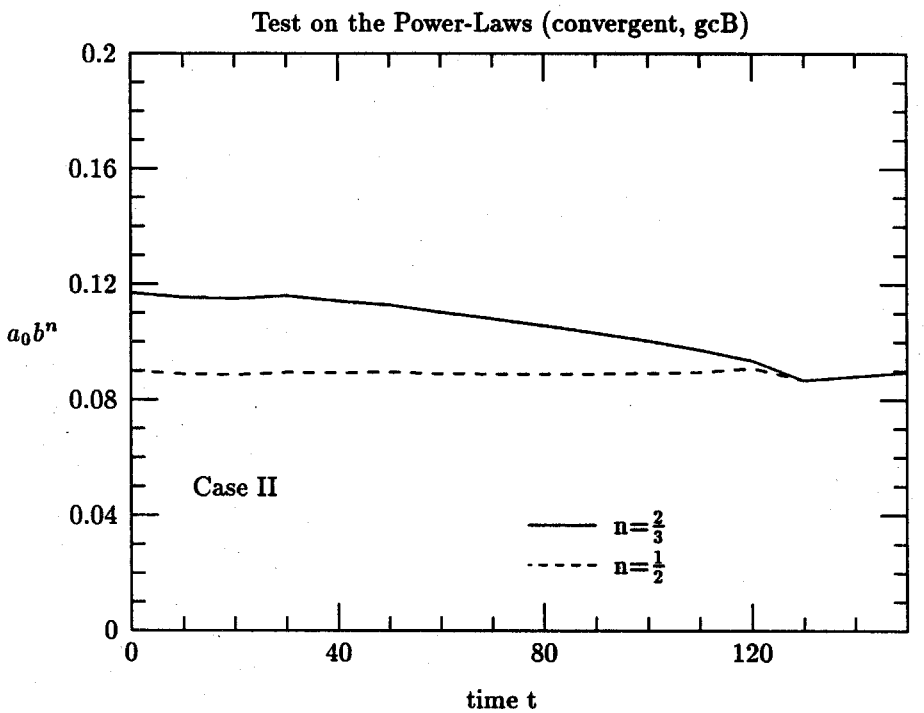

Figure 4.4(j)

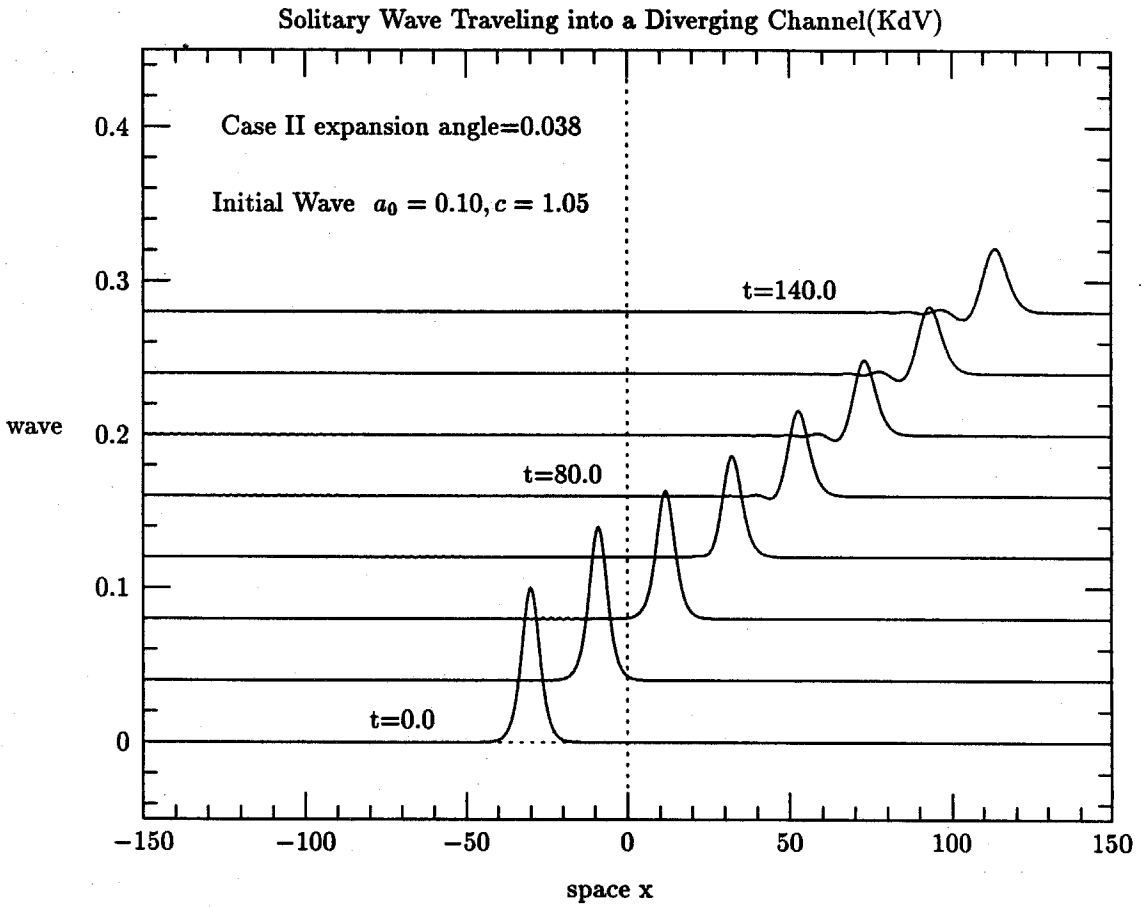
Solitary Wave Traveling into a Diverging Channel(KdV)
Case II expansion angle=0.038
Initial Wave $a_0 = 0.10, c = 1.05$
t=140.0
t=80.0
t=0.0
wave
space x
0.4
0.3
0.2
0.1
0
−150
−100
−50
0
50
100
150

Figure 4.5(a)

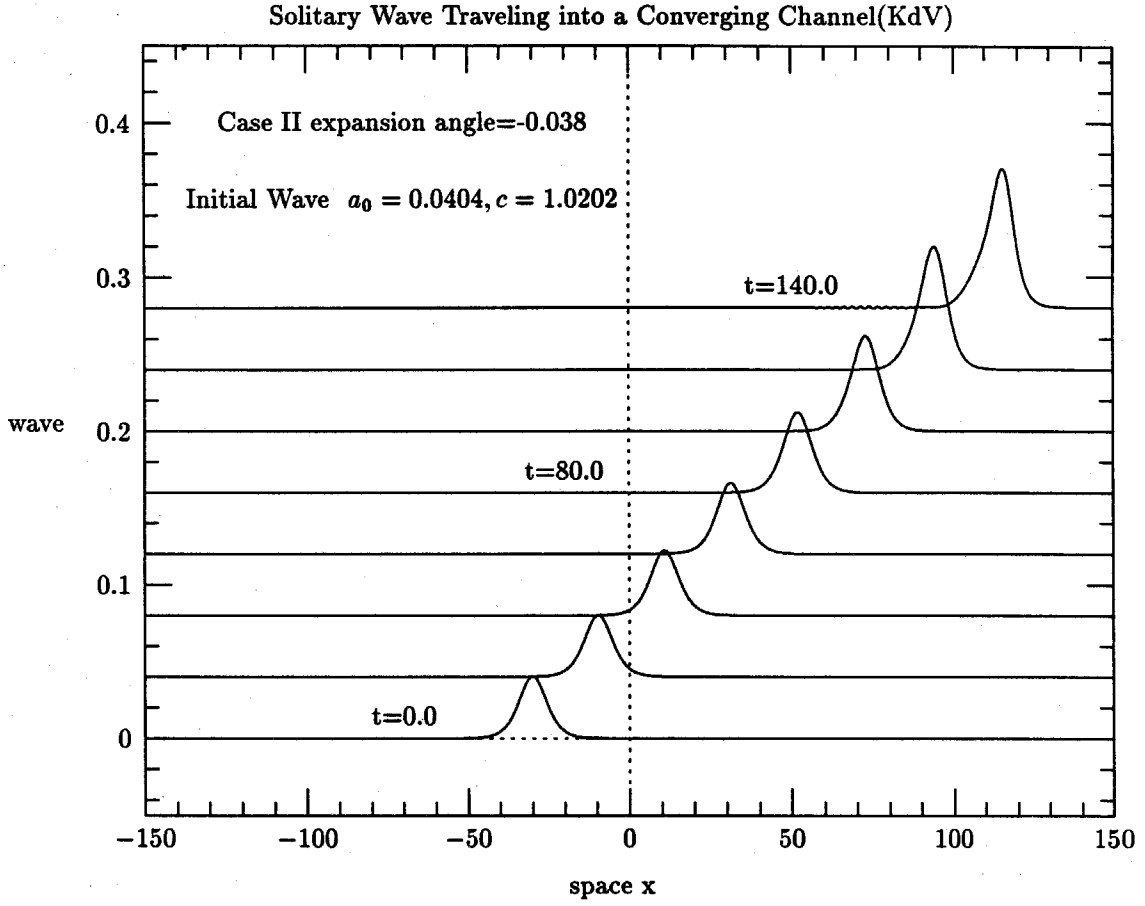
Solitary Wave Traveling into a Converging Channel(KdV)
Case II expansion angle=-0.038
Initial Wave $a_0 = 0.0404, c = 1.0202$
t=140.0
t=80.0
t=0.0
wave
0.4
0.3
0.2
0.1
0
−150
−100
−50
0
50
100
150
space x

Figure 4.5(b)

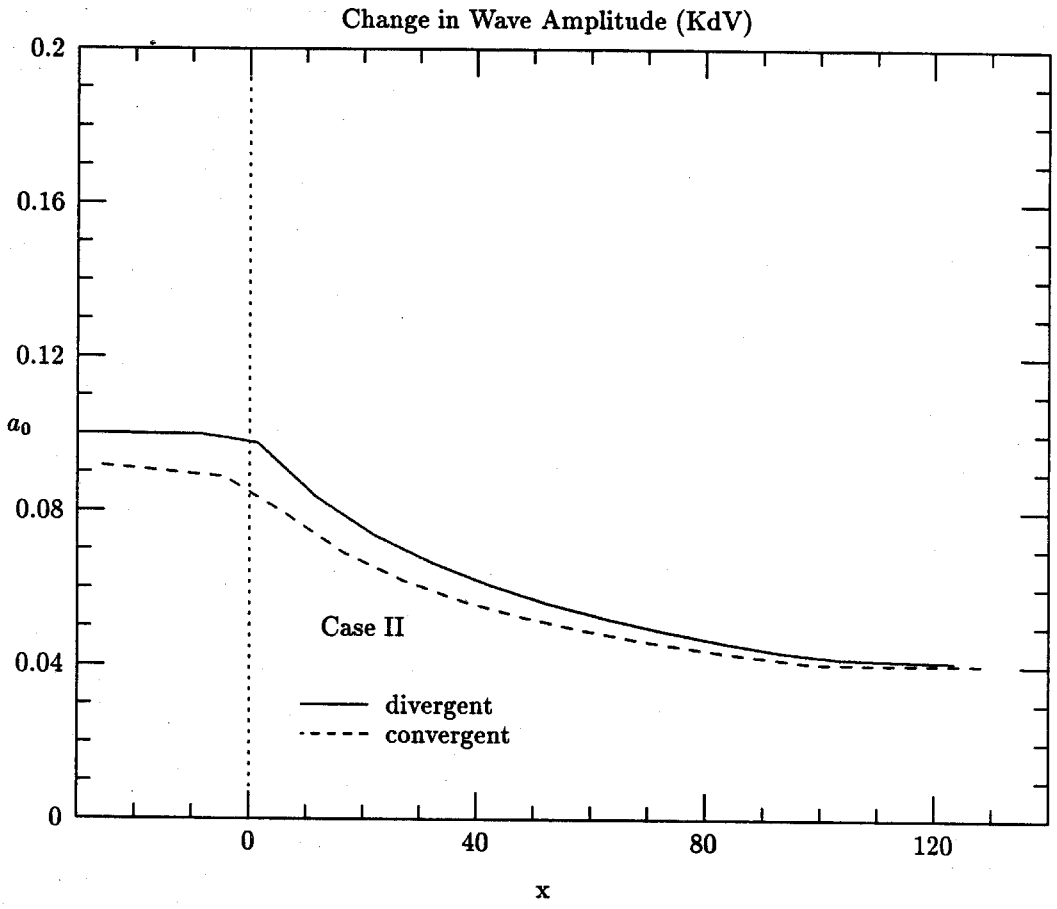
Change in Wave Amplitude (KdV)
0.2
0.16
0.12
a_0
0.08
0.04
0
0
40
80
120
x
Case II
divergent
convergent

Figure 4.5(c)

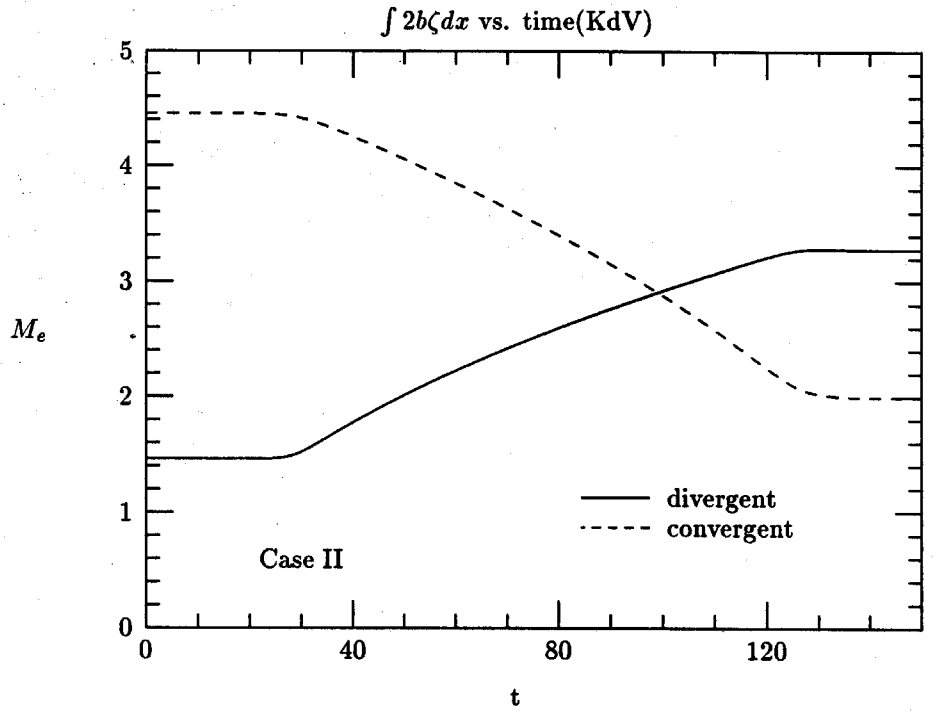

Figure 4.5(d)

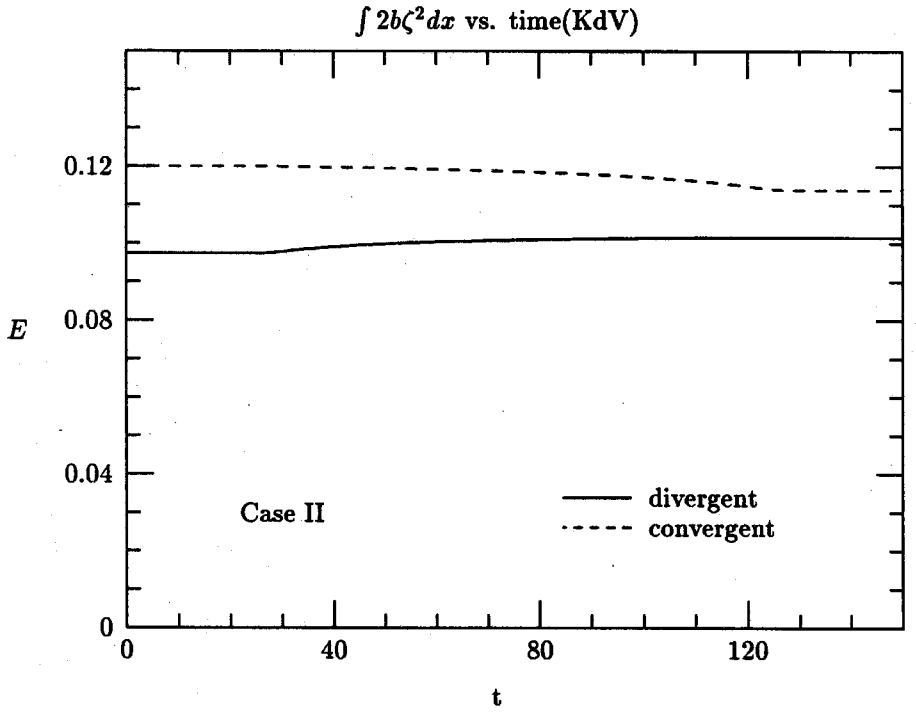

Figure 4.5(e)

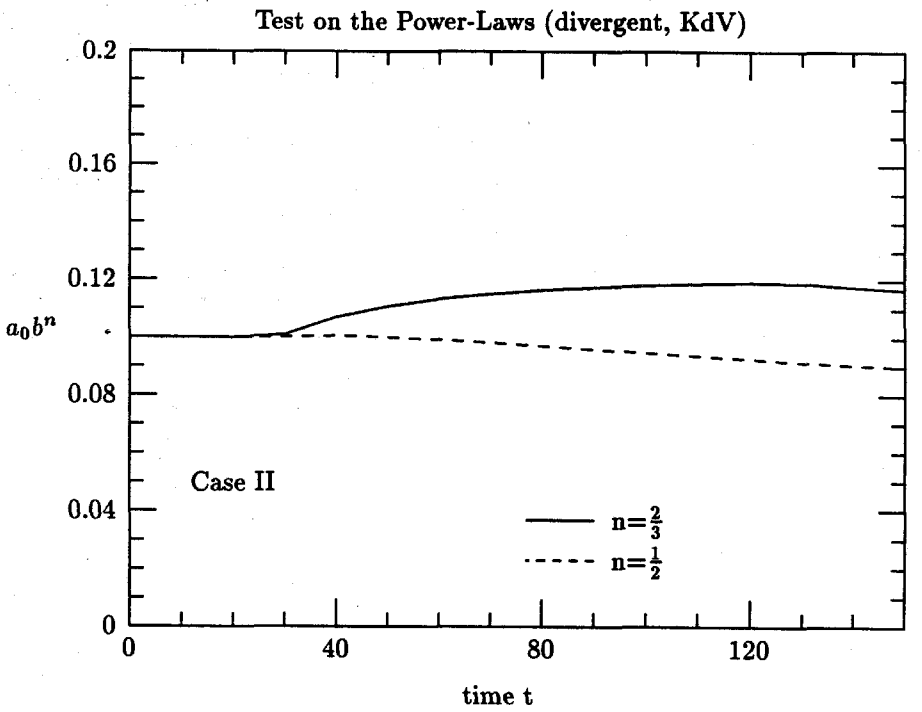

Figure 4.5(f)

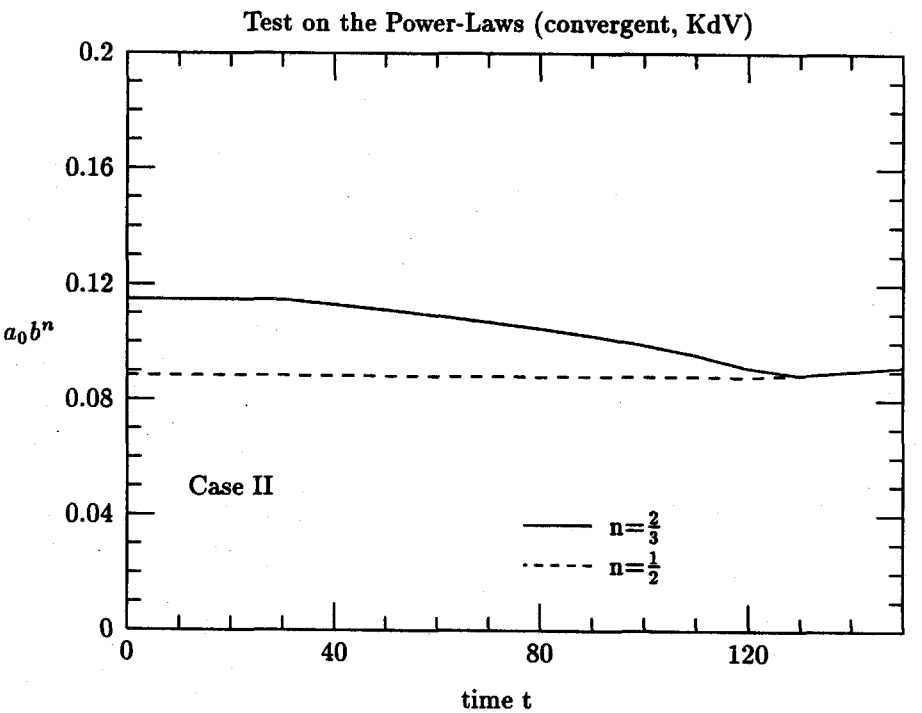

Figure 4.5(g)

in the excess mass and 5.0% decrease in the energy, based on the cKdV model.

4.2.3 Case III $c_0 = 1.0925$, $\alpha = 0.019$, initial width $b_0 = 0.25$, linearly divergent

The present case and the following case, Case IV, are designed to compare the numerical results based on our two long wave models with the experimental data obtained by Chang et al.[2] in 1979. Even though the expansion angle is the same as that in Case I, the initial width of the uniform entrance section is much smaller in the present case. This results in a much larger ratio of the terminal channel width over the initial width, which is 4.3/0.5=8.6 compared with 5.8/2.0=2.9 in Case I. The parameters are so chosen to be consistent with the experimental set up in Chang's studies. With this larger change in the channel width, we expect that more waves will be reflected and the change in the amplitude of the transmitted wave will be greater. In the present case, the initial wave starts at x=-10.0 instead of x=-30.0.

A plot of the wave elevations predicted by the gcB model at different time steps are shown in Figure 4.6(a). Compared with the results based on the cKdV model (see Figure 4.7(a)), the reflected wave field becomes more obvious and a clear front of the reflected wave is seen to travel in the negative x direction with near-critical speed.

Figure 4.8(a) and 4.8(b) show the comparison of results between our two models and Chang's experiments for the change in wave amplitude. While the results based on our two long wave models remain consistent, they show noticeable differences from the experimental results obtained by Chang et al. The numerical results and the experimental data are close near the entering part of the variable channel, while the difference becomes larger near the end of the channel. The maximum relative difference between our numerical results and Chang's

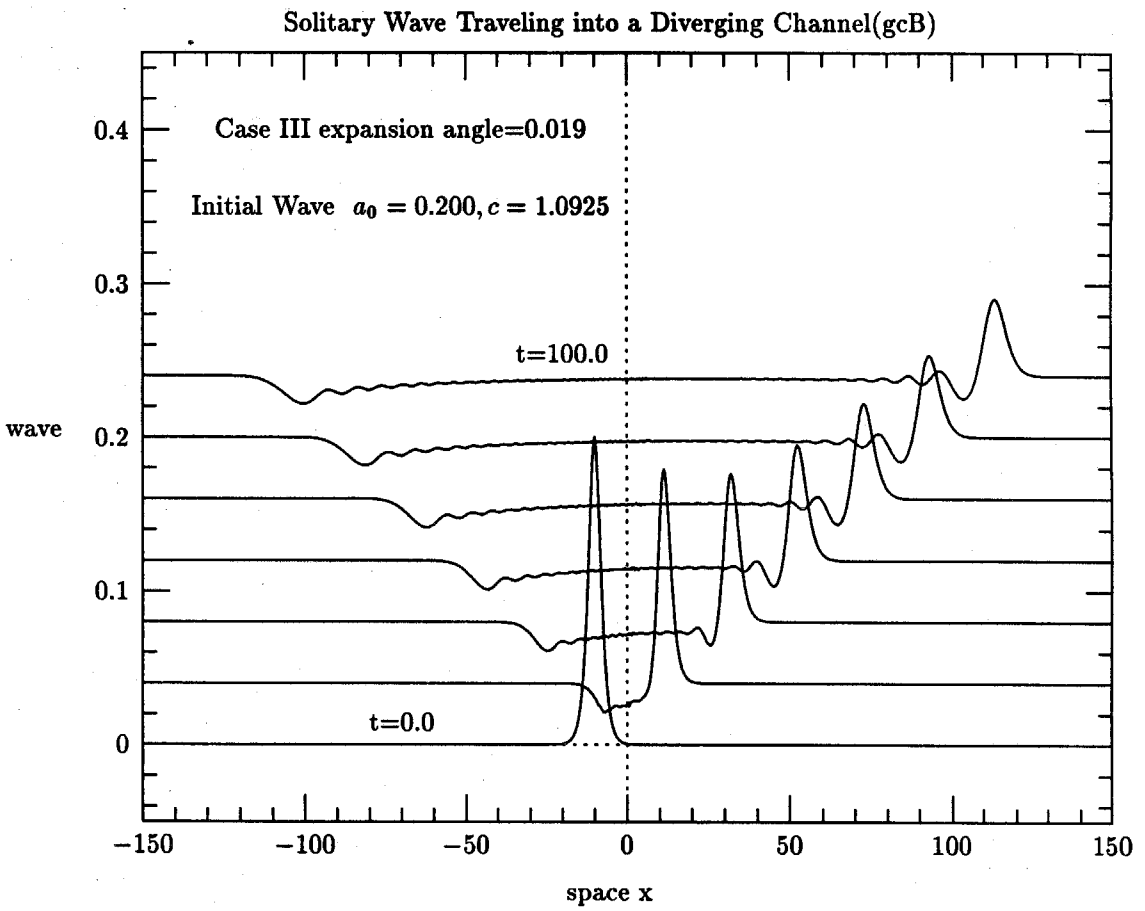
Solitary Wave Traveling into a Diverging Channel(gcB)
Case III expansion angle=0.019
Initial Wave $a_0 = 0.200, c = 1.0925$
t=100.0
t=0.0
wave
space x
0.4
0.3
0.2
0.1
0
−150
−100
−50
0
50
100
150

Figure 4.6(a)

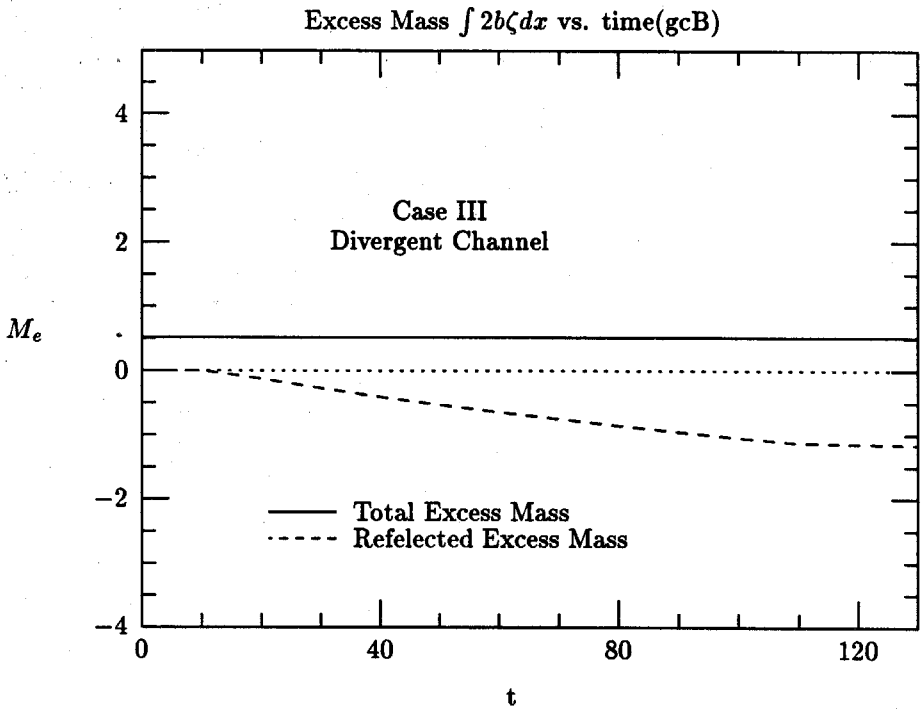

Figure 4.6(b)

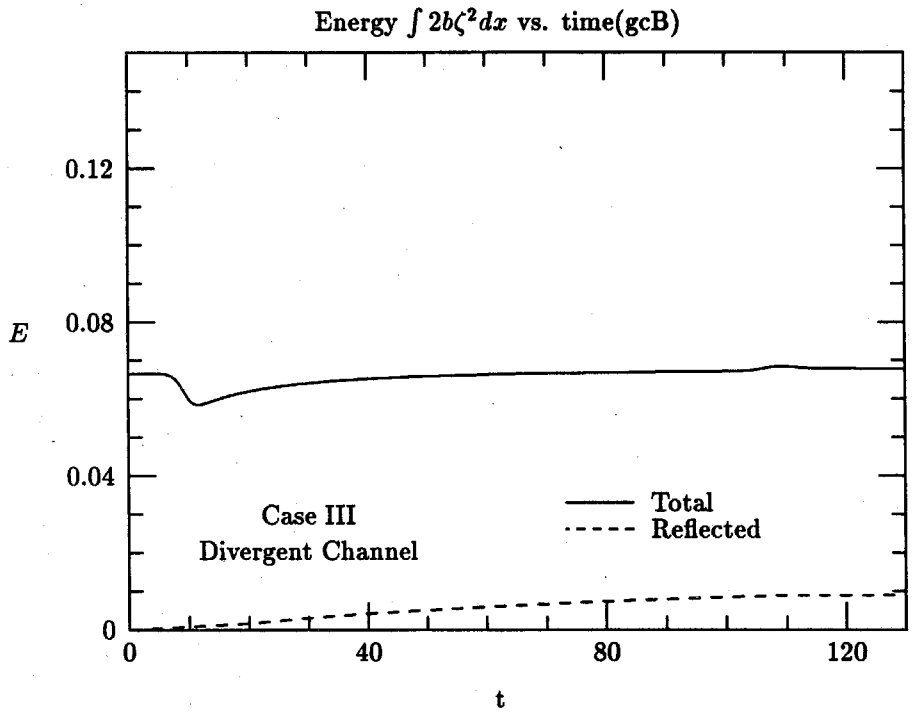

Figure 4.6(c)

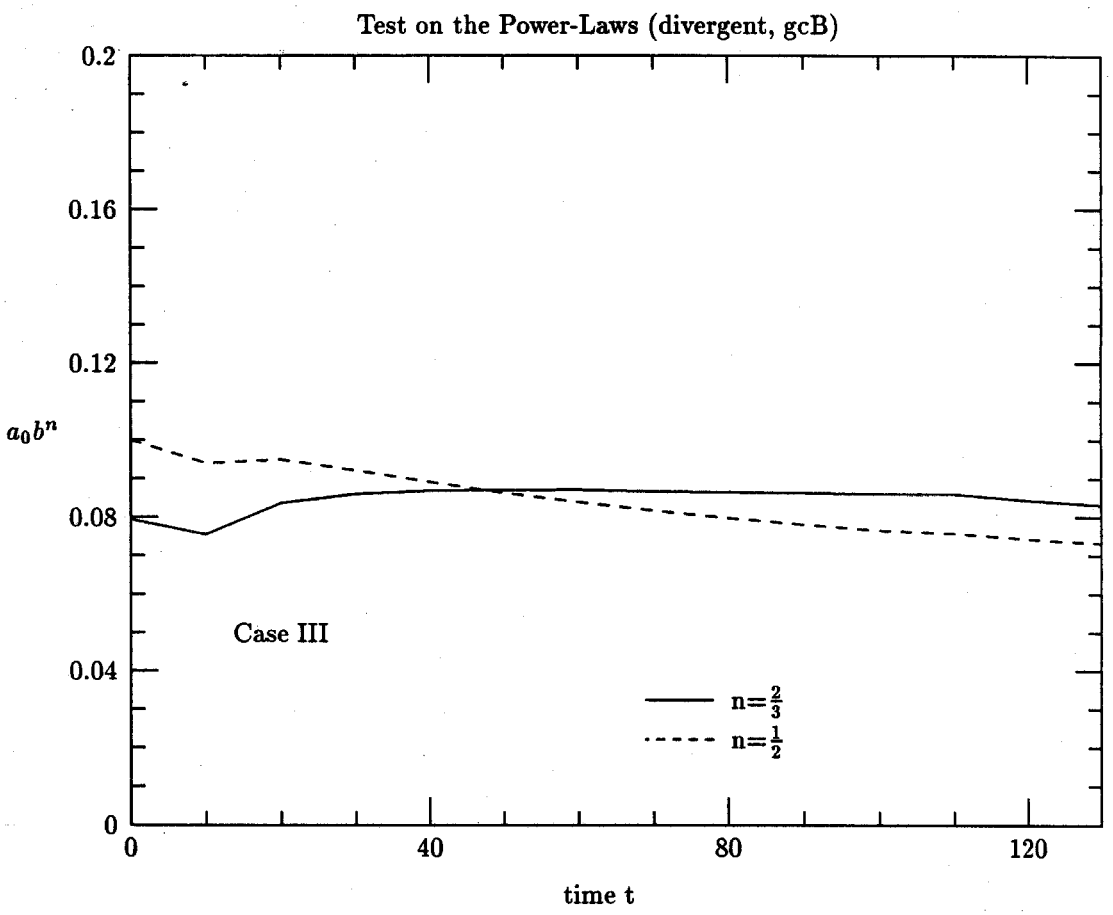
Test on the Power-Laws (divergent, gcB)
0.2
0.16
0.12
$a_0 b^n$
0.08
0.04
0
Case III
n=$\frac{2}{3}$
n=$\frac{1}{2}$
0
40
80
120
time t

Figure 4.6(d)

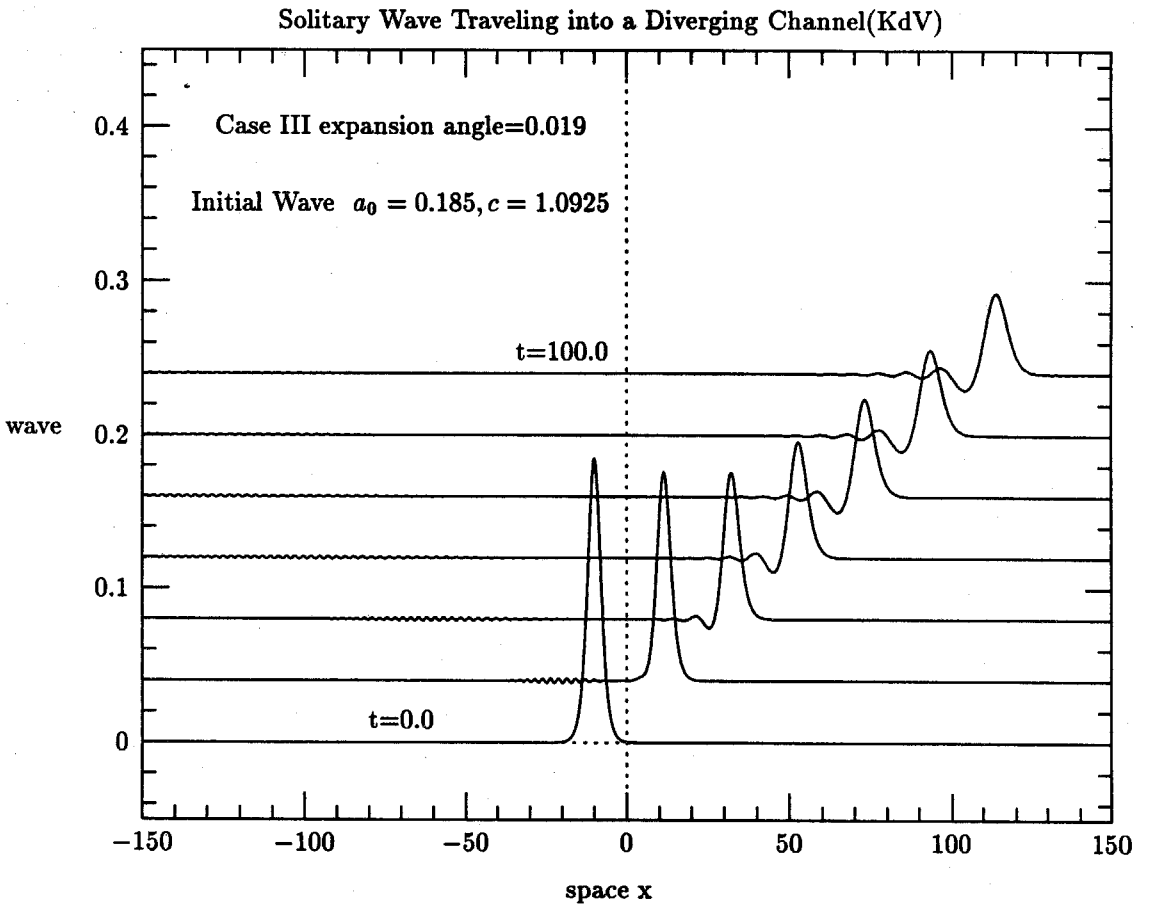
Solitary Wave Traveling into a Diverging Channel(KdV)
Case III expansion angle=0.019
Initial Wave $a_0 = 0.185, c = 1.0925$
t=100.0
t=0.0
wave
space x
0.4
0.3
0.2
0.1
0
−150
−100
−50
0
50
100
150

Figure 4.7(a)

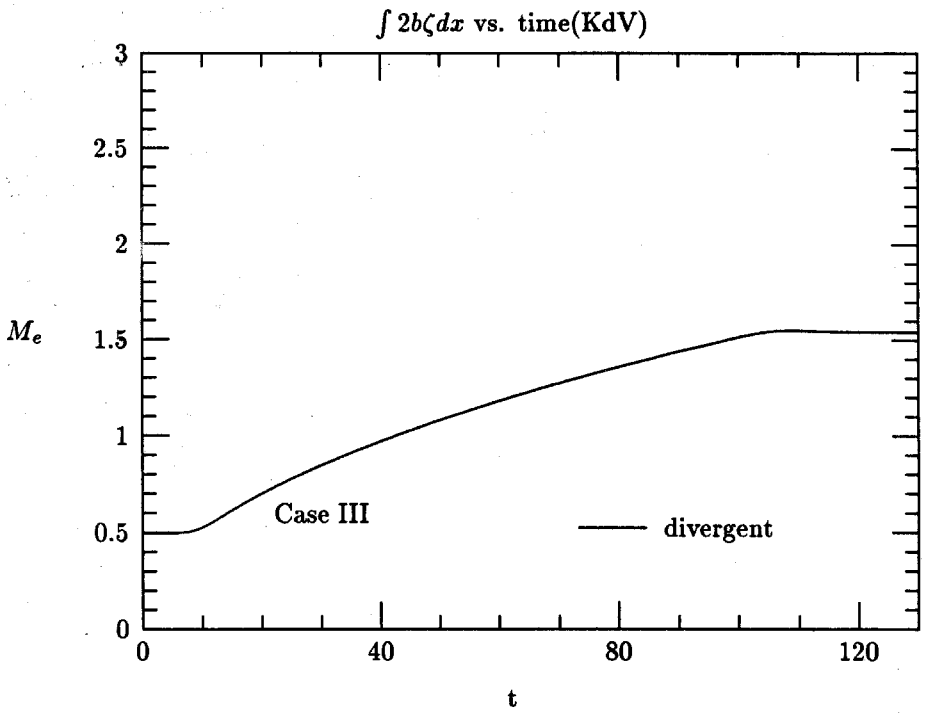

Figure 4.7(b)

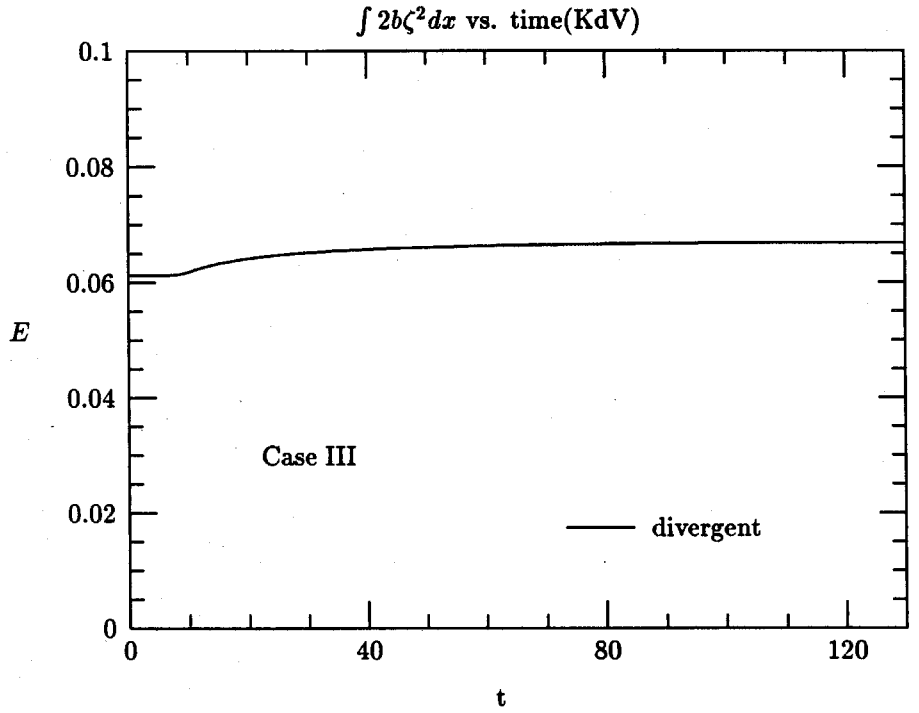

Figure 4.7(c)

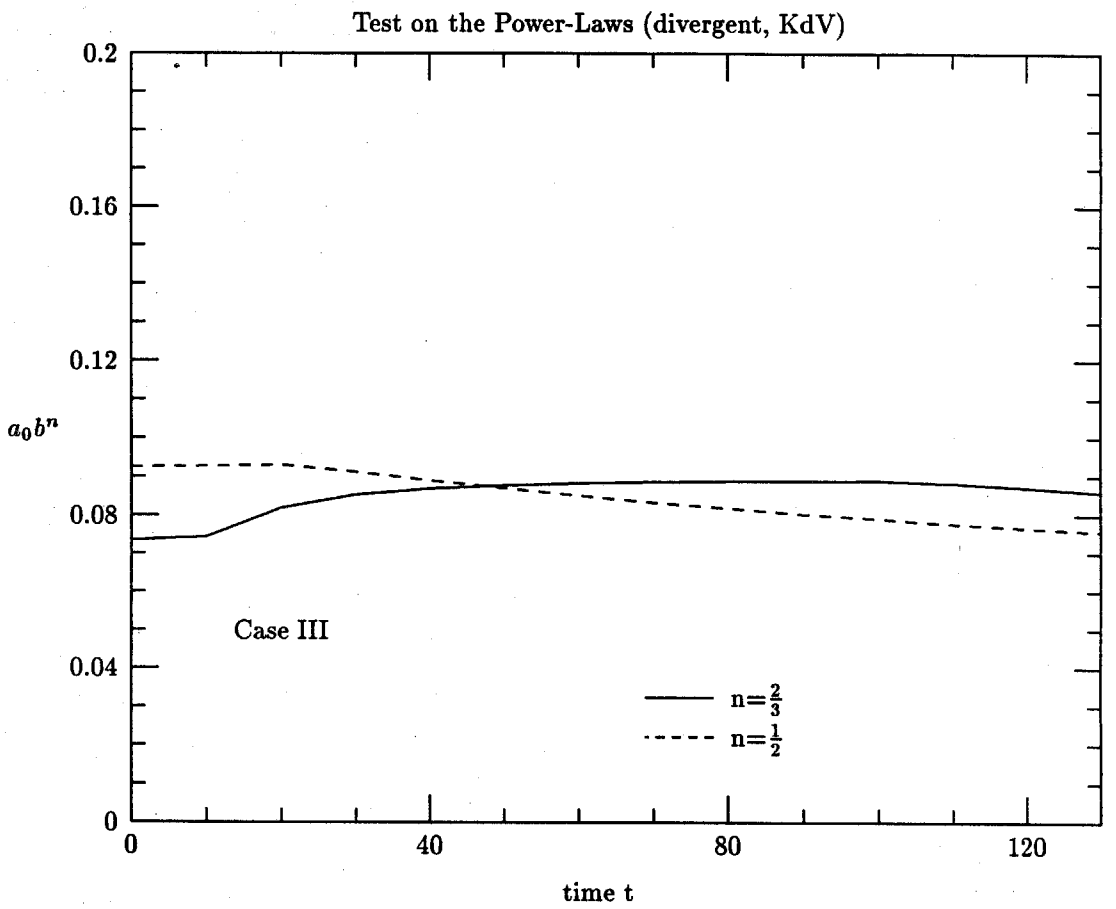
Test on the Power-Laws (divergent, KdV)
0.2
0.16
0.12
$a_0 b^n$
0.08
0.04
0
Case III
n=$\frac{2}{3}$
n=$\frac{1}{2}$
0
40
80
120
time t

Figure 4.7(d)

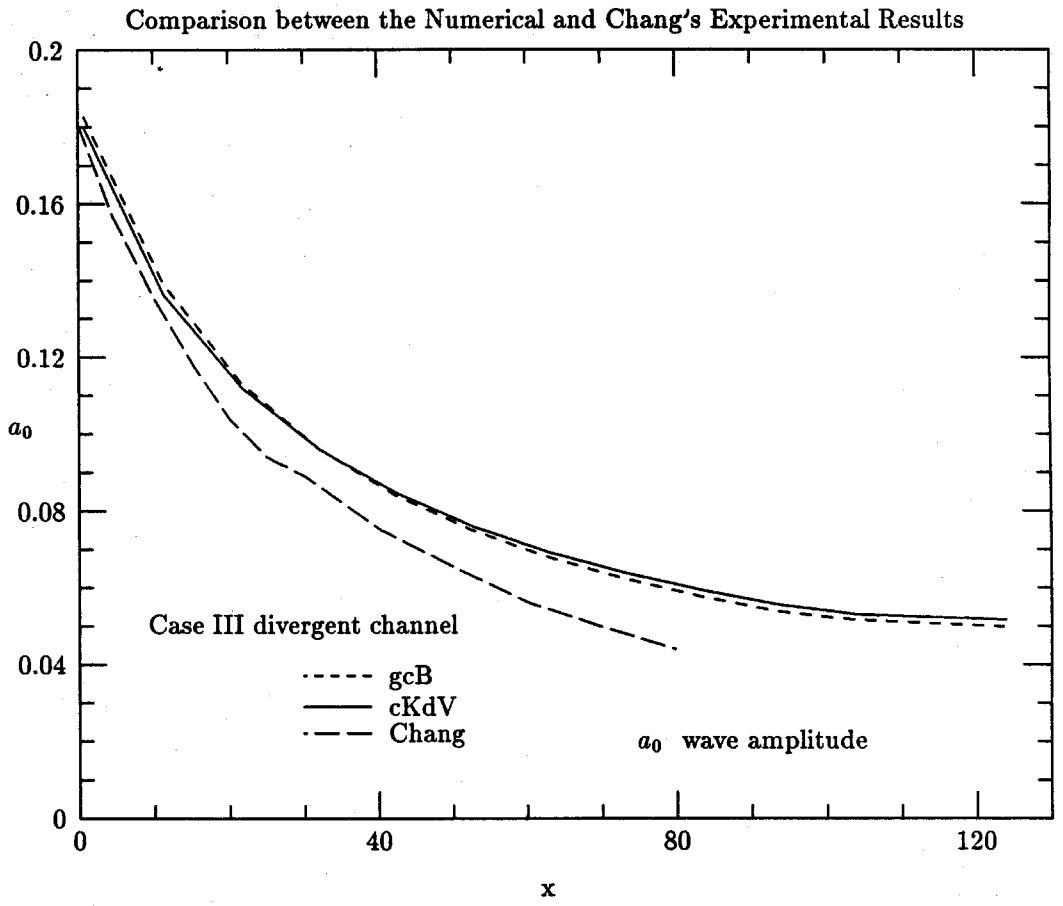
Comparison between the Numerical and Chang's Experimental Results
0.2
0.16
0.12
a_0
0.08
0.04
0
0
40
80
120
x
Case III divergent channel
gcB
cKdV
Chang
a_0 wave amplitude

Figure 4.8(a)

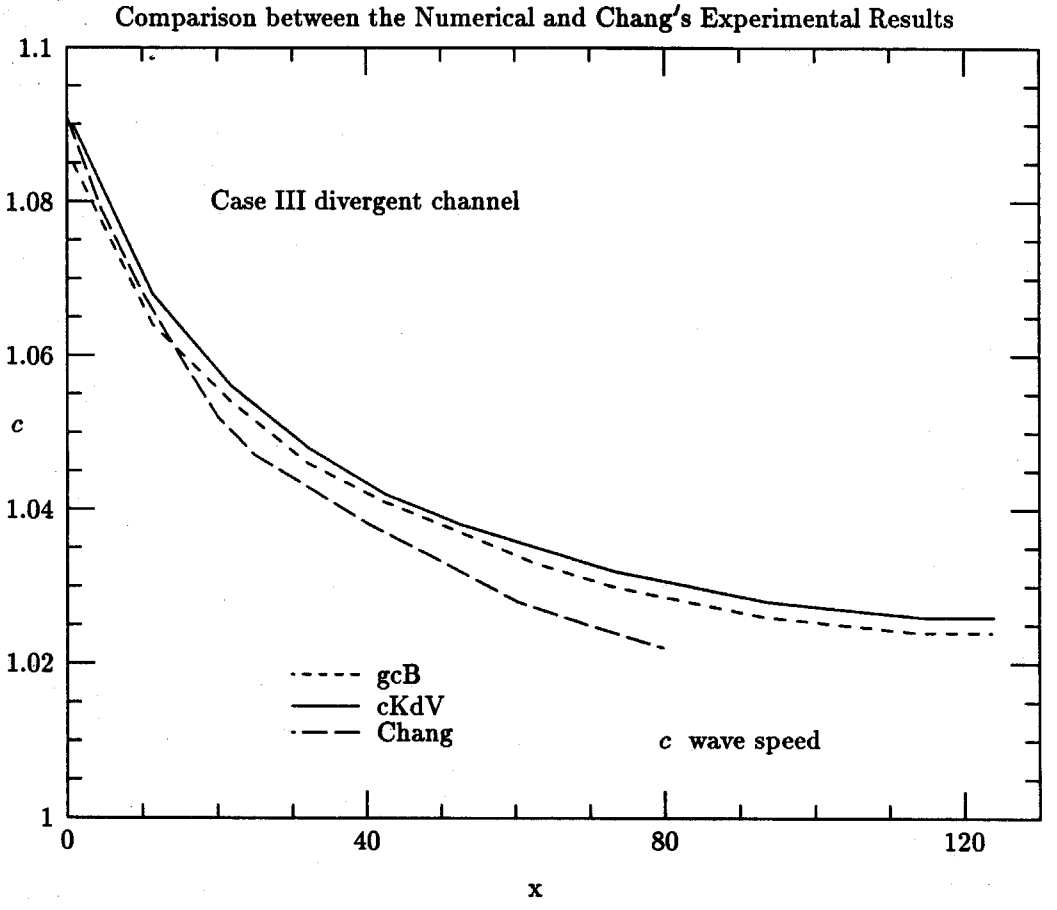
Comparison between the Numerical and Chang's Experimental Results
Case III divergent channel
gcB
cKdV
Chang
c wave speed
c
x
1.1
1.08
1.06
1.04
1.02
1
0
40
80
120

Figure 4.8(b)

experimental results is about 36.8%. This difference may be caused by the numerical and experimental errors. Another reason may lie in the viscous damping of the wave amplitude in the real experiments. This point will be discussed in 4.2.5.

Results associated with other quantities of interest, e.g., the excess mass, the total energy and the power laws, can be found through Figures 4.6(a) to 4.8.

4.2.4 Case IV $c_0 = 1.087$, $\alpha = -0.019$, initial width $b_0 = 1.5$, linearly convergent

In the present case, the initial solitary wave has a speed of c_0=1.087, which corresponds to a wave amplitude of a_0=0.1873 based on the gcB model and a_0=0.174 by the cKdV model. The solitary wave starts at x=-10.0, where the initial channel width of the uniform section is $2b_0$=3.0, then it travels into a convergent section of length s_2=70.0 water depths. The terminal channel width is $2b_1$=0.34. The ratio of the initial channel width over the terminal channel width is 3.0/0.34=8.82.

The comparison between the numerical results and Chang's experimental results is shown in Figure 4.11(a) and 4.11(b). In the present case for a convergent channel, the results based on our theoretical models show excellent agreements with Chang's experimental data throughout the whole variable section, with the maximum relative difference being about 3%. After the wave exits from the variable section with a relatively large amplitude, the gcB model and the cKdV model predict different amplitudes for the transmitted wave. This is understandable, however, since theoretically the two models possess permanent-wave-form solutions of different amplitudes for the same speed, and the difference in amplitude becomes more appreciable as the amplitude increases. (See section 2.10.) The experimental data are not available beyond $x = 60.0$.

In both Case III and Case IV, the mass conservation laws are examined. The following table gives the detailed data of the reflected mass by the gcB model

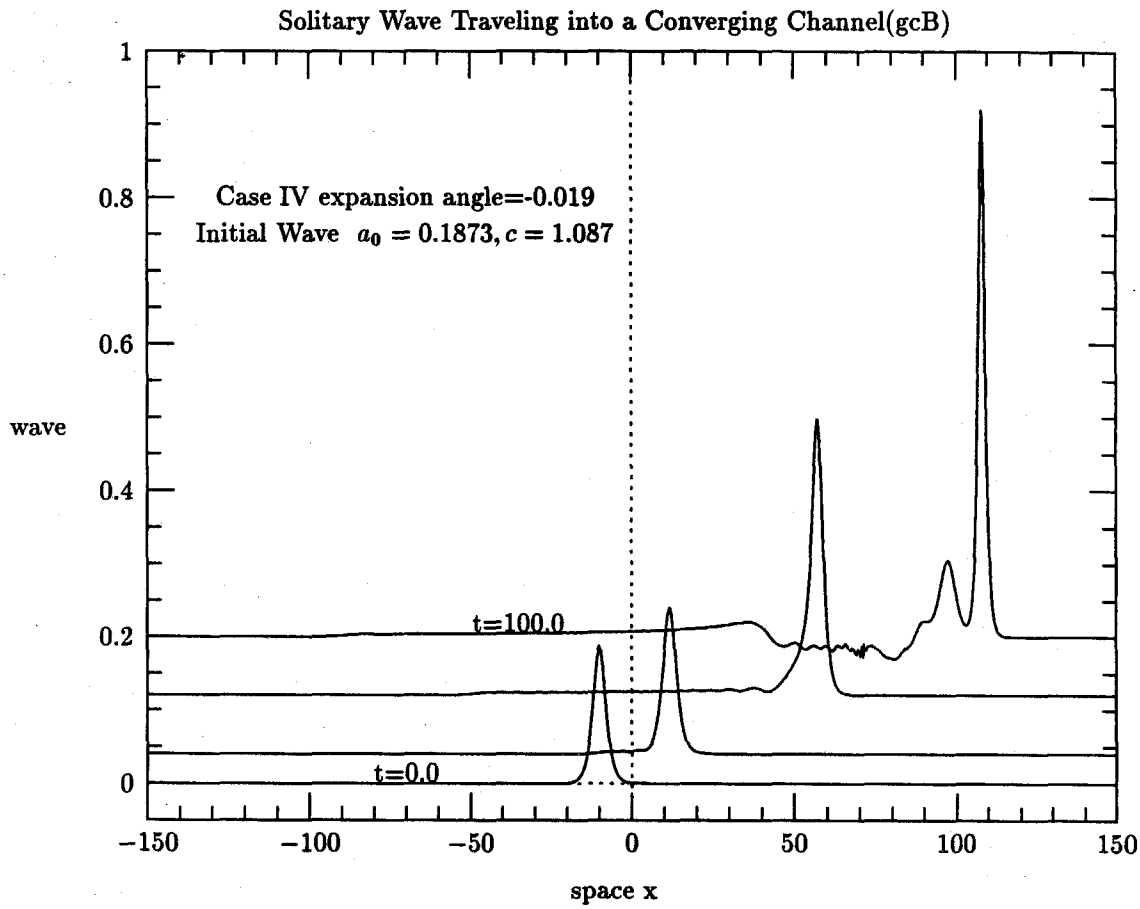
Solitary Wave Traveling into a Converging Channel(gcB)
Case IV expansion angle=-0.019
Initial Wave $a_0 = 0.1873, c = 1.087$
t=100.0
t=0.0
wave
space x
1
0.8
0.6
0.4
0.2
0
−150
−100
−50
0
50
100
150

Figure 4.9(a)

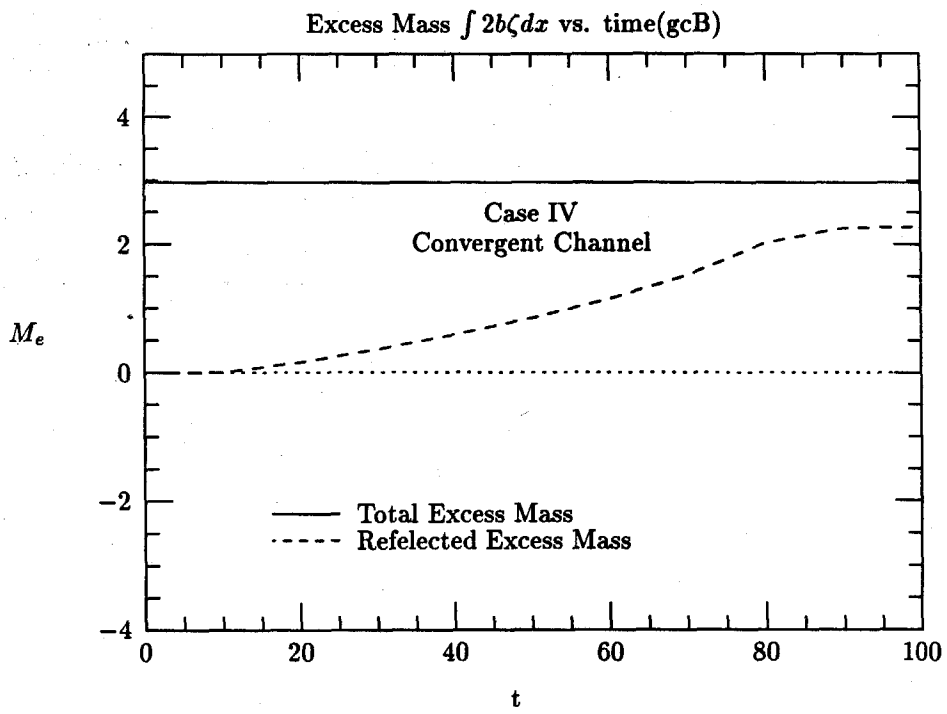

Figure 4.9(b)

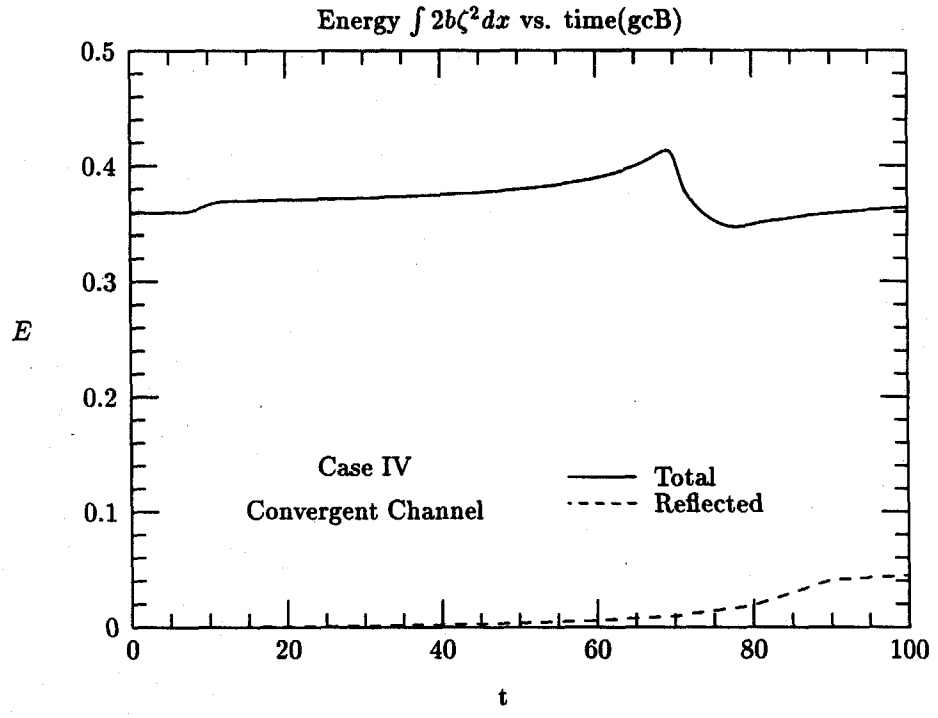

Figure 4.9(c)

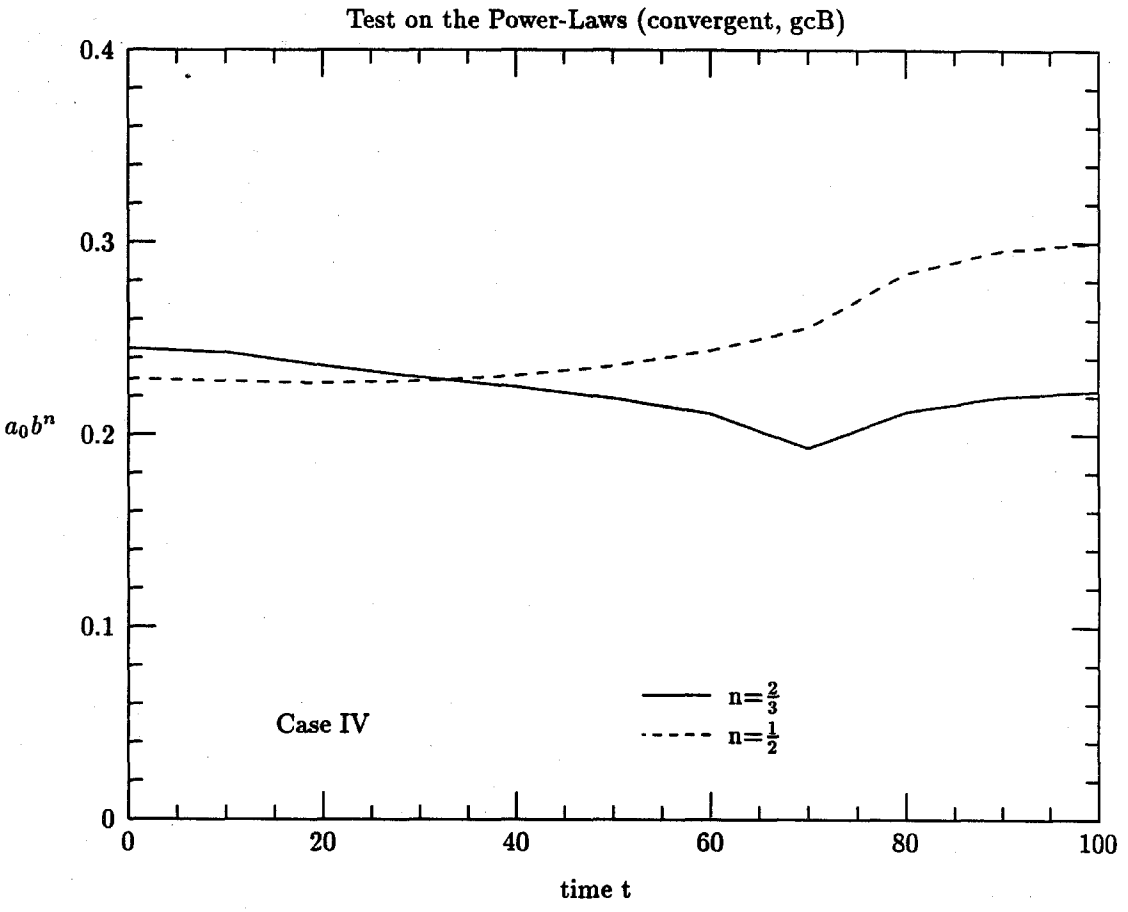
Test on the Power-Laws (convergent, gcB)
0.4
0.3
$a_0 b^n$
0.2
0.1
0
0
20
40
60
80
100
time t
Case IV
n=2/3
n=1/2

Figure 4.9(d)

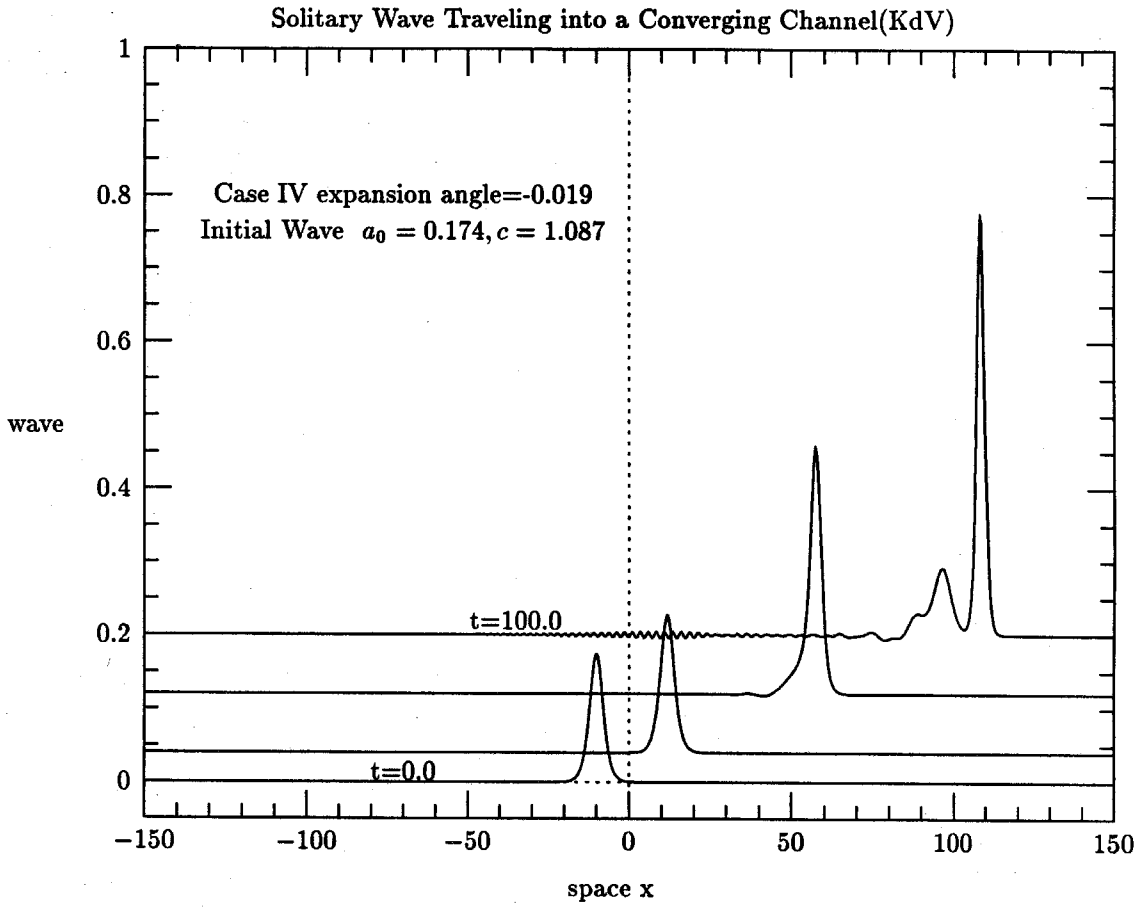
Solitary Wave Traveling into a Converging Channel(KdV)
Case IV expansion angle=-0.019
Initial Wave $a_0 = 0.174, c = 1.087$
t=100.0
t=0.0
wave
space x
1
0.8
0.6
0.4
0.2
0
−150
−100
−50
0
50
100
150

Figure 4.10(a)

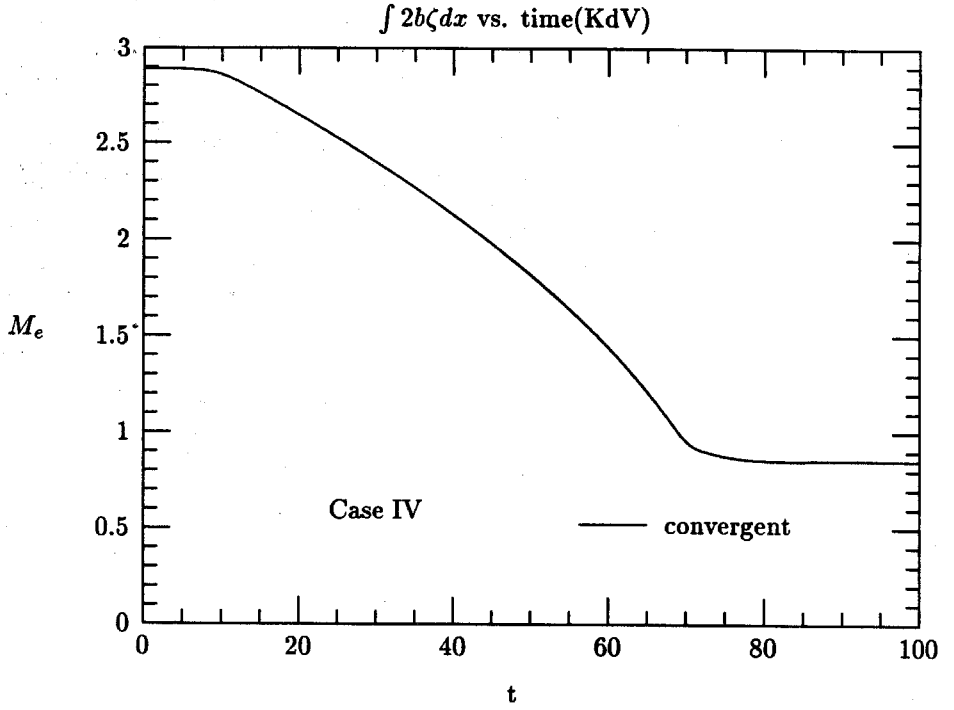

Figure 4.10(b)

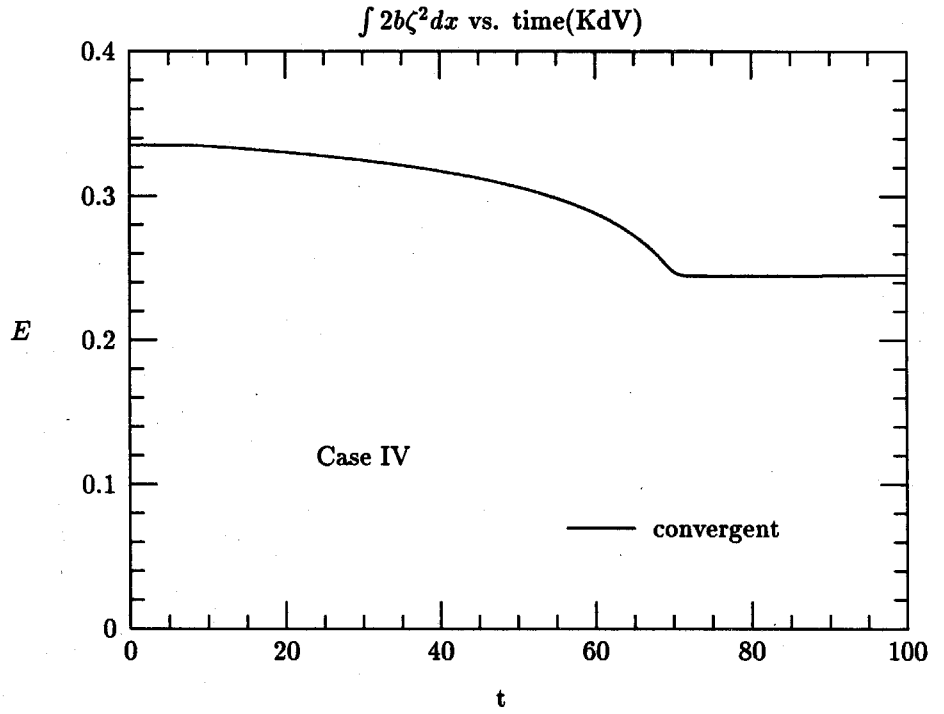

Figure 4.10(c)

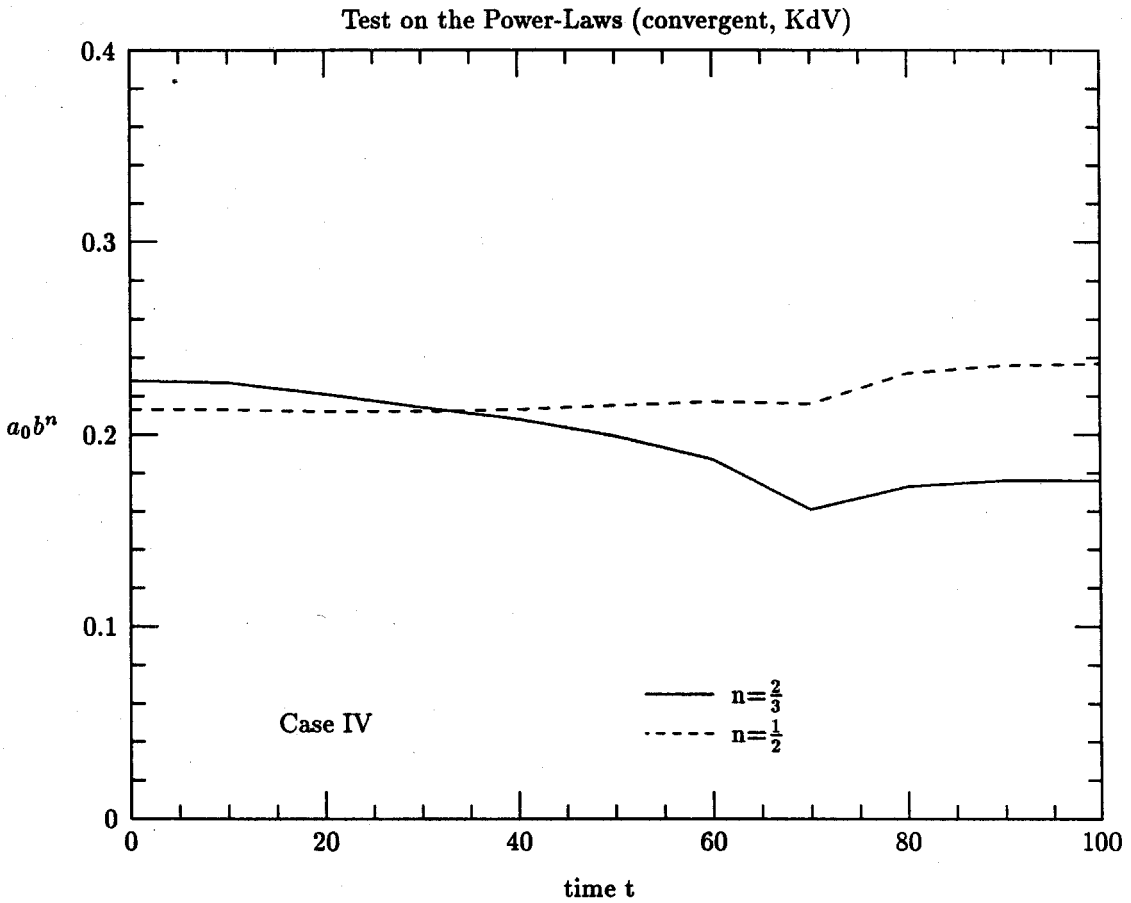
Test on the Power-Laws (convergent, KdV)
0.4
0.3
$a_0 b^n$
0.2
0.1
0
0
20
40
60
80
100
time t
Case IV
n=2/3
n=1/2

Figure 4.10(d)

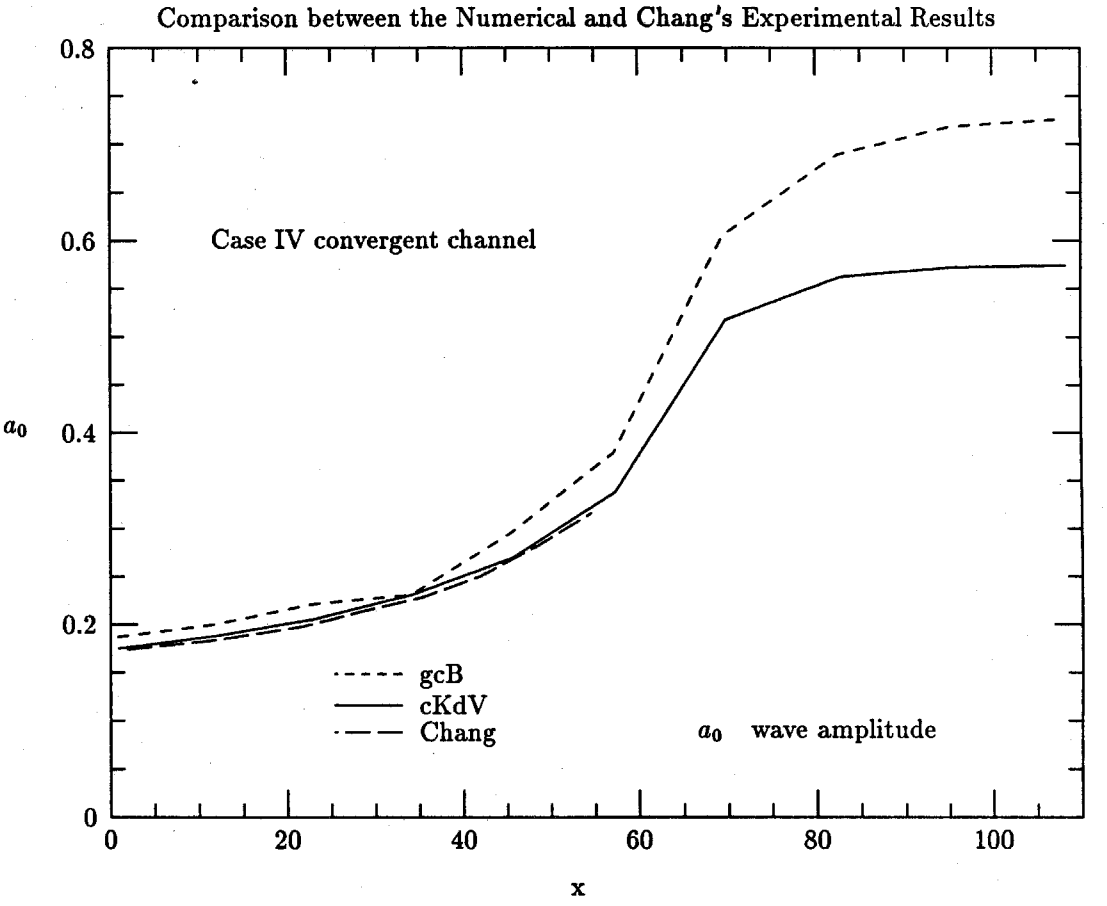
Comparison between the Numerical and Chang's Experimental Results
Case IV convergent channel
gcB
cKdV
Chang
a_0 wave amplitude
a_0
x
0.8
0.6
0.4
0.2
0
0
20
40
60
80
100

Figure 4.11(a)

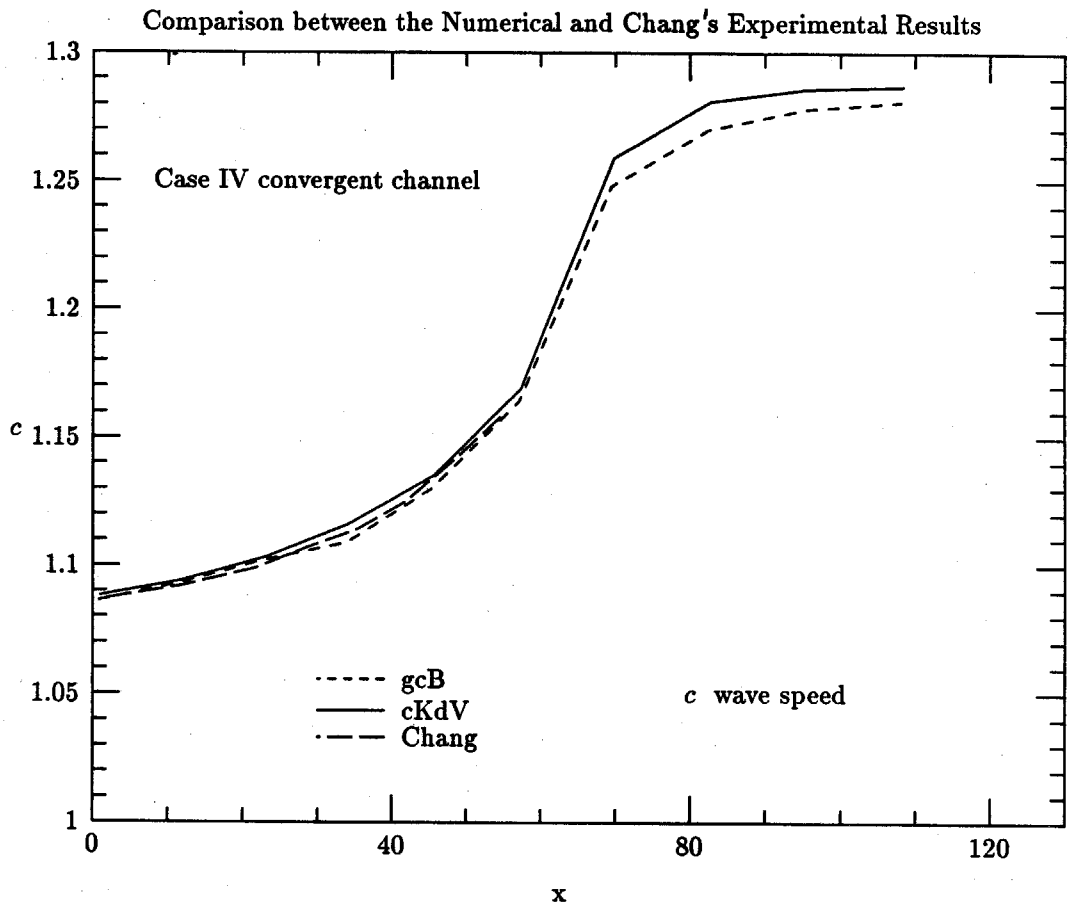
Comparison between the Numerical and Chang's Experimental Results
Case IV convergent channel
gcB
cKdV
Chang
c wave speed
c
x
1.3
1.25
1.2
1.15
1.1
1.05
1
0
40
80
120

Figure 4.11(b)

(M_{rfl}) and the change in the 'total' excess mass by the cKdV model (M_{tk}).

Table 4.4 Mass Conservation Laws

	M_{rfl}	M_{tk}
Case I	75.7%	73.5%
Case II	42.4%	42.2%
Case III	225.9%	210.6%
Case IV	76.5%	70.5%

4.2.5 Viscous Damping of Solitary Waves

Theoretically a solitary wave can travel in a uniform channel for infinitely long time without changing its shape and speed. In a real experiment, however, because of the existence of fluid viscosity, the amplitude of a solitary wave traveling in a straight uniform channel will gradually decrease due to viscous dissipation. The problem of viscous damping of solitary waves was studied by Keulegan[13] in 1948. By applying the boundary layer theory for laminar flows, he derived a simple formula to predict the gradual decrease in amplitude of a solitary wave due to viscous damping. His formula is adopted in the present study to estimate the viscous effect on the change of wave amplitude in Case III and Case IV, where our numerical results on the evolution of a solitary wave traveling in a divergent or convergent channel are compared with the experimental results obtained by Chang et al.

Keulegan's formula appears as

$$(\frac{a_1}{H})^{-\frac{1}{4}} - (\frac{a_{10}}{H})^{-\frac{1}{4}} = K\frac{s}{H}, \tag{4.9}$$

where the coefficient of damping has the value

$$K = \frac{1}{12}(1 + \frac{2H}{W})\sqrt{\frac{\nu}{g^{1/2}H^{3/2}}}. \tag{4.10}$$

In expressions (4.9) and (4.10), a_1 is the decreased amplitude after the solitary wave has traveled a distance of s and a_{10} is the initial amplitude of the solitary wave. H stands for the water depth, W the channel width, ν the kinematic viscosity of the water ($\nu = 1.007 \times 10^{-6} m^2/s$, at $T = 20°c$) and g the acceleration of gravity ($g = 9.8 m^2/s$).

In Case III with a divergent channel, we note that H=0.2 m and a_{10}/H=0.185 in Chang's experiment. We take $W/H = 1/2(2.15 + 0.25) = 1.2$ as the averaged channel width and s/H=80.0 as the distance that the solitary wave has traveled. In Chang's experiments, the channels were not symmetric and they represented the configuration of half-channels in either the $+y$-plane (divergent) or in the $-y$-plane (convergent) in our numerical simulations. The width ($W = 2b$) in the numerical computations is thus twice as that ($W = b$) in the experiments. Substituting these parameters into formula (4.9), we obtain an estimate for the wave amplitude at s/H=80.0 as $a_1/H = 0.174$, which gives a relative change with respect to the original amplitude a_{10}/H=0.185 as about 8.1%. For Case IV, by following the same procedure of calculation, we predict the decrease in wave amplitude due to viscous damping after the solitary wave has traveled 60 water depths as about 5.7%. These results show that the viscous damping of the wave amplitude in these cases are relative large and thus must be considered when we compare the numerical results with the experimental data.

After the correction due to the viscous damping, the numerical results in Case III (Figure 4.8(a)) will have closer agreements with the experimental data. For Case IV this correction will bring the numerical curves (Figure 4.11(a)) below the experimental curve and the relative error after the correction is still small (within 3%) in this case.

4.3 Summary

In this chapter we have applied both the gcB and the cKdV models to study the evolution of a solitary wave traveling in a channel of linearly varying width. Four cases with different sets of parameters are investigated. As we analyzed in Chapter II, the gcB model conserves mass exactly and conserves energy to certain order, while the cKdV model, when applied to study a problem with variable channels, does not conserve mass and energy in general. This is caused by the violation of the assumption of unidirectional motions for the cKdV model. However, comparing the numerical results based on the cKdV model with that based on the gcB model, we found that even though the cKdV model does not conserve the total excess mass, it gives the same prediction for the main transmitted wave as the gcB model. In other words, the neglect of the reflected wave in our theoretical derivations does not affect the validity of the cKdV model for the main transmitted wave.

When a solitary wave travels in a divergent channel, there are waves reflected in the opposite direction opposing the main transmitted wave. The reflected wave has a negative amplitude and its front travels with a near critical speed. Even though the amplitude of the reflected wave is small, its length is relatively long and the reflected wave can carry away quite large amount of mass. This causes a corresponding change in the local excess mass possessed by the main transmitted wave. For a divergent channel, the transmitted wave may gain mass by 75% to 225% after traveling 100 water depths in the variable section. For a solitary wave traveling in a convergent channel, the transmitted wave loses mass by 42% to 72% due to the reflected wave of positive amplitudes. The loss of energy caused by the reflected wave is of higher order.

Our numerical results showed good agreements with Chang's experimental results for a solitary wave traveling in a convergent channel. For a divergent channel, the agreement is not uniform throughout the channel and the maximum relative difference at the end of the channel is about 36.8%.

V. FORCED GENERATION OF RUN-AWAY SOLITONS BY THREE-DIMENSIONAL MOVING DISTURBANCES

In a channel of shallow water, nonlinear long waves can be generated in many ways. A pressure distribution at the free surface, a moving topography along the boundary or a submerged object, when moving with a near-critical speed, can all generate a series of solitons advancing upstream, while a train of weakly nonlinear and weakly dispersive waves develop in the downstream region. The solitary waves generated in front of the moving disturbance propagate upstream with a greater speed than the steadily moving disturbance and are called "run-away solitons". Long waves can also be generated by adding mass at certain rate to the wave system. This simulates the situation of heavy rainfall on rivers. Also, since a solitary wave is a very stable wave form, an initial positive hump of water will eventually develop into one or more solitary waves. A local movement of the surrounding boundary walls, like an earthquake on the sea floor, can also emit long waves on shallow water.

The present study is focused on investigating the generation of run-away solitons by one particular type of the external forcing agencies mentioned above, namely, by a three-dimensional moving disturbance, which may either be a boundary topography or a submerged moving object. Our main interest is to study the effective strength of a three-dimensional moving disturbance and the difference between a surface pressure distribution and a boundary topography as external forcing functions based on the two theoretical models. The effects of the longitudinal length of a moving disturbance, and, further, the general validity criteria for the two long-wave models are also examined.

Both numerical computations and laboratory experiments are carried out to

investigate the specific topics presented in this chapter. The experimental data show good agreement with the numerical results based on our long wave models. These results will be seen to confirm one of the important theoretical conclusions that the effective strength of a three-dimensional topographical moving disturbance in regard to wave generation is directly related to the blockage-ratio of the cross-sectional area due to the presence of the moving topography.

In the following sections, numerical results based on our wave models for a uniform rectangular channel with three-dimensional external forcings will be presented. For channels of other types of cross-sectional shapes, results can be obtained by following the same procedures.

5.1 Governing Equations

To describe the generation of long waves by extarnal moving disturbances in a uniform rectangular channel, we may apply the gcB model (2.110)-(2.111), which for the present case becomes

$$(b\zeta)_t + [b(h+\zeta)u]_x = -\frac{1}{2}(A_d)_t, \tag{5.1}$$

$$u_t + uu_x + \zeta_x = \frac{1}{3}u_{xxt} - p_{ax} - \frac{1}{2}d_{xtt} - \frac{1}{3}B_{xtt}, \tag{5.2}$$

or the corresponding cKdV equation

$$\zeta_t - (1+\frac{3}{2}\zeta)\zeta_x - \frac{1}{6}\zeta_{xxx} = \frac{1}{2}(\frac{1}{2}A_d + p_a)_x, \tag{5.3}$$

where

$$h = 1 - d(x,t),$$

$$b = 1 - B(x,t),$$

$$A_d = 2(B+d).$$

Here equation (5.3) is written for left-going waves. The external forcing functions p_a and A_d (in terms of B and d) are assumed to be small, and in equation (5.2), the higher order terms such as uB_x have been neglected.

The gcB model (5.1)-(5.2) possesses in general good conservation properties. Although the cKdV model in general does not conserve either mass or energy, in the present case for a uniform channel, the cKdV model (5.3) both conserves the total excess mass M_e and preserves the physical energy-work relation.

Two theoretical points regarding the external forcing functions can be drawn from the wave models given by (5.1)-(5.2) and (5.3). First, the cKdV model (5.3) shows that a moving pressure distribution at the free surface and a submerged moving topography play equivalent roles as external forcing functions near resonance. (This is also implied by the gcB model to certain order.) Second, both models indicate that the effective strength of a three-dimensional submerged moving object as an external forcing function is directly related to the blockage ratio A_d of the cross-sectional area.

The higher order derivative terms of the forcing functions d_{xtt} and B_{xtt} in equation (5.2) of the gcB model are assumed small in our theoretical modeling and are neglected in deriving the cKdV model. Examining the magnitude of these two terms, we find that they are highly sensitive to the detailed geometric configuration of the disturbance in the longitudinal direction and may not be truely small when the gcB model is applied for a forcing case that fails to satisfy this assumption, especially if the disturbance is not sufficiently long or smooth enough in the longitudinal direction. The effect of the length of a disturbance, the validity and the practical application of the two long-wave models for the forced case will be further discussed in later sections.

5.2 Wave Resistance and the Drag Coefficient

When a disturbance moves in an inviscid fluid having a free surface, it generally experiences a resistance due to radiation of surface waves. From the energy-work relation (see (2.157), (2.173) and (2.177)), the nondimensional wave resistance or the drag coefficient D_w, is given by

$$FD_w = -2\int_{-\infty}^{+\infty}(p_a\zeta_t - \zeta B_t - \zeta d_t)dx, \tag{5.4}$$

where Froude number F is the dimensionless speed of the moving disturbance.

By applying the first-order linear approximation $\partial/\partial t \simeq \partial/\partial x$ and $F \simeq 1$ for left-going near-resonant external forcings, we have, upon integration by parts,

$$D_w = 2\int_{-\infty}^{+\infty}(p_a + B + d)_x\zeta dx. \tag{5.5}$$

The drag coefficient given by (5.5) is computed with our numerical simulations. It will be seen that D_w is usually a pseudo-periodic function of time for cases where a moving disturbance radiates run-away solitons periodically.

5.3 Numerical Results

We perform numerical computations based on both the gcB model (5.1)-(5.2) and the cKdV model (5.3). The forcing functions p_a, B and d in our equations simulate a free surface pressure distribution, a side-wall topography and a bottom topography, respectively. Figures 5.17(a) and 5.17(b) in section 5.4 give a clear view of the physical configurations of the numerical simulations. In most of the cases presented in this section, the forcing functions $p_a(x,t)$, $B(x,t)$ and $d(x,t)$ are taken to be of the same form as follows:

$$p(x,t) = \begin{cases} \frac{p_m}{2}[1-\cos(\frac{2\pi}{L}(x+Ft))], & \text{for } 0 \le x+Ft \le L; \\ 0, & \text{otherwise.} \end{cases} \tag{5.6}$$

In expression (5.6), p represents the forcing functions in the generic form. The important parameters associated with the forcing functions in the present study are the magnitude p_m, the longitudinal length L and the near-resonant speed F of the disturbance. A plot of the forcing function $p(x,t)$ given by (5.6) for p_m=0.1 and L=10.0 is shown in Figure 5.1.

Our objective of the numerical computations is to investigate the discrepancies between the two wave models, the differences among the three forcing functions p_a, B and d, and the effect of the longitudinal length of the disturbance. Numerical results are obtained for different sets of values of the parameters mentioned above.

5.3.1 Results Based on the cKdV Model

Since the cKdV model cannot differentiate a boundary topography from a free-surface pressure distribution when both are serving as external forcing functions, the inhomogeneous terms at the right-hand side of equation (5.3) may be grouped into one general forcing term as follows:

$$\zeta_t - (1+\frac{3}{2}\zeta)\zeta_x - \frac{1}{6}\zeta_{xxx} = \frac{1}{2}p_x, \tag{5.7}$$

where p can be either a boundary topography or a free-surface pressure distribution.

The cKdV equation (5.7) is computed by using the finite difference scheme (3.7) described in Chapter III. At the initial time t=0, the free-surface elevation is taken to be zero throughout the whole domain. After t >0, the disturbance $p(x,t)$ starts to move to the left with speed F and thereafter maintains this constant velocity. The longitudinal geometric configuration of the disturbance is given by (5.6).

Case I. The effect of the speed of the disturbance.

p_m=0.1, L=10.0 and F varying from 0.8 to 1.05.

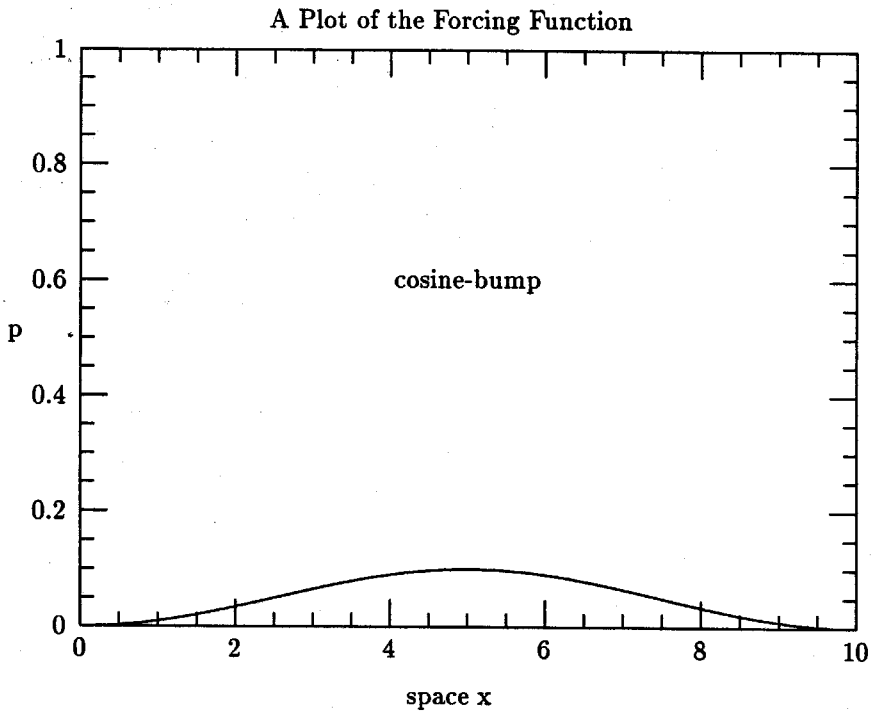

Figure 5.1

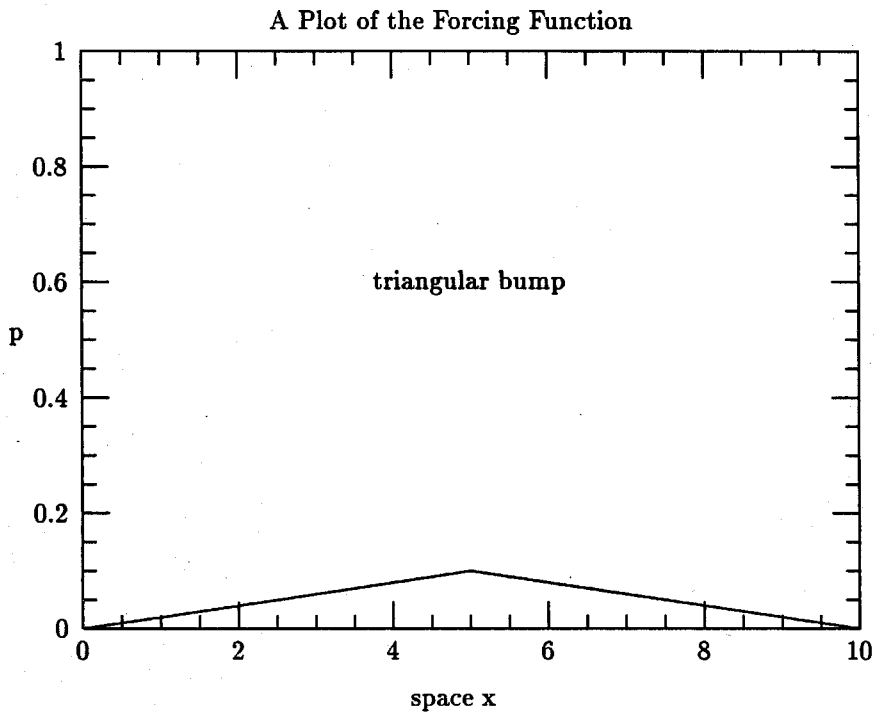

Figure 5.2

The plots of wave elevations at three different time steps (see Figures 5.3(a) to 5.3(c)) give a typical picture of the forced generation of run-away solitons by a steadily moving disturbance. After the disturbance has traveled to the left five hundred water depths with a critical speed, it generates at least ten run-away solitons with an averaged amplitude of $a_0 = 0.5$. Immediately trailing the disturbance there develops a long depressed region, which is then followed by a train of weakly nonlinear and weakly dispersive waves. The time record of the drag coefficient D_w is plotted in Figure 5.3(d). Comparing the number of solitons being generated (Figure 5.3(b)) with the number of periods shown in Figure 5.3(d), we see that the two numbers precisely coincide with each other. This implies that for a steady, positive, forcing disturbance moving with a critical speed, the work done by the disturbance on the wave system mainly contributes to the total energy possessed by the run-away solitons being generated, while the rest of the wave field participates less in the work-energy exchange. This may not be always true, however, such as in the case for a negative forcing.

Figures 5.4(a) and 5.4(b) show the results for wave generations by a subcritical (F=0.8) forcing disturbance. Several solitons are generated but with increasingly smaller amplitude to the asymptote of evanescing soliton production except for a forward-facing shelf of water surface. The depressed region has become very short and the trailing waves have actually become dominant. These salient features are well reflected in the variations of the drag cofficient D_w (Figure 5.4(b)) which at first has a series of attenuated oscillations in magnitude and eventually goes to a constant, indicating the steady radiation of the trailing wave train.

For the super-critical case, as shown in Fiures 5.5(a) and 5.5(b), the period of soliton generation becomes longer as the Froude number increases, while the amplitude of the run-away solitons gets larger.

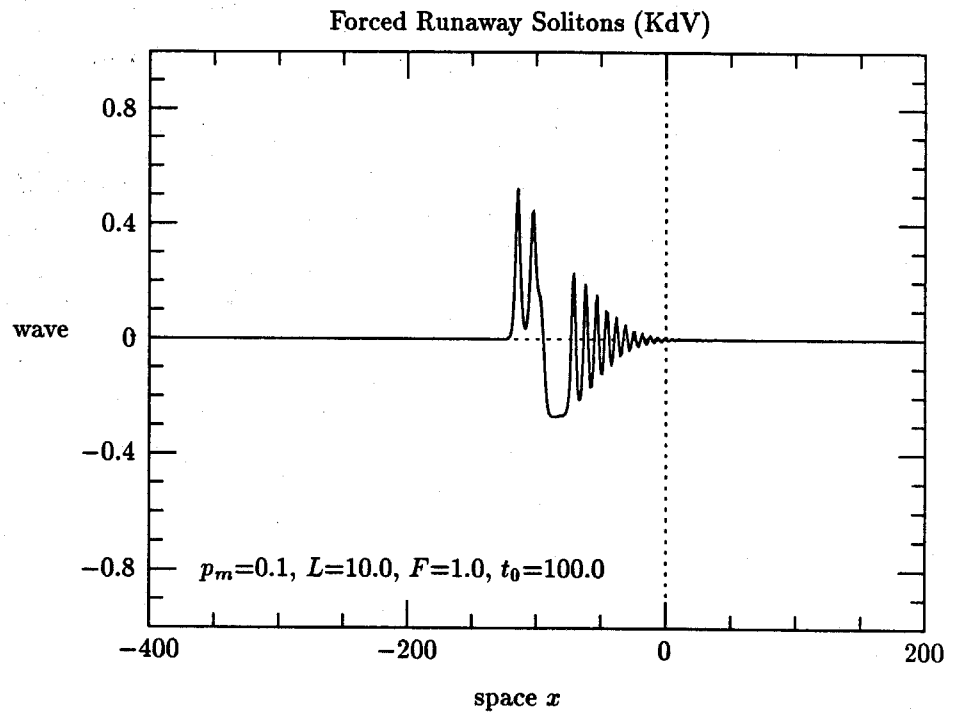

Figure 5.3(a)

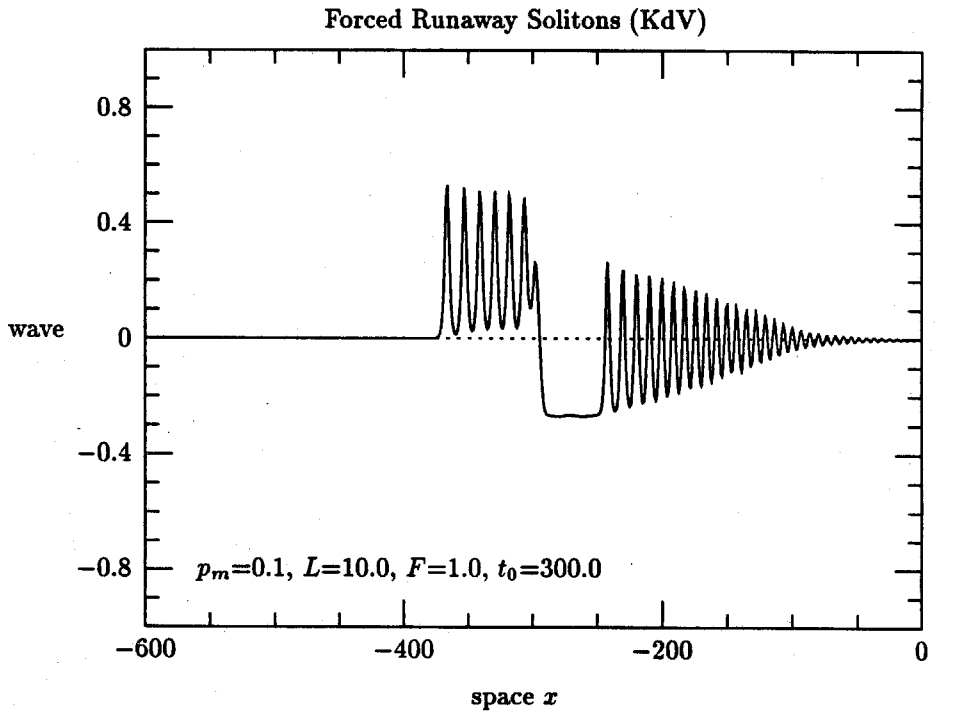

Figure 5.3(b)

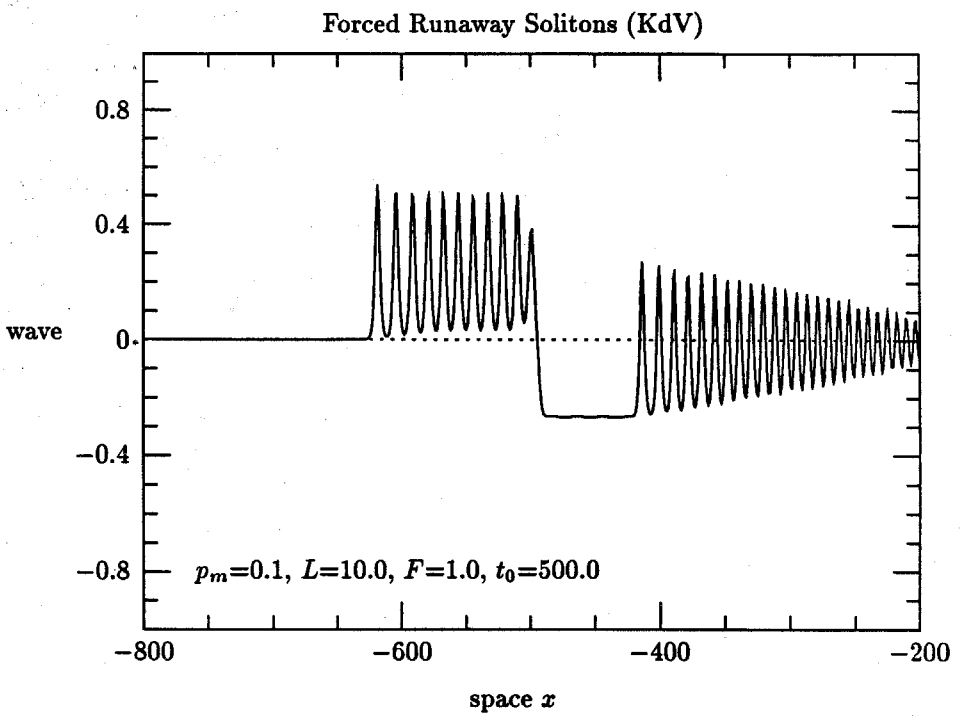

Figure 5.3(c)

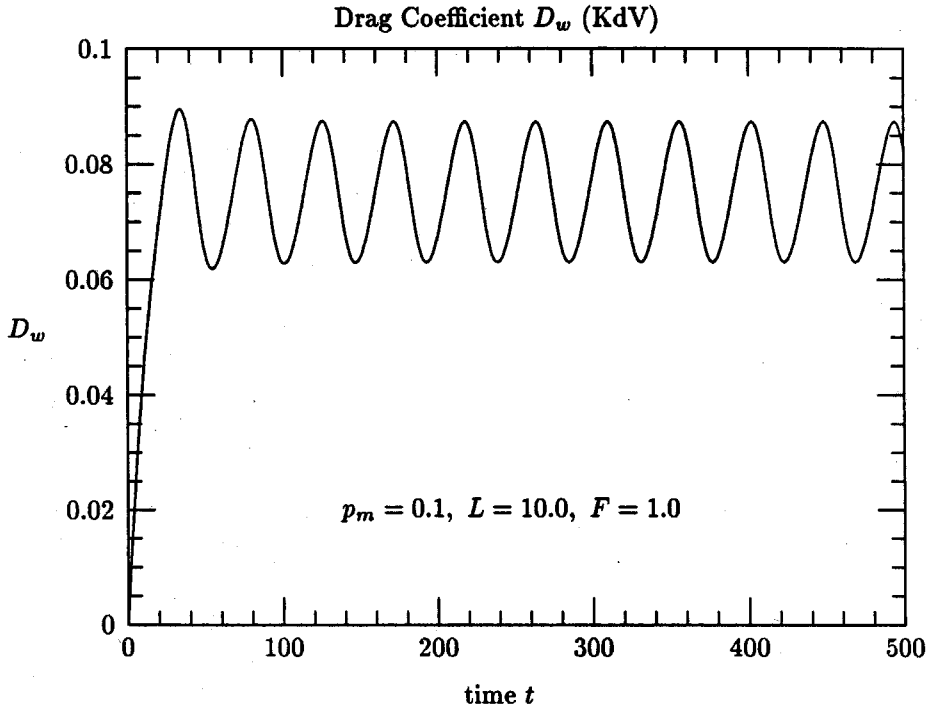

Figure 5.3(d)

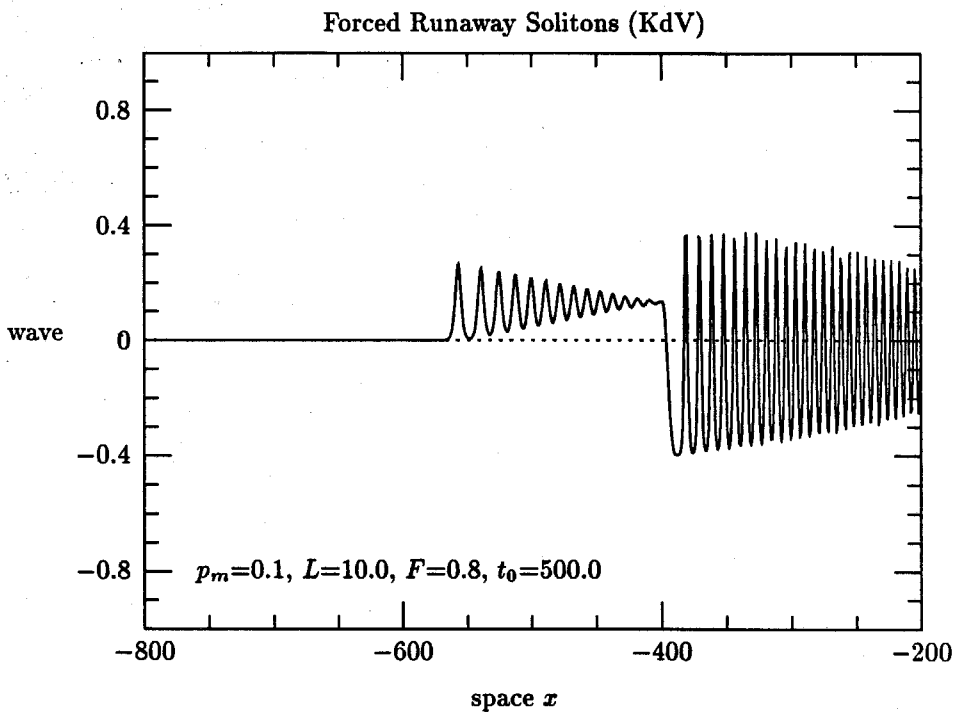

Figure 5.4(a)

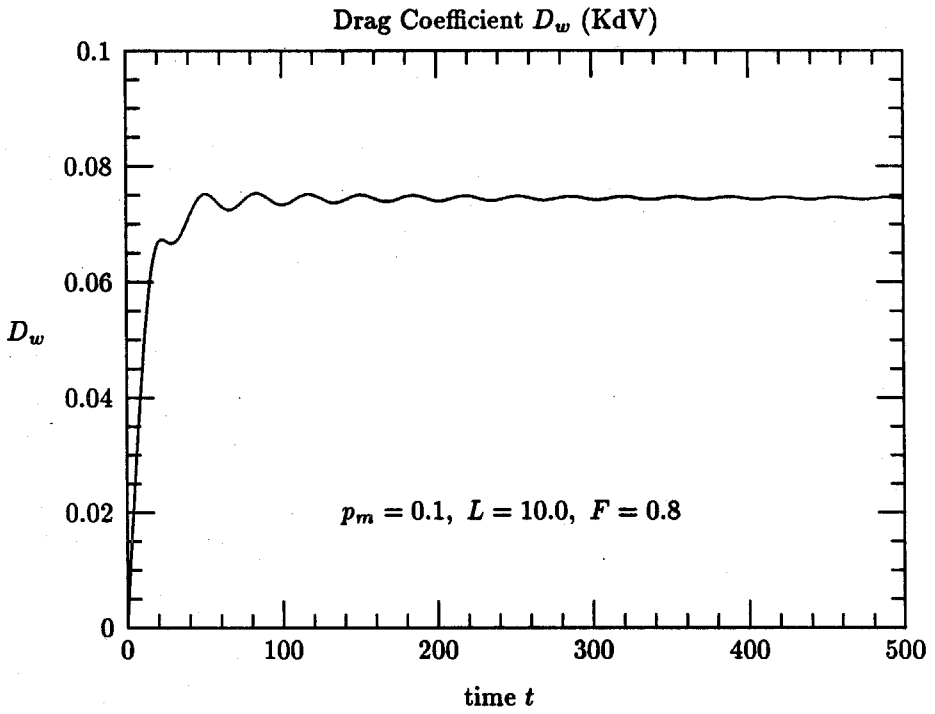

Figure 5.4(b)

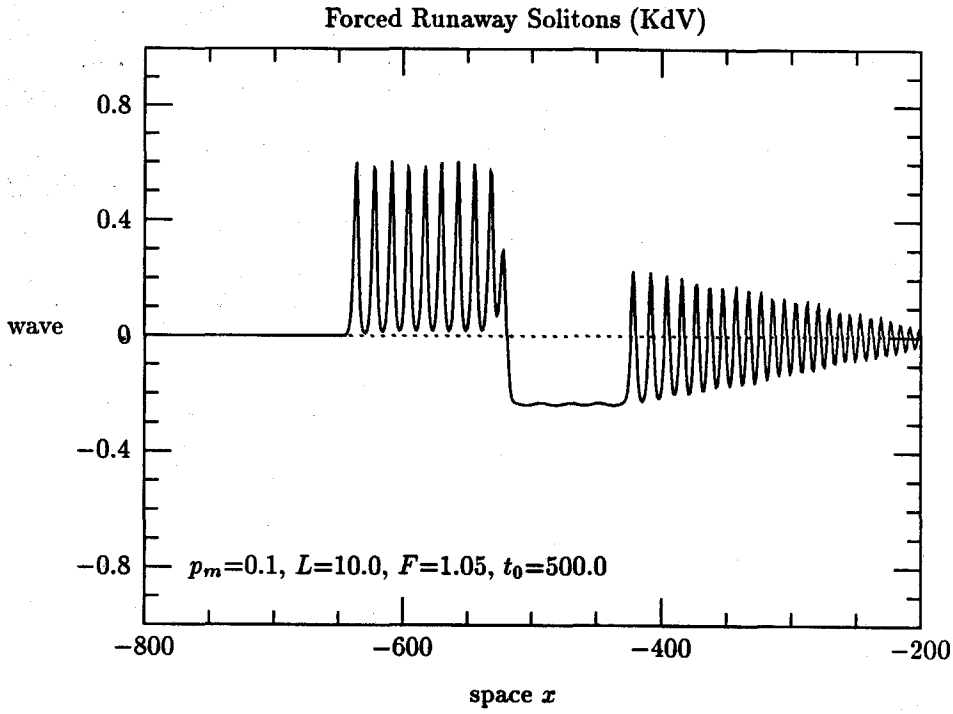

Figure 5.5(a)

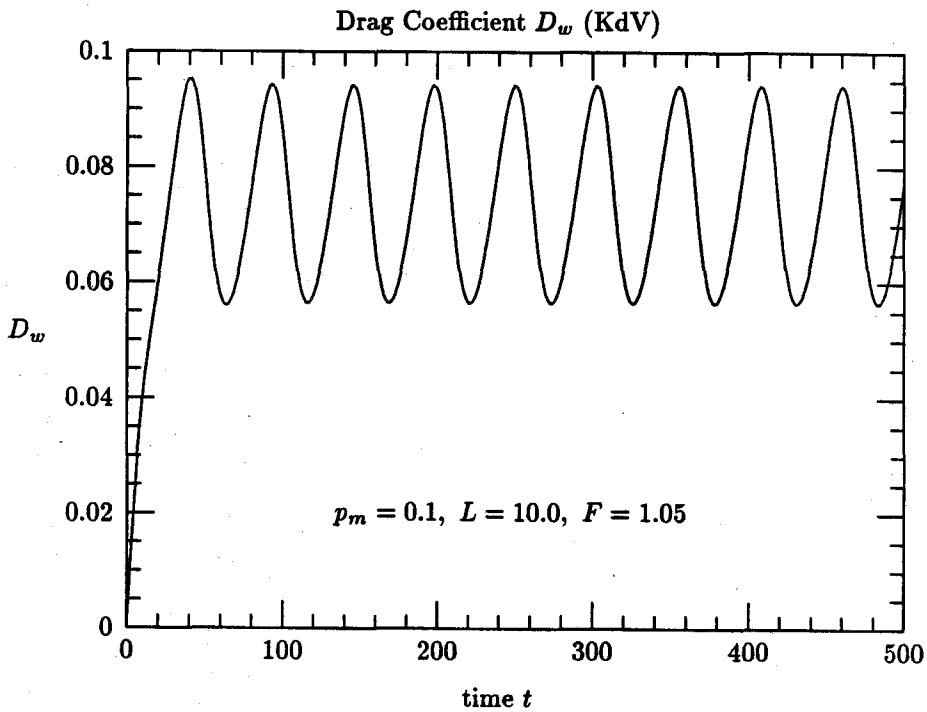

Figure 5.5(b)

Case II. The effect of the height of the disturbance.

p_m=0.2, F=1.0 and L=10.0.

When the maximum height of the disturbance is doubled, there are more solitons (17 compared to 10 in the previous case with F=1.0 and p_m=0.1) being generated during the same time as for the case shown in Figure 5.3. The amplitude of the solitons also becomes larger (0.71 compared to 0.5). The numerical results for this case are shown in Figures 5.6(a) and 5.6(b).

Case III. The effect of the longitudinal length of the disturbance.

p_m=0.1, F=1.0 and L varying from 2.0 to 20.0.

Figures 5.7(a) to 5.8(c) show the comparison among the results obtained for waves generated by disturbances of different longitudinal lengths, while the speed (F=1.0, critical) and the maximum height (p_m=0.1) of the disturbance are kept the same. The following table gives the quantitative data regarding the wave amplitude and the period of generation in the three cases.

Table 5.1 The Effect of the Longitudinal Length of the Moving Disturbance on Wave Amplitude and Period of Generation

L	wave amplitude	period of generation
2.0	0.35	56.0
4.0	0.47	40.0
10.0	0.50	46.0
20.0	0.50	77.0

From these results we observe that for sufficiently long disturbances, the wave amplitude does not differ very much for different longitudinal lengths of the disturbance, while we see significant difference in the time period of wave generation, which is related to the length of the solitary waves generated. Within the validity region of our wave models (i.e., for L long enough), the results show that the

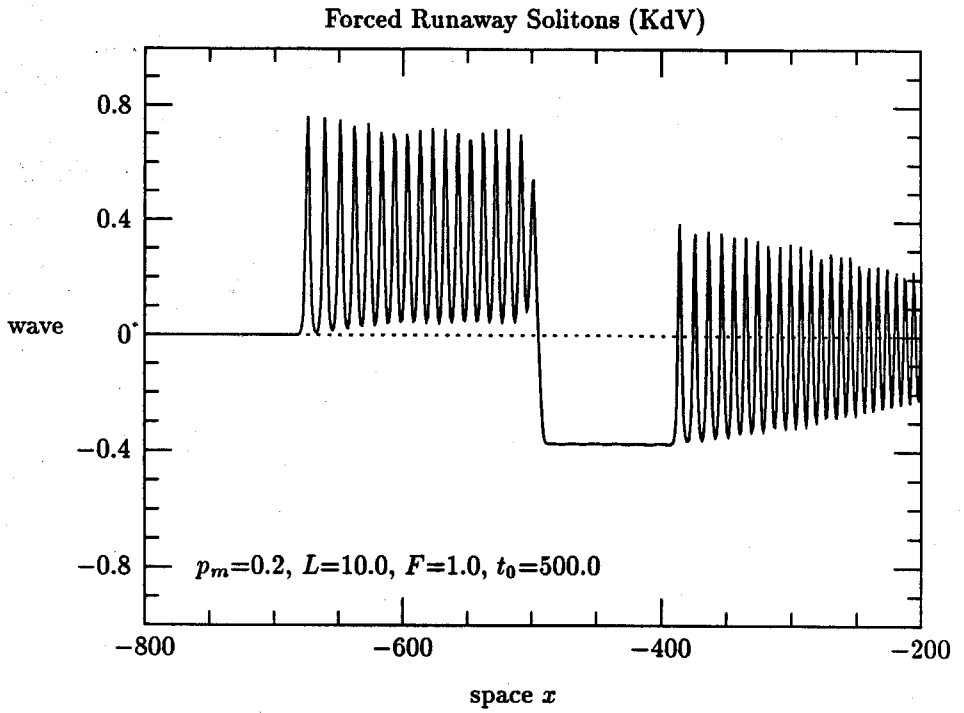

Figure 5.6(a)

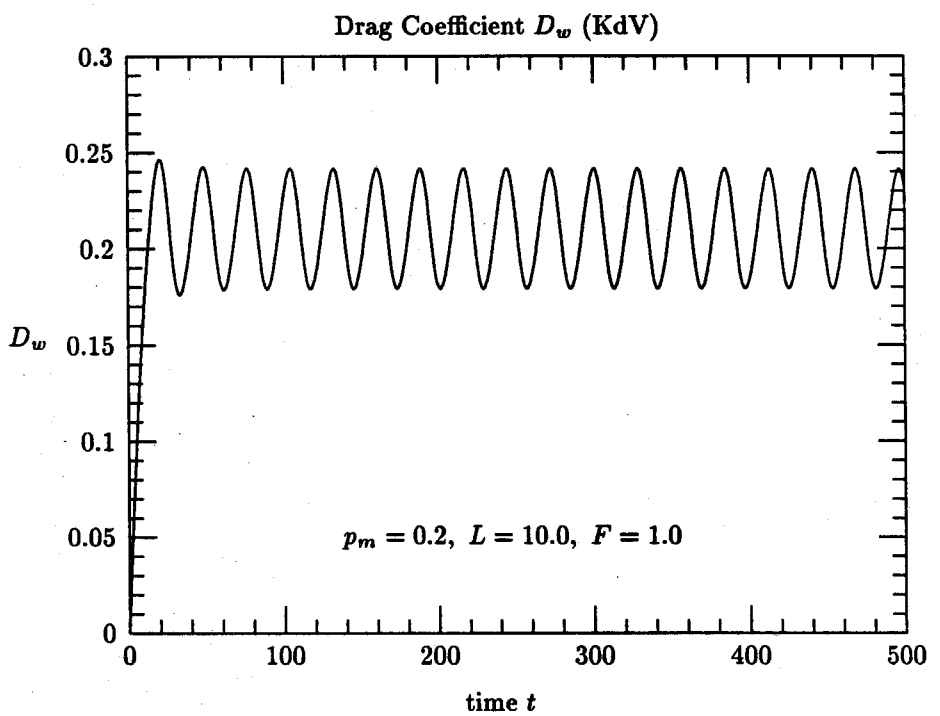

Figure 5.6(b)

Effect of the Longitudinal Length (L) of a Disturbance on Wave Amplitude

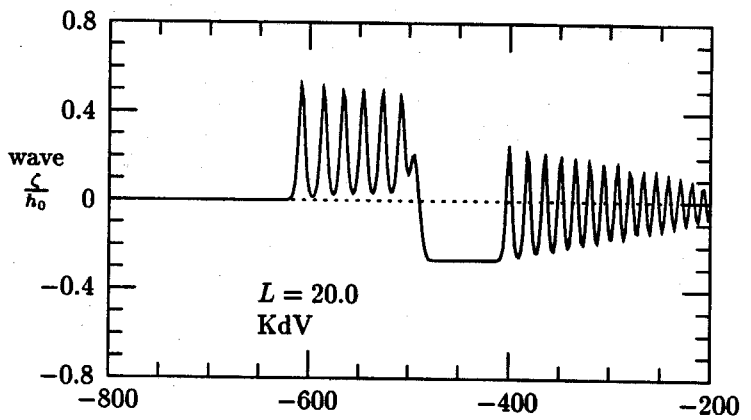

Figure 5.7(a)

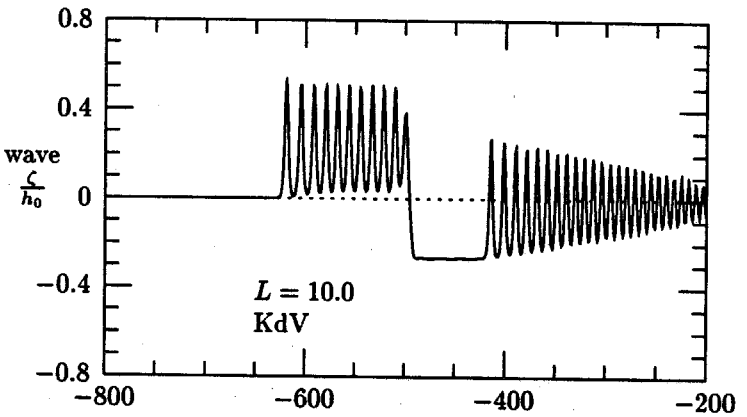

Figure 5.7(b)

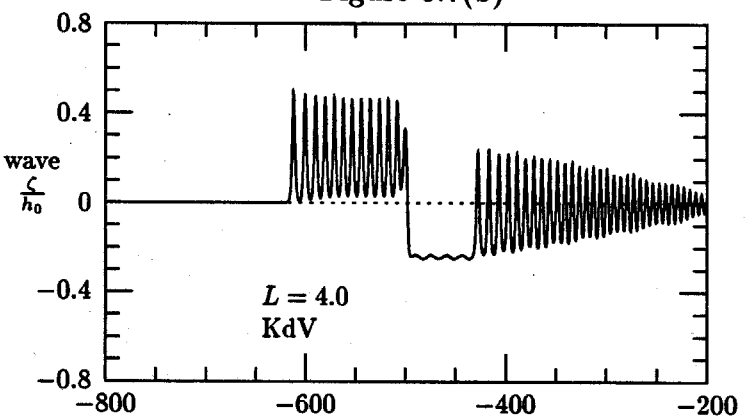

Figure 5.7(c)

Effect of the Longitudinal Length (L) of a Disturbance on Drag Coefficient (D_w)

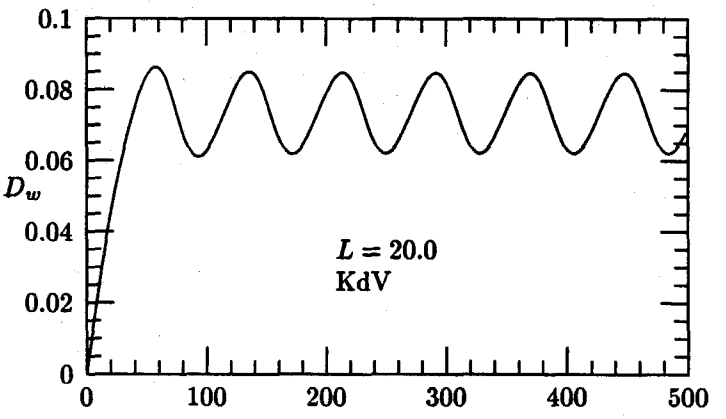

Figure 5.8(a)

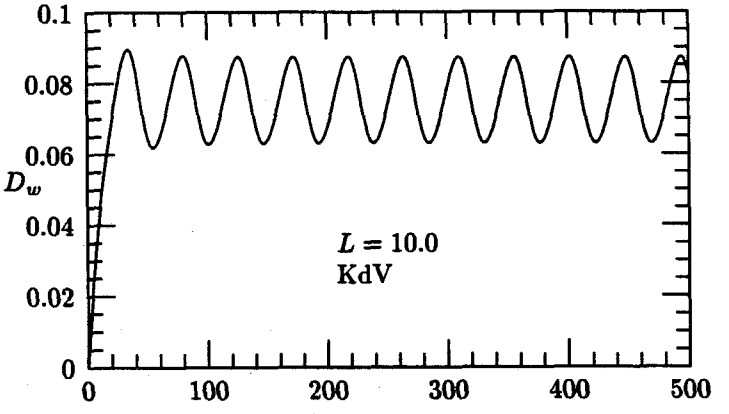

Figure 5.8(b)

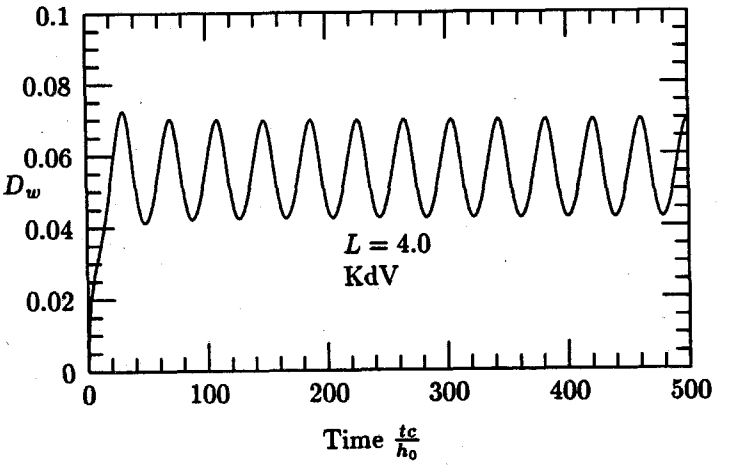

Figure 5.8(c)

longer the disturbance, the longer the wave it generates. When the length of the disturbance is reduced to L=2.0, the wave amplitude of the run-away solitons becomes much smaller and the period of generation gets longer. Later we will see that when the external disturbance becomes too short, the two theoretical wave models will not give consistent predictions for the wave amplitude and the period of generation.

Case IV. The effect of the longitudinal geometric shape of the disturbance.

p_m=0.1, F=1.0, L=10.0 and a triangle-shaped disturbance.

In this case, we use a different forcing function which is described by

$$p(x,t) = \begin{cases} \frac{2p_m}{L}(x+Ft), & 0 \le x+Ft \le \frac{L}{2}; \\ -\frac{2p_m}{L}(x+Ft-L), & \frac{L}{2} < x+Ft \le L; \\ 0, & \text{elsewhere.} \end{cases} \tag{5.8}$$

A plot of the triangle-shaped forcing function given by (5.8) is shown in Figure 5.2. The disturbance has the same length and maximum height as the cosine-forcing in Case I. Table 5.2 gives the comparison of the numerical results between Case I and the present case.

Table 5.2 Comparison between a Cosine and a Trianglar Forcing

	wave amplitude	period of generation
cosine	0.5	46.0
triangular	0.48	52.5

We see that even though in this case the triangular disturbance appears as a slightly weaker forcing (see Figures 5.9(a) and 5.9(b)), the general wave features are quite the same in Case I and Case IV.

5.3.2 Results Based on the gcB Model

As we have observed, the gcB model (5.1)-(5.2) does not indicate that the three forcing functions p_a, B and d are exactly equivalent to each other, as what the cKdV model (5.3) predicts. Thus we are interested in examining the differences

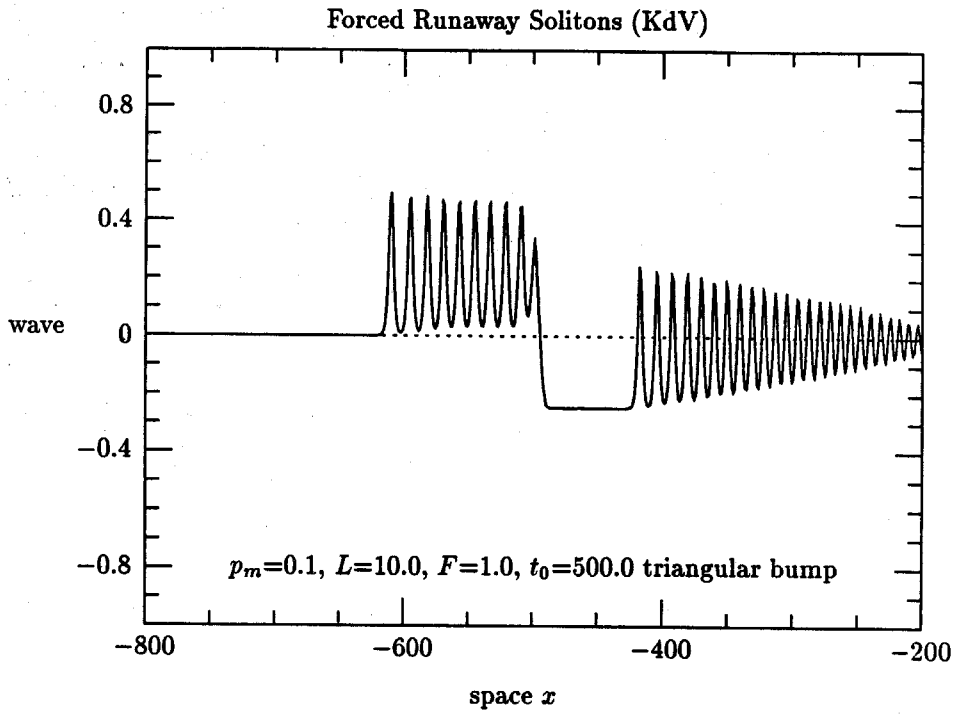

Figure 5.9(a)

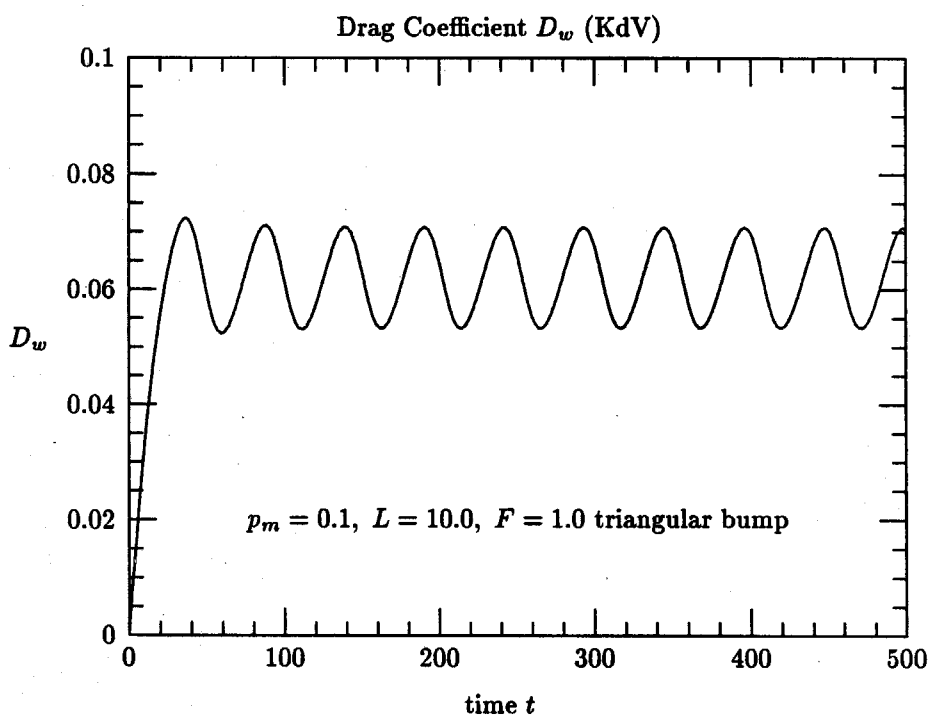

Figure 5.9(b)

among these three forcing functions and the results will be compared with that obtained based on the cKdV model. We will also study the effect of the longitudinal length of the disturbance on the wave generation based on the gcB model, and further discuss the validity criteria of the gcB model.

Case I. Waves Generated by a Free-surface Pressure Distribution.

p_m=0.1, F varying from 0.8 to 1.05 and L varying from 4.0 to 20.0

In this case, we write the gcB model as

$$\zeta_t + [(1+\zeta)u]_x = 0, \tag{5.9}$$

$$u_t + uu_x + \zeta_x = \frac{1}{3}u_{xxt} - p_{ax}, \tag{5.10}$$

where p_a is taken as a cosine-forcing given by (5.6).

The gcB model is computed by applying the predictor-corrector scheme (3.18)-(3.24) discussed in Chapter III. The numerical results for the present case are presented in Figures 5.10(a) to 5.11(b). The comparison of the results between the KdV and the gcB model (Figures 5.11(a) and 5.11(b)) shows that for a free-surface pressure distribution as external forcing functions, the two models give very close predictions for the wave amplitude and the time period of generation. The quantitative data for waves generated by a pressure disturbance moving at the critical speed (F=1.0) and of length L=20.0 can be found in Table 5.3.

Table 5.3 Comparison between the KdV and the gcB Models

models	amplitude	period
KdV	0.50	77.0
gcB	0.53	80.0

Compared to the KdV model, the gcB model is found to predict a longer period of wave generation, while the amplitude of the solitons based on the gcB model is observed slightly greater.

Long Waves Generated by Surface Pressure Distribution (gcB)

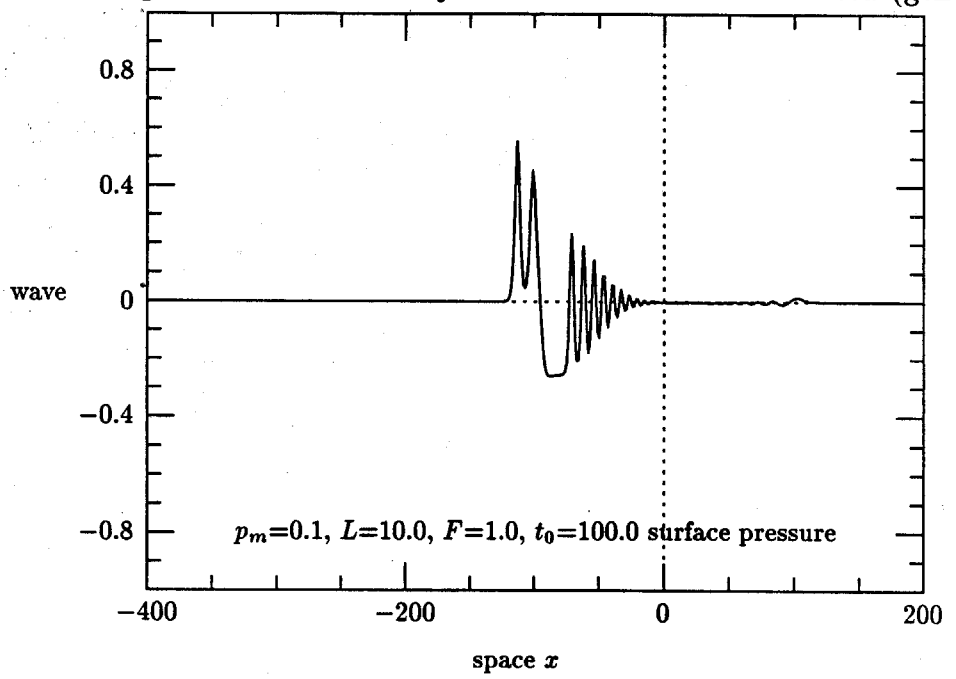

Figure 5.10(a)

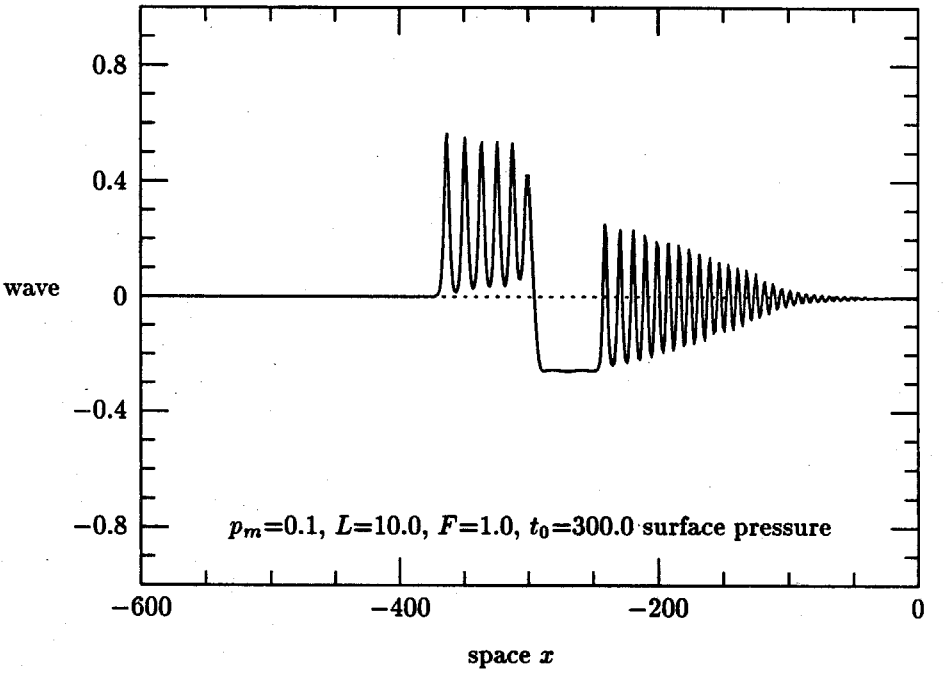

Figure 5.10(b)

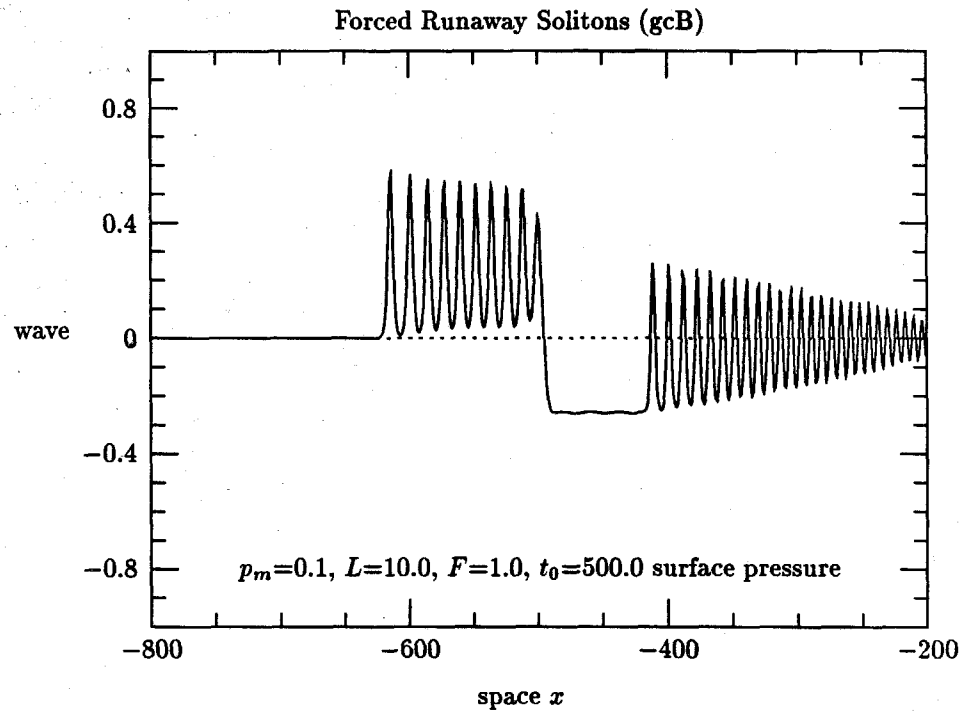

Figure 5.10(c)

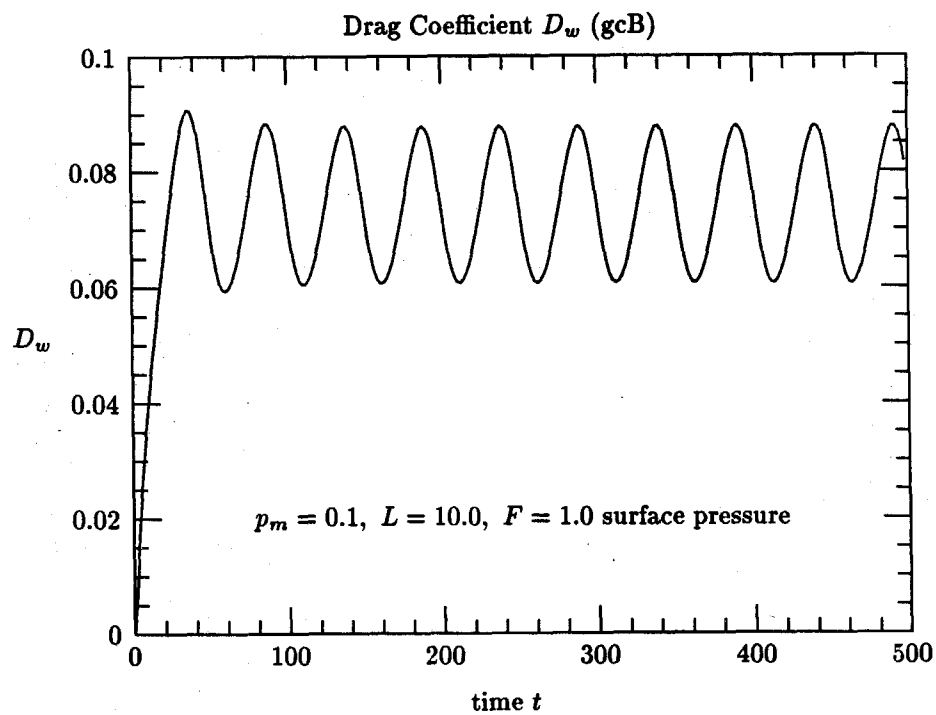

Figure 5.10(d)

Comparison between the gcB Model and the KdV Model

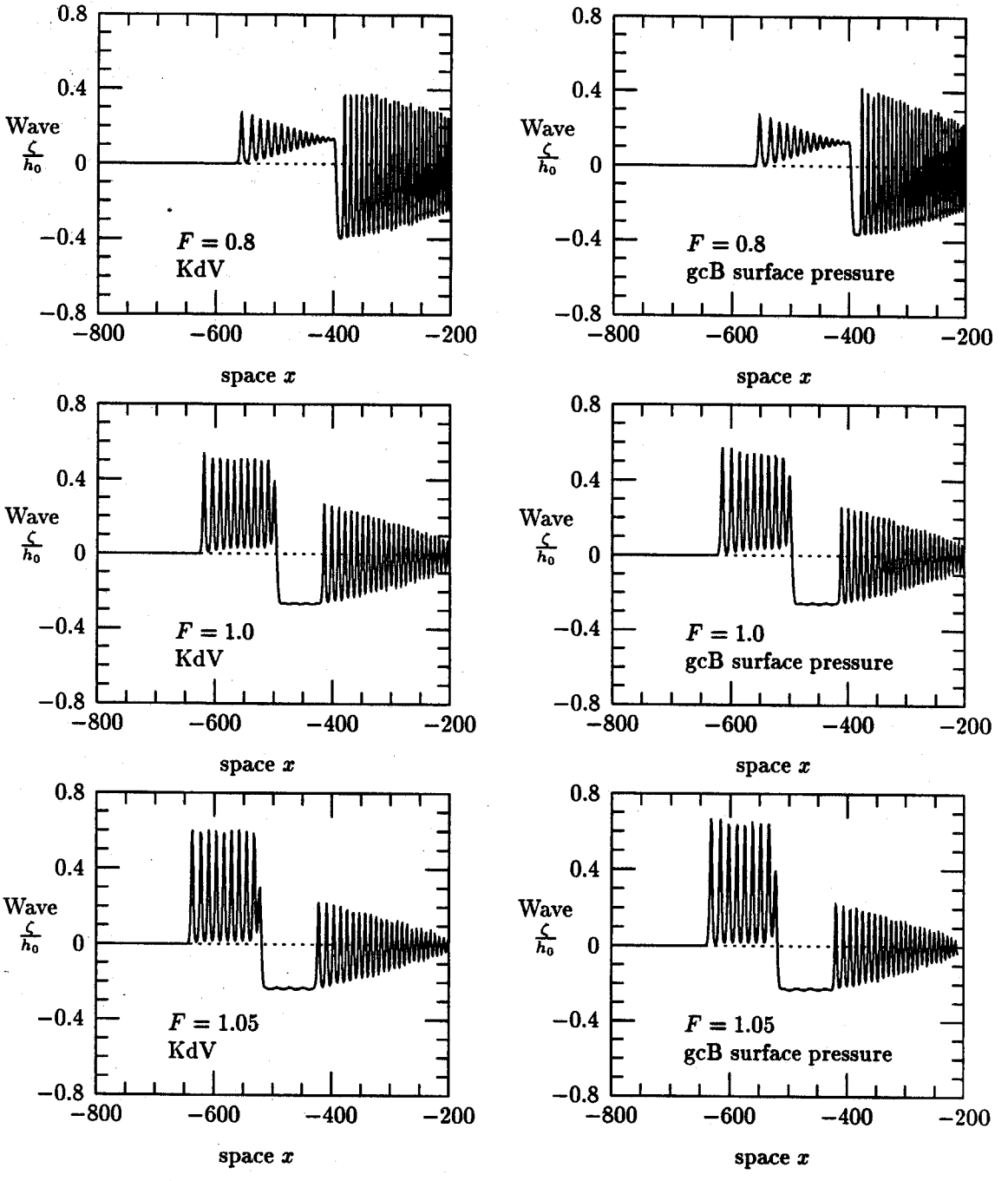

Figure 5.11(a) Wave Amplitude

Comparison between the gcB Model and the KdV Model

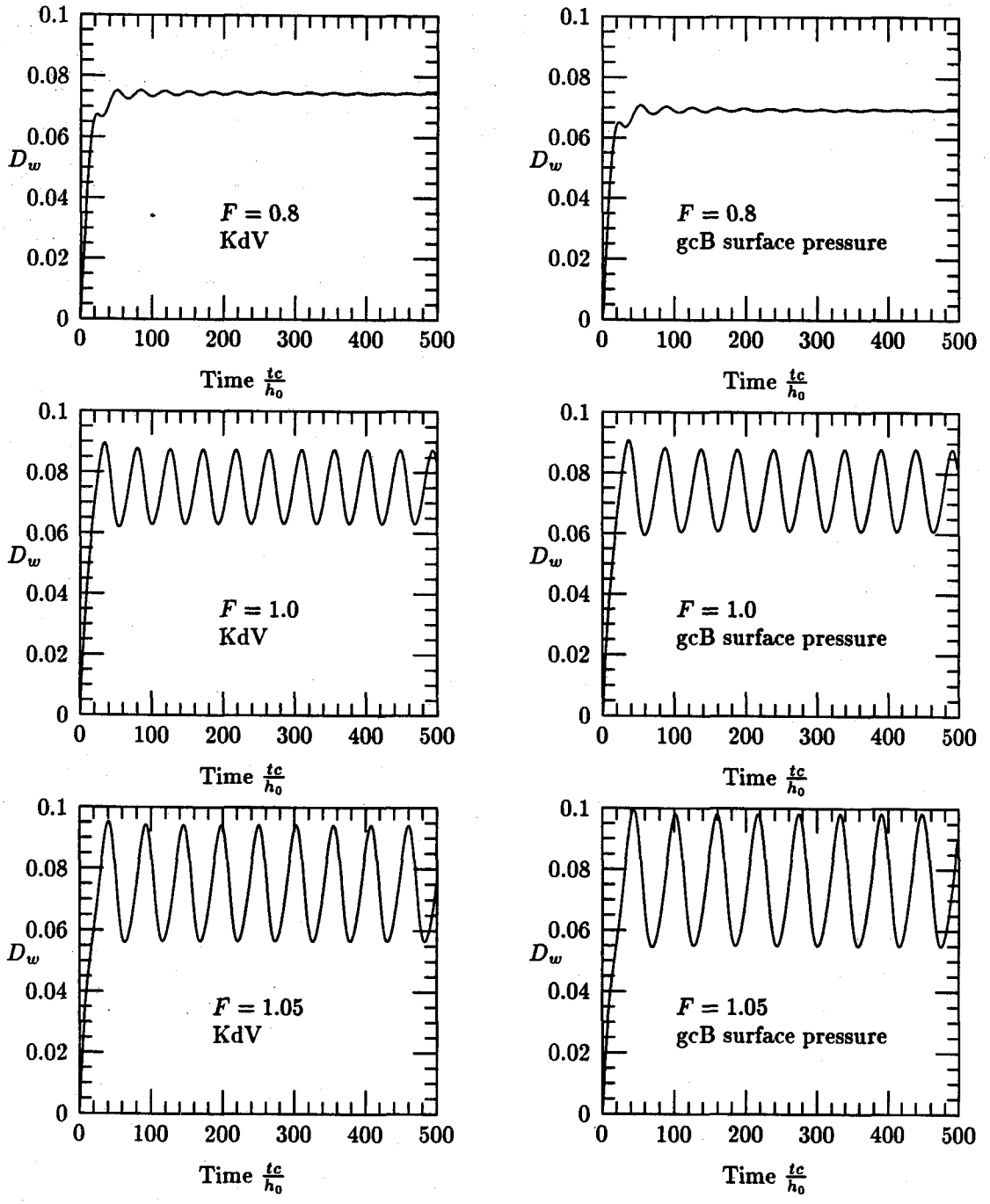

Figure 5.11(b) Drag Coefficient

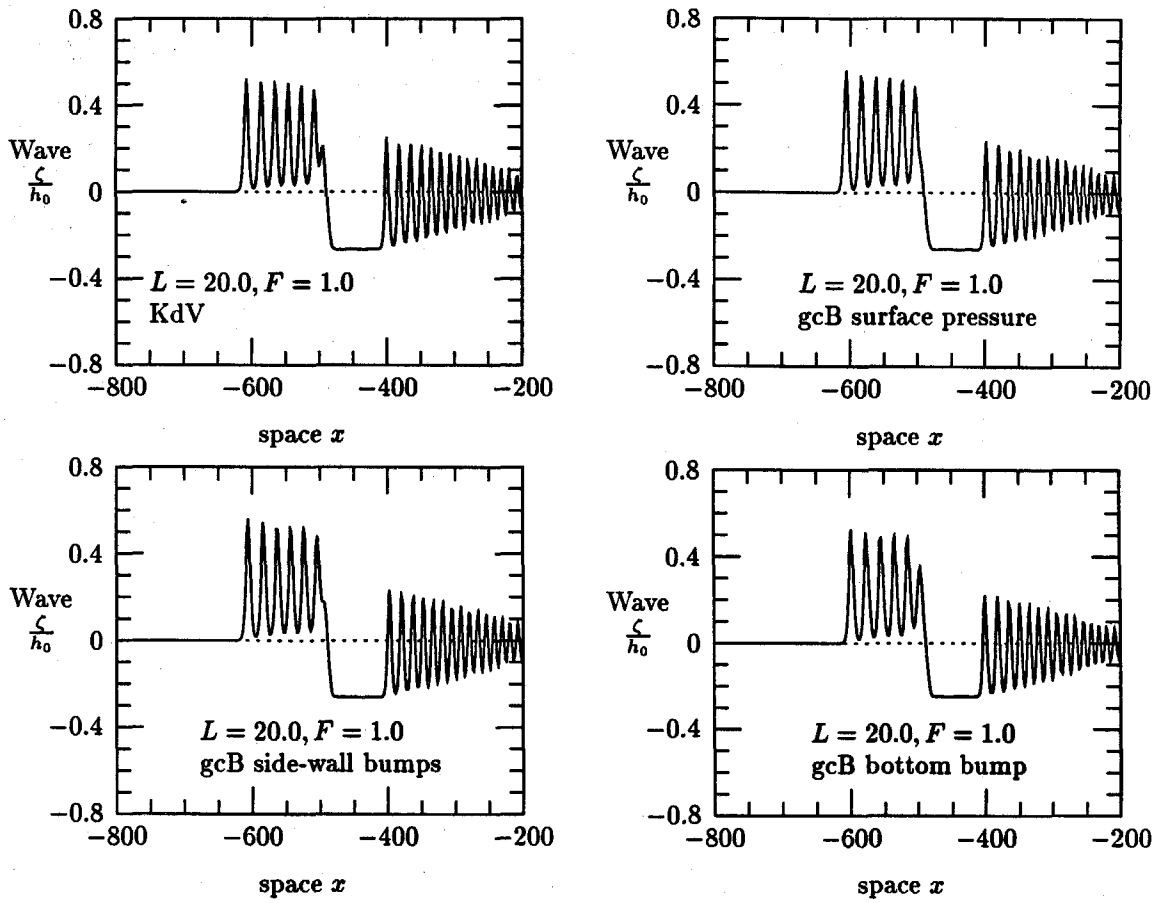

Figure 5.12(a) Wave Amplitude

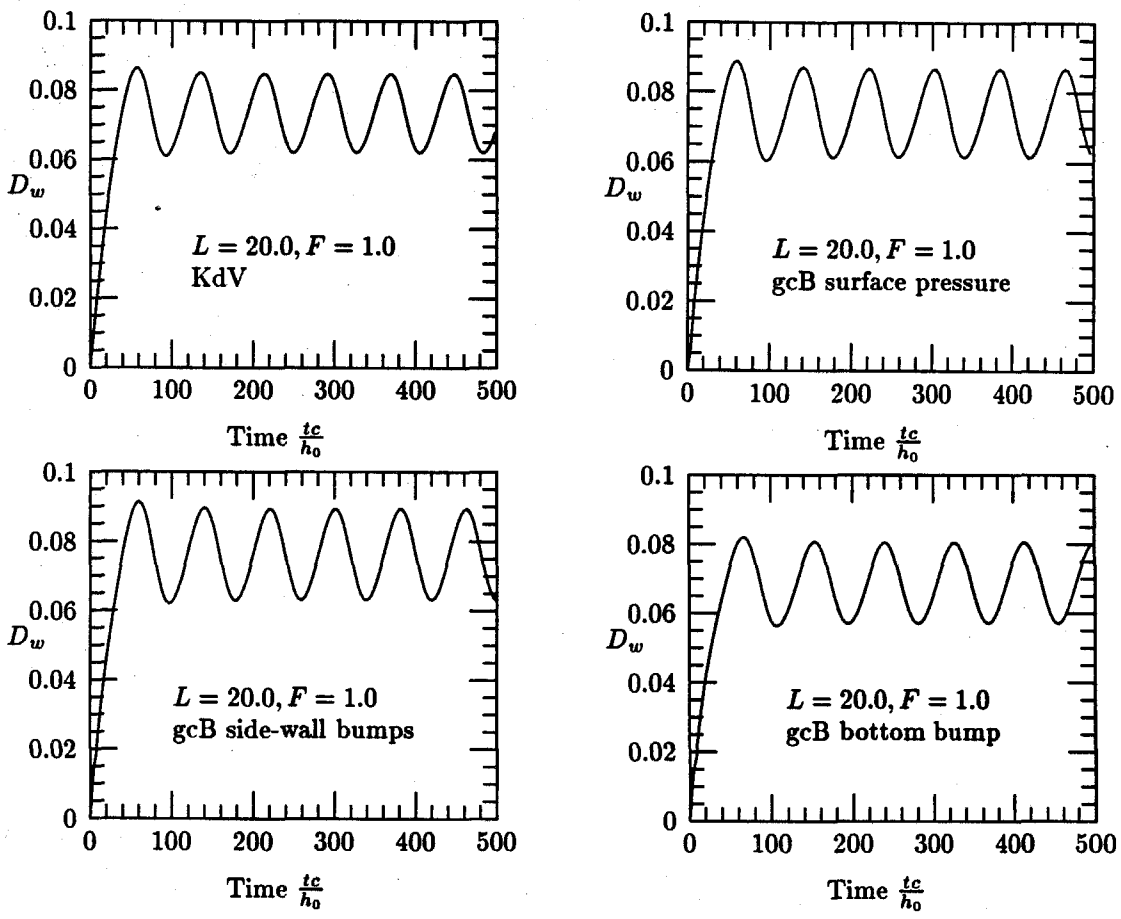

Figure 5.12(b) Drag Coefficient

Figures 5.13(a) and 5.13(b) show the effect of the longitudinal length of the disturbance on the generation of solitary waves. Comparing the results with that based on the KdV model, we can see that for a free-surface pressure disturbance, both models predict the similar change in wave amplitude and period of generation as the length of the disturbance varies.

Case II. Waves Generated by Side-wall Bumps.

B_m=0.1, F=1.0 and L varying from 4.0 to 20.0

With $B(x,t)$ representing a side-wall bump (boundary topography moving along the side-wall), the gcB model for the present case becomes

$$(b\zeta)_t + [b(1+\zeta)u]_x = B_t, \tag{5.11}$$

$$u_t + uu_x + \zeta_x = \frac{1}{3}u_{xxt} - \frac{1}{3}B_{xtt}, \tag{5.12}$$

where the half-width of the channel is $b(x,t) = 1 - B(x,t)$.

The numerical results can be found in Figures 5.14(a)-5.14(b). Table 5.4 shows the comparison between the KdV and the gcB models. The data presented in Table 5.4 are for the case with the parameters F=1.0, B_m=p_m=0.1 and L=20.0.

Table 5.4 Comparison between the KdV and the gcB Models

models	amplitude	period
KdV	0.50	77.0
gcB	0.53	82.0

The results show that when the disturbance is long enough (e.g., L=20.0), the two wave models provide quite consistent results. However, as L decreases, the difference in the results between the two models becomes more appreciable. When L is reduced to L=4.0, the forcing function seems to have been very much weakened based on the gcB model. Similar phenomenon was not found in the

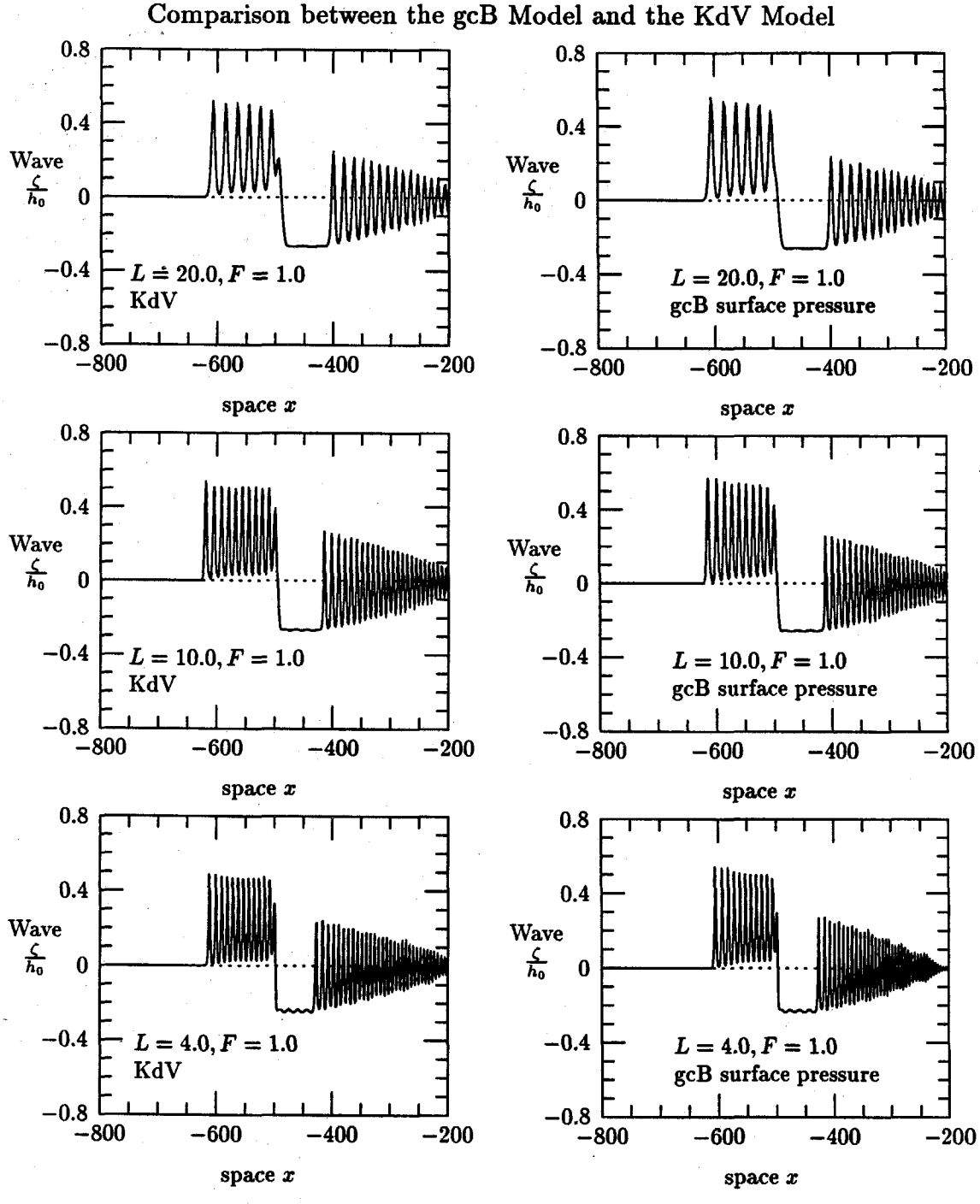

Figure 5.13(a) Wave generation by surface pressure (wave ampl.)

Comparison between the gcB Model and the KdV Model

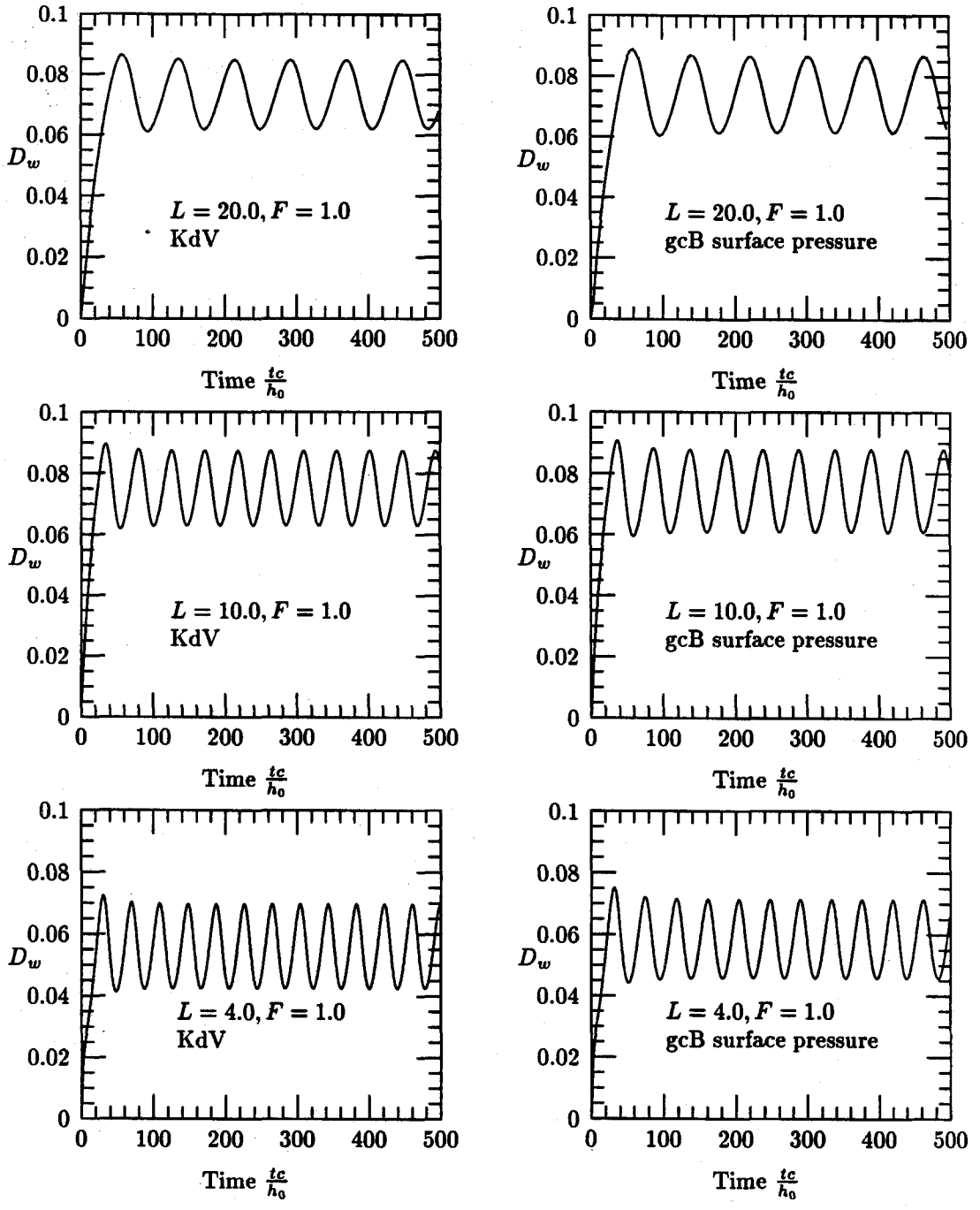

Figure 5.13(b) Wave generation by surface pressure (drag coeff.)

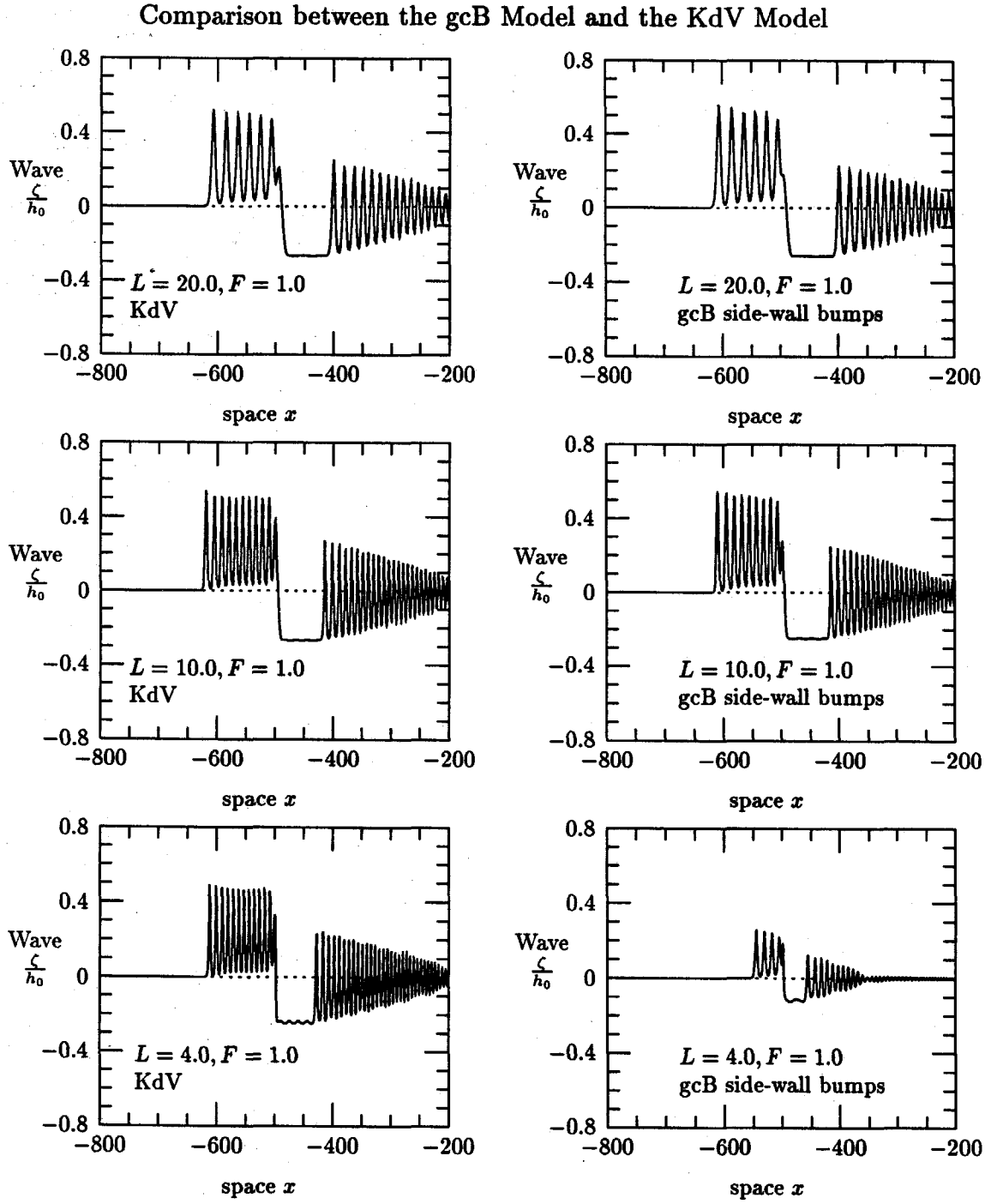

Figure 5.14(a) Wave generation by side-wall bumps (wave ampl.)

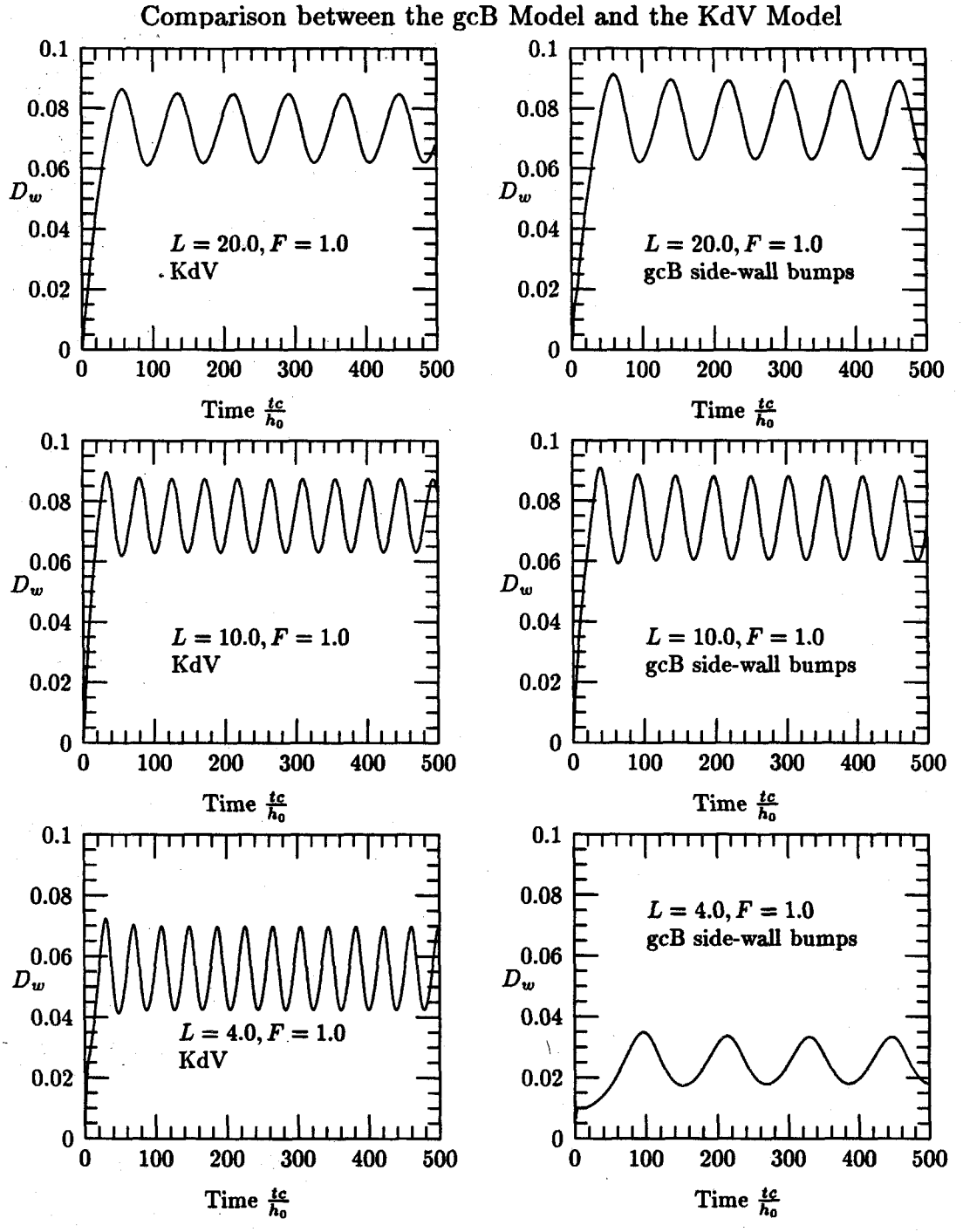

Figure 5.14(b) Wave generation by side-wall bumps (drag coeff.)

previous case with a free-surface pressure disturbance. The reason for this significant difference will be analyzed along with the results from Case III in the following part.

Case III. Waves Generated by a Bottom Bump.

d_m=0.1, F=1.0 and L varying from 4.0 to 20.0

The gcB model for this case appears as

$$\zeta_t + [(1 - d + \zeta)u]_x = d_t, \tag{5.13}$$

$$u_t + uu_x + \zeta_x = \frac{1}{3}u_{xxt} - \frac{1}{2}d_{xtt}, \tag{5.14}$$

where $d(x,t)$ represents a topography moving along the bottom of the channel.

The numerical results are shown in Figures 5.15(a) and 5.15(b). Again we observe that when L is reduced to L=4.0, the forcing is much weakened and the gcB model gives totally different characteristics in the time record for the drag coefficient D_w. Examining the gcB equations, we find that the reason for the discrepancies between the two models lies in the higher order derivative terms B_{xtt} and d_{xtt}. These terms are highly sensitive to the longitudinal geometric configuration of the disturbance. For the forcing functions given by (5.6), the third derivative terms are of the same form as the first derivative terms B_t and d_t which appear in the continuity equation and are considered as the dominant forcing terms. The terms B_{xtt} and d_{xtt} have a negative sign with respect to the terms B_t and d_t for cosine functions. So these third derivative terms introduce the effects of a negative forcing. As the disturbance becomes shorter, the magnitude of B_{xtt} and d_{xtt} becomes larger. In the present case for a bottom bump of length L=4.0, the absolute ratio of $0.5d_{xtt}/d_t$ is 1.23, thus the negative forcing is dominant. This violates the basic assumption in our theoretical modeling that the B_{xtt} and d_{xtt}

Comparison between the gcB Model and the KdV Model

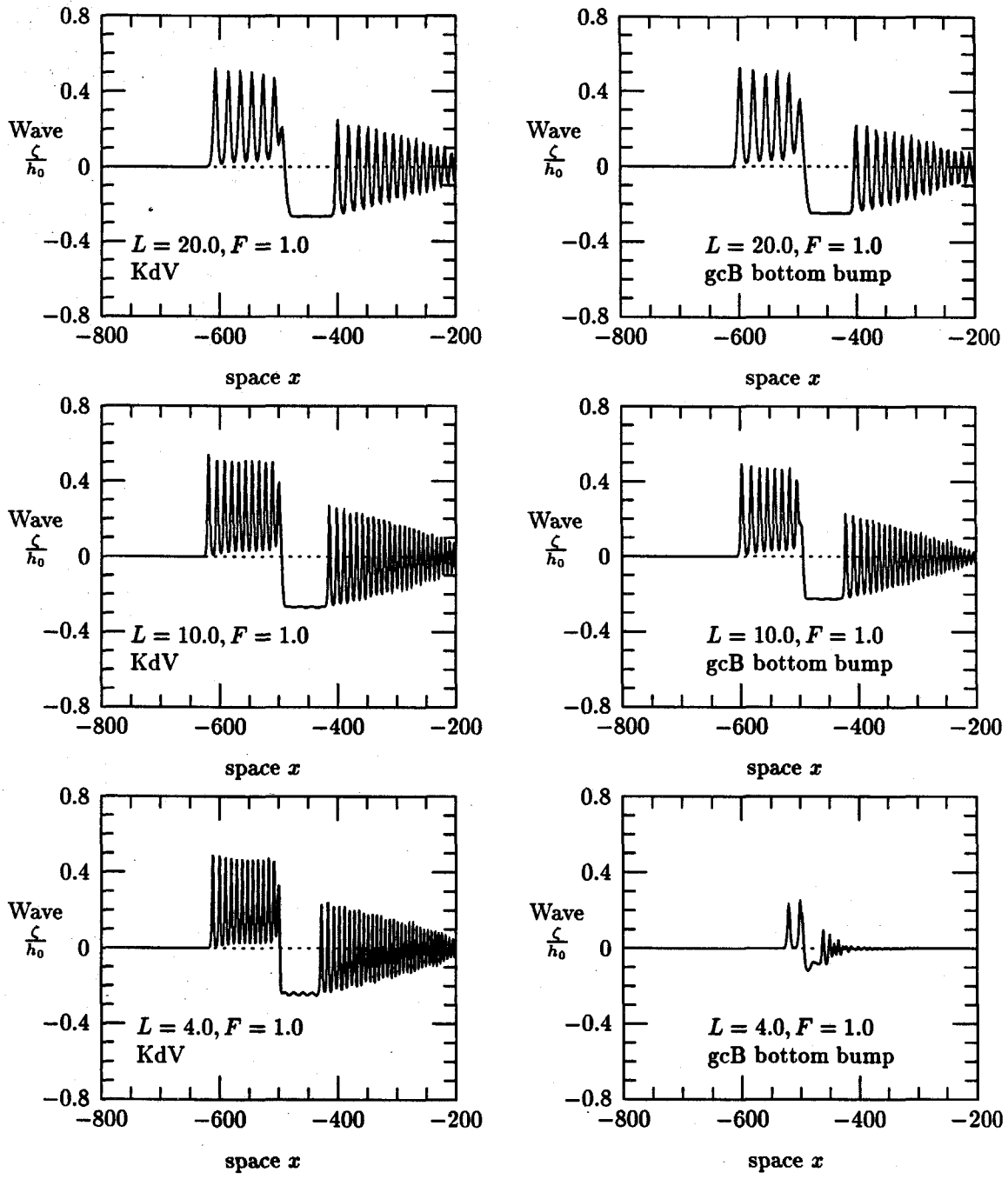

Figure 5.15(a) Wave generation by a bottom bump (wave ampl.)

Comparison between the gcB Model and the KdV Model

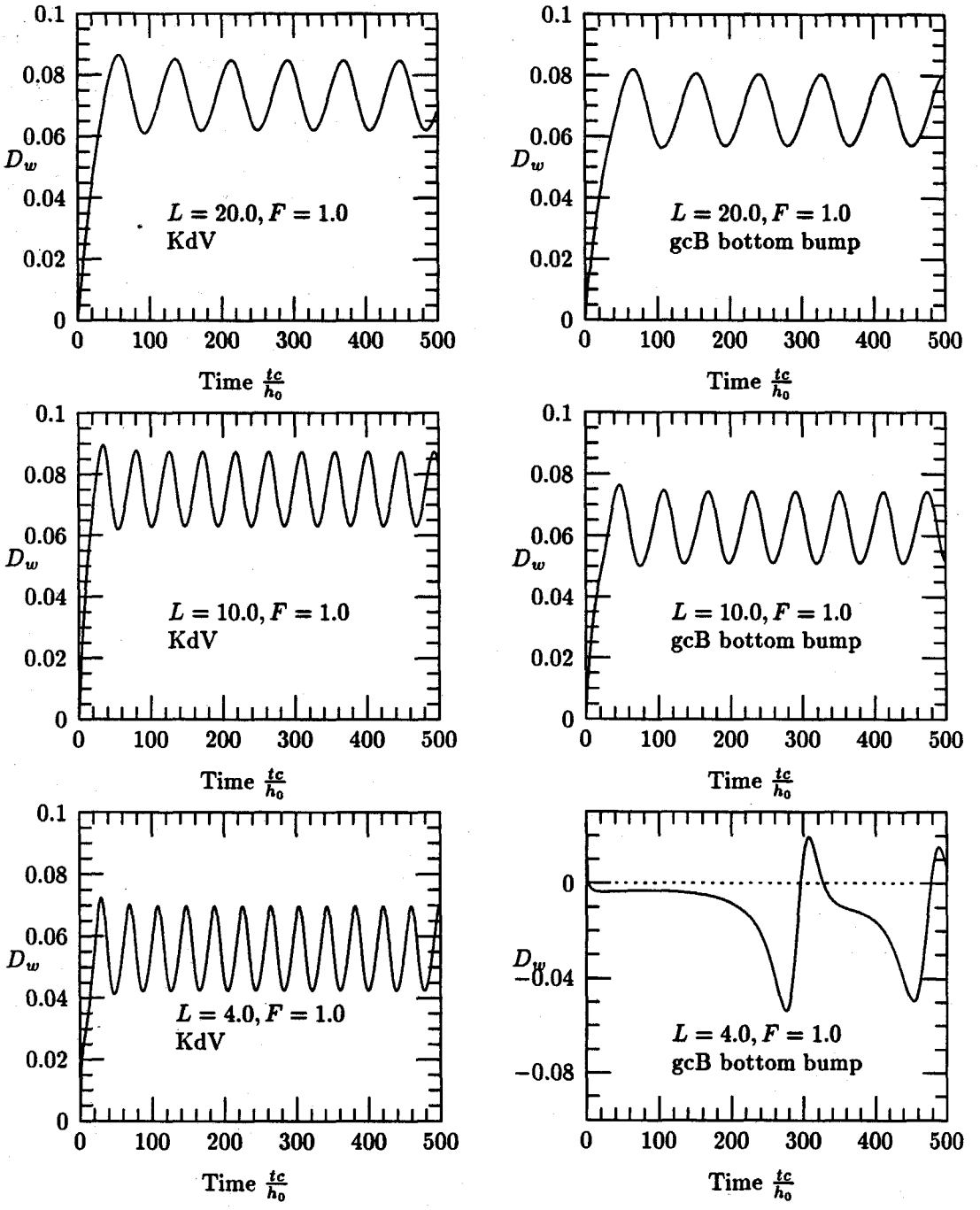

Figure 5.15(b) Wave generation by a bottom bump (drag coeff.)

terms are small. In fact, when we derived the cKdV model in Chapter II, these terms were neglected resulting from our assumption that they are of higher order for long wave models. Thus we may conclude that in order to make the two models to give consistent predictions for the generation of long waves, the models should be applied to disturbances whose length is comparable to the wavelength of the long waves being generated. As for the applications of the two wave models, their practical validity criteria can be determined from the results of laboratory experiments.

5.3.3 fKdV vs. RfKdV

As discussed in section 2.10, the regularized KdV equation (RKdV) was first introduced for consideration of numerical instabilities. If we substitute $\zeta = F(k)e^{i(\omega t - kx)}$ into the linearized KdV equations

$$\zeta_t - \zeta_x - \frac{1}{6}\zeta_{xxx} = 0 \tag{5.15}$$

and

$$\zeta_t - \zeta_x - \frac{1}{6}\zeta_{xxt} = 0, \tag{5.16}$$

we obtain the following dispersion relations

$$\omega = -k - \frac{1}{6}k^3 \tag{5.17}$$

given by the KdV equation (5.15) and

$$\omega = \frac{-k}{1 + \frac{1}{6}k^2} \tag{5.18}$$

by the regularized KdV equation (5.16).

For long waves, $k \ll 1$, so theoretically (5.17) and (5.18) are equivalent. In computational studies, the numerical calculations usually introduce errors of short

wave components, i.e., errors with $k \gg 1$. In that case, relation (5.18) will damp the errors out while relation (5.17) cannot. Relation (5.17) shows that numerical errors for equation (5.16) will travel very fast in the domain of calculation. However, this does not imply that the amplitude of the numerical errors will necessarily grow. Thus, by choosing the proper schemes, both the KdV equation and the regularized KdV equation can be well solved numerically.

One advantage of the regularized KdV equation over the KdV equation may lie in the imposition of boundary conditions in numerical computations. For cases with a physical domain of finite length, as the KdV equation involves a higher order derivative term, it usually needs special treatments at the boundary points. In the present studies, our domains are always from $-\infty$ to $+\infty$ with the unperturbed boundary conditions at the two ends. We do not encounter any difficulties in imposing the proper boundary conditions.

For waves generated by left-going disturbances, the forced KdV equation is written as

$$\zeta_t - (1 + \frac{3}{2}\zeta)\zeta_x - \frac{1}{6}\zeta_{xxx} = \frac{1}{2}p_x \tag{5.19}$$

and the regularized fKdV equation as

$$\zeta_t - (1 + \frac{3}{2}\zeta)\zeta_x - \frac{1}{6}\zeta_{xxt} = \frac{1}{2}p_x. \tag{5.20}$$

The numerical results based on these two equations are shown in Figures 5.16(a) and 5.16(b). In these simulations the waves are generated by a cosine-forcing function with $L = 10.0$ and p_m=0.1. The results based on the two equations are compared for Froude number F ranging from 0.8 to 1.05. We observe that the two equations give very close results for F near 1. In the present case, the RKdV model predicts a longer period of soliton generation than the KdV model for F ranging from 0.8 to 1.05. When L is reduced to 2.0, our numerical results (which

are not plotted in this thesis) show that the RKdV model predicts a longer period for F ranging from 0.95 to 1.05, while for $F < 0.95$, the RKdV model gives a shorter period, compared with the KdV model.

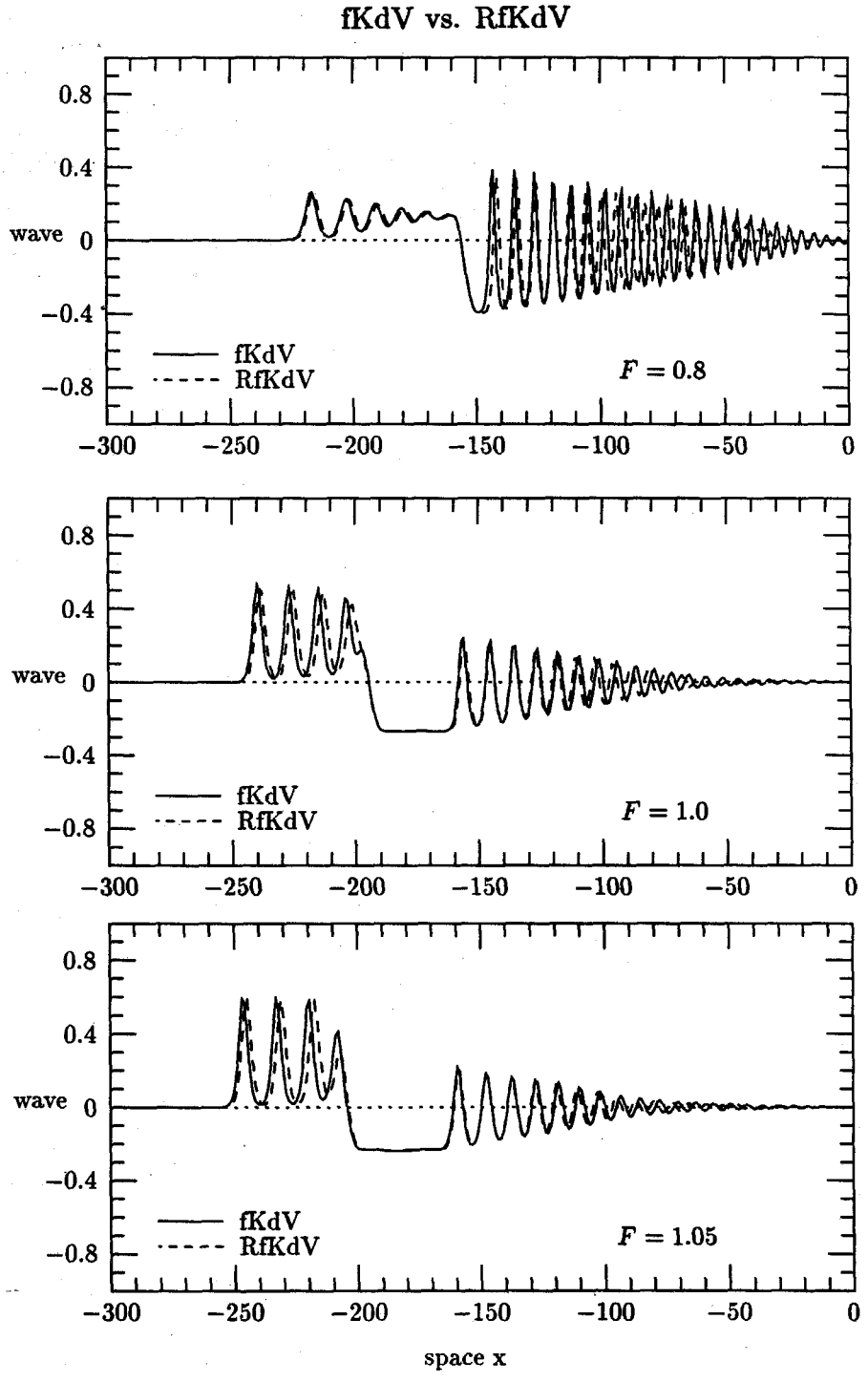

Figure 5.16(a) Wave amplitude

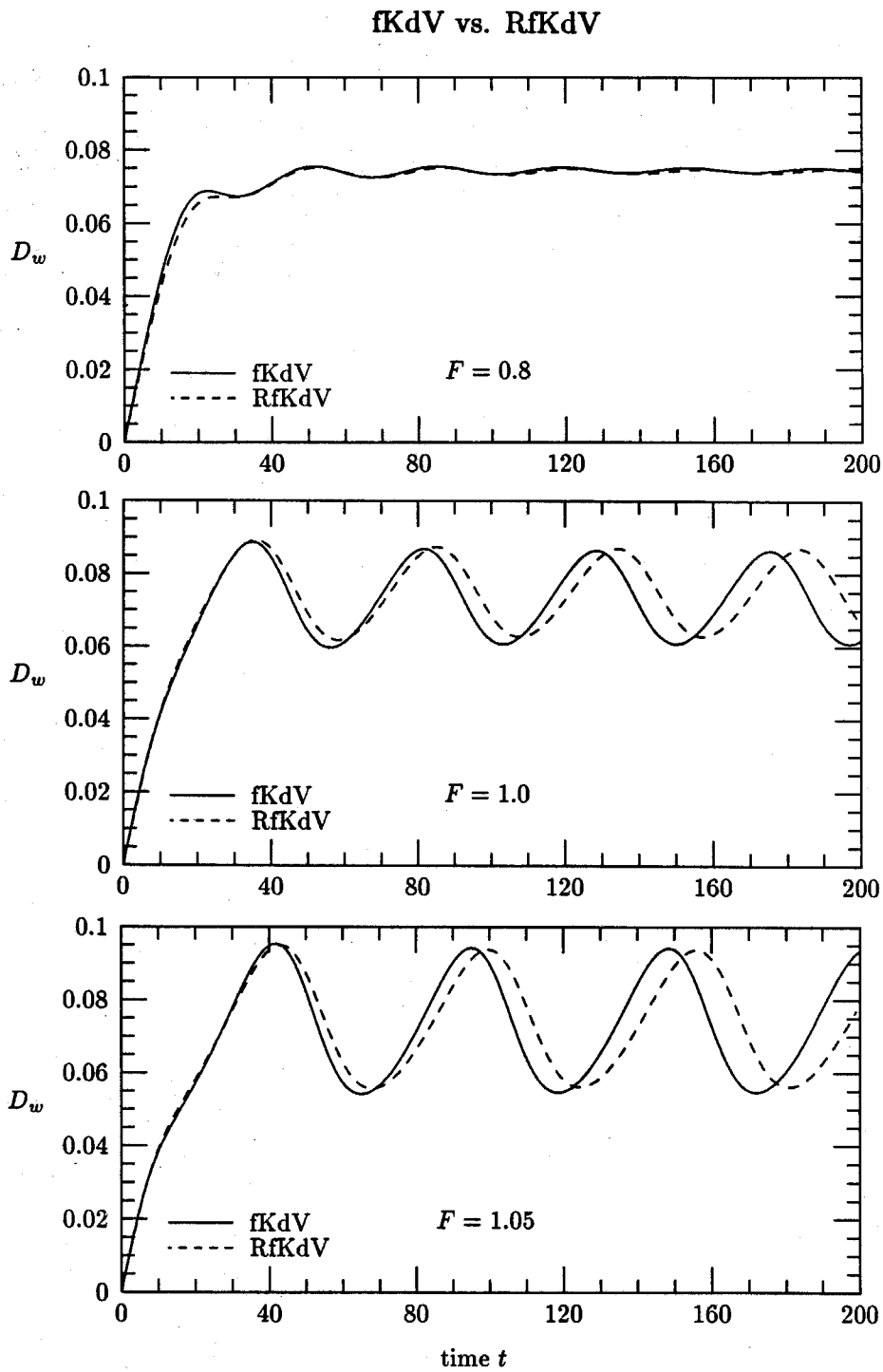

Figure 5.16(b) Drag coefficient

5.4 Experimental Results

Our experiments were designed to explore the criteria of the proposed theoretical models, especially the forced channel KdV model regarding the blockage-ratio concept. One of the important conclusions is that the net effects on long wave generation of a moving obstacle, fully or partially submerged in water, are represented by the blockage-ratio function $A_d(x,t)$ involving only the fraction of the cross-sectional area that moves with respect to the water in the channel. The specific shape of the disturbance and its particular position in the water have no significant effects in the upstream region where run-away solitons propagate, provided the disturbance is of higher order and the channel is not too wide.

We performed the experiments in a rectangular water tank whose side-walls and the bottom bed were constructed of plate glass. The tank is approximately 7.5 m long, 0.75 m wide and 0.6 m deep. Two sets of experiments on long waves generated by submerged moving disturbances were carried out, one with a moving bottom bump as the disturbance and the other with two side-wall bumps. The bumps are made of aluminum and have a circular-arc top surface. The cross sections of all three bumps have the same size. The bumps were rigidly fastened to a carriage which ran along two parallel tracks mounted on top of the side-walls. Figures 5.17(a) and 5.17(b) show a sketch of the experimental set up. In case (I) (Figure 5.17(a)), the bottom bump spanned the whole tank width while in case (II) (Figure 5.17(b)), we carried out the experiments with the side-wall bumps in a narrower subtank (10 cm wide) constructed by setting up a vertical Plexiglas plate in the original tank. In these experiments, the dimensionless speed of the moving bumps varied over the Froude number ($F = U\sqrt{gh_0}$) from F=0.79 to F=1.07 and the water depth was kept at h_0=5.0 cm. The cross section of the bumps is 4.9 cm

A Sketch of the Experimental Set Up

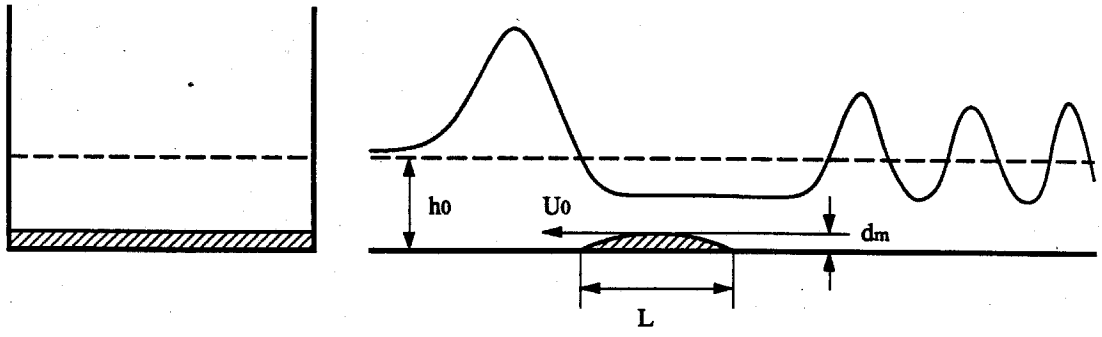

Figure 5.17(a) The end view (the left side); the side view (the right side).

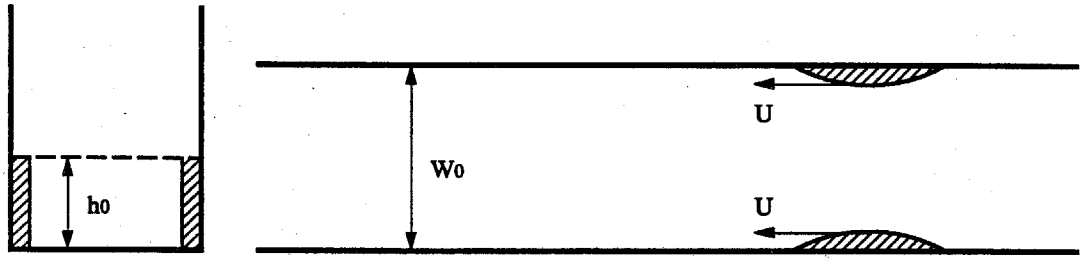

Figure 5.17(b) The end view (the left side); the top view (the right side).

long and has a maximum height of 0.66 cm. (In this case, the nondimensional length of the bumps is L=0.98.) We arranged for the geometric parameters to remain as stated above such that in the two cases, while the disturbances were positioned at different locations, their cross-sectional blockage ratios were nevertheless the same. The maximum blockage ratio A_d in both cases was 0.132.

Our laboratory observations showed that when a submerged disturbance moves in a shallow water tank within the specified transcritical speed range, a series of solitons were generated in front of the disturbance periodically and they advanced with a greater speed to outrun the steadily moving disturbance. Behind the disturbance a train of weakly nonlinear and weakly dispersive waves developed. We measured the wave elevation and the time period of generation of upstream runaway solitons in both cases and compared the results.

Wave elevations were measured by a parallel-wire-resistance-type wave gauge. The wave gauge was mounted on the carriage and thus moved with the disturbance. The position of the moving gauge was about 12 cm upstream from the leading edge of the bumps and at the centerline of the tank in each case. The wave gauge was made of stainless steel wires, 0.16 cm in diameter and separated 1.0 cm apart. The output signals from the wave gauge were measured by an Analog-Digital (A/D) data acquisition system. The digitized data were then processed on a PDP 11/23 computer. The wave gauge was calibrated before each run of the measurement. The measurement errors were $\pm$0.1 cm in measuring water depth and width, 3% in the speed of the carriage, and the relative error for the wave elevation can be estimated as about 4%.

The experimental results are presented in Figure 5.18. Even though in case (II) the disturbance is three-dimensional and we observed three-dimensional wave

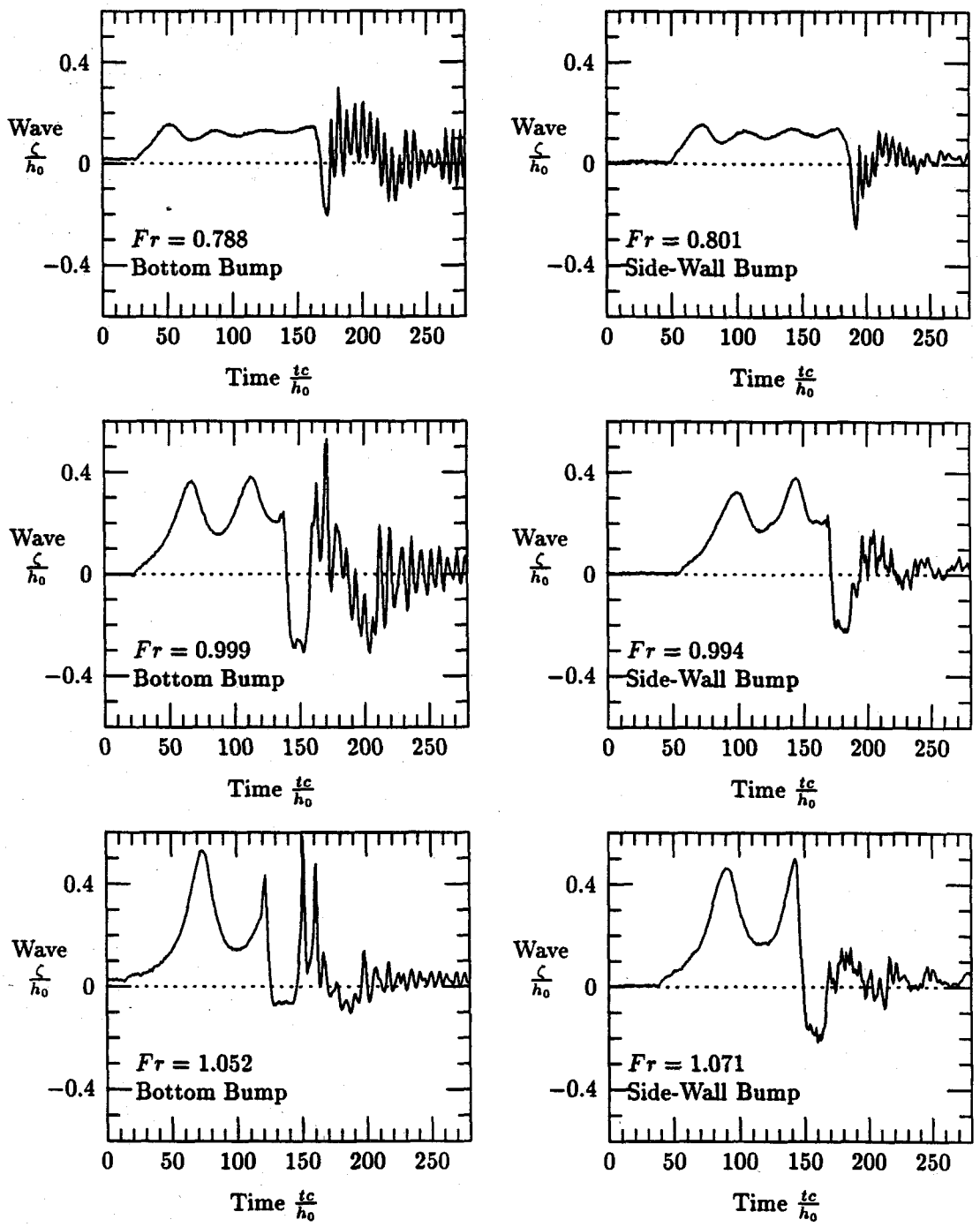

Figure 5.18 The time records of wave elevation.

patterns in the trailing region, the solitary waves generated in front of the disturbance are still two-dimensional, just as what we observed in case (I) where the forcing is two-dimensional. Quantitatively (see Table 5.5), the results show that when the blockage ratio of the cross-sectional area by a moving disturbance is made equal, it will generate forward advancing long waves with the same wave amplitude and the same period of generation, regardless of its specific shape and its particular position in the water. Also, the strong two-dimensional features in the dominant leading wave region confirm the validity of our section-mean approach in the theoretical modeling. A comparison between the experimental and the numerical results for the critical case (F=0.999) is shown in Figure 5.19. The numerical simulations are based on our forced KdV equation for a uniform rectangular channel. In the figure, the solid line represents the experimental data and the dot-dashed line gives the numerical result by using the actual bump height 0.66 cm. These two curves show appreciable difference. This difference is most possibly caused by our neglecting of the viscous effect and the bottom unevenness in the wave tank for the preliminary numerical simulations. The presence of a viscous boundary layer will increase the effective height of the bump and according to the boundary layer theory for a flat plate in steady laminar flow, the increment of the bump height can be estimated to be δ_1=0.06 cm (for this case $R_e = 2.0 \times 10^4$). The unevenness of the water tank is about $\pm$0.1 cm which is not negligible compared with the bump height, 0.66 cm. Considering these effects, we carried out a revised numerical simulation with the corrected bump height 0.8 cm instead of the actual height 0.66 cm (see Lee et al.[15]) and the result is shown by the dashed line in Figure 5.19. This gives a better agreement with the experimental result and the relative differences are 14% in wave amplitude and 10% in time period of generation. The experimentally observed wave field in the trailing region is very

Comparison between the Experimental and Numerical (KdV) Results

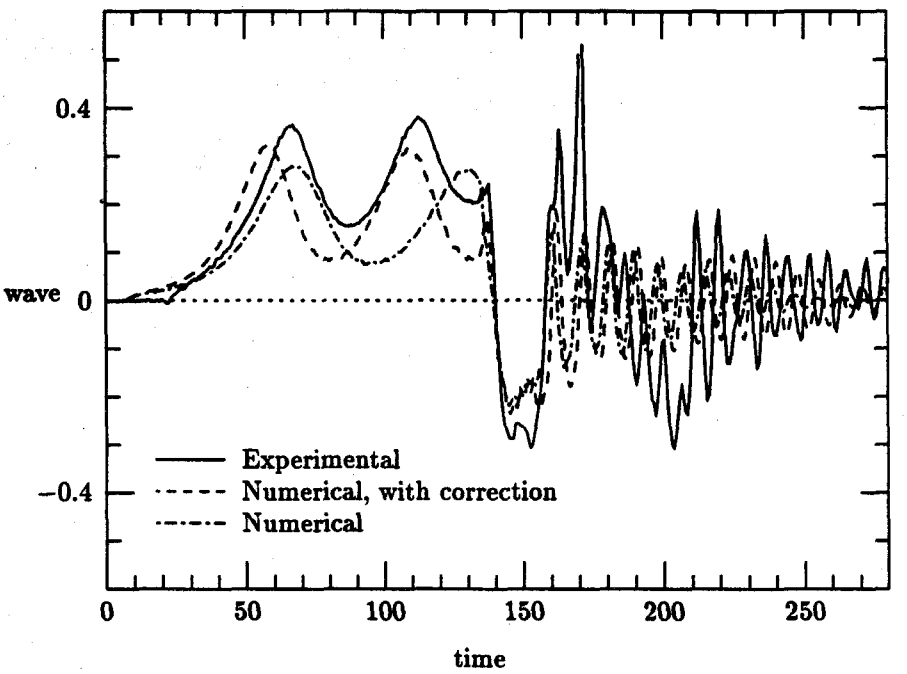

Figure 5.19 Time records of the wave elevation

complicated. Even with the two-dimensional bump, one may observe certain unsteady three-dimensional wave patterns due to the channel side-wall effects and the effects of the bump supporting struts.

In the upstream region where long waves are generated and propagate, aside from the experimental error, the laboratory results show good agreement with the theoretical predictions from our wave models obtained and presented in Chapter II. This also establishes the contention regarding the blockage-ratio concept introduced by Mei[17] in the analysis of the problem of soliton radiation due to a ship model moving at transcritical speeds within a towing tank.

Table 5.5 Comparison of the Wave Amplitude (a_0) and the Period of Generation (T_0) between the Two Experimental Cases

	F	a_0	T_0
	0.788	0.144	34.5
Case(I)	0.999	0.353	45.5
	1.052	0.481	54.1
	—	—	—
	0.801	0.140	37.1
Case(II)	0.994	0.374	45.5
	1.071	0.528	56.0

5.5 Discussions

Our numerical results show that a steadily moving pressure distribution on the free surface or a submerged moving topography with a near-critical speed can generate a series of run-away solitons advancing upstream. The longer the disturbance in the longitudinal direction, the longer the waves it generates. Since both the gcB and the cKdV models are derived for long waves, these two wave

models will give consistent predictions for waves generated by moving disturbances that are sufficiently long. The numerical results indicate that for a cosine-bump with a maximum magnitude of p_m=0.1, L=10.0 is long enough. As the disturbance gets shorter, the two models start to show increasingly noticeable differences. In our experimental measurements, the length of the bumps is of the same order as the water depth (L=0.98). In this case, the numerical simulations based on the KdV model show reasonablly good agreements with the experimental results, while the gcB model fails to give a correct prediction without further modifications. This implies that practically the cKdV model somehow has a broader validity region than the gcB model in this specific forced case discussed in the present chapter. The terms that make the differences between the two models are B_{xtt} and d_{xtt} terms in the momentum equation of the gcB model. These terms are highly sensitive to the detailed geometric configurations of the forcing functions. However, the experimental results show that the generation of long waves is really due to an integrated effect of the moving disturbance and the detailed higher order surfacial curvature of the disturbance should not dominate in this phenomenon. Thus the B_{xtt} and d_{xtt} terms seem to be artificial in this problem. This point needs to be further studied.

VI. SUMMARY AND CONCLUSIONS

Two theoretical models, i.e., the generalized channel Boussinesq two-equation model (gcB) and the channel Kortweg-de Vries one-equation model (cKdV), are derived to describe the generation and propagation of nonlinear long water waves in a variable channel of arbitrary shape. The channel width and depth may vary both in space and in time. The fluid is assumed to be inviscid and the flow incompressible. The wave phenomena that we have investigated include both the evolution of free traveling waves in a variable channel with modulated amplitude and speed, and also the forced generation of nonlinear long waves by external moving disturbances. The effect of a specific geometric configuration of the cross section of the channel is also examined.

To derive the theoretical long-wave models, we start from the Euler equations, with nonlinear boundary conditions at the free surface. Since for long waves in channels, the dominant wave features manifest primarily in the longitudinal direction, we integrate the Euler system over the cross-sectional area of the channel to get a set of section-mean equations. Based on these section-mean equations, we proceed to derive the gcB model by using perturbation expansions for quasi-one-dimensional long waves in shallow water. This two-equation gcB model is further reduced to a one-equation model, i.e., the cKdV model, for the unidirectional motion near resonance. These equations are written in terms of section-mean quantities and describe the dominant wave motions in the longitudinal direction. The detailed three-dimensional wave features in the cross-flow plane can be recovered by substituting the section-mean results obtained from these two models in the perturbation expansions and then applying the Bernoulli equation at the free surface.

Three specific configurations of the channel cross section, namely, rectangular, triangular and semi-circular cross sections, are studied. The theoretical results show that the difference in shape of the cross section only affects the dispersive terms in the equations, provided the mean hydraulic depth remains the same. Quantitatively, we find that the smaller the slope of the channel walls versus the horizontal, the greater the dispersive effect.

Both the gcB and the cKdV models possess steady solutions of permanent form. This wave form is a single positive hump of water with the two edging tails quickly decaying as x goes to $\pm\infty$. We call this wave a solitary wave. The solitary wave solutions for the two models are different. We find that for solitary waves of the same speed, the gcB model requires a higher amplitude. The difference between the steady solutions for the two models are negligible for small amplitudes. As the amplitude of the wave gets larger, the difference becomes more appreciable.

The conservation properties of the two wave models, which include conservation of mass and energy, are analyzed. The gcB model is found to conserve mass exactly and conserve energy to certain order, while in general the cKdV model does not conserve either mass or energy, due to the neglect of the reflected waves in our theoretical modeling.

Both models are applied to study the evolution of a solitary wave traveling in a channel of variable width. The objective of this study is not only emphasized on the physical aspects, but also on a more careful examination of the conservation laws and the validity of the cKdV model. The numerical results show that even though the cKdV model does not conserve mass by a broad margin, it still gives the consistent predictions for the main transmitted wave with the results based on the gcB model. The neglect of the reflected waves in the theoretical derivations does not affect the validity of the cKdV model for the dominant transmitted waves.

To investigate the phenomenon of forced generation of nonlinear long waves by external moving disturbances, we carried out a joint theoretical, numerical and experimental study. The theoretical models show that a pressure distribution moving at the free surface and a submerged topography moving along the boundaries play equivalent roles in generating run-away solitons advancing upstream. For a submerged moving object as an external forcing, its effective strength of forcing is directly related to the blockage ratio of the cross-sectional area, while the detailed geometry or the particular position of the disturbance in the cross-flow plane are less important. We conducted a series of experimental measurements in a shallow water tank to study the generation of forced run-away solitons by submerged moving topographies. The experimental results confirmed the theoretical conclusion on the blockage-ratio concept regarding the effective strength of the external forcing functions. Various numerical computations were also performed to examine the effects of the speed and the length of the forcing agencies. Based on these numerical results, we found that our theoretical models give consistent results for disturbances that are sufficiently long in the longitudinal direction. However, our experimental results show that practically even when the length of the disturbance is of the same order as the water depth, the forced KdV model still gives reasonably good predictions for long wave generations.

The results of our studies have their useful applications in the areas of river dynamics, near-coastal engineering and other related fields. Future research in these areas may include studies on the evolution of long waves propagating in a curved channel and the simulation of wave generations by heavy rainfalls on rivers in the flood season. More experimental studies may need to be performed to investigate the generation and propagation of long waves in a channel of arbitrary cross-sectional shape, other than rectangular cross sections. It will also be of

practical significance to study the dissipation of waves due to the roughness on the channel bottom. Since flood waves in rivers are in general extremely long (can be a hundred times longer than the river depth), the interactions between the surface wave and the bottom sedimentation and the friction must be considered when the results of our models are applied.

Appendix I. A Proof of the Section-Mean Transport Theorem

The theorem (2.10) or (2.11) presented in Chapter II can be proved as follows.

First we take a material volume $V(t)$ which at time t coincides with a vertical column of water lying between two sections at two different x-locations $x = x_1$ and $x = x_2$. Then we integrate the term at the left-hand-side of equation (2.10) from $x = x_1$ to $x = x_2$:

$$\begin{aligned}\int_{x_1}^{x_2}\langle\frac{df}{dt}\rangle &= \int_{x_1}^{x_2}(\int_{-b(x,t)}^{b(x,t)}\int_{-h(x,y,t)}^{\zeta(x,y,t)}\frac{df}{dt}dzdy)dx \\ &= \int_{x_1}^{x_2}[\int_{-b}^{b}\int_{-h}^{\zeta}(\frac{\partial f}{\partial t}+\frac{\partial uf}{\partial x}+\frac{\partial vf}{\partial y}+\frac{\partial wf}{\partial z})dzdy]dx,\end{aligned} \tag{AI.1}$$

where we have used $\nabla \cdot \mathbf{U} = 0$.

Equation (AI.1) can be further written as

$$\begin{aligned}\int_{x_1}^{x_2}\langle\frac{df}{dt}\rangle dx = \int_{x_1}^{x_2}dx[&\frac{\partial}{\partial t}\int_{-b}^{b}\int_{-h}^{\zeta}fdzdy-\int_{-h}^{\zeta}f(x,b,z,t)\frac{db}{dt}dz \\ &-\int_{-h}^{\zeta}f(x,-b,z,t)\frac{db}{dt}dz-\int_{-b}^{b}f(x,y,\zeta,t)\frac{d\zeta}{dt}dy \\ &-\int_{-b}^{b}f(x,y,-h,t)\frac{dh}{dt}dy+\frac{\partial}{\partial x}\int_{-b}^{b}\int_{-h}^{\zeta}ufdzdy \\ &+\int_{-h}^{\zeta}(vf)|_{-b}^{b}dz+\int_{-b}^{b}(wf)|_{-h}^{\zeta}dy].\end{aligned} \tag{AI.2}$$

By applying the boundary conditions (2.3), (2.5) and (2.6) in Chapter II, we can see that all boundary terms at the right-hand-side of AI.2 cancel each other out to give

$$\begin{aligned}\int_{x_1}^{x_2}\langle\frac{df}{dt}\rangle dx &= \int_{x_1}^{x_2}[\frac{\partial}{\partial t}\int_{-b}^{b}\int_{-h}^{\zeta}fdzdy+\frac{\partial}{\partial x}\int_{-b}^{b}\int_{-h}^{\zeta}ufdzdy]dx \\ &= \int_{x_1}^{x_2}[\frac{\partial}{\partial t}\langle f\rangle+\frac{\partial}{\partial x}\langle uf\rangle]dx.\end{aligned} \tag{AI.3}$$

Since (AI.3) holds for any arbitrary x_1 and x_2, we must have

$$\langle\frac{df}{dt}\rangle = \frac{\partial}{\partial t}\langle f\rangle+\frac{\partial}{\partial x}\langle uf\rangle, \tag{AI.4}$$

or

$$A\overline{\frac{df}{dt}} = \frac{\partial}{\partial t}(A\bar{f}) + \frac{\partial}{\partial x}(A\overline{uf}). \qquad (AI.5)$$

Appendix II. A Algorithm to Solve a Tridiagonal Matrix

A tridiagonal system may be written as

$$a_i U_{i-1} + b_i U_i + c_i U_{i+1} = f_i, \quad i = 1, 2, ...N-1, \qquad (AII.1)$$

where a_i's, b_i's, c_i's and f_i's are given coefficients.

To solve (AII.1), we let

$$U_{i-1} \equiv A_i U_i + B_i, \qquad (AII.2)$$

and substitute (AII.2) into (AII.1) to obtain

$$A_{i+1} = -\frac{c_i}{a_i A_i + b_i}, \qquad (AII.3)$$

$$B_{i+1} = \frac{f_i - a_i B_i}{a_i A_i + b_i}. \qquad (AII.4)$$

For i=1,

$$U_0 = A_1 U_1 + B_1,$$

where U_0 is the given boundary condition. We may take $B_1 = U_0$, A_1=0 and substitute these into (AII.3) and (AII.4) to get all A_{i+1}'s and B_{i+1}'s for $i = 1, 2, ...N-1$. Then we solve (AII.2) backwards for $i = N, N-1, ...2$. At the first step we start the iteration of (AII.2) by using the given value of boundary condition U_N.

Appendix III. Von Neumann Analysis for Numerical Stabilities

In this appendix, we apply the von Neuman method to analyze the numerical stabilities of the finite difference schemes (3.7) and (3.8) for solving the KdV equations. The equations are written for cases with a uniform rectangular channel.

Case I. Stability Criterion for Scheme (3.7)

First we localize ζ to ζ_0 in the nonlinear term and drop the forcing term in scheme (3.7). This will give

$$\begin{aligned}\zeta_i^{j+1} =& \zeta_i^{j-1} + \frac{\Delta t}{\Delta x}(1+\frac{3}{2}\zeta_0)(\zeta_{i+1}^j - \zeta_{i-1}^j) \\ &+ \frac{1}{6}\frac{\Delta t}{(\Delta x)^3}(\zeta_{i+2}^j - 2\zeta_{i+1}^j + 2\zeta_{i-1}^j - \zeta_{i-2}^j).\end{aligned} \tag{AII.1}$$

Substituting $\zeta_i^j = \rho^j e^{\sqrt{-1}i\Delta xk}$ into (AIII.1), we obtain

$$\rho^2 - 2\sqrt{-1}(\sin\Delta xk)\frac{\Delta t}{\Delta x}[1+\frac{3}{2}\zeta_0 + \frac{1}{3(\Delta x)^2}(\cos\Delta xk - 1)]\rho - 1 = 0, \tag{AIII.2}$$

where the two roots ρ_1 and ρ_2 satisfy

$$\rho_1\rho_2 = -1, \tag{AIII.3}$$

$$\rho_1 + \rho_2 = -2\sqrt{-1}(\sin\Delta xk)\frac{\Delta t}{\Delta x}[1+\frac{3}{2}\zeta_0 + \frac{1}{3(\Delta x)^2}(\cos\Delta xk - 1)]. \tag{AIII.4}$$

Stability requires $|\rho| = |\frac{\zeta_i^{j+1}}{\zeta_i^j}| \leq 1$. Thus from (AIII.4), we can see that we must have $|\rho_1|$=1 and $|\rho_2|$=1. Using $|\rho_1 + \rho_2| \leq |\rho_1| + |\rho_2| = 2$, we obtain the stability criterion for scheme (3.7) as

$$\frac{\Delta t}{\Delta x}(1+\frac{3}{2}|\zeta_0|) + \frac{2}{3}\frac{\Delta t}{(\Delta x)^3} \leq 1. \tag{AIII.5}$$

Case II. Stability Criterion for Scheme (3.8)

By following exactly the same procedure as in the previous case, we get the following relation for ρ based on scheme (3.8)

$$\rho^2 - 2\sqrt{-1}\frac{3\Delta t\Delta x}{2\sin^2\frac{\Delta xk}{2} + 3(\Delta x)^2}(1+\frac{3}{2}\zeta_0)(\sin\Delta xk)\rho - 1 = 0, \qquad (AIII.6)$$

where the two roots satisfy

$$\rho_1\rho_2 = -1, \qquad (AIII.7)$$

$$\rho_1 + \rho_2 = -2\sqrt{-1}\frac{3\Delta t\Delta x}{2\sin^2\frac{\Delta xk}{2} + 3(\Delta x)^2}(1+\frac{3}{2}\zeta_0)(\sin\Delta xk). \qquad (AIII.8)$$

By requiring $|\rho_1 + \rho_2| \leq 2$, we obtain the stability criterion for scheme (3.8) as

$$\Delta t \leq \sqrt{\frac{1}{3}}(1+\frac{3}{2}\zeta_0). \qquad (AIII.9)$$

REFERENCES

[1] Camassa, R. and Wu, T.Y. 1989 The Korteweg-de Vries model with boundary forcing, *Wave Motion II, Elsevier Science Publishers B.V. (North-Holland)*, 495-506

[2] Chang, P., Melville, W.K. and Miles, J.W. 1979 On the evolution of a solitary wave in a gradually varying channel, *JFM*, **95**, 401-414

[3] Chu, C.K., Xiang, L.W. and Baransky, Y. 1983 Solitary waves induced by boundary motion, *Comm. Pure and Appl. Math.*, **36**, 495-504

[4] David, D., Levi, D. and Winternitz, P. 1987 Integrable nonlinear equations for water waves in straits of varying depth and width, *Studies in Applied Math*, **76**, 133-168

[5] Dodd, R.K., Eilbeck, J.C., Gibbon, J.D. and Morris, H.C. 1982 Solitons and nonlinear wave equations, *Academic Press*

[6] Ertekin, R.C. 1984 Soliton generation by moving disturbances in shallow water: Theory, computation and experiments, Ph.D. thesis, University of California, Berkeley, CA

[7] Ertekin, R.C., Webster, W.C. and Wehausen, J.V. 1986 Waves caused by a moving disturbance in a shallow channel of finite width, *JFM*, **169**, 275-292

[8] Goring, D.G. 1978 Tsunamis – the propagation of long waves onto a shelf, Ph.D. thesis, California Institute of Technology, Pasadena, CA.

[9] Hammack, J.L. and Segur, H. 1974 The Korteweg-de Vries equation and water waves, part 2, Comparison with experiments, *JFM*, **65**, 289-314

[10] Johnson, R.S. 1973 On the development of a solitary wave moving over an uneven bottom, *Proc. Camb. Phil. Soc.*, **73**, 183-203

[11] Katsis, C. and Akylas, T.R. 1987 On the excitation of long nonlinear water

waves by a moving pressure distribution, part 2, Three-dimensional effects, *JFM*, **177**, 49-65

[12] Kaup, D.J. and Newell, A.C. 1978 Solitons as particles, oscillators, and in slowly changing media: a singular perturbation thoery, *Proc. R. Soc. Lond. A*, **361**, 413-446

[13] Keulegan, G.H. 1948 Gradual damping of solitary waves, *J. Res. Nat. Bur. Stand.*, **40**, 487-457

[14] Lee, S.J. 1985 Generation of long waves by moving disturbance, Ph.D. thesis, California Institute of Technology, CA

[15] Lee, S.J., Yates, G.T. and Wu, T.Y. 1989 Experiments and analyses of upstream-advancing solitary waves generated by moving disturbances, *JFM*, **199**, 569-593

[16] Lepelletier, T.G. 1980 Tsunamis – harbor oscillations induced by nonlinear transient long waves, Ph.D. thesis, California Institute of Technology, Pasadena, CA

[17] Mei, C.C. 1986 Radiation of solitons by slender bodies advancing in a shallow channel, *JFM*, **162** 53-67

[18] Miles, J.W. 1976 Damping of weakly nonlinear shallow-water waves, *JFM*, **76**, 251-257

[19] Miles, J.W. 1979 On the Korteweg-de Vries equation for a gradually varying channel, *JFM*, **91**, 181-190

[20] Miura, R.M., Gardner, C.S. and Kruskal, M.D. 1968 Korteweg-de Vries Equation and Generalizations. II. Existence of conservation laws and constants of motion, *J. Mathematical Phys.*, **vol.9, no.8**, 1204-1209

[21] Peregrine, D.H. 1967 Long waves on a beach, *JFM*, **27**, 815-827

[22] Peregrine, D.H. 1968 Long waves in a uniform channel of arbitrary cross

section, *JFM*, **32**, part 2, 353-365

[23] Peters, A.S. 1966 Rotational and irrotational solitary waves in a channel with arbitrary cross section, *Comm. on Pure and Appl. Math.*, **Vol.19**, No.4, 445-471

[24] Shen, M.C. 1969 Asymptotic theory of unsteady three-dimensional waves in a channel of arbitrary cross section, *SIAM J. Appl. Math.*, **Vol.17**, No.2, 260-271

[25] Shen, M.C. and Zhong, X.C. 1981 Derivation of K-d V equations for water waves in a channel with variable cross section, *J. de Mecanique*, **Vol.20**, No.4, 789-801

[26] Shuto, N. 1974 Nonlinear long waves in a channel of variable section, *Coastal Engn. in Japan*, **17**, 1-12

[27] Whitham, G.B. 1974 Linear and nonlinear waves, *John Wiley & Sons*, New York

[28] Wu, D.M. and Wu, T.Y. 1982 Three-dimensional nonlinear long waves due to moving surface pressure, *In Proc. 14th Symp. on Naval Hydrodynamics*, 103-125, National Academy of Sciences, Washington, D.C.

[29] Wu, T.Y. 1981 Long waves in ocean and coastal waters, *ASCE*, **107**, No.EM3, June

[30] Zabusky, N.J. and Kruskal, M.D. 1965 Interaction of solitons in a collisionless plasma and the recurrence of initial states. *Phys. Rev. Lett.*, **15**, 240-243

[31] Zelt, J.A. 1986 Tsunamis: the response of harbours with sloping boundaries to long wave excitation, Ph.D. thesis, California Institute of Technology, Pasadena, CA